# The impact of radio-emitting supermassive black holes on their environment: the LOFAR view of the Virgo cluster

Francesco de Gasperin

München 2012

# The impact of radio-emitting supermassive black holes on their environment: the LOFAR view of the Virgo cluster

**Francesco de Gasperin**

Erstgutachter: Simon White

Zweitgutachter: Joseph Mohr

Tag der mündlichen Prüfung: 21. September 2012

# Contents

# List of Figures

# List of Tables

# Summary

The main topic of this Ph.D. thesis is the study of accreting super-massive black holes in active galactic nuclei (hereafter AGN). AGNs are fairly complex objects, for which we are not yet close to a complete understanding. The processes dominating their formation, accretion and interaction with the environment are related to an extraordinary variety of diverse physical domains: general relativity, accreting disks, jets, plasma physics, synchrotron emission and much more. The regime of low accretion rate, albeit being one of the most intriguing AGN expressions, have started to be explored only recently. Active nuclei accreting at these low rates are usually faint and therefore defined as *Low-Luminosity AGN* or LLAGN. They swallow less material (relatively to their mass) than bright quasars, but they are able to generate powerful jets. These jets have a strong impact on the surrounding environment, creating a direct physical link between the black hole and the hosting galaxy (or even cluster). Such a link has become an unavoidable ingredient of cosmological simulations and is fundamental for the understanding of the Universe as we see it now.

Given the ubiquitous production of radio jets in LLAGNs, the best tools for their analysis are radio-telescopes. Consequently, a substantial amount of work in my Ph.D. has been devoted to discovering and exploiting the capabilities of a novel, and for some aspects revolutionary, radio-telescope, the Low-Frequency Array (LOFAR). This telescope is able to observe in the unexplored band of $30-240$ MHz, that are the lowest accessible frequencies for a ground-based telescopes. LOFAR started to be operational in summer 2009, and after two years of intense commissioning activity the instrument was mature enough to produce its first scientific results, one of those being the main achievement of this work.

I will start presenting a wide overview of the AGN phenomenon, principally under an observational point of view, defining AGN operationally (Sec. 1.1) and discussing their classification

(Sec. 1.2). Then, I will present the black hole accretion model as an explanation for AGN activity, focussing on its spectral energy distribution and, in particular, on the radio emission it produces (Sec. 1.3). Finally, I will describe the influence that an AGN has on its hosting environment, from galactic to cluster scales (Sec. 1.4).

As an introduction to my investigations, I will present a multi-frequency study of a relatively small, but well-selected, sample of radio-loud LLAGN. I will discuss the observations of such a sample taken at X-ray, optical and radio wavelengths, and critically review the mechanisms which produce their emissions (Sec. 2.4), to finally draw some conclusions on the underlying physics. The results led to the association of X-ray and radio production to the same physical mechanism, i.e. synchrotron emission from the base of the jet.

In the third chapter, I will describe the LOFAR telescope, starting with a modern overview of radio-interferometry and aperture synthesis. Then, I will describe the details of the instrument and of its performances (Sec. 3.2), and I will analyse the challenges of low-frequency radio observations (Sec. 3.3). Finally, I will show some examples of the commissioning work carried out by a large team of astronomers, including myself (Sec. 3.4).

In the last part of the thesis, I will present the first LOFAR observations of the Virgo cluster, focussing in particular on Virgo A (M87), which shows one of the most clear examples of AGN-cluster interaction. Images of M87 at low radio frequencies, never explored before at these high spatial resolution and dynamic range, are presented (Sec. 4.3). I performed a detailed spectral analysis of the extended radio-halo of M87, in order to disentangle different synchrotron models and place constraints on source magnetic field, age and energetics (Sec. 4.4). In the last chapter of the thesis, instead, I will focus on the other sources present in the field, quantifying LOFAR radio flux densities and morphologies of 13 late- and 2 early-type galaxies which belong to the Virgo cluster. A detailed analysis of their emission will be presented (Sec. 5.3), together with a study of their radio-FIR (far infrared) correlation (Sec. 5.4).

The LOFAR observations described in this work provided an unprecedented view of the LLAGN physics and of the mechanisms which rule the AGN interaction with the surrounding environment. These results are also one of the very first scientific outcomes of a new-generation radio-telescope and reveal the extraordinary possibilities opened by these instruments.

# Zusammenfassung

Das Hauptthema dieser Doktorarbeit ist die Erforschung von akkretierenden super massere-ichen Schwarzen Löcher in Aktiven Galaktischen Kernen (AGN). Das Regime der niedrigen Akkretionsrate wird erst seit Kurzem erforscht, obwohl es eins der faszinierendsden AGN Aspekte ist. Die Akkretion von AGN bei desen niedrigen Raten ist meistens schwach und wird deshalb als *Low-Luminosity AGN* oder LLAGN bezeichnet. Sie nehmen weniger Material (relativ zu ihrer Masse) als die hellen Quasare auf, aber sie können starke Jets erzeugen. Diese Jets haben einen großen Einfluss auf das umgebende Umfeld, in dem sie eine direkte physikalische Verbindung zwischen dem Schwarzen Loch und der beinhaltenden Galaxie (oder sogar Cluster) erzeugen. So eine Verbindung ist zu einem unvermeidlichen Bestandteil der kosmologischen Simulationen geworden und ist fundamental für das Verständis des Universums, wie wir es heute sehen.

Angesichts der allgegenwärtigen Produktion von Radio-Jets in LLAGNs sind Radio-Teleskop die besten Werkzeuge um diese zu analysieren. Infolgedessen ist ein wesentlicher Teil meiner Doktorarbeit, dem Erforschen und Ausnutzen der Leistungsfähigkeit des neuen Radio-Teleskop Low-Frequency Array (LOFAR), gewidmet. Dieses Teleskop kann den unerforschten Bereich von $30-240$ MHz beobachten, die niedrigsten zugänglichen Frequenzen für ein Erdgebundenes Teleskop.

Ich werde damit anfangen eine breite Übersicht über der AGN Phänomene zu geben, haupt-sächlich vom Standpunkt eines Beobachters. Danach werde ich das Modell akkretierender Schwarze Löcher als eine Erklärung für die Aktivität von AGN darlegen, wobei ich mich auf die spektral Energie Verteilung (Sec. 1.3) konzentriere. Schließlich werde ich den Einfluss den AGN auf ihre Umgebungen haben beschreiben (Sec. 1.4).

Als einen Einstieg in meine Erforschungen werde ich eine Multi-Frequenz-Studie von einer

gut selektierten Stichprobe von LLAGN zeigen. Ich werde die Beobachtungen von solch einer Probe diskutieren und die Mechanismen, die ihre Emission produzieren, kritisch überprüfen (Sec. 2.4), um schließlich ein paar Schlussfolgerungen auf die zugrunde liegende Physik zu ziehen. Die Ergebnisse führen zu der Assoziation, dass Röntgen- und Radio-Strahlen von dem gleichen physikalischen Mechanismus erzeugt werden, d.h. Synchrotronstrahlung von der Basis des Jets.

Im dritten Kapitel werde ich das LOFAR-Teleskop beschreiben, beginnend mit einem Überblick über moderne Radiointerferometrie und Apertursynthese. Danach werde ich die Details der Instrumente und deren Funktionen beschreiben (Sec. 3.2) und ich werde die Herausforderungen von niederfrequenter Radio Beobachtung analysieren (Sec. 3.3). Schließlich werde ich ein paar Beispiele geben für die Arbeit, die von einem großen Team von Astronomen, einschließlich mir, zur Inbetriebnahme des Teleskop durchgeführt wird (Sec. 3.4).

Im letzten Teil meiner Arbeit werde ich die ersten LOFAR Beobachtungen vom Virgo-Galaxien-Haufen zeigen, mit Fokus auf Virgo A (M87), was eines der eindeutigsten Beispiele für AGN-Galaxiehaufen-Wechselwirkung zeigt. Dort werden auch Bilder von M87 bei niederen Radio Frequenzen, die noch nie zuvor bei dieser hohen räumlichen Auflösung und dynamischen Bereich untersucht wurden, gezeigt (Sec. 4.3). Ich führte eine detaillierte spektrale Anlyse des ausgedehnten Radio-Halo von M87 durch, um verschiedene Synchroton-Modelle zu unterscheiden und Einschränkungen auf Quellmagnetfelder, Alter und Energetik zu ermöglichen (Sec. 4.4). Schießlich werde ich mich im letzten Kapitel der Dissertation auf die anderen im Bildfeld vorhandenen Quellen konzentrieren und dabei deren LOFAR Radioflussdichten und Morphologie bestimmen. Es wird eine detaillierte Analyse ihrer Emission dargelegt (Sec. 5.3), zusammen mit einer Untersuchung der Korrelation von Radio und FIR (fernes Infrarot, Sec. 5.4).

Die in dieser Arbeit beschriebenen LOFAR Beobachtungen gaben einen umfassenden Überblick über die LLAGN Physik und die Mechanismen, die die Interaktion von AGN mit ihrer Umgebung bestimmen. Diese Ergebnisse sind auch eine der allerersten wissenschaftlichen Resultate einer neuen Generation von Radioteleskopen und zeigen die außergewöhnlichen Möglichkeiten, die dieses Instrument eröffnet.

# Active Galactic Nuclei

Active Galactic Nuclei (hereafter AGN) are compact regions in the centre of galaxies. Their principal characteristic is to have a luminosity that is much higher than normal galactic centres in one or more wavebands. Galaxies with an AGN are called *active galaxies* and they can be up to $10^4$ times more luminous than a typical galaxy. This radiation is likely produced by accretion of matter onto a super-massive black hole (SMBH) at the centre of the host galaxy[1].

## 1.1 Operational definition

The issue of the activity of galactic nuclei was first raised by Victor Ambartsumian in the early 1950s. Although nowadays the black hole model, firstly introduced by Lynden-Bell (1969) to explain AGN activities, has achieved a widespread acceptance (Rees 1984), its not yet fully confirmed because direct signatures of accretion onto SMBH are much harder to detect, as compared to their indirect signals. Unfortunately, there are many ways to detect an AGN but there is no single characteristic present in each of them. I list here some of the AGN most common properties in order to define them operationally:

**Small angular size** This is probably the most striking property of AGNs. Much of the emission they produce comes usually from a very small location in the centre of the hosting galaxy. However, for many close-by AGNs, the emission from the surrounding galaxy easily overwhelm the emission from the AGN, making its detection difficult. By contrast, especially for most distant objects, the emission from the AGN can be so much brighter than that from the galaxy, to be the only visible one. All those considerations also depend strongly on the wavelength. For example, most AGNs have a much grater ratio of X-ray

---

[1]By *super-massive* black holes I mean objects with masses ranging from $10^6$ to $10^{10}$ $M_\odot$, with $M_\odot \simeq 2 \times 10^{33}$ g.
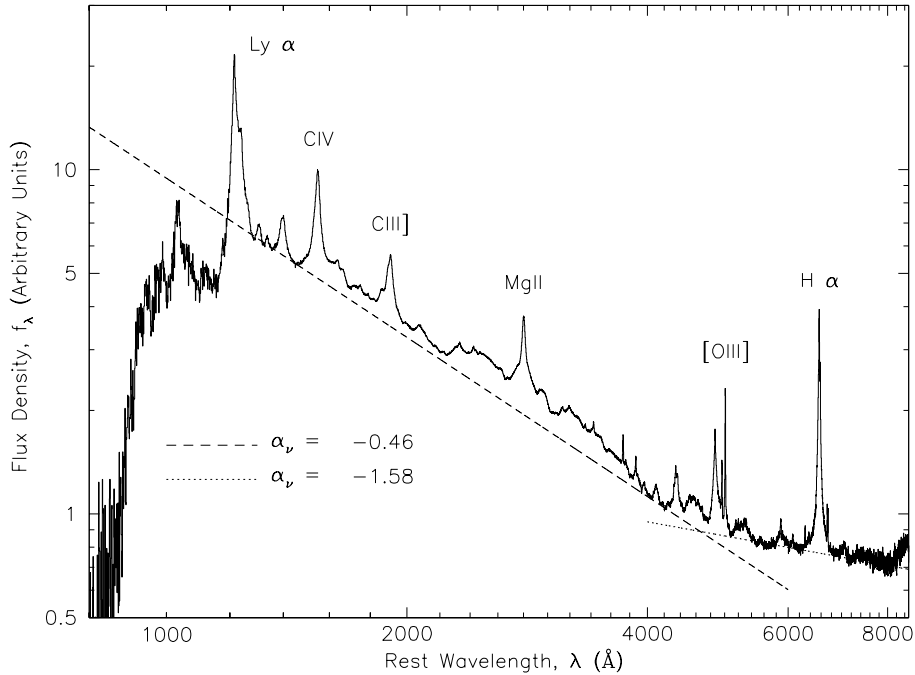
Figure 1.1: Composite quasar spectrum from the Sloan Digital Sky Survey (SDSS). Power-law fits to the estimated continuum flux are also shown. Image from Vanden Berk et al. (2001).

to optical luminosity than the hosting galaxies. Thus, their X-ray images are essentially point sources, as for the cases described in Chap. 2. On the other hand, radio emission often extends over sizeable regions, frequently much larger than the hosting galaxy, as for the case described in Chap. 4.

**High luminosity** The luminosity of a typical AGN is between $10^{42}$ and $10^{48}$ erg s$^{-1}$, while the characteristic luminosity of a galaxy is $\sim 10^{44}$ erg s$^{-1}$. This means that we see AGNs that have from a fraction of percent up to a few thousands times the power output their host galaxy. However these considerations may be biased in different ways: we may not be able to detect weak, low-luminosity, AGNs (see Chap. 2); AGNs can be obscured by extremely thick dust extinction; finally, relativistic beaming can also substantially distort the angular distribution of light coming from AGNs, and the standard assumption of isotropic radiation leads to biased results.

**Variability** In essentially all wavebands, most AGNs show variability in the luminosity. However, the typical amplitude measurable over human timescales (i.e. a few years) is often less than 10%. A small subset of AGNs vary much more clearly, with changes up to a factor of 100 in a few years. Unlike stars, whose variability is dominated by some particular frequencies, AGNs vary with no special timescales and their power density spectra are typically dominated by red noise.
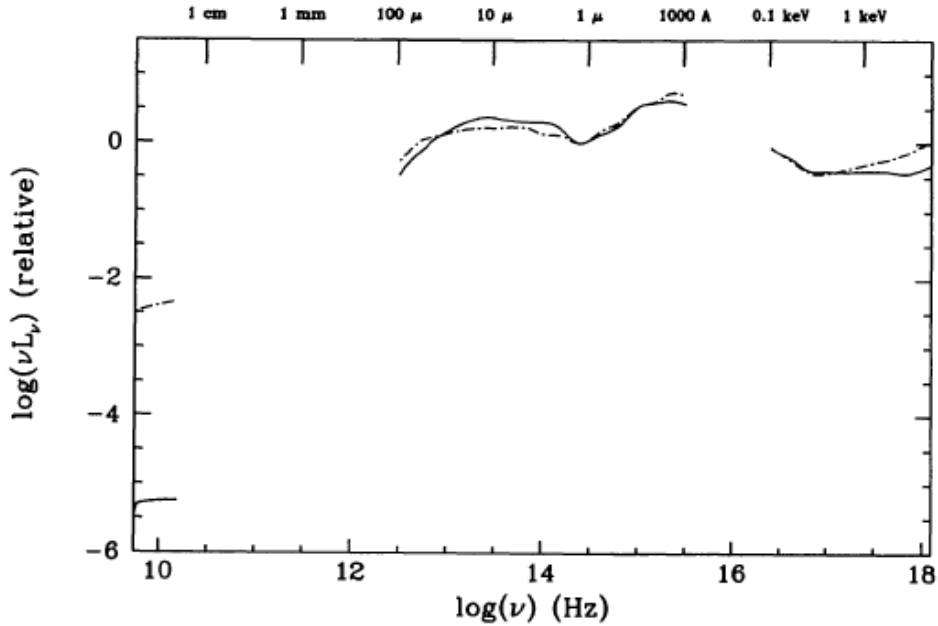
Figure 1.2: Mean quasar spectral energy distribution normalised at 1.25 μm for radio-loud (dashed-line) and radio-quiet (solid-line) quasars. Apart from a clear difference in the radio regime, an X-ray excess is also present in radio-loud quasar. The local maxima in the UV or "big blue bump" at ∼ 1000 Å and in the infrared at ∼ 10 μm are also clearly visible. Image from Elvis et al. (1994).

**Polarisation** Light from stars is intrinsically unpolarised, but the interstellar dust can raise their linear polarisation up to ∼ 0.5%. Most AGNs are also on average weakly polarised (∼ 0.5−2%), but enough to be statistically distinguishable from stars and galaxies. Again, a small fraction of AGNs are much more strongly linearly polarised (∼ 10%).

**Emission lines** Stars and galaxies spectral lines are usually rather weak and mostly in absorption. AGN lines are instead mostly in emission and are often very prominent (with equivalent widths ∼ 100 Å). When AGN optical lines are visible, we almost always see Lyα, the Balmer lines, the Civ 1549 doublet, [Oiii] 5007 and several others (see Fig. 1.1). We can also often detect X-ray lines emission, the best-known of which is the iron Kα line around 6.4 keV (Reynolds 2003). The lines come in two categories: broad ($FWHM > 1000 \text{ km s}^{-1}$) and narrow ($FWHM < 1000 \text{ km s}^{-1}$). The widths of these lines are interpreted as Doppler shifts, and therefore are indicative of gas motions in the regions where they are emitted.

**Broadband emission** To a first approximation, we can model the emission from galaxies as the sum of the emissions of many stars. Within this approximation, we can also assume that each star emits a black body and that in a given galaxy the stellar mix is usually such

that a particular surface temperature dominates. Thus, a typical galaxy emits nearly all its power within about a decade of frequencies. A possible modification to this picture is due to interstellar dust, which absorbs and re-radiates stellar emission in the far-infrared. Most AGN spectra, instead, look very different from this picture, and we can find objects where $\log(\nu F_\nu)$ (the energy flux per logarithmic bandwidth) is almost flat over a factor of $10^5$ in frequency. For this reason, the spectra of AGN are usually characterised as a power law of the form $F \propto \nu^\alpha$ where $\alpha$ is the spectral index. Two features are almost ubiquitous in AGN spectra: an UV and an IR "bump" (see Fig. 1.2). The former is often interpreted as thermal emission from an accretion disc surrounding a central black hole (see e.g., Shang et al. 2005). The latter is believed to be due to thermal emission from warm dust at greater distances from the central engine and it has a much more diverse morphology.

**Radio continuum emission** Radio emission was historically the first method used to recognise an AGN, although we now know that only a small fraction ($\sim 10 - 20\%$) of AGNs have a radio emission that is at least 0.1% of their total luminosity. However, even in the cases where the radio emission is particularly strong, it never accounts for more than $\sim 1\%$ of the bolometric luminosity (see Fig. 1.2). In contrast to the continuum at higher energies (far-IR up to far-UV), which is dominated by thermal emission, the radio emission must have a non-thermal origin. It shows indeed a spectrum characteristic of synchrotron radiation.

## 1.2 Classification

It is convenient to divide AGN into two classes, conventionally called radio-quiet and radio-loud. The first class present an excess in radio emission compared to the second, and both show at least one of the typical AGN features described in Sec. 1.1. It is still not certain whether this division represents a true bimodality or is a product of observational biases. Possible explanations for the radio-quiet/radio-loud diversity may be due to a different spin of the central black hole (Sikora et al. 2007) or in two different accretion states (see Sec. 1.4.1). This latter idea follows the behaviour of X-ray binaries, which are known to switch between two states, one exhibits radio jets with a high-intensity and hard X-ray spectra, while the other does not present strong radio emission from jets, while the X-ray spectra is softer (Körding et al. 2006).

### 1.2.1 Radio-quiet AGNs

Radio quiet AGNs represent the majority of the accreting black holes population. Observationally, they are usually classified according to their luminosity and/or optical spectra characteristics.

**Low-ionization nuclear emission-line regions (LINERs)** these systems show only weak nuclear emission-line regions and no other typical signatures of AGNs. It is still debated whether these object are really AGNs or not. In the first case, they would be the radio-quiet AGNs with the lowest luminosity. Some may be radio-quiet analogues of the low-excitation radio galaxies (LEG), see Secs. 1.2.2 and 2.1.

**Seyfert galaxies** They show optical nuclear continuum emission, narrow and (sometimes) broad emission lines, (sometimes) strong nuclear X-ray emission and (sometimes) a weak radio jet without extended lobes. They are divided into two types: Seyfert 1s, which present broad emission lines, and Seyfert 2s, which present only narrow lines. The host galaxies of Seyferts are usually spiral or irregular galaxies.

**Radio-quiet quasars/QSOs** These objects are the more luminous siblings of the Seyfert galaxies. The distinction between the two classes is arbitrary and is usually expressed in terms of a limiting optical magnitude. Radio-quiet quasars always show strong optical continuum emission, X-ray continuum emission, and broad and narrow optical emission lines. Their host galaxies can be spirals, irregulars or ellipticals.

### 1.2.2 Radio-loud AGNs

Radio loud AGNs represent around 10% of the global AGN population. They are dividend into the following groups.

**Radio-loud quasars** These objects behave exactly like radio-quiet quasars with the addition of emission from a jet, together with nuclear and often extended radio emission.

**Blazars – BL Lac and optically violent variable (OVV) quasar** These object are rapidly variable and polarized in optical, radio and X-ray emission. The main difference between the two sub-groups is that BL Lac objects do not show any emission lines. Although lines may become visible when the variable component is minimal (Vermeulen et al. 1995). OVV quasar are instead normal radio-loud quasar with the addition of variability. Both in BL Lac objects and OVV quasars, the high variability of the emission is believed to originate directly from the relativistic jet that is oriented close to the line of sight.

Table 1.1: Normal galaxies and AGNs characteristics

| Galaxy Type | Active Nuclei | Emission Lines | | X-rays | UV (excess) | Far-IR (excess) | Radio | Jets | Variable | Radio loud |
|---|---|---|---|---|---|---|---|---|---|---|
| | | Narrow[4] | Broad[5] | | | | | | | |
| Normal | no | weak | no | weak | no | no | no | no | no | no |
| Starburst | no | yes | no | some | no | yes | some | no | no | no |
| LINERs | yes | yes | no | weak | no | no | no | no | no | no |
| Seyfert I | yes | yes | yes | some | some | yes | few | no | yes | no |
| Seyfert II | yes | yes | no | some | some | yes | few | yes | yes | no |
| Quasar[3] | yes | yes | yes | some | yes | yes | some | some | yes | 10% |
| BL Lac[1] | yes | no | no | yes | yes | no | yes | yes | yes | yes |
| OVV[1] | yes | no | faint | yes | yes | no | yes | yes | yes | yes |
| Radio galaxy | yes | some | some | some | some | yes | yes | yes | yes | yes |

[1] BL Lac and OVV are sometimes called Blazars – [3] radio quiet Quasar are sometimes called quasi stellar objects (QSO). – [4] A few hundreds of km s$^{-1}$. – [5] several thousands of km s$^{-1}$.

**Radio galaxies** These objects show both nuclear and extended radio emission and their host galaxies are essentially always ellipticals. They can be divided into low-excitation galaxies (LEG) and high-excitation galaxies (HEG). LEGs show no strong narrow or broad emission lines, and their X-ray nuclear emission is likely originated in the jets. They are the best candidates for AGN with radiatively inefficient accretion (see also Chap. 2). On the contrary, HEG (or narrow-line radio galaxies) have emission-line spectra similar to those of Seyfert 2s.

## 1.2.3 Unification

More than 20 years ago a unified model of AGN emerged. According to its tenets that the apparent differences between different types of AGNs arise because of their different orientations with respect to the observer, as I describe in more detail below.

### Radio-quiet

Radio-quiet AGNs are essentially Seyfert galaxies at low-luminosities and quasars at high-luminosities. The unification model unifies type 1 and type 2 Seyfert galaxies assuming that for the first the observer has a direct view of the active nucleus. In the latter instead, the accretion region view is blocked by a torus-shaped or patchy structure of obscuring material, which prevents us from detecting the optical continuum emission, the broad-lines and core (soft) X-ray emission. Therefore, the two types of objects are the same, albeit observed from a different orientation.
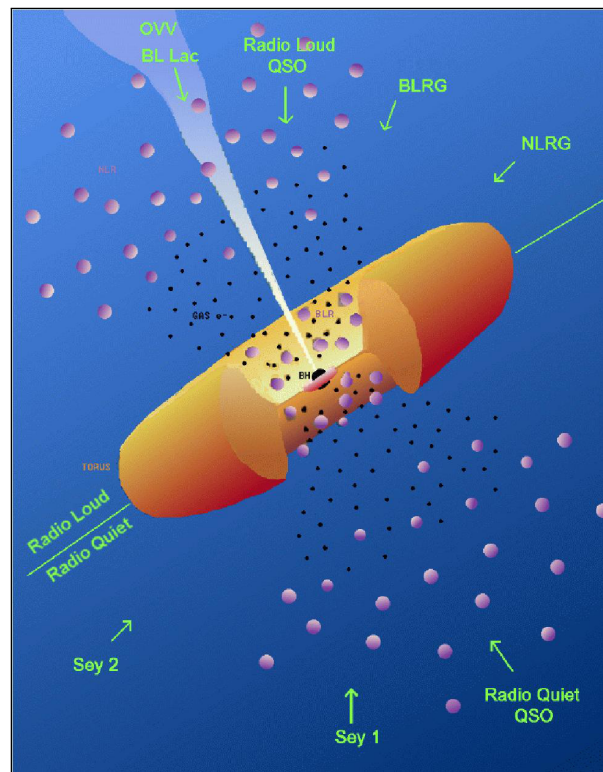
Figure 1.3: The basic structure for active galactic nuclei, as postulated by unified schemes.

The obscuring torus should be large enough to obscure the accretion and the broad-line region but it does not obscure the narrow-line region, which is seen in both classes of objects. Material outside the torus scatter some of the nuclear emission into our line of sight, allowing us to see some optical and X-ray continuum also in Seyfert 2s. Moreover, in some Seyfert 2s, strongly-polarised broad emission lines are also detected, showing that they have been scattered. This proves that Seyfert 2s contain an hidden Seyfert 1s. Finally, thermal emission from the relatively cold torus is now routinely detected by infrared observations of Seyfert 2s, supporting the global picture. At higher luminosities, Seyfert 1s are replaced by quasars, although the corresponding "quasar 2s" are elusive at present.

**Radio-loud**

As for Seyfert 1/2 unification, we can unify the high-luminosity radio-loud quasars (unobscured nucleus) with narrow-line radio galaxies (obscured nucleus). Indeed, X-ray observations of radio galaxies show evidence of obscuration from a torus, while quasars do not. A note of care must be taken in this case, as radio-loud objects may also have a soft X-ray unabsorbed jet-related component (see also Chap. 2 and Barthel 1989). Finally, at angles close to the line of sight, relativistic beaming effect dominates. In this last configuration, blazar of some variety

are most likely seen.

Numerically, the population of radio galaxies is completely dominated by low-luminosity, low-excitation galaxies (LEG). These objects do not show strong nuclear emission lines (broad or narrow), have optical continua which appear to be entirely jet-related (Chiaberge et al. 2002), and their X-ray emission is also consistent with coming purely from a jet (see Chap. 2). They cannot be unified with quasars, since the torus can never hide the narrow-line region to the required extent, and since infrared studies show that there is no evidence for a torus (Ogle et al. 2006). As I will argue in Chap. 2, they probably form a separate class of low-accretion objects in which accretion is radiatively inefficient, and only jet-related emission is important. At small angles to the line of sight, they will appear as BL Lac objects. M87 is a clear example of a low-accreting radio galaxy that show typical features of a BL-Lac object as super-luminal motion (Biretta et al. 1999) and fast variability (Harris et al. 2009), when the central core is observed.

## 1.3 The Black Hole Model

Not many physical mechanisms are able to provide extremely high luminosities from extremely compact regions and variable over short timescales as it is observed in AGNs. Accretion into a SMBH can potentially give very efficient conversion (up to $\sim 40\%$ of the infalling material rest mass) of potential and kinetic energy to radiation. SMBH are now believed to exist in the centres of most, or all, massive galaxies. Furthermore, when the mass of the SMBH is measurable, it correlates well with the velocity dispersion of the galaxy bulge (the $M - \sigma$ relation Ferrarese & Merritt 2000; Gebhardt et al. 2000; Tremaine et al. 2002; Gültekin et al. 2009) and with bulge luminosity (see e.g. Marconi & Hunt 2003). It is natural to expect that AGN-like characteristics car arise whenever a supply of material for accretion comes within the sphere of influence of the central black hole.

Among the many possible arguments, I decided to provide here one reason in favour of the accretion onto compact objects as the most plausible engine for AGNs. The idea was elaborated by Soltan (1982). Assuming an average mass-energy conversion efficiency of $\eta \sim 0.1$ (as predicted from standard accretion theory, see Sec. 1.3.1), it is possible to transform the mean energy density of AGN radiation into a mean mass density of AGN remnants. The mean energy density of AGN radiation can be derived once the luminosity functions of AGN at different redshifts are provided. This calculation is presented in Krolik & Di Matteo (1999) and provides a mean energy density of

$$\langle U \rangle = 2 \times 10^{-26} \, (L_{\mathrm{bol}}/10 L_{\mathrm{B}}) \, (A/3) \, \mathrm{erg \, cm^{-3}} \,, \tag{1.1}$$

where the author convert the B-band luminosity $L_{\mathrm{B}}$ to a bolometric luminosity $L_{\mathrm{bol}}$ assuming a conversion factor of 10. The factor $A$ has a value of a few and takes into account that the

bolometric correction depends on redshift and that the photon energies diminish with the cosmological expansion. To put the mean AGN energy density in perspective, starlight energy density (*in* the Galaxy) is a factor of $\sim 10^4$ greater while, CMB energy density is a factor of $\sim 10^3$ greater. It is now possible to use the efficiency factor $\eta$ to convert this mean energy density in a mean mass density of AGN remnants, obtaining

$$\langle M_{\mathrm{rem}} \rangle = 2 \times 10^{-36} \, (L_{\mathrm{bol}}/10L_{\mathrm{B}}) \, (A/3) \, (\eta/0.1) \ \mathrm{g \, cm}^{-3} \, . \tag{1.2}$$

This provide an average remnant mass per galaxy of the order of $10^7 \, (\eta/0.1) \, M_\odot$. Any mechanism with a lower efficiency factor than accretion onto a black hole (nuclear reactions have $\eta \simeq 10^{-4}$) would have consumed a considerable fraction of galaxies mass.

Astrophysical black holes form a two parameters family. They can in fact be completely characterized by their mass $M_{\mathrm{BH}}$ and by their spin $a$ (specific angular momentum in geometrical units, Misner et al. 1973)[2]. The mass provides the intrinsic black hole scale of length, time and energy and allows us to relate the observational properties of stellar black holes and supermassive black holes simultaneously (see e.g. Merloni et al. 2003, and Sec. 2.4.3). On the other hand, black holes almost certainly spin quite rapidly, since the material that surrounds them has always far more specific angular momentum than the maximum that a black hole can have.

The smallest observable structure of a black hole is its gravitational radius

$$r_{\mathrm{g}} = \frac{GM_{\mathrm{BH}}}{c^2} \equiv \frac{r_{\mathrm{S}}}{2} \, , \tag{1.3}$$

where $G$ is the gravitational constant, $M_{\mathrm{BH}}$ is the black hole mass, $c$ is the speed of light and $r_{\mathrm{S}}$ is defined as the Schwarzschild radius. For instance, Sagittarius A$^*$, the SMBH in the centre of the Milky Way, has a Schwarzschild radius of 0.1 AU (using $M_{\mathrm{BH}} = 4 \times 10^6 \, M_\odot$, Ghez et al. 2008). In the near future, very long baseline interferometry (VLBI) observations at mm-band will produce maps with enough angular resolution ($\sim 10$ µarcsec, that is $\sim 0.1$ AU at 8 kpc) to observe the centre of our Galaxy down to the central black hole Schwarzschild radius scales. These observations will finally provide definitive evidence on the hypothesis that SMBH are the engines responsible for AGN activity.

### 1.3.1 Accretion

In the standard model, AGN accretes cold material close to the central black hole. The gas flow most likely forms an accretion disc, where (not yet fully understood) dissipative processes

---

[2]Charge is a third parameter that is usually used to characterize a black hole. However, under astrophysical conditions, black hole are thought to discharge almost immediately.

transport matter inwards and angular momentum outwards, while heating the disc itself. To give a complete overview, I decided to start this section with the simplest model possible: smooth time-steady spherically-symmetric accretion, or Bondi accretion (Bondi 1952).

**Bondi accretion**

This type of accretion, although modelled in a very simplistic way, is realistic in situations where the accreting gas is so hot that its temperature approaches the virial temperature (the thermal energy of the particle is comparable to their gravitational binding) or where the pressure of trapped photons is so great to provide a significant support against gravity.

Assuming that at large distance from the black hole the gas moves slowly (relative to the black hole) and it has a defined temperature and a density, then we can use standard fluid dynamics to describe its motion. The continuity equation for mass conservation is

$$\frac{\partial \rho}{\partial t} + \nabla \cdot (\rho \boldsymbol{v}) = 0 \,, \tag{1.4}$$

where $\rho$ is the gas density, $\boldsymbol{v}$ is its velocity. The right hand side is zero since there are no sources or sinks of matter. In a spherical symmetry and for a time-steady flow its solution is

$$\dot{M} = 4\pi r^2 \rho v \,. \tag{1.5}$$

In a rigorous treatment one should now use the force equation, which in turn provides the Bernoulli equation and solve the latter and the continuity equation assuming an equation of state (Bondi 1952). Alternatively, an approximate derivation, using scaling relations, can be found if the effective radius is acquired by equating the escape velocity of the gas and the sound speed $c_s$

$$\sqrt{\frac{2GM}{r}} = c_s \rightarrow r = \frac{2GM}{c_s^2} \,. \tag{1.6}$$

Flow outside this radius is subsonic, and the density is almost uniform. Within it, the gas becomes supersonic and moves towards a free-fall solution. Therefore, the accretion rate becomes

$$\dot{M} = \frac{4\pi \rho G^2 M^2}{c_s^3} \,. \tag{1.7}$$

This equation provides a characteristic scale of the accretion given a central mass and a gas density and sound speed. In the Bondi scenario one neglects back-reactions of the radiation on the flows. The dominant emission mechanism will be thermal *bremsstrahlung*, which is proportional to the density and temperature. Therefore the emission is expected to be dominated by the flow near the event horizon, which has high density and temperature, and the accretion process is expected to be very inefficient in producing radiation.

This description, as said, has so far ignored that the central object can generate a vast amount of radiation. This radiation generate an outward force on a free proton that is

$$F_{\text{rad}} = \frac{1}{c} \int d\nu \, \boldsymbol{F}_\nu \, \kappa(\nu) m_{\text{p}} \,, \tag{1.8}$$

where $F_\nu$ is the radiation flux density per unit frequency $\nu$ and $\kappa(\nu)$ is the opacity per unit mass. For ionized hydrogen $\kappa = \sigma_{\text{T}}/m_{\text{p}}$, where $\sigma_{\text{T}}$ is the Thomson scattering cross-section for the electron and $m_{\text{p}}$ is the mass of a proton. Therefore, rewriting in term of luminosity $L_\nu$ the flux density $F_\nu = L_\nu/(4\pi r^2)$, one can find

$$F_{\text{rad}} = \sigma_{\text{T}} \int d\nu \frac{L_\nu}{4\pi c r^2} \,. \tag{1.9}$$

in the radial direction. Equating $F_{\text{rad}}$ with the gravitational force $F_{\text{grav}} = GMm_{\text{p}}/r^2$ one obtains

$$L_{\text{Edd}} = \frac{4\pi GMm_{\text{p}}c}{\sigma_{\text{T}}} \simeq 1.5 \times 10^{38} \frac{M}{M_\odot} \text{ erg s}^{-1} \,. \tag{1.10}$$

This is for a given mass $M$ the critical luminosity (or Eddington luminosity $L_{\text{Edd}}$) beyond which the radiation force must overpower gravity. Given the observed AGN luminosities of $10^{43} - 10^{47}\text{erg s}^{-1}$, it is easy to find that the minimum demanded central mass is in the range $10^5 - 10^9 \, M_\odot$. The same value for the Eddington luminosity can be found in the axisymmetric case (see e.g. Frank et al. 2002), i.e. for accretion discs, that I describe below.

## 1.3.2   Accretion discs

Accreting gas has almost certainly enough angular momentum to form a disc or a torus. It is indeed expected that the matter orbiting around the central black hole, penetrate another inclined orbit plane and collide with other matter mixing the angular momentum and eventually concentrating on a single common plane.

The approach of material towards a black hole requires eliminating almost all the material's initial angular momentum. Since the total angular momentum of the disc is conserved, any angular momentum loss of the mass falling into the center, has to be compensated by an angular momentum gain of the mass far from the center. This means that angular momentum should be transported outwards. This is a slow process and allow the disc to radiate away much of its binding energy, therefore disc accretion is much more efficient than Bondi accretion in producing radiation.

Shakura & Sunyaev (1973) proposed turbulence in the gas as the source of viscosity $\nu$ which in turn provides heat generation and transport of angular momentum. The only non-zero component of the stress tensor $t_{r\phi}$ provides a viscous torque $\mathcal{G}$ of

$$\mathcal{G} = 2\pi r^3 \nu \Sigma \frac{\partial \Omega}{\partial r} \,, \tag{1.11}$$

where $\Sigma$ is the surface density of the disc, $\Omega$ is the angular velocity and $\nu$ is the viscosity. If $\partial\Omega/\partial r < 0$, then $\mathcal{G} < 0$ and the angular momentum is transported outwards. The main assumption of the model is that the viscosity $\nu$ has to be proportional to the total (gas+radiation) vertically-averaged pressure in the disc $p$, i.e.

$$\nu = \alpha p \,, \tag{1.12}$$

where $0 < \alpha < 1$ is the so called *viscosity parameter* and is also the reason why this model is sometimes called the $\alpha$-model. The larger $\alpha$ is, the more efficient is transport of angular momentum outwards, which leads to higher radial velocity of the flow and lower surface density of the disc.

   At accretion rates below a few per cent of $L_{Edd}$ the gas pressure dominates throughout the accretion disc. However, when the accretion rate increases, a radiation pressure-dominated region develops in the inner part of the disc. Then the disc becomes unstable and the optically thick, geometrically thin disc model is probably not realistic any more. An alternative model, known as the $\beta$-disc (Lightman & Eardley 1974; Piran 1978), solves this problem assuming that the viscosity is proportional only to the gas pressure.

**Emitted spectrum**

The spectrum of a Shakura-Sunyaev disc is, to a first approximation, a superposition of black-body spectra of different temperatures. The local temperature at the radius $r$ is given by

$$T(r) = \left[ \frac{3GM\dot{M}}{8\pi\sigma r^3} \left( 1 - \sqrt{\frac{6r_s}{r}} \right) \right]^{1/4} \text{ K} \,, \tag{1.13}$$

where $\sigma$ is the Stefan-Boltzmann's constant.

   For AGN typical masses the expected spectrum of the accretion disc peaks in the optical-ultraviolet waveband, while for stellar black holes it peaks in the soft X-ray, as observed. In addition, a corona of hot material forms above the accretion disc and can inverse-Compton scatter photons up to X-ray energies. The radiation from the accretion disc excites cold atomic material close to the black hole and this radiates via emission lines. Finally, a large fraction of the AGN's primary output may be obscured by interstellar gas and dust close to the accretion disc, but (in a steady-state situation) this will be re-radiated at some other waveband, typically in the infrared.

**Low accretion rates**

At accretion rates far below the Eddington rate the gas density is low, and the gas may be unable to radiate energy at a rate that balances viscous heating, therefore radiation escape-time

exceeds the time scale of accretion (Jaroszynski et al. 1980). Then, a part of the produced radiation is advected under the black hole horizon instead of being all radiated away as in the Shakura-Sunyaev disc. As a result, the radiative efficiency of the flow is diminished. Accretion flows where advection occurs are named ADAFs, i.e. Advection Dominated Accretion Flows (Narayan & Yi 1994).

In stellar mass black holes, which cycle between different states, the "high soft state" (high luminosity, soft X-ray spectrum) may correspond to thin disc accretion and the "low hard state" to something like an ADAF (for a review see e.g. Done 2010). AGN might go through similar cycles on a longer time-scale.

From the point of view of accretion theory, there are therefore two main classes of accreting objects which can be divided on the basis of their radiative efficiency $\eta \equiv L/\dot{M}c^2$, where $L$ is the luminosity produced by the accretion flow and $\dot{M}$ is the accretion rate (thus $\dot{M}c^2$ is the rate at which rest mass energy is accreted). If the dissipated energy is radiated away on timescales shorter than the time it takes the gas to flow into the black hole, the gas cools rapidly, a thin disc is formed and the efficiency $\eta$ is then in the range $0.06 - 0.4$ (depending on the black hole spin). By contrast, if the gas cannot radiate it energy it form a hot thick accretion disc with $\eta \ll 1$. In the rest of the thesis, I will mainly focus on this second class of objects.

### 1.3.3 Jets and lobes

It is generally observed that black holes in the inefficient accretion regime, where cooling is dominated by advective processes rather than radiation, can drive powerful, collimated outflows in the form of relativistic jets. Perhaps the best example of such a powerful "low efficiency" black hole is the radio galaxy Virgo A described in Chap. 4, which is the product of inefficient accretion onto the supermassive black hole at the center of M87, which itself is located in the center of the Virgo cluster.

Jets are highly collimated and fast outflows that emerge in opposite directions from close to the disc (the direction of the jet ejection must be determined either by the angular momentum axis of the disc or the spin axis of the black hole). Observational evidence for small-scales jet production comes from observations of M87 (see Fig. 1.4 and Walker et al. 2009), where the jet must be produced within a few hundreds of Schwarzschild radii from the central black hole. Therefore, acceleration of jets is a typical multi-scale problem which spans from scales comparable to the Schwarzschild radii up to the kilo parsec scales. Simulating these phenomena is rather challenging for computational physics. Most simulations show that the speed of the ejected outflow is close to the escape speed at the location of the ejection. This automatically produces jets whose velocity is greater in the centre and slower at the boundaries. This can account for the very edge-brightened appearance of jets, like that shown in Fig. 1.4. Furthermore,
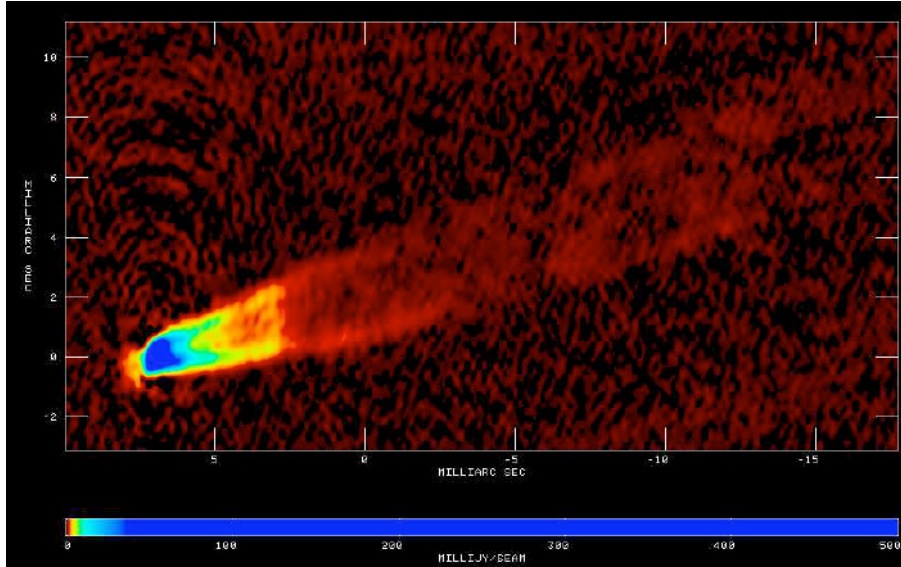
Figure 1.4: High-frequency VLBI mapping of the M87 jet, at 43 GHz from Walker et al. (2009). Thanks to VLBI observations we know that the jet must form as close as a few hundreds Schwarzschild radii.

in maximal-case Kerr rotating black holes stable orbits can exist down to the event horizon, thus generating faster outflows ($\sim 0.9\,c$, i.e. a Lorentz factor $\gamma \simeq 2$).

The jets have the most obvious observational effects in the radio band. However, they radiate in all bands from the radio through to the gamma-rays via the synchrotron and inverse-Compton processes. An open issue is the jets contents: it could be positron/electron pair plasma, hadron dominated, or the jet could carry most of their energy as Poynting flux (see also Sec. 4.4.3 for the case of M87).

Once launched, the jet can carry away non-negligible fraction of the energy stored in the disc converting it into kinetic energy. It may remain collimated for very long distances, flowing through the galaxy and into the surrounding cluster, finally creating large lobes when the swept-up mass is able to decelerate the jet. As an example, in M87 the extended radio lobes generated by the jets are $\sim 80$ kpc wide. The magnetic field is carried along with the jet as it propagates and it reaches its minimum energy aligning with the flow.

As the jet propagates, it carries with it an enormous amount of kinetic flux, and even though the flow is usually lower-density than the surrounding medium, because of its high speed it will deposit large amounts of energy into the surrounding regions. Therefore, jets are able to interfere with the life of the galaxy, triggering star formation in their path as well as shocks that result in heating of the galactic and cluster medium, mixing the inter-stellar medium (ISM) and uplifting cold gas from the galactic centre. For example, simulations by O'Neill et al. (2005) indicate that even light jets will deposit approximately half of their kinetic flux as thermal energy in the surrounding medium. In the case of massive galaxies in the clusters' centres, like

(a) 3C31 $P = 23.92$ W Hz$^{-1}$    (b) 3C272.1 $P = 22.71$ W Hz$^{-1}$    (c) 3C296 $P = 24.08$ W Hz$^{-1}$

(d) 3C47 $P = 26.97$ W Hz$^{-1}$    (e) 3C219 $P = 26.34$ W Hz$^{-1}$    (f) 3C438 $P = 26.84$ W Hz$^{-1}$
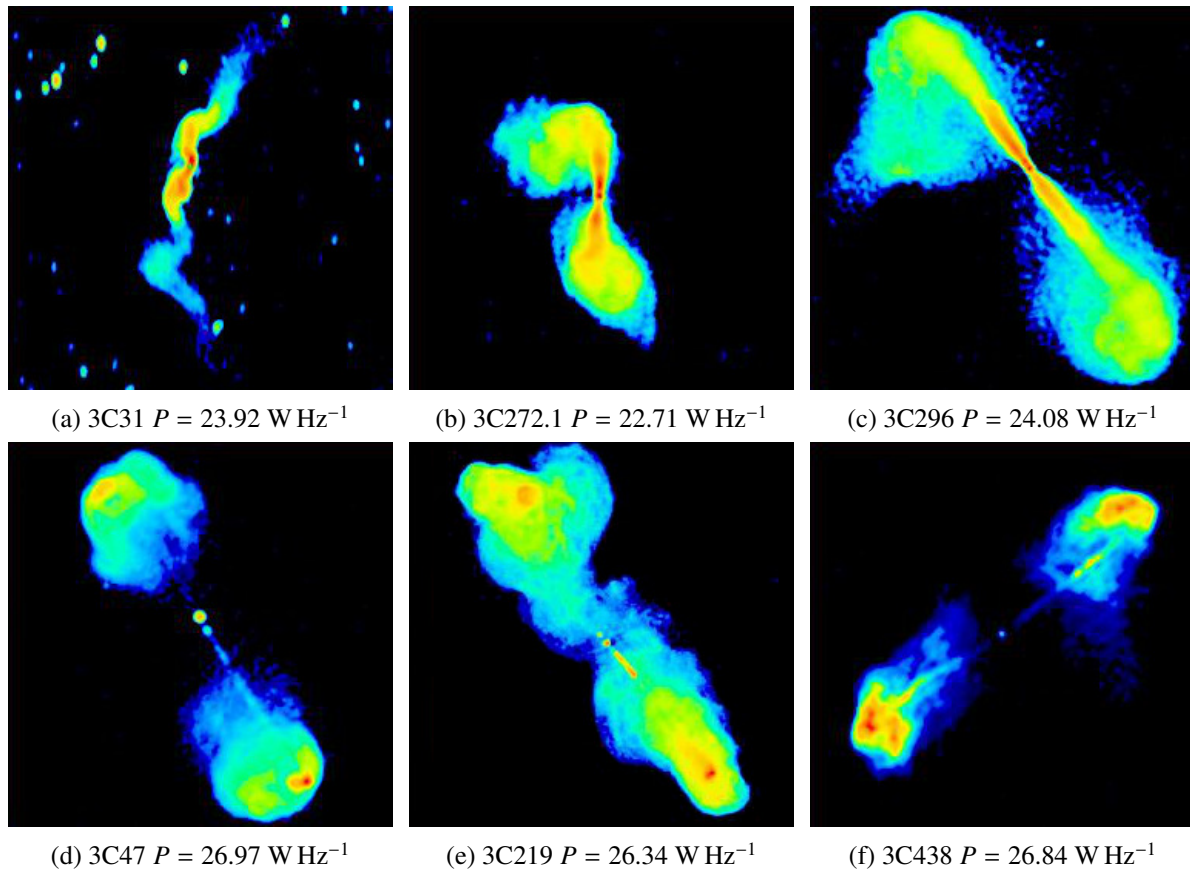
Figure 1.5: In the first line three examples of some famous FRI sources. In the second line three examples of FRII sources. $P = \log P_{178}$ is the logarithm of the radio power at the (emitted) frequency of 178 MHz. Images from http://www.jb.man.ac.uk/atlas/.

M87, half of this flux would go directly into dissipative heating of the intra-cluster medium (ICM), which is believed to be needed to support the re-heating of the cluster gas against cooling flows. The remaining part of the energy would reside primarily in the surrounding extended emission, which is observed on large scales (see Chap. 4).

On large scales, the radio morphology of a radio-emitting galaxy can be fairly complex, but usually one sees highly collimated outflows on one or both sides of the nucleus, terminating in diffuse lobes. In Fig. 1.5 some typical examples of radio galaxies are displayed. In the first row there are three examples of Fanaroff-Riley type 1 radio galaxies (FR I), while in the second row Fanaroff-Riley type 2 (FR II) radio galaxies are shown. The difference between the two groups is in the emitted radio power (FR IIs have an emitted radio power at 178 MHz typically of $P_{178} > 10^{25}$ W Hz$^{-1}$) and in the morphology (FR IIs have straighter jets which terminates in hotspots).

**Emitted spectrum**

Synchrotron radiation from relativistic electrons travelling in the magnetic field of the jet or in the magnetic fields present in the ICM is responsible for radio emission from jets and lobes. Electrons in a magnetic field propagate along helical trajectories, thus they are constantly accelerated by the Lorentz force and consequently they emit at a typical frequency of

$$\nu_c = \frac{3\gamma^2 eB}{4\pi m_e} \approx 4.2\,\gamma^2 \left(\frac{B}{1\,\mathrm{G}}\right)\mathrm{MHz}\,, \tag{1.14}$$

where $\gamma$ is the Lorentz factor, $B$ is the magnetic field strength, $e$ is the electron charge and $m_e$ is the mass of the electron. At frequencies $\ll \nu_c$, the spectrum of a single electron is $\propto \nu_c^{1/3}$, whereas at larger frequencies it has an exponential cut-off. Travelling in a typical magnetic field of $\sim 100\,\mu$G electrons can radiate at cm-wavelengths if they have a $\gamma \simeq 10^4$. A mechanism to accelerate particles to such velocities is believed to be Fermi acceleration (also called diffusive shock acceleration). Fermi acceleration naturally produces a power-law distribution of particle energies (Longair 1994), with a number density $N(E)\mathrm{d}E \propto E^{-\delta}\mathrm{d}E$. Synchrotron radiation from a population of particles that has a power-law energy distribution will also be a power-law, but with a spectral index of $\alpha = (\delta - 1)/2$.

At low radio frequencies another phenomenon can become dominant, that is synchrotron self-absorption. This happen when the optical depth for absorption due to the synchrotron process becomes significant, therefore when the density is high. The spectrum of a self-absorbed source is reduced at low frequencies. When multiple self-absorbed spectra with different turnover frequencies are summed together the overall result is a flat spectrum. This is the reason why AGN cores show a much flatter spectrum compared to extended emission.

The electrons lose energy through emission. The power emitted by an electron with Lorentz factor $\gamma$ integrated over all frequencies is given by the Larmor relativistic formula

$$P = \frac{\mathrm{dE}}{\mathrm{dt}} = \frac{2}{4}\frac{e^2\gamma^4}{c^3}\dot{v}^2\,, \tag{1.15}$$

where $\dot{v}$ is the electron acceleration and for an electron moving in a magnetic field it is $\dot{v} = (e\beta B)/(\gamma m_e)$, where $\beta = v/c$. From this equation it is easy to derive

$$P = \frac{4}{3}\sigma_T c\beta^2\gamma^2 U_B\,, \tag{1.16}$$

where $\sigma_T = 8\pi r_0^2/3$ is the Thomson scattering cross-section, $r_0 = e^2/m_e c^2$ is the classical electron radius and $U_B = B^2/8\pi$ is the energy of the magnetic field. The characteristic time in which an electron loses energy is then obtained from its energy $E = \gamma m_e c^2$ and its energy loss rate $\mathrm{dE}/\mathrm{dt} = -P$ as

$$t_{\mathrm{cool}} = \frac{E}{P} = 2.4 \times 10^5 \left(\frac{\gamma}{10^4}\right)^{-1}\left(\frac{B}{10^{-4}\,\mathrm{G}}\right)^{-2}\mathrm{yr}\,. \tag{1.17}$$

Since $\gamma$ is proportional to $\nu^{1/2}$ (see Eq. 1.14), higher frequency electrons are depleted faster than low frequency ones, which therefore trace more ancient emissions. Since the characteristic frequency (Eq. 1.14) of synchrotron radiation depends on both the radiating particle's Lorentz factor $\gamma$ and the magnetic field $B$, it is impossible to measure both quantities independently. In Sec. 4.4.3 I will show how we can overcome this problem with a few theoretical assumptions.

A second process which typically occurs in AGNs is inverse-Compton scattering. The scattered photons can come from a variety of sources: from the synchrotron emission just described (often referred to as synchrotron self-Compton or SSC), from the broad or narrow-line regions, the torus, starlight, or the cosmic microwave background.

### 1.3.4 Activation

A problem I have so far ignored is when and how a galaxy switches from a quiescent to an active state. We know indeed that a $10^8\ M_\odot$ black hole accreting at the Eddington limit would exhaust the fuel for its activity in a few tens of million years. Therefore, the quasar phase represent just a short fraction of a galaxy's life and some mechanism must be responsible for "switching on" the AGN forcing large amounts of material into the galaxy's central regions.

Sanders et al. (1988) firstly noticed a connection between strongly interacting galaxies and AGN activity. Wilson & Colbert (1995) then developed the merging theory proposing that major mergers of two disc galaxies could provide a mechanism for producing an AGN, particularly a radio-loud one. This because mergers of spin aligned black holes can produce a highly-rotating black hole. Berti & Volonteri (2008) simulated different scenarios of black hole evolution through short-lived (chaotic) accretion episodes, prolonged accretion episodes with mergers and mergers only. They found that secular processes of accretion will lead to highly rotating black holes (with a dimensionless spin $a = J/M^2 > 0.9$) while the mergers-only scenario would produce only a limited fraction of fast rotating black holes. Finally, short-lived (chaotic) accretion is not able to spin-up the black hole to considerable values.

In many models, black hole spin is a necessary prerequisite for jet formation and it is a requirement for a high energy conversion efficiency $\eta$ in black holes. In Sec. 1.3 we derived a minimum value for $\eta \sim 0.1$ to justify the amount of X-ray background radiation. A non-rotating black hole provides a maximum $\eta = 0.057$, that is not enough to match the observations. Unfortunately, black hole spin is an elusive parameter to measure but, as said, one could expect AGN in general, and radio loud AGN in particular, to have highly rotating black holes powering their emission. To summarise, the way to spin-up black holes to the required values for jet production and needed energy conversion efficiency, is probably both through mergers and accretion (Berti & Volonteri 2008), most likely between redshifts of 2 and the current epoch much of the AGN evolution is secular and not merging-driven while mergers may trigger quasar-mode

accretion at redshifts 2-3 (Hopkins et al. 2006).

An observational evidence on the black holes merging scenario come again from M87 and it is explained in the work from Batcheldor et al. (2010). In this work the authors shows that M87 supermassive black hole does not lie in the galaxy's dynamical center, but it is offset by 7 pc in projection. The most consistent explanation for this result is that the black hole is displaced as a result of gravitational recoil resulting from the merging of two supermassive black holes.

## 1.4   Feedback

It has been recently realised that black holes in AGN may play a major role in determining the final stellar mass of the hosting galaxy's bulge and stellar velocity dispersion. The process by which this occur is known as AGN feedback and it is caused by the interaction of the energy and the particles generated by the accretion onto the black hole and the host galaxy. The major difficulty in finding the proper process responsible for this effect is the enormous difference in size between the black hole and the galaxy (up to $1{:}10^9$).

Two feedback modes have been identified, and the most convincing "evidence" for their presence comes not from actual observations of black holes, but from semi-analytic models of galaxy formation: in order to explain the galaxy luminosity function and galaxy color distribution, modellers have to assume two types of feedback. One that disperses and heats the star-forming gas at the end of a star-formation cycle (generally triggered by mergers), effectively halting star formation – the "quasar mode" or "radiative mode" – and one that maintains the gas in typical elliptical galaxies in its tenuous, hot state – this is the "radio" or "kinetic mode". In the first case the black hole accretes col gas at values close to its Eddington limit and in a radiative efficient way, while in the second case the black hole operates at much lower accretion regimes, fuelled by hot gas and generates powerful jets.

**Radiative mode**

In the radiative mode, momentum balance between radiation emitted by a black hole with mass $M_{\rm BH}$ at the Eddington limit and gas accretion by gravitational attraction into the galaxy provides

$$\frac{L_{\rm Edd}}{c} = \frac{4\pi G M_{\rm BH} m_p}{\sigma_{\rm T}} = \frac{G M_{\rm gal} M_{\rm gas}}{r^2} = \frac{f G M_{\rm gal}}{r^2} = \frac{fG}{r^2}\left(\frac{2\sigma r^2}{G}\right)^2 = \frac{f4\sigma^4}{G}, \qquad (1.18)$$

where $\sigma_{\rm T}$ is the Thomson cross-section, $f$ is the fraction of gas in the galaxy, $\sigma$ is the velocity dispersion and $m_p$ is the proton mass and $r$ is the galaxy's radius (see also Fabian 1999). I also assumed an isothermal galaxy, so to be able to use the Virial theorem: $M_{\rm gal} = 2\sigma^2 r/G$.

Rearranging the first and the last term of the previous equation, we find

$$M_{\rm BH} = \frac{f\sigma^4\sigma_{\rm T}}{4\pi G^2 m_p c} \tag{1.19}$$

This relation is in very good agreement with the empirical M-$\sigma$ relation (Tremaine et al. 2002) for a gas mass fraction $f \simeq 0.1$ and it is a first, although weak, observational evidence for AGN feedback (see also King 2005).

However, interaction between the central black hole and the galaxy's gas cannot rely on radiation pressure on electrons (as in the standard Eddington-limit formula), this because a quasar at Eddington limit will be far below this limit when the galaxy's mass is included as another mass attracting the gas towards the centre. Therefore, the interaction must be stronger and either due to winds or to the dust embedded in a galaxy's gas. Dust particles are charged in a quasar environment and bind to the partially-ionized gas atoms. As a consequence $L_{\rm Edd}$ may be reduced by a factor $\sigma_{\rm T}/\sigma_{\rm d}$, where $\sigma_{\rm d}$ being the equivalent dust cross-section per proton. A typical values for this ratio is $\sim 1000$ (Fabian et al. 2008). This means that a quasar at the Eddington limit is at the effective Eddington limit for dusty gas of a surrounding object 1000 times more massive. It is noteworthy that $M_{\rm gal}/M_{\rm BH} \sim 1000$.

**Kinetic mode**

In the case of more massive galaxies and galaxies in the centre of groups and clusters, we often detect a surrounding X-ray emission due to the presence of large amounts of gas. This gas is cooling due to the energy lost by this emission which, being *bremsstrahlung* radiation, is proportional to the square of its density, rising steeply towards the clusters' centres. As the material in the centre of the cluster cools out, the pressure of the overlying ICM cause more material to flow inwards generating the so called *cooling flow*. The typical time-scale for the ICM to cool is relatively short, less than a billion years and a flow of hundreds or even thousands $M_\odot$ yr$^{-1}$ is expected (Fabian 1994). Observed mass cooling rates, in absence of heat sources, should significantly grow the stellar mass of the galaxy in question and excite strong lines expected from FeXVII as the gas cools below 0.7 keV. Observationally, none of these effects has been reported. A possible explanation is that the AGN in the centre of the cool core is feeding back energy into its surroundings at a rate balancing the loss of energy through cooling. In fact, almost all the galaxies in the centre of clusters have an active radio source (Dunn et al. 2010).

Some of the steps of this process are now quite well understood, although many aspects are still under investigation (see Chap. 4). The accretion flow onto the black holes generates powerful jets which in turn inflate bubbles of relativistic plasma that are strongly over-pressured relative to the environment (see Fig. 1.6). These bubbles must expand, and the rapid energy

release implies that this expansion is supersonic in the frame of the environment. As the bubble expands, the pressure inside it and in the shell eventually approaches the pressure of the environment and the expansion becomes sub-sonic. The initially generated shock wave of the supersonic expansion will continue to coast outward, leaving behind a sub-sonically expanding cavity. Once the pressure of the source drops below the dynamic pressure of motions in the environment, the bubble buoyantly rises through the ICM and new bubbles form (Churazov et al. 2000; McNamara et al. 2000; Brüggen & Kaiser 2002). Finally, it turns into a *ghost* bubble as it becomes undetected in radio observations at 1.4 GHz. This jet-bubbling process is not very episodic, but it is more or less continuous (thus the very high detection rate) and it is present in cluster (see Chap. 4), groups and single galaxies (see Chap. 5).

One of the most important results from the discovery of X-ray cavities in clusters is a robust, independent way to estimate the kinetic power of cluster radio sources. It is based on the fluid mechanics of inflated bubbles: in order to inflate a cavity in the intra-cluster gas, the jet must (i) displace the material in the environment into a shell surrounding the cavity, which is of the order of $E_{pV} \sim 4pV$ (and depends on the details of the inflation history of the bubble) and (ii) replace it with relativistic, magnetized gas. At a minimum, the amount of energy needed to do this is the work done on the cluster gas and the internal energy of the radio plasma.

One open problem is how the energy provided by the AGN is dissipated and spread. The jet are intrinsically anisotropic but this anisotropy is not visible in clusters' temperature maps, so heating must be much more isotropic. Furthermore, turbulence in the ICM is relatively low and abundance gradients show no large and violent mixing. Therefore, the bubbling process must be something gentle and continuous. Concentric ripples due to expanding sound waves or weak shocks associated with the repetitive blowing of bubbles are detected in many bright cluster as Perseus (Fabian et al. 2006), Virgo (Forman et al. 2005) and the Centaurus (Sanders et al. 2008) cluster.

### 1.4.1   The the radio mode feedback efficiency

In order to estimate the global impact of radio-mode feedback we need to have a complete census of the radio emitting AGN population. This population can be divided into steep and flat spectrum sources, characterized by a power-law synchrotron spectrum $F_\nu \propto \nu^\alpha$ (where $F_\nu$ is the source flux density and $\nu$ is the frequency), with slope $\alpha_{\text{flat}} = -0.1$ and $\alpha_{\text{steep}} = -0.8$, respectively. Under this assumption, a redshift dependent luminosity function can be derived for the two populations separately, by fitting simple models to a very large and comprehensive set of data on multi-frequency source counts and redshift distributions, obtained by radio surveys at $\nu < 5$ GHz (Massardi et al. 2010). The comoving number densities in bins of increasing radio power (at 1.4 GHz) from the resulting best fit luminosity function models are shown in the
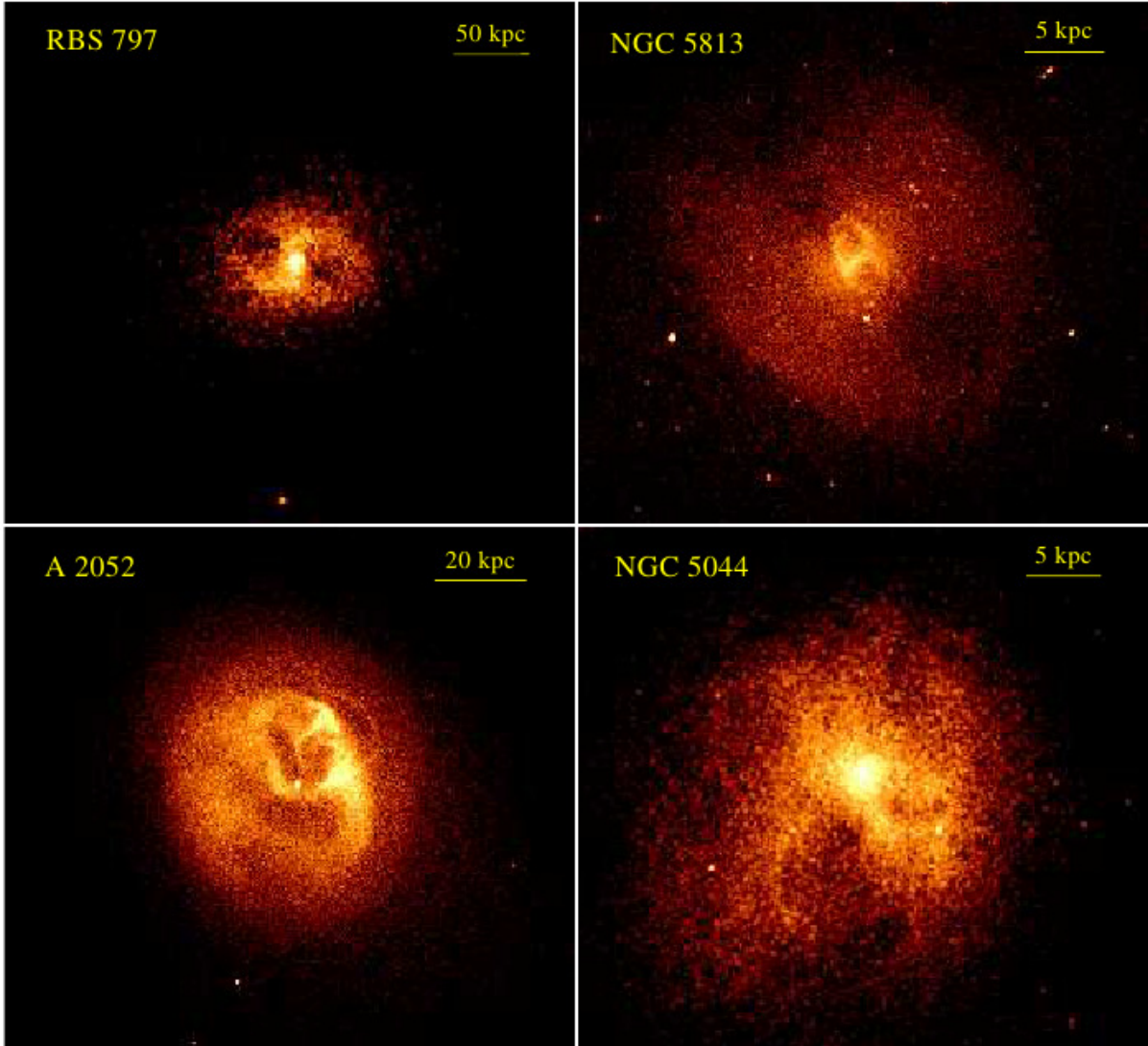
Figure 1.6: Chandra X-ray images showing the interaction of the central AGN on surrounding gas over a wide range of scales. *Top left*: massive cluster RBS 797 at $z = 0.354$ (Cavagnolo et al. 2011). *Top right*: nearby central group elliptical galaxy NGC 5813 at $z = 0.006$ (Randall et al. 2011). *Bottom left*: rich cluster A 2052 at $z = 0.035$ (Blanton et al. 2011). *Bottom right*: NGC 5044 group at $z = 0.0093$ (David et al. 2011). Bubbles in RBS 797 have volumes about 1000 times larger than the inner bubbles of NGC 5813.

left panel of Fig. 1.7. Radio AGN, both with steep and flat spectrum, show the distinctive feature of a differential density evolution, with the most powerful objects evolving more strongly towards higher redshift, a phenomenological trend that, in the current cosmologist jargon, is called "downsizing". From Fig. 1.7b, instead, it is clear that most of the radio emission visible in the Universe is generated by low-luminosity AGN, and this is true at least until $z = 1.2$.

Deep radio surveys show that the radio loudness, defined relative to the bolometric flux, actually increases for decreasing Eddington ratios ($L_{bol}/L_{Edd}$, with $L_{bol}$ the bolometric luminos-
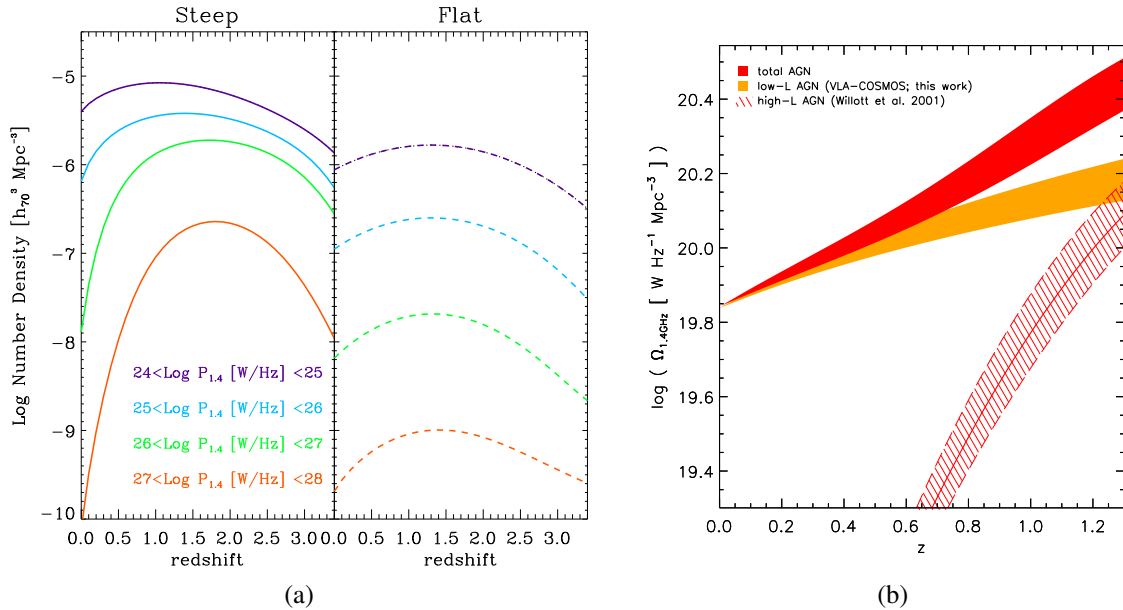
Figure 1.7: *Left*: best fit number density evolution of radio sources of different power, taken from the models of Massardi et al. (2010), for steep and flat spectrum sources in the left and right panels, respectively. *Right*: evolution of the comoving 20 cm integrated luminosity density for VLA-COSMOS AGN (orange curve) galaxies for $z < 1.3$. Also shown is the evolution of the high-luminosity radio AGN (hatched region, from Willott et al. 2001, the thick and dashed lines correspond to the mean, maximum and minimum results, respectively). The evolution for the total AGN population, obtained by co-adding the VLA-COSMOS and high luminosity AGN energy densities, is shown as the red-shaded curve (from Smolčić et al. 2009).

ity, see Fig. 1.8a and Ho 2002). This means that black holes become relatively more efficient at liberating energy in the form of jets as their luminosity and accretion rate drops, such that all black holes at sufficiently low accretion rate appear to be driving some form of radio-loud outflow.

A full theoretical understanding of the phenomenon is still missing, but it has been shown that low-efficiency accretion leads to the formation of geometrically thick flows, as opposed to the geometrically thin accretion discs found in Seyfert galaxies and quasars (as explained in Sec. 1.3.2). In such a geometrically thick (quasi-spherical) flow, it might be much easier to build up significant magnetic flux, even just from stochastic turbulent dynamo processes in the disc, which could in turn drive the jet.

The observed characteristics of low-luminosity AGNs: the omni-presence of radio cores and the increase in radio loudness at low luminosities can be explained assuming that the (advectively cooled) accretion flow for these objects is scale invariant (Heinz & Sunyaev 2003). For example, low luminosity accretion flow around a 10 $M_\odot$ black hole, accreting at a fixed, small fraction of the Eddington accretion rate, will be a simple, scaled down version of the
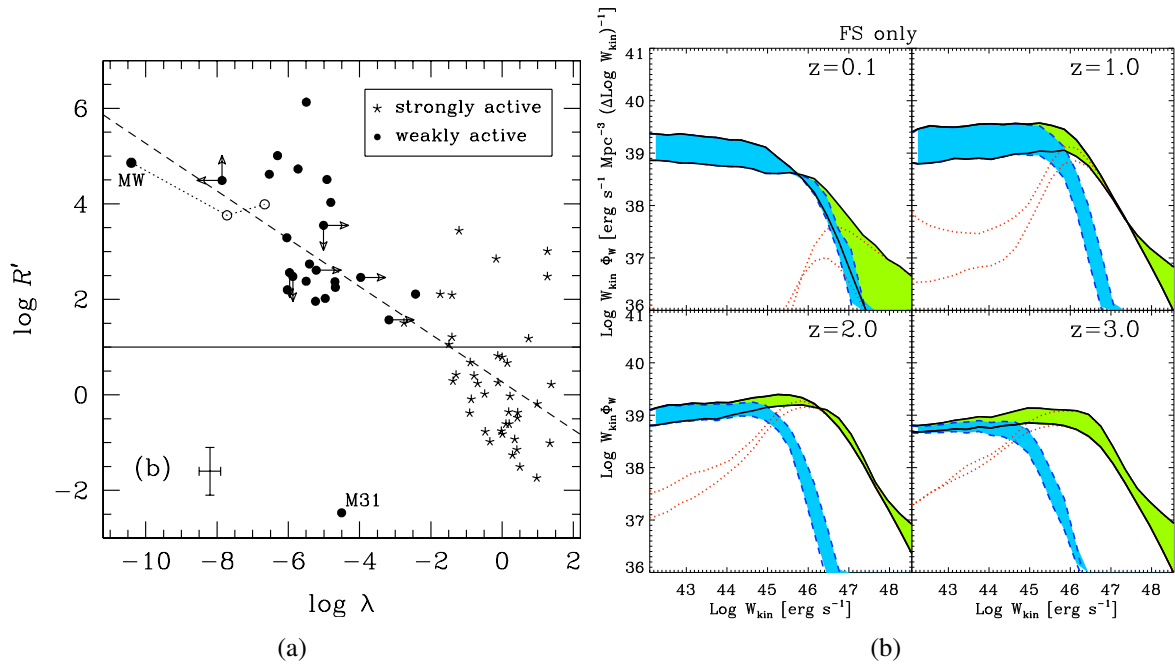
Figure 1.8: *Left*: radio loudness $R'$ (here defined as 5 GHz radio flux to 2500 Å flux) as a function of Eddington ratio $\lambda = L_{bol}/L_{Edd}$ (from Ho 2002). *Right*: kinetic jet luminosity function derived from flat spectrum radio sources, for different redshift bins. Green curve shows all radio sources, blue shows radio sources in the radio mode, red shows radio sources in quasar mode (from Merloni & Heinz 2008).

same flow around a billion solar mass black hole (with the spatial and temporal scales shrunk by the mass ratio). The jet formation in such a flow should be similarly scale invariant. This assumption is sufficient to derive a very generic relation between the radio luminosity $L_\nu$ emitted by such a scale invariant jet and the total (kinetic and electromagnetic) power carried down the jet $P_{jet}$

$$L_{radio} \propto P_{jet}^{\frac{17+8\alpha}{12}} M^{-\alpha} \sim P_{jet}^{\frac{17}{12}}, \tag{1.20}$$

where $M$ is the mass of the black hole and $\alpha \simeq 0$ is the observable, typically flat radio spectral index of the synchrotron power-law emitted by the core of the jet. This relation is a result of the fact that the synchrotron photosphere (the location where the jet radiates most of its energy) moves further out as the size scale and the pressure and field strength inside the jet increase (corresponding to an increase in jet power). As the size of the photosphere increases, so does the emission.

For a given black hole, the jet power should depend on the accretion rate as $P_{jet} \propto \dot{M}$ (this assumption is implicit in the assumed scale invariance). On the other hand, the emission from optically thin low luminosity accretion flows itself depends non-linearly on the accretion rate, roughly as $L_{acc} \propto \dot{M}^2$, since two body processes like *bremsstrahlung* and inverse Compton scattering dominate, which depend on the square of the density. Thus, at low accretion rates,

$L_{\text{radio}} \sim L_{\text{acc}}^{\frac{17}{24}}$, which implies that black holes should become more radio loud at lower luminosities.

This relation can be used to estimate the jet power of other sources based on their radio properties alone, once calibrated using a sample of radio sources with known jet powers. Furthermore, given a radio luminosity function $\Phi_{\text{rad}}$ and an appropriate correction for relativistic boosting, we can derive the kinetic luminosity function of jets (Merloni & Heinz 2008):

$$\Phi_{\text{kin}}(P_{\text{jet}}) = \Phi_{\text{rad}} \left[ L_0 \left( \frac{P_{\text{jet}}}{P_0} \right)^{\frac{1}{\zeta}} \right] \frac{1}{\zeta} \frac{L_0}{P_0} \left( \frac{P_{\text{jet}}}{P_0} \right)^{\frac{1-\zeta}{\zeta}} . \tag{1.21}$$

The resulting kinetic luminosity functions for the flat spectrum radio luminosity functions from Dunelop & Peacock (1990) and De Zotti et al. (2005) are plotted in Fig. 1.8b. Since the figure plots $P \cdot \Phi_{\text{P}}$, the curves show *directly* the total contribution of AGN at a given jet power to the total feedback power at a given redshift. At the low luminosity end, these curves are roughly flat, implying that low luminosity sources contributed a significant fraction of the total power. These low-luminosity AGNs are responsible for radio mode feedback, and they dominate the total jet power output at low redshift.

Finally, one can integrate the kinetic luminosity function over all the redshifts obtaining the total kinetic energy density released by jets over the history of the universe ($u_{P_{\text{jet}}} \sim 3 \times 10^{57}$ ergs Mpc$^{-3}$). By comparing this to the local black hole mass density $\rho_{\text{BH}}$ we can derive the average conversion efficiency $\eta_{\text{jet}}$ of accreted black hole mass to jet power:

$$\eta \equiv \frac{u_{P_{\text{jet}}}}{\rho_{\text{BH}} c^2} \approx 0.2\% - 0.5\% .$$

In other words, about half a percent of the accreted black hole rest mass energy is converted into jets (averaged over the history of the black hole). Most black hole mass was accreted during the quasar epoch, when black holes were mostly radio quiet (in the "quasar mode"). Therefore, about 90% of the mass of a given black hole was accreted at zero efficiency (assuming that 10% of quasars are radio loud). Thus, the average jet production efficiency during radio loud accretion must be at least a factor of 10 higher, about $2\% - 5\%$, comparable to the radiative efficiency of quasars.

It is the complex physics that describes the interaction of such low-luminosity, radiatively-inefficient AGN with their ambient, that will be the main subject of Chaps. 2 and 4 of this thesis.

# Low Luminosity AGN

## 2.1 Introduction

To further our understanding of LLAGN, in this chapter I will focus on three accretion/jet-power estimators among the different signatures of nuclear activity arising at different wavelengths: optical line emission, nuclear X-rays and nuclear non-thermal radio emission. In the standard "unified model" for AGNs (Urry & Padovani 1995), optical narrow emission lines come from gas located several hundreds pc away from the central engine. These lines are excited by ionizing radiation produced in the innermost accretion flow and escaping along the polar axis of the obscuring torus that surrounds the black hole. Since this ionized gas is so distant from the central engine, the obscuring torus does not affect greatly its flux, thus narrow optical emission lines suffer only moderate amounts of dust obscuration due to the interstellar medium. This suggests that [OIII] emission line luminosity can be a good estimator for the AGN accretion power. On the contrary, X-ray emission arises directly from the hot corona surrounding the accretion disc or from the base of a relativistic jet (for radio-loud objects). As such, it represents a more faithful estimator of the accretion power, although it could be heavily obscured by high column density through the dusty torus in objects where we look at the AGN from a close to edge-on sight-line. Finally, powerful non-thermal radio emission is the observational signature of the presence of a jet whose relativistic particles emit synchrotron radiation going through strong magnetic fields. Radio emitting jets are ubiquitous, particularly at low intrinsic powers (see e.g. Ho 2008, and references therein), and it has been postulated that it

also could be used to estimate the AGN kinetic and total power output (Falcke & Biermann 1995; Best et al. 2006).

As emerged in recent years (see Hardcastle et al. 2009, and references therein), radio loud objects can be divided into two main populations:

*high excitation galaxies (HEG):* quasars and high-power narrow line radio galaxies that are likely to be the same population, seen at different orientation;

*low excitation galaxies (LEG):* active radio galaxies of low intrinsic power characterized by emission line spectra of low excitation, that probably form the parent population of the mostly lineless BL-Lac objects.

Recent studies (Chiaberge et al. 2002; Whysong & Antonucci 2004; Hardcastle et al. 2006, 2009) have proposed that LEG lack any of the conventional apparatus of the AGNs (i.e. radiatively efficient accretion disc, X-ray corona and obscuring torus) and that their radio and X-ray nuclear emission can be explained as a result of the properties of the small-scale jet.

Significant progress has also been achieved in understanding how the radio properties of AGN relate to other parameters such as black hole mass and accretion rate (Ho 2002). Merloni et al. (2003) and Falcke et al. (2004) considered heterogeneous black hole samples spanning a broad range in black hole mass and X-ray luminosity, and found a strong correlation between the radio luminosity $L_R$ from the unresolved radio cores of AGNs, the black hole mass M and the 2-10 keV X-ray luminosity $L_X$ of the form (Merloni et al. 2003):

$$\log L_R = 7.44 + 0.6 \log L_x + 0.78 \log(M/M_\odot). \tag{2.1}$$

These scalings with mass and luminosity can be well explained by the theory of synchrotron emitting compact relativistic jets and radiatively inefficient accretion flows (Blandford & Konigl 1979; Heinz & Sunyaev 2003). These works explicitly demonstrated that the black hole mass should be considered as a fundamental parameter in the determination of the observed relations between emission components in various bands.

In this chapter I will push forward these investigations on the relations between different accretion and power output estimators in super massive black hole (SMBH). In particular, I will test whether the loose empirical [OIII] – X-ray correlation found in type 1 AGN, as well as the fundamental plane of black hole activity, hold in an unbiased sample of type 2 AGN in the local universe. Compared to previous work on this subject (see e.g. Heckman et al. 2005), this study is unique because I select objects in a very narrow range of black hole masses, thus disentangling the effects of mass and accretion rate on the observed [OIII] - X-ray - radio correlations.
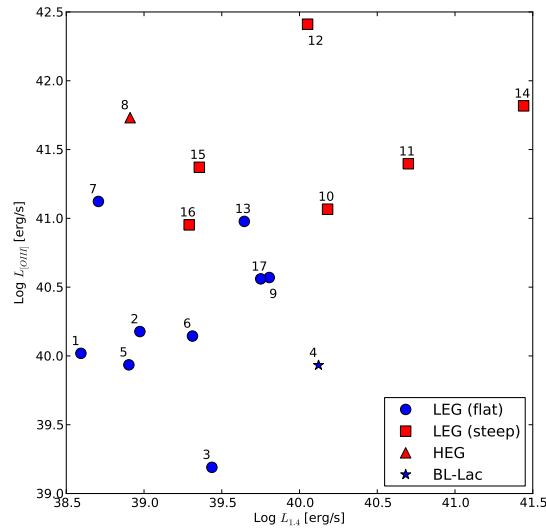
Figure 2.1: Sources in our sample plotted in a radio (1.4 GHz) – optical ([OIII]) luminosity plane. Sources are selected in order to cover wide range of luminosity both in the radio and the optical. Points are coloured according to their spectral index in the radio band (red: steep-spectrum – blue: flat-spectrum, see Sec. 2.3.2 for details). Square markers are for LEG steep-spectrum objects, round markers are for LEG flat-spectrum objects while the triangle marker is the HEG and the star marker is the BL-Lac. For the classification criteria see Sec. 2.3.2 and 2.3.3

The chapter is organised as follows: in the next section I will describe the sample, while in Sec. 2.3 I will lay out the most important calibration steps used for the X-ray, radio and optical data reduction. Then in Sec. 2.4 I will examine the relation between different power estimators. Finally in Sec. 2.5 I will discuss their implications.

## 2.2 Sample selection

In order to answer some of the important questions posed in the previous section, together with my collaborators I have performed a snapshot X-ray/radio survey of a new, well defined sample of low-luminosity AGN. The sample used for our analysis was originally extracted from 2712 radio luminous type 2 AGN (Best et al. 2005) contained in the 212000 galaxies of the second data release of the SDSS. From this sample we selected 17 objects with the following characteristics:

- The black hole masses have been derived from velocity dispersion measurements of each galaxy (Tremaine et al. 2002; Heckman et al. 2004). We require black hole masses to be $8 \leq \log M_{BH} \leq 8.5$ (the range is comparable to the uncertainty in the estimate of $M_{BH}$).

This particular window was chosen to maximize the number of objects with $z \leq 0.11$ that are radio loud.

- A second cut was made on the redshift: $0.05 \leq z \leq 0.11$. The SDSS spectra are obtained using $3''$ diameter fibres and at larger distances, the AGN emission is significantly contaminated by starlight from the host galaxy.

- The objects were chosen to span a wide range in dust-corrected [OIII] luminosity ($L_{\mathrm{[OIII]}} \sim 10^{5.5} L_\odot$ up to to $L_{\mathrm{[OIII]}} = 10^{9.2}\ L_\odot$), and the entire observed range in radio luminosity, $10^{38.5}\ \mathrm{erg\ s}^{-1} \leq L_{\mathrm{R}} \leq 10^{41.3}\ \mathrm{erg\ s}^{-1}$.

- In order to not be biased by cluster environment and to facilitate the X-ray data reduction, we chose objects that were at least $7'$ away from the centre of galaxy clusters.

142 AGN satisfy all these conditions. Because of their intrinsic weakness, a full multi-wavelength survey of the entire sample was deemed too time-consuming. Instead, we chose to focus on a randomly selected sub-sample of 17 objects to cover the $L_{\mathrm{[OIII]}} - L_{\mathrm{R}}$ parameter space widely. The final choice of the sample size was made by trading off the total observing time requested for maximizing the chances of source detection in the X-rays and ensuring that enough sources are included for statistical tests.

Properties of the galaxies in the selected sample are listed in Table 2.1 while in Fig. 2.1 we plot the sample on the [OIII]-radio plane using line luminosities from SDSS data release 7. At the time of the sample selection the last SDSS release available was the fourth. Subsequent analysis and better calibration of the SDSS spectroscopic data imply that some [OIII] luminosity values differ slightly between the two releases due to different data reduction procedures and this is the reason why two objects (9 and 17) are quite near in the [OIII]-radio plane while, as stated above, we selected them to cover that space as uniformly as possible. Finally, we stress that in the sample selection process we did not exclude any source on the basis of the ionization state of the emission line complex, so that no bias for or against the HEG/LEG nature of the sources had been introduced. After our observations were taken, Plotkin et al. (2008), using radio and optical data, have classified one of them as a BL-Lac with a strong boosting in the radio and X-ray emission. This is source number 4 in Table 2.1, and is a clear outlier in most of the diagrams present throughout the chapter. We decided to leave it in the sample for completeness of information.

Throughout this chapter luminosity distances are calculated adopting $H_0 = 70\ \mathrm{km\ s}^{-1}\ \mathrm{Mpc}^{-1}$, $\Omega_m = 0.3$ and $\Omega_\Lambda = 0.7$.

Table 2.1: The LLAGN sample

| Object | ID | RA J2000 | DEC J2000 | $z$ | $\log L_{\rm [OIII]}$ | $\log L_{\rm X}$ [2-10 keV] | $\log L_{\rm R}$ [1.4 GHz] | $\log L_{\rm R}$ [4.8 GHz] | [8.4 GHz] | $\alpha_{\rm R}$ | $\log M_{\rm BH}$ |
|---|---|---|---|---|---|---|---|---|---|---|---|
| (1) | (2) | | | (3) | (4) | (5) | (6) | (7) | (8) | (9) | (10) |
| 2MAS1601+46 | 1 | 16:01:09.07 | 46:23:17.8 | 0.08 | $40.0 \pm 0.13$ | $41.0^{+0.34}_{-0.84}$ | 38.6 | 39.2 | 39.4 | 0.12 | 8.0 |
| 2MAS0837+53 | 2 | 08:37:17.99 | 53:15:16.8 | 0.06 | $40.2 \pm 0.08$ | $< 41.5$ | 39.0 | 39.9 | 40.1 | -0.08 | 8.3 |
| 2MAS1349+05 | 3 | 13:49:07.22 | 05:04:12.1 | 0.08 | $39.2 \pm 0.30$ | $41.0^{+0.38}_{-0.34}$ | 39.4 | 39.7 | 39.9 | 0.23 | 8.0 |
| CGCG043-05 | 4 | 12:53:47.01 | 03:26:30.4 | 0.07 | $39.9 \pm 0.07$ | $43.2^{+0.20}_{-0.17}$ | 40.1 | 40.6 | 40.8 | 0.17 | 8.5 |
| SDSS0141-09 | 5 | 01:41:16.35 | -08:35:39.3 | 0.05 | $39.9 \pm 0.04$ | $< 41.0$ | 38.9 | 39.4 | 39.6 | 0.05 | 8.0 |
| 2MAS1612+00 | 6 | 16:12:09.29 | 00:03:33.1 | 0.06 | $40.1 \pm 0.06$ | $41.3^{+0.18}_{-0.88}$ | 39.3 | 40.0 | 40.2 | 0.16 | 8.4 |
| SDSS2122-08 | 7 | 21:25:12.48 | -07:13:29.9 | 0.06 | $41.1 \pm 0.01$ | $42.3^{+0.11}_{-0.13}$ | 38.7 | 38.9 | 39.2 | -0.13 | 8.3 |
| 2MAS1109+02 | 8 | 11:09:57.14 | 02:01:38.6 | 0.06 | $41.7 \pm 0.00$ | $42.6^{+0.67}_{-0.76}$ | 38.9 | 39.1 | 39.1 | 0.94 | 8.0 |
| 2MAS0836+53 | 9 | 08:36:42.83 | 53:34:32.5 | 0.10 | $40.6 \pm 0.03$ | $41.7^{+0.20}_{-0.23}$ | 39.8 | 40.6 | 40.8 | 0.08 | 8.5 |
| 2MAS1349+04 | 10 | 13:49:09.63 | 04:04:48.3 | 0.08 | $41.1 \pm 0.04$ | $40.4^{+0.70}_{-1.19}$ | 40.2 | 40.2 | 40.2 | 1.04 | 8.3 |
| 2MAS0912+53 | 11 | 09:12:01.68 | 53:20:36.6 | 0.10 | $41.4 \pm 0.01$ | $41.2^{+0.32}_{-0.60}$ | 40.7 | 41.0 | 41.2 | 0.41 | 8.3 |
| 2MAS0810+48 | 12 | 08:10:40.28 | 48:12:33.2 | 0.08 | $42.4 \pm 0.01$ | $41.1^{+0.72}_{-0.33}$ | 40.1 | 40.2 | 40.2 | 0.94 | 8.1 |
| 2MAS1542+52 | 13 | 15:42:28.36 | 52:59:50.9 | 0.07 | $41.0 \pm 0.03$ | $42.0^{+0.37}_{-0.32}$ | 39.6 | 40.1 | 40.6 | -1.14 | 8.5 |
| 4C52.370 | 14 | 16:02:46.39 | 52:43:58.4 | 0.11 | $41.8 \pm 0.03$ | $41.7^{+0.31}_{-0.37}$ | 41.4 | 41.5 | 41.5 | 0.94 | 8.5 |
| LCRS1010-02 | 15 | 10:12:39.87 | -01:06:22.9 | 0.10 | $41.4 \pm 0.03$ | $41.1^{+0.63}_{-0.39}$ | 39.4 | 39.9 | 40.1 | 0.32 | 8.2 |
| 2MAS0101-00 | 16 | 01:01:01.11 | -00:24:44.4 | 0.10 | $41.0 \pm 0.02$ | $40.9^{+0.34}_{-1.00}$ | 39.3 | 39.7 | 39.8 | 0.72 | 8.4 |
| SDSS2305-10† | 17 | 23:08:17.29 | -09:46:22.5 | 0.10 | $40.6 \pm 0.07$ | $41.3^{+0.28}_{-0.25}$ | 39.8 | 40.1 | 40.4 | 0.10 | 8.3 |

NOTE: Col. (1): Name of the object. Col. (2): Identification number. Col. (3): Redshift. Col. (4): [OIII] luminosity $\log(L_{\rm [OIII]}$ [erg s$^{-1}$]) corrected for dust absorption. Col. (5): X luminosity $\log(L_{\rm X}$ [erg s$^{-1}$]) (corrected for absorption). Col. (6): Radio luminosity at 1.4 GHz $\log(L_{1.4}$ [erg s$^{-1}$]). Col. (7): Radio luminosity at 4.8 GHz $\log(L_{4.8}$ [erg s$^{-1}$]) (mean 5 $\sigma$ error: 0.023 dex). Col. (8): Radio luminosity at 8.4 GHz $\log(L_{8.4}$ [erg s$^{-1}$]) (mean 5 $\sigma$ error: 0.024 dex). Col. (9): Radio spectral index, defined with $F \propto \nu^{-\alpha}$. Col (10): SMBH mass $\log(M$ [$M_\odot$]). Object signed with a † is resolved in the radio maps.

## 2.3   Data Analysis

Our sample of 17 objects has been observed with *Chandra X-ray telescope* (see Section 2.3.1) and with the VLA (see Section 2.3.2). Information about their [O_III] luminosities is taken from SDSS and is analysed as explained in Section 2.3.3.

All errors due to inaccurate evaluation of distances are considered negligible, while we account for an error of 0.25 dex in the black hole mass (Tremaine et al. 2002). Throughout the chapter linear fits have been performed using the Buckley-James method (Buckley & James 1979; Isobe et al. 1986) to account for upper limits. With this regression algorithm, the most probable values of the upper limits are evaluated through the Kaplan-Meier non-parametric distribution (Kaplan & Meier 1958) and then used as observed values for a linear fit that is performed using the orthogonal distance regression to take into account errors both in the dependent and in the independent variable. Correlation tests were performed using a generalized Kendall correlation test (Isobe et al. 1986) that accounts also for upper limits and, if needed, for partial correlation (Akritas & Siebert 1996).

### 2.3.1   X-ray

All of the AGN were observed on the S3 chip of the Advanced CCD Imaging Spectrometer (ACIS; Garmire 2003) aboard the *Chandra X-ray Observatory*. Data were taken in timed exposure mode with the standard frame time at the default location on the S3 chip and telemetered to the ground in very faint mode. Data reduction and point source extractions were completed using CIAO versions 4.2, and ACIS Extract version 2010-02-26 (AE; Broos et al. 2010), respectively. During extraction, the source position was adjusted based on the mean position of the extracted counts to more accurately calculate the point source photometry (except for the two sources with upper limits). The position refinement was always well within *Chandra*'s absolute position uncertainty.

We used Sherpa version 4.2 to jointly fit the unbinned source and background spectrum of each source (Freeman 2001) using the C-statistic, which is similar to the Cash (1979) statistic but with an approximate goodness-of-fit measure, and the MONCAR[1] minimization algorithm. We used this statistical method for the fitting to avoid losing the little spectral information that we have for most of our spectra, which frequently have very few counts (e.g., Nousek & Shue 1989). We fit each source with an absorbed power-law model (XSZPHABS × XSPOWERLAW). In all cases, the background exhibited the signs of hard particle background and was fit by two power laws and thermal component, which achieved a good fit. These ad hoc models are only used to constrain the background component of the spectra.

---

[1]http://cxc.harvard.edu/sherpa4.2/ahelp/montecarlo.py.html

Since degeneracies in the fit parameters will frequently arise for very faint sources, we followed a specialized scheme for these sources based on the number of counts in the source extraction region. If we extracted less than 5 counts (0.5-8 keV) for a source, the power-law index and the hydrogen column density for the fit were frozen to 1.7 and the Galactic value, respectively. If we extracted more than 5 but less than 26 counts (0.5-8 keV), we froze only the power-law index to 1.7 and let the hydrogen column density float, although, in this case, it was always poorly constrained. For all other sources with more than 26 counts (0.5-8 keV), we allowed all fit parameters to float.

As can be seen in Table 2.2, the AGN span a wide range of brightness. We put upper limits on the luminosities of two of the sources with only two counts each (identified with number 2 and 5 in Table 2.1). On the other hand, there were also two sources (IDs 4 and 7 in Table 2.1) that had non-negligible pileup fractions[2] (39.3% and 4.6% of the counts, respectively) and were therefore fit with the standard pileup model. Only two sources (number 8 and, to a lesser amount, 13) have significant additional intrinsic absorption above that expected for the galactic foreground (Dickey & Lockman 1990). However, the determination of the column density for all of our sources is highly uncertain.

The unabsorbed X-ray luminosities listed in Table 1 were calculated from each of the model fits and the uncertainties were calculated as follows. The unabsorbed luminosity is evaluated at each point in a three-dimensional grid 100 points on a side, each dimension corresponding to the number of undetermined parameters in the source model (the absorption, power-law photon index, and power-law normalization). Then the minimum and maximum luminosity is selected within the confidence interval for the appropriate change in statistic value ($\Delta C = 3.53$ for one sigma and three interesting parameters; e.g., Avni 1976). The photon index is constrained to be 0.7-2.7 and the column density must be at least the galactic minimum in the direction of the source. In many cases, the uncertainties in the luminosity estimated with this method are very different from those estimated from the counts using Bayesian methods (Kraft et al. 1991).

Finally, we note that, since the *Chandra* observations were carried out over the span of one year (late 2006 – early 2008), variability between the time of X-ray observations and radio observations could affect some of our results.

## 2.3.2 Radio

Radio data were taken in 2007 using the VLA in A configuration with a total observation time of 10 hours. The calibration procedure has been performed using CASA software (version 3.0.1) developed at NRAO[3]. At the time of the observations, 12 out of 26 antennas were already

---

[2]http://cxc.harvard.edu/ciao/ahelp/acis_pileup.html

[3]http://casa.nrao.edu/

Table 2.2: X-ray data analysis

| ID | ID *Chandra* | Obs. date | Exposure time [s] | Source counts | Exp. bkg counts | Photon Index | $N_H[10^{22}\ \mathrm{cm}^{-2}]$ | Probability no source |
|----|----|----|----|----|----|----|----|----|
| (1) | (2) | | | (3) | (4) | (5) | (6) | (7) |
| 1 | 8244 | 2008-01-16 | 11629 | 12 | 0.07 | 1.70 | $1.33^{+14.3}_{-1.33} \times 10^{-2}$ ‡ | $4.93 \times 10^{-23}$ |
| 2 | 8245 | 2007-09-30 | 6938 | 2 | 0.06 | 1.70 | $3.51 \times 10^{-2}$ † | $1.52 \times 10^{-03}$ |
| 3 | 8246 | 2007-03-15 | 10888 | 29 | 0.06 | $2.31^{+1.85}_{-0.35}$ | $1.99^{+42.2}_{-1.99} \times 10^{-2}$ ‡ | 0.00 |
| 4 | 8247 | 2007-03-04 | 8021 | 1044 | 0.10 | $2.53^{+1.14}_{-0.37}$ | $6.25^{+11.5}_{-5.19} \times 10^{-2}$ | 0.00 |
| 5 | 8248 | 2007-10-03 | 5109 | 2 | 0.03 | 1.70 | $3.04 \times 10^{-2}$ † | $3.47 \times 10^{-4}$ |
| 6 | 8249 | 2007-04-11 | 5950 | 22 | 0.04 | 1.70 | $7.42^{+16.4}_{-7.42} \times 10^{-2}$ ‡ | 0.00 |
| 7 | 8250 | 2007-06-29 | 6880 | 260 | 0.05 | $1.68^{+0.21}_{-0.16}$ | $6.00^{+6.65}_{-6.00} \times 10^{-2}$ | 0.00 |
| 8 | 8251 | 2007-04-10 | 6938 | 15 | 0.04 | 1.70 | $33.3^{+14.7}_{-17.9}$ | $2.87 \times 10^{-30}$ |
| 9 | 8252 | 2006-12-16 | 15933 | 101 | 0.13 | $2.23^{+0.28}_{-0.19}$ | $3.58^{+6.67}_{-3.58} \times 10^{-2}$ ‡ | 0.00 |
| 10 | 8253 | 2007-03-07 | 11005 | 3 | 0.06 | 1.70 | $1.97 \times 10^{-2}$ † | $3.09 \times 10^{-05}$ |
| 11 | 8254 | 2007-06-07 | 18782 | 21 | 0.15 | 1.70 | $1.78^{+14.5}_{-1.78} \times 10^{-2}$ ‡ | $3.32 \times 10^{-37}$ |
| 12 | 8255 | 2007-10-08 | 11008 | 12 | 0.07 | 1.70 | $1.67^{+3.12}_{-1.67} \times 10^{-1}$ | $7.36 \times 10^{-23}$ |
| 13 | 8256 | 2007-06-04 | 8912 | 20 | 0.05 | 1.70 | $4.25^{+1.99}_{-1.26}$ | $1.96 \times 10^{-44}$ |
| 14 | 8257 | 2007-06-03 | 19911 | 30 | 0.13 | $1.34^{+1.10}_{-0.47}$ | $1.14^{+4.72}_{-1.14} \times 10^{-1}$ | 0.00 |
| 15 | 8258 | 2007-01-13 | 16940 | 10 | 0.09 | 1.70 | $3.99^{+7.53}_{-3.99} \times 10^{-1}$ | $1.88 \times 10^{-17}$ |
| 16 | 8259 | 2008-02-09 | 16808 | 8 | 0.13 | 1.70 | $3.17^{+41.6}_{-3.17} \times 10^{-2}$ ‡ | $1.97 \times 10^{-12}$ |
| 17 | 8260 | 2007-10-20 | 17934 | 59 | 0.11 | $2.42^{+0.27}_{-0.26}$ | $3.09^{+2.60}_{-3.09} \times 10^{-2}$ ‡ | 0.00 |

NOTE: Col. (1): Identification number. Col. (2): Identification number used in *Chandra* observations. Col. (3): number of source counts ($0.5 - 8$ keV) in the 90% PSF. Col. (4): expected background counts in source region ($0.5 - 8$ keV). Col. (5): is the best fits for the photon index and relative upper/lower limit increments. When the value is frozen to 1.7 (see text for details) the upper and lower limits are not calculable and therefore omitted. Col. (6): is the column densities $N_H$ and relative upper/lower limit increments. † indicates that $N_H$ is frozen to the galactic minimum. ‡ indicates that the best fit happens to be at the galactic minimum. Col. (7): "prob_no_source" value, defined in section 5.10.3 of the AE user manual (http://www.astro.psu.edu/xray/docs/TARA/ae_users_guide/). Sherpa's "conf" routine has been used to calculate the uncertainties in the photon index and column density (col. 5 and 6). Sherpa's "conf" method gives similar uncertainties to the grid method used in the calculation of the uncertainty in the luminosity, except that Sherpa's "conf" routine tends to underestimate the uncertainty relative to the grid method (e.g., on the order of a few tens of percent for the photon index).

equipped with EVLA receivers. The presence of two different types of receivers on the antennas caused different response from the correlator whether a mixed baseline (VLA-EVLA) or a non-mixed one (VLA-VLA and EVLA-EVLA) were processed. To solve the problem, a baseline-based calibration was performed using the CASA task blcal. Finally, some cycles of self-calibration have been done on all sources.

We observed our sample in two different bands (4.8 and 8.4 GHz) and from these flux values radio spectral indexes have been extracted. Sources with a spectral index ($F \propto \nu^{-\alpha}$) higher than
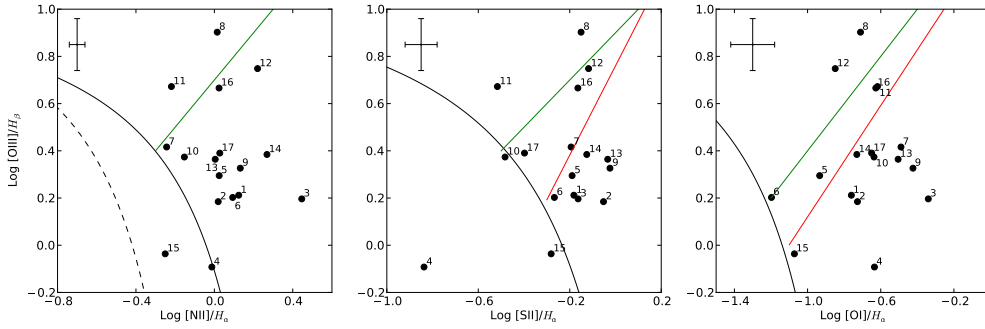
Figure 2.2: Diagnostic diagrams for our 17 sources. Black solid lines (Kewley et al. 2006) separate star forming galaxies, on the bottom left of each diagram, from AGNs. The region between dashed and solid lines (Kewley et al. 2006) identify *composite galaxies* with both star forming and AGN activity. Red lines (Kewley et al. 2006) separate Seyfert galaxies (above) from LINERs (below). Green lines (Buttiglione et al. 2009) separate HEG (top) from LEG (bottom) sources. Average error bars are shown in the top left corner of each plot.

$\alpha = 0.3$ are classified as steep-spectrum, while other sources are classified as flat-spectrum. Values from the FIRST survey (1.4 GHz) were not taken into account during the spectral index extraction process because source fluxes could have changed since FIRST observations. From the spectral analysis we find that ten out of seventeen sources of our sample have a flat spectrum, while in one case (source 13), the spectrum is inverted.

To check the radio calibration procedure we computed the spectral index average values using the three different bands (1.4, 4.8 and 8.4 GHz) two by two. If the main driver for changes in the spectral shape between any two bands is time variability, then some of the sources would have an increased spectral index while some other a lowered one, with an average value of zero. This means that the three averaged spectral index values should be similar. We find an averaged spectral index $\alpha_{4.8-8.4} = -0.29 \pm 0.12$ between 4.8 and 8.4 GHz, $\alpha_{1.4-4.8} = -0.24 \pm 0.10$ between 1.4 and 4.8 GHz and $\alpha_{1.4-8.4} = -0.25 \pm 0.09$ between 1.4 and 8.4 GHz. They are all compatible, enforcing the idea that individual differences between spectral indices including the low-frequency FIRST observations are mostly due to time variability.

The sample was selected to be unresolved at the FIRST resolution (5″) and only one source (number 17) shows clear evidence of a resolved structure in our new observations, that is a 1″ long, jet-like feature in the west-north-west direction. Finally radio fluxes were corrected to be all at the same rest-frame frequency using the derived spectral indexes. Errors on radio fluxes have been set to 5 times the background RMS obtained analysing final maps.

### 2.3.3   Optical

We have re-analysed the available SDSS spectra for the sources in our sample in order to assess the physical nature of the emission lines. Optical spectroscopic information plays a major role in understanding emission properties of central engine of radio galaxies. A first classification using spectral lines was made by Heckman (1980) and Baldwin et al. (1981). They proposed to use optical lines ratios to distinguish between Hɪɪ regions ionized by star forming activities and regions ionized by AGNs. Some years later Veilleux & Osterbrock (1987) revised these definitions using only ratios of lines with a small separation in wavelength, in order to reduce the reddening problem and the impact of flux calibration errors. They introduced these lines combinations: [Oɪɪɪ]$\lambda$5007/H$\beta$, [Nɪɪ]$\lambda$6583/H$\alpha$, [Sɪɪ]$\lambda\lambda$6716, 6731/H$\alpha$ and [Oɪ]$\lambda$6364/H$\alpha$. The separation between AGN and Hɪɪ regions was also calibrated by Kewley et al. (2001) and again by Kewley et al. (2006) using $\sim$ 85 000 emission line galaxies from the SDSS catalogue. Seyfert galaxies and LINERs occupy in these diagnostic diagrams different places and the authors suggested that the observed dichotomy correspond to two AGN subpopulations associated with different accretion modes.

Attempts to apply these diagnostic diagrams to radio loud galaxies were made by Laing et al. (1994) on a sub-sample of 3CR radio-galaxies. Following the suggestion by Hine & Longair (1979) that FRII sources can be divided into two subclasses, they separated their sample into high excitation galaxies (HEG, defined as galaxies with [Oɪɪɪ]/H$\alpha$ > 0.2 and equivalent width of [Oɪɪɪ] > 3 Å) and low excitation galaxies (LEG). Following this idea, we have divided our radio loud sample in HEG and LEG using the criteria described in Buttiglione et al. (2009), where they take advantage from the combination of the optical diagnostic planes. They define LEG all the sources with $\log([OIII]/H\beta) - [\log([NII]/H\alpha) + \log([SII]/H\alpha) + \log([OI]/H\alpha)] /3 <$ 0.95.

We calculated lines luminosities using the spectra extracted from the SDSS data release 7 (Abazajian et al. 2009). For our purposes we are interested both in the [Oɪɪɪ] observed line fluxes and in the dust corrected line fluxes. When dust attenuation needs to be taken into account we measure H$\alpha$ and H$\beta$ line intensities and use the Balmer decrement method. We assume an intrinsic H$\alpha$/H$\beta$ of 2.87 (Osterbrock 1989). The attenuation correction we use is a double power law (Charlot & Fall 2000) of the form:

$$\frac{\tau_\lambda}{\tau_v} = (1 - \mu)\left(\frac{\lambda}{5500\text{Å}}\right)^{-1.3} + \mu\left(\frac{\lambda}{5500\text{Å}}\right)^{-0.7} \tag{2.2}$$

where $\tau_v$ is the total effective optical depth in the $V$ band. With this double power law we account for the attenuation due the presence of discrete clouds random distributed (first term) and the attenuation due to the ISM (second term), so $\mu$ is the fraction of total $\tau_v$ caused by ambient

interstellar medium. We set $\mu = 0.3$ based on observed relations between UV continuum slope and the H$\alpha$ to H$\beta$ line ratios.

We have generated emission line diagnostic (BPT, after Baldwin et al. 1981) diagrams to compare the emission lines ratios: [O$_{\text{III}}$]$\lambda 5007$/H$\beta$, [O$_{\text{I}}$]$\lambda 6003$/H$\alpha$, [S$_{\text{II}}$]$\lambda 6717, 7631$/H$\alpha$ and [N$_{\text{II}}$]$\lambda 6584$/H$\alpha$ (see Figure 2.2).

Following the previously explained classification from Buttiglione et al. (2009) we can classify the majority of our sources as LEG and be confident only for source 8 to be classified as an HEG. Some sources (11 and 12) fall in an intermediate position since they do not satisfy requested line luminosity ratios in all diagnostic diagrams and they are then classified as LEG. We must notice that with this division all sources optically classified as LINERs are now classified as LEGs and source number 8, optically classified as a Seyfert, is an HEGs. The difference in the classifications is mainly for borderline objects (in our sample: 11, 12 and 16) that are conventionally classified as Seyfert galaxies but in Buttiglione et al. (2009) classification are instead LEGs (see Figure 2.2). Contrary to what was found by Buttiglione et al. (2009) we have some strong [O$_{\text{III}}$] emitters ($L_{\text{[OIII]}} > 10^{41.5}$) that do not have $\log$ [O$_{\text{III}}$]/H$\beta \sim 1$, but lower values, e.g. source 12 and 14. Finally, object number 4 is an outlier in many plots. The reason is that this source, as classified by Plotkin et al. (2008) using radio and optical data, is a BL-Lac with a strong boosting in the radio and X-ray emission.

## 2.4 Comparison among [O$_{\text{III}}$], X-ray and radio properties

In this section we analyse the correlations and properties that connect [O$_{\text{III}}$], X-ray and radio emissions from the sample of sources described in Sec. 2.2. As a preliminary step, we have performed a partial correlation analysis on the sample (and various sub-samples), both for the observed luminosities and for those corrected for absorption/extinction, as discussed in the previous section. We adopt the Akritas & Siebert (1996) method to control for censored data. Table 2.3 shows a summary of such a study, where the presence of a correlation between two variables is tested accounting for the common dependence on the third (test variable). In the next subsections relations between different accretion power estimators are evaluated and discussed in detail: in Sec. 2.4.1 we present the analysis of the relationship between [O$_{\text{III}}$] and X-ray emission in our sample, while in Sec. 2.4.2 we exploit the knowledge of radio spectra to provide an interpretation of the X-ray and [O$_{\text{III}}$] information. Finally, in Sec. 2.4.3 we discuss the X-ray – radio correlation (or lack of it) in light of previous studies on the fundamental plane of active black holes.

Table 2.3: Partial correlation coefficients

| Indep. variable | Dep. variable | Test variable | Prob. of non correlation | |
|---|---|---|---|---|
| | | | observed | corrected |
| All sample | | | | |
| X-ray | Radio | [OIII] | 0.93 | 0.98 |
| Radio | [OIII] | X-ray | 0.29 | 0.06 |
| [OIII] | X-ray | Radio | **0.01** | 0.09 |
| LEG | | | | |
| X-ray | Radio | [OIII] | 0.60 | 0.48 |
| Radio | [OIII] | X-ray | 0.12 | **<0.01** |
| [OIII] | X-ray | Radio | 0.23 | 0.44 |
| Radio steep-spectrum sources | | | | |
| X-ray | Radio | [OIII] | 0.38 | 0.82 |
| Radio | [OIII] | X-ray | 0.22 | **0.02** |
| [OIII] | X-ray | Radio | **<0.01** | 0.09 |
| Radio flat-spectrum sources | | | | |
| X-ray | Radio | [OIII] | 0.45 | 0.48 |
| Radio | [OIII] | X-ray | 0.87 | 0.88 |
| [OIII] | X-ray | Radio | **0.05** | **0.05** |

NOTE: In boldface those values where the significance is $\geq 95\%$.
Object number 4 is not considered.

## 2.4.1 Accretion estimators: the relationship between [OIII] and X-ray emission

In Heckman et al. (2005) the authors emphasized the strong difference that arises if one considers AGN samples of Seyfert galaxies selected by X-ray luminosity or using the [OIII] line luminosity. For a sample of hard X-ray selected AGNs (flux limit in the $3 - 20$ keV band of $2.5 \times 10^{-11}$ erg s$^{-1}$ cm$^{-2}$), they find a mean $\log(L_X/L_{[OIII]})$ of 2.15 dex and $\sigma = 0.51$ dex. Type 1 and type 2 sources are separated in terms of emission intensities, but do not present significant difference in the mean ratio between X-ray and [OIII] luminosities. In the left panel of Fig. 2.3 the Heckman et al. (2005) X-ray selected dataset is shown together with our sample, without applying any absorption/extinction corrections, for ease of comparison (absorption-corrected correlations are discussed in the following sections). Sources in our sample have a systematically lower X-ray to [OIII] ratio (see Table 2.4), this is in agreement with the different selection criteria used for the two samples. In the Heckman et al. (2005) X-ray selected sample a higher X-ray emission is indeed expected.

In the right panel of Fig. 2.3 we compare instead our dataset with the [OIII]-selected sample of Heckman et al. (2005) ([OIII]$\lambda$5007 fluxes greater than $2.5 \times 10^{-13}$ erg cm$^{-2}$ s$^{-1}$, correspond-
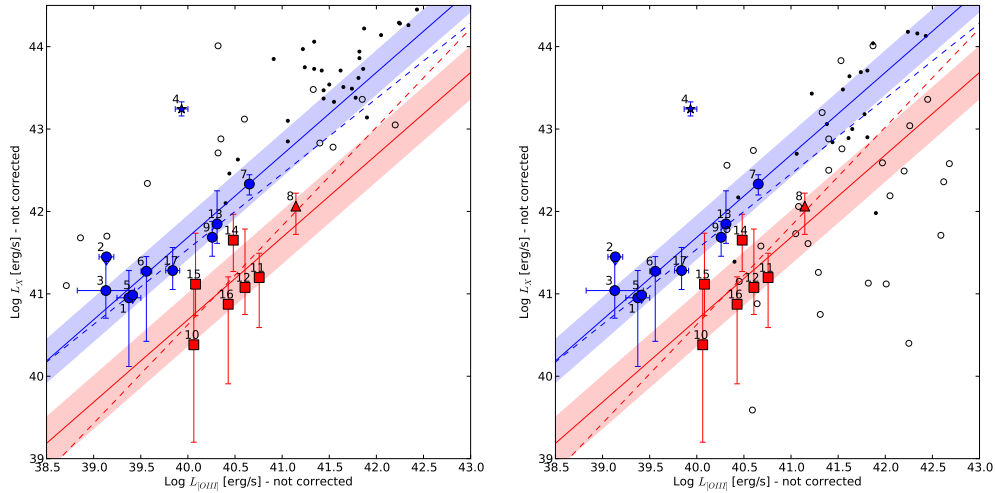
Figure 2.3: *Left panel*: our sample on a X-ray [2-10 keV] – optical ([OIII]) plane (uncorrected for absorption). Symbols are as in Fig. 2.1. Black dots are Type 1 objects from Heckman et al. (2005) hard X-ray selected sample, while circles are Type 2. Red and blue solid lines are the mean ratio between $\log L_X$ and $\log L_{[OIII]}$ calculated using respectively steep and flat sources (coloured patches are at one sigma). Dashed lines are linear regressions (object number 4 is excluded). *Right panel*: the same plot but compared with the [OIII] selected sample from Heckman et al. (2005).

Table 2.4: $\log(L_X/L_{[OIII]})$ for uncorrected data

| Sample | $\log(L_X/L_{[OIII]})$ | $\sigma$ |
|---|---|---|
| | [dex] | [dex] |
| Heckman et al. (2005) - X-ray selected | 2.15 | 0.51 |
| Heckman et al. (2005) - [OIII] selected (type 1) | 1.59 | 0.48 |
| Heckman et al. (2005) - [OIII] selected (type 2) | 0.57 | 1.06 |
| This work | 1.25 | 0.57 |

ing to $L_{[OIII]} \gtrsim 10^{40}$ erg s$^{-1}$). As noted by Heckman et al. (2005), type 1 AGNs are detected at the expected rate, while around 2/3 of the type 2 AGNs would have been missed by the X-ray selection criteria. Their conclusion is that the missing type 2 AGNs are almost certainly heavily X-ray absorbed. Our sample shows a different behaviour. Our objects in fact do not show a random scatter in X-ray luminosity for a given [OIII] line luminosity, rather are quite aligned with the Heckman et al. (2005) [OIII]-selected type 1 sample. This can be quantified in terms of the average luminosity ratios of the samples: in Heckman et al. (2005) [OIII]-selected type 2 AGNs have an average $\log(L_X/L_{[OIII]})$ of 0.57 with a $\sigma$ of 1.06 dex. Our sample has instead a higher X-ray to [OIII] average ratio of 1.25 dex with a much smaller $\sigma$ of 0.57 dex. Interestingly, this relation is much more similar to what Heckman et al. (2005) find for the unobscured
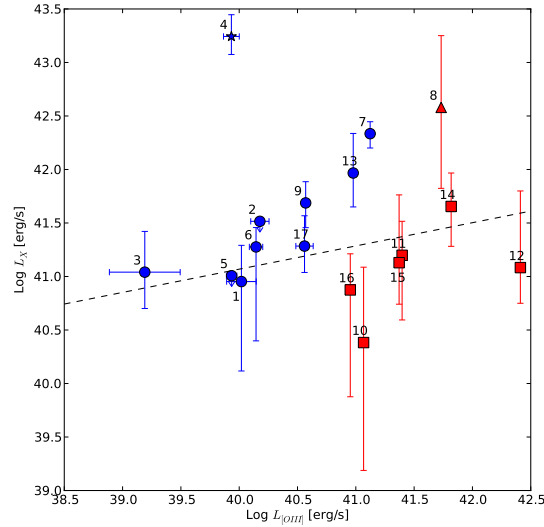
Figure 2.4: The same relation shown in Figure 2.3 after correction for absorption both in [OIII] and X-ray. Black line is the linear regression (object 4 excluded, slope: $0.22 \pm 0.13$, no evident correlation present as stated in Table 2.3). Symbols are as in Figure 2.1.

[OIII]-selected AGNs ($\log(L_X/L_{[OIII]}) = 1.59$ dex, $\sigma = 0.48$ dex).

If we exclude the peculiar BL-Lac object (number 4), the Kendall partial correlation test shows an unexpected, although not strong, correlation between [OIII] and X-ray emissions with a significance of 99% (92% if we keep the BL-Lac). This correlation is not present in the type 2 – [OIII] selected sample of Heckman et al. (2005). A similar trend is instead present in the X-ray selected sample, where X-ray absorption removes all the sources in the lower right part of the X-ray – [OIII] plane, and in the type 1 objects in both Heckman et al. (2005) samples, where obscuration is not important.

How can these difference be explained? The similarities between Seyfert 1 objects and our sample of low luminosity AGNs in the [OIII]-X-ray plane suggest a lack or a reduced incidence of molecular/dusty structures (like the dusty torus present in Seyfert galaxies). The effect of such a structure would be to absorb X-ray emission coming from the inner part of the AGN. This is also confirmed by the X-ray spectral analysis, which does not find any sign of absorption in any source of the sample (apart from number 8, that is also the only HEG identified in the sample). The extinction-corrected [OIII]-X-ray plane, shown in Fig. 2.4, is indeed similar to the uncorrected one, although due to the lack of high photon counts, our absorption-corrected data have big error bars.

From this analysis we can conclude that, absorption being minimal, X-ray emission could be used as a good selection criteria for LEG sources at these low [OIII] luminosities.
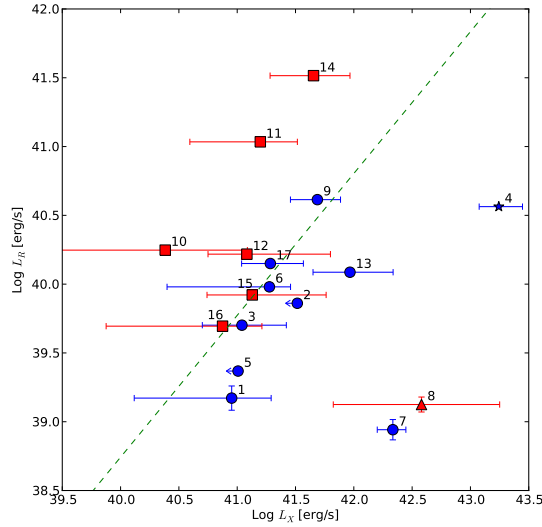
Figure 2.5: X-ray – radio (4 GHz) correlation. Green line is from a sample of Low Luminosity Radio Galaxy (Panessa et al. 2007). Symbols are as in Fig. 2.1.

## 2.4.2 The radio contribution

Our multi-wavelength dataset reveals another interesting fact. We find that a part of the scatter in the X-ray – [OIII] relation can be directly linked to the radio spectra of the sources. Splitting the sample into radio steep- ($\alpha \geq 0.3$) and flat-spectrum ($\alpha < 0.3$) sources, we find that the two sub-samples are still correlated in the [OIII]-X-ray plane (at a significance level > 99% for flat-spectrum sources and of 95% for steep-spectrum sources, see Table 2.3) and their linear fits slopes are compatible (flat: $0.91 \pm 0.09$ – steep: $1.2 \pm 0.5$). But the steep-spectrum sources are systematically ($\sim 1$ order of magnitude) more [OIII] luminous than flat-spectrum sources for a given X-ray luminosity. Radio emission spectrum thus plays a role in the location of the source in the $L_{[OIII]} - L_X$ plane, both for the dust-uncorrected (Figure 2.3) and for the dust-corrected one (Figure 2.4).

One possibility is that our flat-spectrum sources occur in a gas-poorer environment, consequently their jets undergo a small interaction with the medium, so that, in the radio band, the very core of the AGN is the brightest part of the object. The flat spectrum is then explained as superimposition of many self-absorbed synchrotron spectra generated by the AGN core (Blandford & Konigl 1979). These sources will also have a fainter [OIII] emission because there is less gas to ionize. This picture is reinforced by the fact that sources with steep spectrum show on average more dust extinction. In these sources [OIII] flux is corrected for absorption (with the Balmer decrement method described in Sec. 2.3.3) by a factor of $17 \pm 7$ on average, while flat-spectrum sources have an average correction of a factor $2.9 \pm 0.8$.
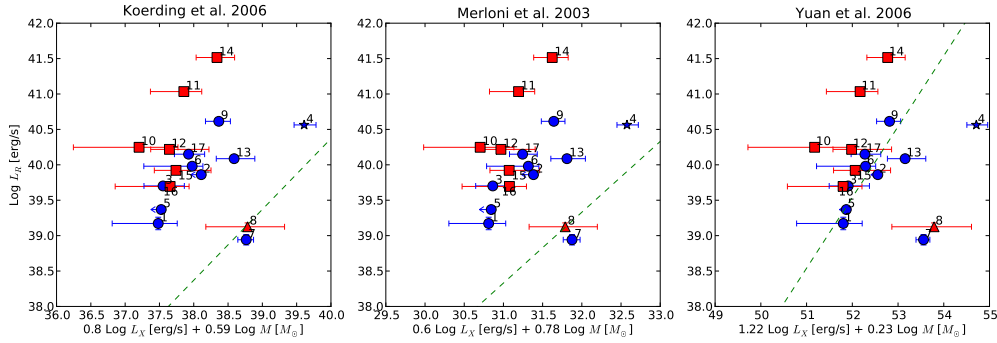
Figure 2.6: Fundamental plane of active black hole relations. Green dashed lines shows the expected relation as found by Körding et al. (2006) (left), by Merloni et al. (2003) (centre) and by Yuan et al. (2009) (right). Symbols are as in Fig. 2.1.

In the radio – X-ray plane (Fig. 2.5) there is no evident correlation between the two variables and the separation between steep- and flat-spectrum sources is not present any longer. However, sources of our sample classified as LEG lie in the same location (with the important exception of source 7) found by Panessa et al. (2007) for a sample of Low Luminosity Radio Galaxy (green line in Fig. 2.5) extracted from the FR I galaxies of the 3C catalogue (Balmaverde et al. 2006). FR I galaxies are indeed almost always classified as LEG, and Seyfert galaxies are usually $2 - 3$ order of magnitude more powerful in X-ray for a given radio emission.

### 2.4.3   The fundamental plane of active black holes

Almost all sources of our sample lie above the fundamental plane of black hole activity described in Körding et al. (2006) (Fig. 2.6, left panel) and in Merloni et al. (2003) (Fig. 2.6, central panel). These two planes were derived using AGNs selected with rather different criteria. For the first using only AGNs where X-ray emission is believed to be jet-dominated while for the second explicitly excluding jet-dominated systems. An explanation of such behaviour in terms of underestimating the X-ray extinction from the spectra and, therefore, a shift towards the left side in Fig. 2.6 is unlikely. Even taking into account all difficulties in estimating the unabsorbed X-ray emission, the vast majority of our sources (14 out of 17) would need to be so heavily obscured as to bring their X-ray emission down by a factor $\sim 100$. Such a large fraction of heavily obscured objects would be very unusual, with current estimates of the incidence of Compton thick AGN at these redshifts (albeit these are for somewhat higher luminosities) ranging between 20% and 50% (see e.g. Goulding et al. 2011).

Also, the possibility of overestimating radio emission due to boosting effect appears improbable. A boosting effect should affect mainly sources with a flat spectrum, that is likely to be connected with emission from AGNs core and jets, and would have affected both radio and

X-ray emissions, while what we find is an excess of radio and a lack of X-ray emission. Furthermore, this would have brought forth a much larger scatter in the fundamental plane relation and the presence of some broadening in emission lines that are missing.

In fact, LEG sources in our sample describe a tighter relation (again with the exception of source 7) than what expected from the fundamental plane of Merloni et al. (2003). This relation has an intrinsic dispersion of $\sigma_\perp = 0.60$, while our LEG sample has a dispersion that is a factor 1.7 smaller ($\sigma_\perp = 0.35$, that goes down to $\sigma_\perp = 0.26$ without source 7). The expected dispersion of the fundamental plane of Körding et al. (2006) ($\sigma_\perp = 0.28$) is instead compatible with what we find. It must also be noted that part of the dispersion in our data certainly arises from the errors associated to (at least) our very weak X-ray luminosities and consequent difficulties in estimating absorptions.

We find that neither Merloni et al. (2003) nor Körding et al. (2006) fundamental planes are able to correctly recover the relation between radio and X-ray emissions for our sample of LLAGN. This is indeed expected in the first case, where the majority of jet-dominated objects were excluded from the derivation. In the Körding et al. (2006) version of the fundamental plane relationship instead only jet-dominated system (low-hard state XRB, LLAGN and FRI radio galaxies) were exploited for derivation, nevertheless our data do not follow that relation either.

Similar results were found by Hardcastle et al. (2009), they tested the fundamental plane with a set of powerful radio galaxies from the 3CRR catalogue whose jet and accretion X-ray components can be disentangled using deep XMM spectroscopy. They found that, when considering only the accretion-related X-ray component, their sources lie in the predicted position on the fundamental plane of Merloni et al. (2003). Using the jet related component instead, the sources move to the same location where our sample of low luminosity objects lie. This underline the care that needs to be taken before using fundamental plane relations with objects that could be jet-dominated.

In Yuan & Cui (2005) an interpretation of the fundamental plane in terms of ADAF-jet model is given together with a prediction that the X-ray emission should originate from jets rather than ADAFs when the X-ray luminosity in the 2-10 keV band is lower than a critical value $L_{X,crit}$ (equation 7 in Yuan & Cui 2005). In such a situation, the slope of the relation between radio and X-ray luminosity is steeper and the normalization higher than that predicted by Merloni et al. (2003). Yuan et al. (2009) tested these ideas with a sample of 22 low luminosity AGNs and found a relation very close to that defined by our sample (left panel in Fig. 2.6) and close to the prediction of Yuan & Cui (2005) for X-ray emission produced at the base of the jet. However, the critical X-ray luminosity predicted by Yuan & Cui (2005), for the object in our sample, should correspond to $\log L_{X,crit} \approx 39.6$ erg/s, while all our objects have higher X-ray luminosities. Nevertheless, it should be noted that the Yuan & Cui (2005) criterion is

to be intended in a statistical sense and not as a sharp division between two populations, and the exact value of the critical luminosity may depend on the specific incarnation of the ADAF (viscosity, electron to ion heating efficiencies, etc.). Even so, the location of our sources in the radio luminosity - X-ray luminosity - SMBH mass space enhance the interpretation that X-ray emission in our sample (at least for LEG sources) is probably related to the jet synchrotron emission rather than the Comptonization emission from the (radiatively inefficient) accretion flow.

## 2.5   Discussion

As we argued in Section 2.4.1, at least for LEG sources, the absence or a reduced incidence of dusty/molecular gas may explain the [OIII]-X-ray correlation and the unusual missing signs of X-ray absorption in all LEG X-ray spectra (signs of absorption are only found in the HEG source). Moreover, part of the scatter in the observed [OIII]-X-ray relations is directly linked to the radio spectra of the sources, and we have argued in Sec. 2.4.2 that our flat-spectrum sources live in a gas poorer environment, and consequently their jets undergo a small interaction with the ambient medium.

   Independent evidence for an intrinsic difference in the amount of cold/obscuring material in low luminosity AGN has been gathered recently. Elitzur & Ho (2009) showed that, in a nearly complete sample of nearby AGN, the broad line region disappears at low intrinsic luminosities, and interpreted this fact within the disc-wind scenario for the broad line region (BLR) and toroidal obscuration in AGN (Elitzur 2008). If the BLR constitutes the inner, dust-free part of the cold molecular obscuring torus (see e.g. Netzer 2008), then a similar behaviour should be expected also for other indicators of intrinsic nuclear absorption. Indeed Tran et al. (2011), using optical spectropolarimetry on a set of 3 low luminosity type 2 AGNs, found no sign of broad line region nor obscuring torus. Furthermore, Burlon et al. (2011) found for the first time tantalizing evidence that the fraction of obscured AGN in a complete, hard-X-ray selected sample of nearby AGN, declines at $L_X < 10^{42}$ erg s$^{-1}$.

   In Sec. 2.4.3 we pointed out a different behaviour between LEG sources and those defining the Merloni et al. (2003) fundamental plane, and this is explainable with a different X-ray production mechanism between the population used to construct the fundamental plane and our sample. In the fundamental plane, X-ray emission is assumed to be generated by a (radiatively inefficient) accretion flow while, in LEG objects presented here, a much weaker (about 2 order of magnitude) X-ray emission could be generated by the jet itself. The tight correlation ($\sigma_\perp = 0.35$) between radio and X-ray emission for LEG objects enhances this conclusion, and is in agreement with the analysis of Yuan et al. (2009). Future studies on the relation between radio

and X-ray emissions and the object mass in a bigger sample can unveil possible new relations similar to the fundamental plane but tuned for low luminosity, jet-dominated objects. Based on the results presented here, such a plane will lie above the fundamental plane found in Merloni et al. (2003) and will have a smaller scatter as a consequence of the tight relation between radio and X-ray production in such kind of sources.

With respect to the analysis performed in Merloni et al. (2003), we remark here that the heterogeneity of their sample selection prevented any uniform classification of the X-ray spectra in terms of the amount of obscuration present. Based on the work presented here, it is likely that a large part of the scatter in the original fundamental plane relation could be due to the inclusion of both gas poor and gas rich sources in the original analysis.

Taken together, these considerations open the possibility to use X-ray emission as an unbiased estimator of source total power for low luminosity AGN, provided robust indicators of a lack of cold gas in the observed systems is available. [OIII] emission, although useful in the detecting and classification procedure, can be biased by the amount of dust present in the AGN surroundings, as we can infer by different position of steep- and flat-spectrum sources in Fig. 2.4.

## 2.6 Conclusions

In this chapter I have analysed a set of sources extracted from the SDSS catalogue. For these sources I have measured *Chandra* X-ray flux, radio luminosity in two bands from the VLA and optical spectral information extracted from the SDSS database. Our sources span a wide range in optical [OIII] and radio luminosities but they have very similar SMBH masses ($\sim 10^8 \ M_\odot$) and are all located over a narrow redshift range ($0.05 < z < 0.11$).

Although this sample spans a wide range of [OIII] and radio luminosities, we found that 15 out of 17 sources are classified as LEG. The sample shows a correlation on the uncorrected [OIII]-X-ray luminosity plane that is not seen in samples of type 2 AGNs with higher [OIII] luminosity (Heckman et al. 2005). An absent or reduced obscuring torus can explain this relations and different amount of gas in the AGN surroundings can account, to first order, for its scatter. This last property is well connected to the radio spectral index. This has important implications for selecting criteria in upcoming low-luminosity AGN surveys. For LEG samples, the lack of X-ray obscuration means that X-ray emission can be used as a good selection quantity with no obscuration selection biases. Nevertheless, radio core emission is still the easiest way to identify this class of objects (Ho 2008), although more information (i.e. from optical spectra) is still required for object classification.

Summarizing, my conclusions:

- At low luminosities ($L_X < 10^{42}$ erg s$^{-1}$) a selection criteria based on [O<span style="font-variant:small-caps">iii</span>] emission is not required in order to minimize the loss of of obscured sources. At low luminosity, X-ray and [O<span style="font-variant:small-caps">iii</span>] emissions are correlated and there are no evident signs of X-ray absorption.

- We found that all steep spectrum sources have around an order of magnitude more [O<span style="font-variant:small-caps">iii</span>] emission than flat-spectrum sources with similar X-ray luminosity. We argue that the amount of interstellar medium available for interaction in the proximity of the AGN is responsible for this distinction in the radio spectrum and for the difference in the production of the [O<span style="font-variant:small-caps">iii</span>] line.

- In the radio – X-ray relation (and so in the fundamental plane of active black holes), LEG sources have a smaller dispersion and a reduced X-ray production compared to other types of AGN (i.e. Seyfert galaxies and quasars). This can be explained associating X-ray and radio production to the same physical mechanism, i.e. synchrotron emission from the base of the jet, in very good agreement with recent investigation (see e.g., Hardcastle et al. 2009) although obtained from sample selected with different criteria.

# The Low-Frequency Array

As explained in Chap. 1, the study of low-luminosity, radiatively inefficient AGNs is tightly related to radio-astronomy. The first radio maps and surveys of the sky were done by Reber (1940) and Ryle & Smith (1948). In 1950 Bolton et al. (1949) identified three radio sources with external galaxies: Virgo A (M87), Cygnus A, and Centaurus A (NGC 5128). Each of these objects was later optically identified as an active galaxy. This is just a small example about how radio-astronomy has been a fundamental mean to explore active galaxies from its beginning and even more when aperture synthesis interferometry became available, whose development was worth the Nobel prize to Martin Ryle and Antony Hewish in 1974 (Ryle & Hewish 1960). In the next section I will explain the basic concepts of aperture synthesis interferometry, focussing on the Low-Frequency Array (LOFAR) explained in Sec. 3.2. In Sec. 3.3 I will focus on some typical problems related to low-frequency radio astronomy and in Sec. 3.4 I will describe the LOFAR imaging pipeline and some examples of the commissioning activity results.

## 3.1   Radio interferometry

First radio-telescopes were simple single dish instruments. The Angular resolution of a single dish telescope in arcsec is $3437 \, \lambda/D$, where $\lambda$ is the observing wavelength and $D$ is the dish (antenna) diameter. As an example the antenna as the Effelsberg radio-telescope ($D = 100$ m), observing at 21 cm has an angular resolution of $\sim 9'$. Indeed, the principal limitation of these instruments is their relatively low angular resolution. This limitation is even more evident at lower frequencies ($\lesssim 1$ GHz). To overcome this problem in the last 40 years many radio-interferometers have been commissioned. Some of them are the Westerbork Radio Synthesis Telescope (WRST) with 10 antennas of 25 m (1956), the Jansky Very Large Array (VLA) with 27 antennas of 25 m (1980), the Australia Telescope Compact Array (ATCA) with 6 antennas

of 22 m (1988), the Giant Meterwave Radio Telescope (GMRT) with 30 antennas of 45 m (1995), the Atacama Large Millimeter Array (ALMA) with 54 dishes of 12 m and 12 dishes of 7 m (2008) and the Low-Frequency Array (LOFAR) which will be described in Sec. 3.2.

Interferometers are constituted by a number of antennas whose signals are combined to "simulate" a big single-dish radio-telescope, the diameter of which is comparable to the longer distance between two interferometer antennas. It is then possible to reach very-high angular resolutions by positioning antennas far apart. In the most extreme case, with intercontinental interferometry the single antennas are located up to a few 10 000 km apart and the angular resolution at mm-wavelengths can reach down to the $\mu$-arcsec regime. In this case the various antennas are not directly linked and data are usually recorded at each of the telescopes to be jointly processed in a second step, with obvious limitation of the maximal sensitivity achievable dictated by data storage and post-processing capacities. The various techniques implemented to deal with such large antennas separations, or *baselines*, have the common name of very long baseline interferometry (VLBI).

I will now describe the basic principles of radio interferometry. However, instead of re-obtain the fundamental equations in the standard way, such that proposed in textbooks like the notorious "Synthesis Imaging in Radio Astronomy" (Taylor et al. 1999), I will use here the *radio interferometry measurements equations* (RIME) formalisms proposed by Hamaker et al. (1996) and then re-presented by Smirnov (2011a,b). The reason is twofold: (i) this procedure, albeit being more formal, is more intuitive for the typical problems connected with LOFAR, and (ii) this formalism is the one implemented in the LOFAR calibration software.

**Units**

To avoid any confusion, I will list here the fundamental quantities and relative units usually used in radio-astronomy. We call *specific intensity*, *surface brightness* or simply *brightness*

$$I_\nu = \frac{\mathrm{d}E}{\mathrm{d}t\,\mathrm{d}\nu\,\mathrm{d}A\,\mathrm{d}\Omega} \ [\mathrm{erg\,s^{-1}\,cm^{-2}\,Hz^{-1}\,Sr^{-1}}]\,, \tag{3.1}$$

where $E$ [erg s$^{-1}$] is the energy emitted in bandwidth $\mathrm{d}\nu$ over time $\mathrm{d}t$, $t$ [s] is the exposure time, $\nu$ [Hz] is the frequency, $A$ [cm$^2$] is the collecting area of the telescope and $\Omega$ [Sr] is the observed solid angle on the source or the telescope beam size[1]. A key property of the surface brightness is that it is independent from the source distance and it is thus a specific property of the source.

To derive other quantities, we must integrate $I_\nu$:

- Flux Density: $F_\nu = \int I_\nu\,\mathrm{d}\Omega$ [erg s$^{-1}$ cm$^{-2}$ Hz$^{-1}$], commonly expressed in Jy = $10^{-23}$ erg s$^{-1}$ cm$^{-2}$ Hz$^{-1}$ = $10^{-26}$ W m$^{-2}$ Hz$^{-1}$.

---

[1]Unless specified with *beam* I mean the primary lobe of the antenna radiation pattern or, more formally, the opening angle of the smallest resolvable angular unit.

- Power received: $P_\nu = \int F_\nu \, \mathrm{d}A$ [erg s$^{-1}$ Hz$^{-1}$].

- Luminosity: $L = 4\pi D^2 F_\nu$ [erg s$^{-1}$ Hz$^{-1}$], where $D$ is the source luminosity distance. $L$ is also an intrinsic property of the source and assumes an isotropic emission.

It is common practice to report the brightness $I_\nu$ in unit of Jy/beam, where the beam has units of [Sr]. In this way a point source has the peak flux equal to its total flux independently from the beam size. Model images of sources are beam-independent, so their flux is usually in unit of Jy/(pixel area).

Finally, it is also common to express the brightness in term of brightness temperature. We know in fact that at low-frequencies a black body specific intensity $B_\nu$ approaches the Rayleigh-Jeans limit

$$B_\nu(T) = \frac{2h\nu^3}{c^2} \frac{1}{e^{\frac{h\nu}{kT}} - 1} \xrightarrow{h\nu/kT \ll 1} \frac{2\nu^2 kT}{c^2}; \ T \approx \frac{B_\nu c^2}{2\nu^2 k}, \tag{3.2}$$

where $k$ is the Boltzmann constant, $h$ is the Planck constant and $T$ is the temperature. We call *brightness temperature* $T_B$ the temperature a black body would have to be to duplicate the observed specific intensity $I_\nu$ of a (grey body) object at a frequency $\nu$, i.e. $B_\nu(T_B) = I_\nu$. Only in the case of black-body radiation $T_B$ is it the same at all frequencies.

## 3.1.1 The RIME formalism

Let us begin with a quasi-monochromatic signal from a single source. In any point in space and time the signal is described by the complex vector $\boldsymbol{e}$. In an orthonormal $xyz$ coordinate system, with $z$ along the direction of propagation from the antenna to the source, $\boldsymbol{e}$ can be represented by a column vector of two complex numbers:

$$\boldsymbol{e} = \begin{pmatrix} e_x \\ e_y \end{pmatrix} \tag{3.3}$$

The fundamental assumption in RIME is *linearity*: all transformations along the signal path are linear with respect to $\boldsymbol{e}$. Every linear transformations of $\boldsymbol{e}$ can be represented by a matrix multiplication like $\boldsymbol{e}' = \boldsymbol{J}\boldsymbol{e}$, where $\boldsymbol{J}$ (the *Jones matrix*) is a $2 \times 2$ complex matrix. Multiple effects along the signal propagation path correspond to repeated matrix multiplications or *Jones chains*.

As the signal hits the antennas' receivers, it is converted into two complex voltages ($v_a$ and $v_b$) which represents the two polarisations. We can represent this process as another matrix multiplication

$$\boldsymbol{v} = \begin{pmatrix} v_a \\ v_b \end{pmatrix} = \boldsymbol{J}\boldsymbol{e}, \tag{3.4}$$

In this equation, $\boldsymbol{J}$ is the cumulative product of all propagation effects along the signal path including electronic effects in the antenna and in the receiver.

Two antennas $p$ and $q$ measure two independent voltages described by $\boldsymbol{v}_p, \boldsymbol{v}_q$. These are then sent to the correlator, which produces four pairwise correlations between the components of $\boldsymbol{v}_p$ and $\boldsymbol{v}_q$

$$\langle v_{pa} v_{qa}^* \rangle, \langle v_{pa} v_{qb}^* \rangle, \langle v_{pb} v_{qa}^* \rangle, \langle v_{pb} v_{qb}^* \rangle \tag{3.5}$$

where $\langle ... \rangle$ denote averaging over some time and frequency and $x^*$ is the complex conjugate of $x$. It is now convenient to organise these four correlations into the so-called *visibility matrix*

$$\mathsf{V}_{pq} = 2 \begin{pmatrix} \langle v_{pa} v_{qa}^* \rangle & \langle v_{pa} v_{qb}^* \rangle \\ \langle v_{pb} v_{qa}^* \rangle & \langle v_{pb} v_{qb}^* \rangle \end{pmatrix} = 2 \langle \boldsymbol{v}_p \boldsymbol{v}_q^H \rangle, \tag{3.6}$$

where the apex $H$ represents the conjugate transpose operation.

We now consider a signal $\boldsymbol{e}$ which travels from a distant point along two different paths, to antennas $p$ and $q$. As discussed above, each propagation path has its own total Jones matrix $\boldsymbol{J}_p$ and $\boldsymbol{J}_q$. Combining Eqs. 3.4 and 3.6, we get

$$\mathsf{V}_{pq} = 2 \langle \boldsymbol{J}_p \boldsymbol{e} (\boldsymbol{J}_q \boldsymbol{e})^H \rangle = 2 \langle \boldsymbol{J}_p (\boldsymbol{e}\boldsymbol{e}^H) \boldsymbol{J}_q^H \rangle = 2 \boldsymbol{J}_p \langle \boldsymbol{e}\boldsymbol{e}^H \rangle \boldsymbol{J}_q^H = 2 \boldsymbol{J}_p \begin{pmatrix} \langle e_x e_x^* \rangle & \langle e_x e_y^* \rangle \\ \langle e_y e_x^* \rangle & \langle e_y e_y^* \rangle \end{pmatrix} \boldsymbol{J}_q^H, \tag{3.7}$$

where we assumed $\boldsymbol{J}_p$ and $\boldsymbol{J}_q$ constant over the averaging interval. The bracketed quantities in this last equation are related to the Stokes parameters (Hamaker et al. 1996) via

$$2 \begin{pmatrix} \langle e_x e_x^* \rangle & \langle e_x e_y^* \rangle \\ \langle e_y e_x^* \rangle & \langle e_y e_y^* \rangle \end{pmatrix} = \begin{pmatrix} I + Q & U + iV \\ U - iV & I - Q \end{pmatrix} = \mathsf{B} . \tag{3.8}$$

*B* is called the *brightness matrix*. This provides the RIME of a single point source

$$\mathsf{V}_{pq} = \boldsymbol{J}_p \mathsf{B} \boldsymbol{J}_q^H , \tag{3.9}$$

which ties together the observed visibilities $\mathsf{V}_{pq}$, the intrinsic source brightness $\mathsf{B}$ and the per-antenna terms $\boldsymbol{J}_p$ and $\boldsymbol{J}_q$. It is also possible to expand $\boldsymbol{J}_p$ and $\boldsymbol{J}_q$ into their associated Jones chains, which results in

$$\mathsf{V}_{pq} = \boldsymbol{J}_{pn} (...(\boldsymbol{J}_{p2} (\boldsymbol{J}_{p1} \mathsf{B} \boldsymbol{J}_{q1}^H) \boldsymbol{J}_{q2}^H)...) \boldsymbol{J}_{qm}^H . \tag{3.10}$$

This corresponds to various effects in the signal path applied to the original source brightness B. Note that the order of the effect is important, since matrices not always commute. The two signal paths towards the two antennas can in principle be entirely dissimilar, making the chain asymmetric. Furthermore, different propagation effects are described by different kinds of Jones matrices. The simplest kind of matrix is a scalar, and it is generated by a transformation
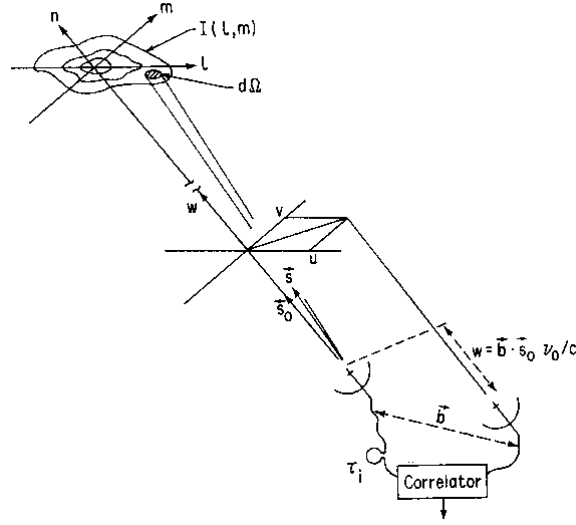
Figure 3.1: Right-handed coordinate systems used to express the interferometer baselines positions $\boldsymbol{u}$ = $(u, v, w)$ and the source brightness distribution $\boldsymbol{l} = (l, m, n)$, from Taylor et al. (1999).

that affects both components of $\boldsymbol{e}$ equally. An obvious example is a phase delay. More complex matrices are for example those due to a differential Faraday rotation effects. In this case these matrices are rotation matrices, where all the four terms are non-zero, underlying the intermix the two components of $\boldsymbol{e}$.

In the ideal case of a completely uncorrupted observation, there is one fundamental effect remaining, that is the phase delay associated with signal propagation due to the geometric path-length difference from the source to antennas $p$ and $q$. Considering antenna $p$ located at coordinates $\boldsymbol{u}_p = (u_p, v_p, w_p)$ (see Fig. 3.1), the phase difference at point $\boldsymbol{u}_p$ relative to a generic $\boldsymbol{u} = 0$, for a signal arriving from direction $\boldsymbol{s}$, is given by

$$\kappa_p = 2\pi\lambda^{-1}(u_p l + v_p m + w_p(n - 1)),\tag{3.11}$$

where $l, m, n = \sqrt{1 - l^2 - m^2}$ are the direction cosines of $\boldsymbol{s}$ (see Fig. 3.1), and $\lambda$ is signal wavelength. It is a good choice to define $\boldsymbol{u}$ in units of wavelength, which allows us to omit the $\lambda^{-1}$ term. We can now describe a phase delay matrix (scalar) $K_p$ with

$$K_p = \mathrm{e}^{-i\kappa_p} = \mathrm{e}^{-2\pi i(u_p l + v_p m + w_p(n-1))},\tag{3.12}$$

which in turn provides the RIME for a single uncorrupted point source

$$\mathsf{V}_{pq} = K_p \mathsf{B} K_q^H.\tag{3.13}$$

we call this visibility matrix the *source coherency*, and write it as $\mathsf{X}_{pq}$.

In the real world we have some corrupting effects acting on our signals, we can write them in a total Jones $\boldsymbol{J}_p$ (Eq. 3.9) together with the nominal phase delay $K_p$ as

$$\boldsymbol{J}_p = \boldsymbol{G}_p K_p \,, \tag{3.14}$$

where $\boldsymbol{G}_p$ represents all the corrupting effects. We can then formulate the RIME for a single corrupted point source as

$$\mathsf{V}_{pq} = \boldsymbol{G}_p \mathsf{X}_{pq} \boldsymbol{G}_q^H \,. \tag{3.15}$$

Note that we are not sure that the phase delay $K$ is the last effect to take place (e.g. all antenna-related effect happen later), but since it is a scalar and it commutes with all the Jones matrices, we are always allowed to move it close to the brightness matrix.

## 3.1.2   Direction dependant effects

Direction dependant effects are one of the most challenging problems that low-frequency radio-telescopes as LOFAR have to face. They are directly linked to the low-frequency regime at which LOFAR operates. Observing long-wavelength implies extremely wide field of view, moreover the absence of dishes to collect the radiation implies that at any time *all* the sky is observed. Consequently, the fluxes coming from sources far apart are detected after passing through different atmospheric conditions (in the low-frequency regime is the ionosphere which create major troubles) and different instrument responses.

Let's now put $N$ sources in the sky. Each source contributes to the final visibilities with a $\mathsf{V}_{pq}$, and they add up linearly. The signal propagation path is different for each source $s$ and antenna $p$, but each path can be described by its own Jones matrix $\boldsymbol{J}_{sp}$. The fact that Jones matrix now depends also on the source $s$ is the first step in attacking direction dependant effects. Eq. 3.9 now becomes

$$\mathsf{V}_{pq} = \sum_s \boldsymbol{J}_{sp} \mathsf{B}_s J_{sq}^H \tag{3.16}$$

Some elements in the chain may be the same for all sources, e.g. antenna effects such as an electronic gain. Let collapse the chain into a product of three Jones matrices

$$\boldsymbol{J}_{sp} = \boldsymbol{G}_p \boldsymbol{E}_{sp} K_{sp} \,, \tag{3.17}$$

where $\boldsymbol{G}_p$ is the source-independent side of the Jones chain and $\boldsymbol{E}_{sp}$ is the source-dependent remainder of the chain. $K_{sp}$ is the usual phase term. We can then rewrite Eq. 3.16 as follows

$$\mathsf{V}_{pq} = \boldsymbol{G}_p \left( \sum_s \boldsymbol{E}_{sp} K_{sp} \mathsf{B}_s K_{sq}^H \boldsymbol{E}_{sq}^H \right) \boldsymbol{G}_q^H \,, \tag{3.18}$$

where $G_p$ are the so-called direction-independent effects (DIE) and $E_{sp}$ are the direction-dependent effects (DDE). It is worth to notice that in RIME terminology, the beam gain is just another Jones matrix in the chain, which force $E_{sp} \to 0$ for sources outside the beam.

In the general case, the sky is not a sum of discrete sources, but a continuous brightness distribution $\mathsf{B}(s)$, where $s$ is a unit direction vector. Jones matrices are now in the form $J_p(s)$ and Eq. 3.16 becomes

$$V_{pq} = \int_{4\pi} J_p(s)\,\mathsf{B}(s)\,J_q^H(s)\,d\Omega\,. \tag{3.19}$$

Projecting this spherical integral on the plane $(l, m = l)$ tangential to the field centre we obtain

$$V_{pq} = \iint_{lm} J_p(l)\,\mathsf{B}(l)\,J_q^H(l)\frac{dl\,dm}{n},\quad \text{where } n = \sqrt{1 - l^2 - m^2}\,. \tag{3.20}$$

Finally, decomposing the $J$ matrix into its components and putting together the $K$ terms we obtain

$$V_{pq} = G_p \left( \iint_{lm} \frac{1}{n}\bar{E}_p\mathsf{B}\bar{E}_q^H e^{-2\pi i(u_{pq}l + v_{pq}m + w_{pq}(n-1))}\,dl\,dm \right) G_q^H \tag{3.21}$$

This is a more general formulation of the famous van Cittert-Zernike theorem, which states that the spatial autocorrelation function of the electromagnetic field is the Fourier transform of the brightness distribution. In this case, this definition is extended to include the polarization and direction dependant effects. It is important to consider the presence of the $p$ and $q$ indices of the $E$ matrices in Eq. 3.21. They stress that we are measuring a 2D Fourier transform of a sky that is different for every baseline. This violates the fundamental idea of traditional selfcal[2], which assumes that we are measuring the Fourier Transform of one common sky.

### 3.1.3 Imaging

The visibilities defined in Eq. 3.6, are complex quantities and their amplitudes have units of flux density, i.e. Jansky [Jy] $= 10^{-23}$ erg s$^{-1}$ cm$^{-2}$ Hz$^{-1}$. They are connected to the spatial frequency spectra of the sky brightness distribution in a direction parallel to the baseline's one via Eq. 3.21. In order to sample many spatial frequencies in many directions, we want to combine as many antennas as possible and use the rotation of the Earth to modify the relative position of the baselines with respect to the sky. This technique is called *aperture synthesis*. The visibilities are usually displayed in a plane at right angles to a direction from which radiation is being received from the sky, called *uv*-plane (the same defined in Sec. 3.1.1 and in Fig. 3.1). When the interferometer observes a point on the celestial sphere, the Earth rotation causes the *u*

---

[2]The calibration procedure which uses the observed sky as its own calibrator through an iterative process.

and $v$ components of the baseline to trace out an elliptical locus in the $uv$-plane. More precisely, since the brightness is a real function, its Fourier transform is hermitian (i.e., $V(-u, -v) = V^H(u, v)$) and in practice two lines are traced in the $uv$-plane for each baseline. Finally, an interferometer which has $n$ antennas, will have $n(n-1)/2$ baselines, each of them producing two tracks on the $uv$-plane. An examples of these $uv$-tracks on real LOFAR data is in Fig. 4.3.

Even with a good sampling of the $uv$-plane (or $uv$-coverage), it is impossible to cover it completely. Therefore, the interferometer acts as a filter towards the spatial frequencies fixed by the shortest and the longest baselines and detects only structures in the range between $\lambda/\boldsymbol{u}_{\max}$ and $\lambda/\boldsymbol{u}_{\min}$ radians. We can imagine the $uv$-coverage as a function $g_{uv}$ which is scalar and equal to 1 in the position where we have a data point and 0 for all the rest and it is usually named *point spread function* or *synthesized beam* (not to be confused with the antenna beam discussed in Sec. 3.3.3). The "true" visibility function (Eq. 3.21) is then multiplied by $g_{uv}$ and when we try to find the real brightness distribution (assuming no errors of any sort) inverting Eq. 3.21 we obtain a "dirty" brightness distribution $\mathsf{B} * \hat{g}_{lm}$ (where $\hat{\phantom{g}}$ denotes the Fourier transform and $*$ is the convolution operator) which is the convolution of the true brightness with the Fourier transform of the $uv$-coverage function. In order to obtain a more realistic image of the brightness distribution, the dirty images must be "deconvolved" with the synthesized beam. The CLEAN algorithm (Högbom 1974) and its evolutions is the most widely used procedure, see e.g. Clark (1980) (introduction of "minor" and "major" cycles), Schwab (1984) (clean components subtracted from the *un*-gridded visibility data), Cornwell (2008) (multi-scale cleaning) and Rau & Cornwell (2011) (multi-scale multi-frequency cleaning).

## 3.2   The LOFAR project

The Low-Frequency Array (LOFAR, Röttgering et al. 2003; Falcke et al. 2007, van Haarlem et al. 2012 to be submitted) is an innovative radio telescope that is optimized for the frequency range from 30 to 240 MHz, but also with the ability to observe down to 10 MHz. LOFAR does not have any moving parts and its hardware is based on simple and inexpensive components. The telescope receivers are two different kind of dipoles: the low-band antennas (LBA, see Fig. 3.2a), which cover the frequency range $10 - 90$ MHz, and the high-band antennas (HBA, see Fig. 3.2b), which cover the frequency range $110 - 240$ MHz. LBAs are inverted-V crossed-dipoles oriented NE-SW and SE-NW, they are designed to operate from the atmospheric spectral cut-off of the radio window at 10 MHz up to the onset of the commercial FM radio band of 90 MHz. Due to the presence of strong radio-frequency interference (RFI), this range is operationally limited to 30-80 MHz by default. To do this, a digital filter is employed to suppress the response below 30 MHz; however this filter can be de-select and the telescope

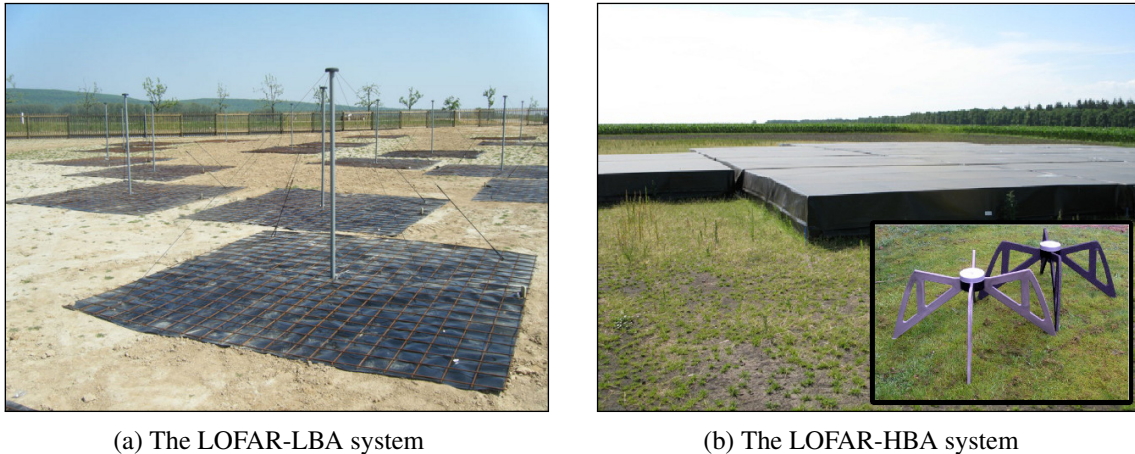(a) The LOFAR-LBA system          (b) The LOFAR-HBA system

Figure 3.2: LOFAR antenna systems. On the left side the LBA system, which consists of simple dual polarization droop dipoles above a conducting ground plane. On the right side the HBA system, which are blocks (tiles) of 16 dual dipole antennae (in the small figure) arranged in a $4 \times 4$ grid. The total number of dipoles is $\sim 40\,000$ for the HBA and $\sim 5\,000$ for the LBA.

can observe down to 10 MHz. The HBA are instead organized into tiles made of a $4 \times 4$ array of bowtie-shaped crossed dipoles. Each HBA tile is equipped with an analogue 5-bit beam former, which forms a single tile beam by combining the signal from these 16 antenna elements in phase. This limits the field of view of an individual tile to approximately 30° (FWHM at 150 MHz).

Dipoles are organized into soccer-field sized stations yielding, for each station, effective aperture sizes that range from 30 m to 80 m, depending on the frequency. Each set of dipoles within a station works as a phased aperture array, i.e., a delay is applied to the relative phases of the signals feeding the dipoles in such a way that the radiation pattern of the array is reinforced in a targeted direction and suppressed in undesired ones. By applying different delays, LOFAR can therefore "point" (create a beam) in more than one direction simultaneously and the number of beams is limited only by the bandwidth necessary to transfer the signal to the correlator and its computational power. For the stations in the Netherlands only 48 (out of 96) LBA dipoles can be currently used simultaneously. Among the different possibilities, mainly two possible configurations of the LBA dipoles are commonly used: LBA-INNER and LBA-OUTER. In these configurations the active dipoles are located respectively in the inner zone (suited for observations $\gtrsim$ 40 MHz) and in the outer zone (suited for observations $\lesssim$ 40 MHz) of the station field. The more concentrated are the dipoles in the inner zone, the more the side-lobe levels are reduced and the field of view (FoV) is wider, but at the cost of a reduced sensitivity. Each core station has the HBA grouped into two different sub-stations located at the edge of the station. These sub-stations can be used together or as standalone stations (DUAL observing mode), to increase the number of baselines.
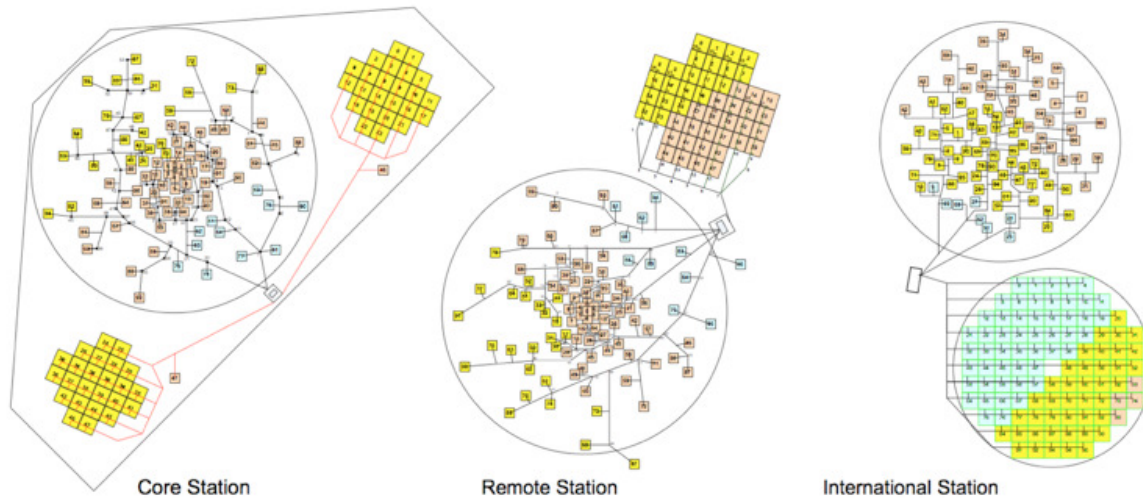
Figure 3.3: The three different stations (not to scale) available in the LOFAR array. Core stations has the HBAs divided into two sub-stations.

The complete configuration of LOFAR will consist of an array of stations distributed over 100 km within the Netherlands and out to 1000 km throughout Europe, which will provide sufficient resolution ($\approx 1''$ at 30 MHz) to allow optical identification of radio sources, even at low frequencies. At the time of writing, a total of 33 stations have been built in the Netherlands and 8 more across Europe (5 in Germany, 1 in the UK, 1 in France and 1 in Sweden)[3]. There are three kinds of LOFAR station layouts which are classified as *Core*, *Remote* or *International* stations, according to their distance from the centre of the array (see Fig. 3.3). The the array centre lies a central *super*-station (see Fig. 3.4), called *superterp*, which is located near Exeloo (NL) and is the composition of six core stations.

Once the data are collected from the stations they are transported to the central processing location via a Wide-Area Network, using dedicated light paths. Data are then correlated by a Blue Gene/P that contains 12480 processor cores providing 42.4 TFLOPS peak processing power. For a detailed description of the correlator see Romein et al. (2010).

### 3.2.1 Key science projects

LOFAR has six main key science projects (KSP) which drove its design. I will briefly describe them here, presenting some of the very first results:

**Extragalactic surveys** LOFAR is an instrument explicitly designed for surveys (large FoV and high sensitivity). Such surveys at several frequencies will provide unique catalogues

---

[3]An updated map of the station status can be found here: http://www.astron.nl/~heald/lofarStatusMap.html

Figure 3.4: The LOFAR "superterp". It is part of the core of the extended telescope and is located near Exloo, the Netherlands.

of radio sources for investigating several areas of astrophysics, including formation and evolution of super massive black holes, galaxies and clusters of galaxies. As an example at 50 MHz a single beam of LOFAR will be able to map (at theoretical sensitivity and with a feasible amount of time): one $z > 6$ radio galaxy, 5 Abell cluster, 5 NGC galaxies, 5 lensed radio sources and several giant radio galaxies. The survey KSP main goals are: (i) the study of high-redshift radio galaxies, we expect to detect protoclusters up to $z \sim 8$ and more than 100 galaxies at $z > 6$ (Miley & Breuck 2008). (ii) The study of radio emitting clusters, that so far is limited to a sample of $\sim 40$ objects (Ferrari et al. 2008), expecting to detect about 100 new clusters at $z \gtrsim 0.6$. The study of the cluster radio emission will provide important information on how thermal balance in cluster is obtained and clues on the magnetic field strength and topology on cluster scales. A first example of these studies is presented in van Weeren et al. (2012) (iii) The study of cosmic star-formation history, sampling millions of star forming galaxies at the epoch when the bulk of galaxy formation occurred. A preliminary study on a sample of nearby active/star-forming galaxies is presented in Chap. 5. (iv) The detailed study of active galactic nuclei (AGN) Physics and AGN evolution. Obtaining high-resolution images of nearby radio galaxies, LOFAR is able to study the AGN interaction with the intra-cluster magnetised medium, the AGN-galaxy feedback and several other key physical parameters. One of

the first radio galaxy deep study made with LOFAR is presented in Chap. 4.

**The epoch of reionization** one of the main tasks of LOFAR is the search for the redshifted 21 cm line emission from the Epoch of Reionization (EoR). It is currently believed that the period after recombination, when the universe turned neutral or "Dark Ages", lasted until around $z = 20$. Then, simulations (Ciardi & Ferrara 2005) and CMB studies (Komatsu et al. 2011) suggest that there may have been an extended reionization phase, the start possibly being around $z \sim 15 - 20$ and ending at $z \sim 6$. Thanks to LOFAR we will be able to probe the redshift range from $z = 11.4$ (115 MHz) to $z = 6$ (200 MHz). EoR studies will bring first light on questions like: when the first objects formed and how much ionizing radiation did they produce? How did this bubble of ionized material expand? Given the very low brightness temperature and the angular scale of the expected EoR signal, the only part of LOFAR that has the sensitivity to detect the EoR signal is the LOFAR core. A number of fields with minimal Galactic foreground emission will be observed for a total of several thousands of hours, reaching brightness temperatures of 50 - 100 mK per resolution element per MHz bandwidth, close to that of the redshifted 21 cm emission from the EoR (Zaroubi et al. 2012). Studying the power-spectra as function of redshift (frequency) allows us to probe the EoR as it unfolded over cosmic time.

**Transients** LOFAR has some of the most important characteristics to exploit the new parameter space given by temporal-monitoring: wide field of view, omni-directional antennae, high-speed data transport and computing power. In this way transient radio phenomena, will be discovered, localised and automatically shared with other facilities (e.g. gamma-ray, optical, X-ray observatories). On the other hand, the electronic repointing capability of LOFAR enables it to start a completely new observation in well under one minute once an internal or external (from other telescopes) trigger is received. The transient phenomena that LOFAR will detect may be associated with exploding stars, black holes emissions, flares, radio bursts from exoplanets or SETI signals.

**Pulsars** The majority of pulsar studies were at higher frequencies > 300 MHz because of interstellar medium dispersion and scattering. But the LOFAR high time resolution, flexible beam-formed observing modes, multi-beaming and large FoV are well-suited for pulsar studies (Stappers et al. 2011). These capabilities will allow the frequent monitoring of many pulsars to look for time anomalies such as glitches and profile changes. Furthermore, radio emission form some neutron stars can be detected only at the lowest radio frequencies (Deshpande & Radhakrishnan 1994). Finally, all-sky surveys are already begun looking for new radio pulsars targeting nearby galaxies, globular clusters and supernova remnants. First results which constrain some of the properties of the interstellar

medium and discuss pulse profile evolution are presented in Hassall et al. (2012).

**Astroparticle physics** High-energy and ultra-high-energy cosmic rays (HECRs and UHECRs) are those particles which hit the atmosphere with energies between $10^{15} - 10^{20.5}$ eV. Both the sites and processes for accelerating particles are unknown. Possible candidate sources of these HECRs are shocks in radio lobes of powerful radio galaxies (see Sec. 4.5.3), intergalactic shocks created during the epoch of galaxy formation, Hyper-novae or Gamma-ray bursts. When a cosmic particle hit a nucleus of an atom in the terrestrial atmosphere, it produces secondary particles, which react again producing more secondary particles. As a result an extensive air shower (EAS) is generated. Among the many particles, the EAS is composed also by electrons and positions which emit radio-waves travelling through the terrestrial magnetosphere. LOFAR will directly observe this radio emission when generated by EAS from primary particles in energy range $10^{15} - 10^{19}$ eV. The EAS are aligned along the direction of motion of the primary cosmic particle, which can then be recovered. At higher energies , LOFAR will detect (or put upper limits) to the Cherenkov flashes from UHECR at $10^{20} - 10^{20.5}$ eV in the lunar regolith.

**Cosmic magnetism** Most of our knowledge of astrophysical magnetic fields has come from radio-frequency observations of synchrotron radiation from relativistic cosmic-rays. These observations trace the total field strength (from the synchrotron intensity), the orientation and degree of ordering of fields in the plane of the sky (from the polarized component of the radiation), and the component of ordered fields along the line of sight (via Faraday rotation). Very little is known about the origin and evolution of cosmic magnetic fields in the space around galaxies and between galaxies. LOFAR will provide excellent measures of the spectral characteristics of the synchrotron radiation (see Sec. 4.4.3) which is directly linked to the magnetic field strength. Furthermore, LOFAR will increase the observable extent of radio emitters which is now limited by the diffusion speed of cosmic rays away from their sources and by the extent of the magnetic fields. At high radio frequencies ($1 - 10$ GHz) the radio emission from discs of normal galaxies is restricted to about 1 kpc from the sources of cosmic rays. Low-frequency radio emission traces low-energy particles which suffer less from energy losses and hence can propagate further away (up to several tens of kpc) from their sources into regions with weak magnetic fields. As the result, radio halos of galaxies and clusters are expected to appear much larger at low frequencies. Examples of this effect are presented in Sec. 5.3. Finally, Faraday rotation measurements through the new techniques of rotation measurement (RM) synthesis (Brentjens & de Bruyn 2005) will provide another important tool to investigate weak magnetic fields.

**Solar physics and space weather**  The Sun is an intense and extremely variable radio source. Intense radio bursts are associated with phenomena of the solar activity, like flares and coronal mass ejections. Solar observations with LOFAR will also include routine monitoring of the solar activity as the root of Space Weather. LOFAR has already observed two solar burs in March and October 2011 (Fallows et al. 2012; Mann et al. 2012).

### 3.2.2  Performances

**Sensitivity**

The radiometer equation provides the signal-to-noise ratio of a radio-telescope as

$$\frac{S}{N} = \frac{T_{\text{src}}}{T_{\text{rms}}} = \frac{T_{\text{src}}}{T_{\text{sys}}} \sqrt{\tau \Delta \nu} \, , \tag{3.22}$$

where $T_{\text{src}}$ is the brightness temperature of the observed source, $T_{\text{sys}}$ is the system temperature, $T_{\text{rms}}$ is the noise in the system (the RMS fluctuations in the system temperature), $\Delta \nu$ is the bandwidth (in Hz) and $\tau$ is integration time (in seconds). Temperatures are to be intended as brightness temperatures defined in Sec. 3.1. $T_{\text{sys}}$ describes the power received due to both the sky and that generated by the receivers. Using Eq. 3.2, with some manipulations one can rewrite $T_{\text{sys}}$ in terms of *system equivalent flux density* $F_{\text{sys}}$[4]

$$F_{\text{sys}} = \frac{T_{\text{sys}}}{A/2k} = \frac{2kT_{\text{sys}}}{A} \, . \tag{3.23}$$

This is a very useful form to compare the sensitivity of two different systems since it puts together $T_{\text{sys}}$ and the effective aperture $A$ (that is the geometric aperture multiplied by an efficiency factor). It also simplifies the sensitivity calculation, in fact if the flux $F_\nu$ of a source is known and the $F_{\text{sys}}$ is known, then one can easily calculate the integration time needed to make a given S/N detection as

$$\frac{S}{N} = \frac{F_\nu}{F_{\text{sys}}} \sqrt{\tau \Delta \nu} \, , \tag{3.24}$$

In a LOFAR intensity map, signals from different baselines and two polarizations are combined. Furthermore, LOFAR stations have different effective apertures, therefore the noise level in a final image is given by

$$N = W \left[ 2 \left( 2 \, \Delta \nu \, \Delta t \right) \left( \frac{N_c \left( N_c - 1 \right)/2}{F_c^2} + \frac{N_c N_r}{F_c F_r} + \frac{N_r \left( Nr - 1 \right)/2}{F_r^2} \right) \right]^{-1/2} \, , \tag{3.25}$$

where $W$ denotes a factor that increase the noise due to the weighting scheme, $N_c$ and $N_r$ are the number of core and remote stations respectively and $F_c$ and $F_r$ denote the system equivalent flux

[4]For LOFAR $F_{\text{sys}}$ is measured and tabulated online at http://www.astron.nl/radio-observatory/astronomers/lofar-imaging-capabilities-sensitivity/sensitivity-lofar-array/sensiti.

Table 3.1: LOFAR sensitivity

| Frequency [MHz] | $\lambda$ [m] | Superterp [mJy] | NL Core [mJy] | NL Full [mJy] | EU Full [mJy] |
|---|---|---|---|---|---|
| 15 | 20.0 | 547.00 | 127.00 | 75.80 | 63.80 |
| 30 | 10.0 | 101.00 | 23.60 | 14.00 | 9.76 |
| 45 | 6.67 | 43.50 | 10.10 | 6.03 | 4.28 |
| 60 | 5.00 | 33.70 | 7.86 | 4.67 | 3.33 |
| 75 | 4.00 | 56.20 | 13.10 | 7.79 | 5.56 |
| 120 | 2.50 | 1.94 | 0.47 | 0.28 | 0.20 |
| 150 | 2.00 | 1.54 | 0.37 | 0.22 | 0.16 |
| 180 | 1.67 | 1.76 | 0.43 | 0.25 | 0.18 |
| 200 | 1.50 | 1.91 | 0.46 | 0.28 | 0.20 |
| 210 | 1.43 | 1.99 | 0.48 | 0.29 | 0.21 |
| 240 | 1.25 | 2.21 | 0.53 | 0.32 | 0.23 |

Theoretical LOFAR sensitivity for 1 hour integration time, an effective bandwidth of 3.57 MHz, and dual polarization. A weighting factor $W$ of 1.3 is applied. The columns correspond to 6 core stations for the "Superterp", 23 core stations for "NL Core", 40 (planned) core and remote stations for "NL Full" and the complete 48 stations array for the "EU Full".

densities for the core and the remote stations respectively. In Table 3.1 the expected sensitivity of LOFAR in various configuration is summarised.

During the commissioning of the telescope we found that the major contribution to the maps noise was not that generated by the system, but was mainly coming from limitation in the dynamic range[5]. Given the wide field of view of LOFAR, in almost every observable field at least one strong source is present. Even with a reduced bandwidth (e.g. 4 MHz) and a reduced integration time (e.g. 4 hours) an average dynamic range of $\gtrsim 100\,000$ is needed to reach the thermal noise. Residual calibration errors form the beam/ionospheric corrections are likely the dominant effects in setting maps' noise level.

**Field of view**

The Full Width Half Maximum (FWHM) of a LOFAR Station beam is determined by

$$\text{FWHM} \simeq \alpha_1 \frac{\lambda}{D}, \tag{3.26}$$

where $\lambda$ is the observing wavelength and $D$ denotes the station diameter. $\alpha_1$ depends on the station tapering and it is measured to be $\sim 1.3$. Fig. 3.5 shows a plot of the FWHM with respect

---

[5]The dynamic range is defined as the ratio between the peak brightness in an image and the off-source error level. It is therefore a single number representing the degree of contrast visible in an image.
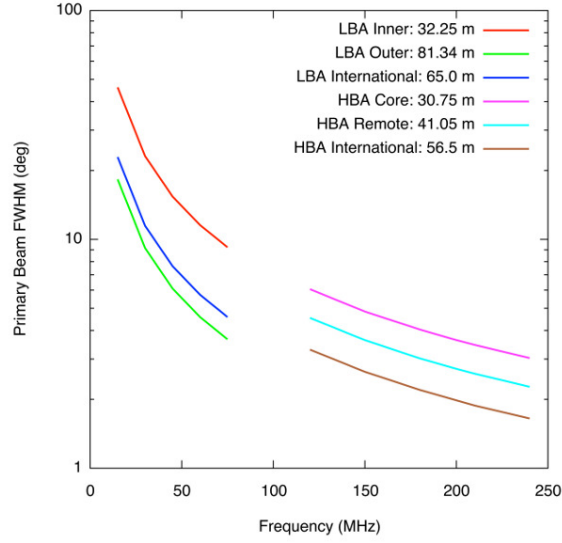
Figure 3.5: Primary beams (FWHM) as a function of frequency for the different configurations of LOFAR stations.

to the frequency. The FoV is simply defined as

$$\mathrm{FoV} = \pi \, \frac{\mathrm{FWHM}^2}{2} \tag{3.27}$$

With the sensitivity and the FoV we can compute the *speed of survey* (SoS) that is SoS $\propto$ FoV $T_{\mathrm{sys}}^{-2}$. Combining the SoS for LOFAR with number count predictions at these frequencies, one finds that for the HBA, surveys at 120 MHz are the most efficient in terms of detected sources, regardless of how steep the spectral index is assumed to be. For the LBA and for $\alpha = -0.8$ radio surveys at 60 MHz are the most efficient. For sources with a very steep spectrum of $\alpha = -1.6$ the 30 MHz frequency is preferred, but the difference with the 45 MHz system is only at the few percent level.

**Resolution**

The resolution of the LOFAR array is given by

$$\mathrm{Resolution} \simeq \alpha_2 \frac{\lambda}{\mathrm{L}} \,, \tag{3.28}$$

where $\lambda$ is the observing wavelength and $L$ is the maximum baseline length. $\alpha_2$ depends on the array configuration and the weighting scheme and is $\sim 0.8$ for uniform weighting. At present, international stations provide LOFAR with an angular resolution of $\sim 0''.15$ at 240 MHz and $\sim 1''$ at 30 MHz, while the dense core of 24 stations provides the necessary sensitivity to the extended emission. Fig. 3.6 shows the resolution versus the observing frequency for different array configurations.
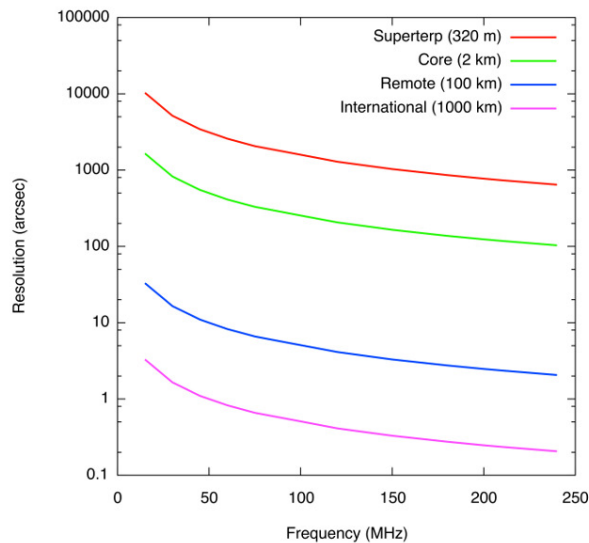
Figure 3.6: The resolution of LOFAR as a function of frequency for some array configurations.

## 3.3 The lowest frequencies

LOFAR covers the lowest frequencies observable from the Earth surface. In this section I will analyse three of the most serious problems we have to face while observing at these regimes: the radio interference, the ionosphere and the beam shape. This is definitely not a complete list of the possible effects arising at these frequencies, but they are the first we had to deal with during the first three years of commissioning.

### 3.3.1 Radio frequency interference

The low-frequencies covered by LOFAR are considerably affected by RFI. In Fig. 3.7 I report a study on RFI distribution in the LOFAR band. The gap around 100 MHz is almost entirely not accessible to LOFAR due to the FM-radio band being at these frequencies.

RFI has natural or man-made origin. The former is caused by lightning static during summer time observations, dust particles which attract charged particles in the proximity of antennas, solar bursts, geo-magnetic storms or ionospheric scintillations. The man-made interferences have many origins which reside in the electronic equipments present in the antennas itself, satellites, radio communications, airplanes, electrified fancies, radars, high-power electric lines... Most of these RFI are either in a constant small frequency range or are broadband but in a short time range (see Fig. 3.8).

Despite the numerous possible techniques one can adopt to remove RFI (see e.g., Barnbaum & Bradley 1998; Leshem et al. 2000; Baan et al. 2004, for some possible techniques), almost any observation needs to be post-processed due to residual RFI effects. The most used
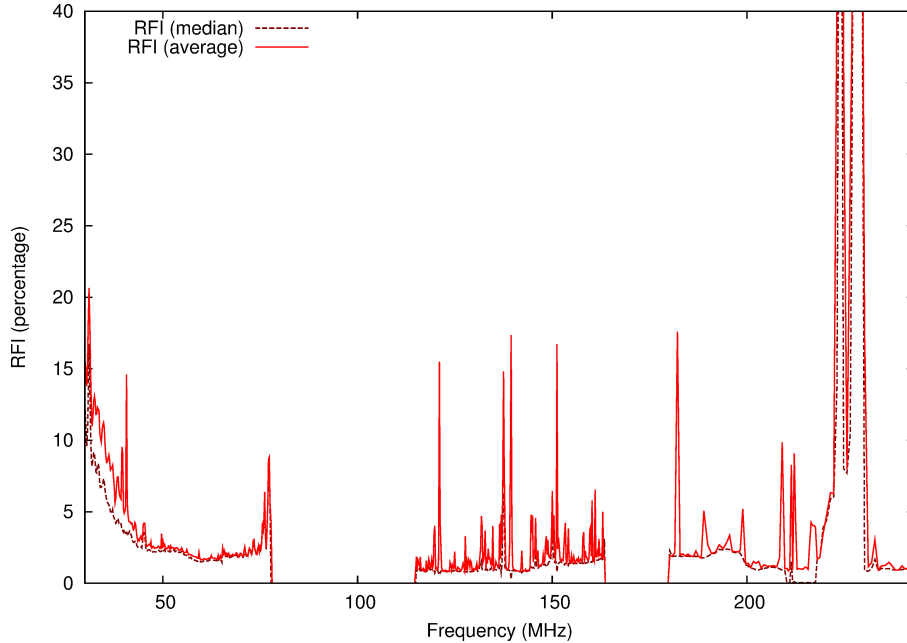
Figure 3.7: The RFI distribution in the observable frequencies of LOFAR. In most of the frequencies, the RFI situation cause only a few percent of data loss. Towards 30 MHz and lower, RFI becomes harder to deal with. The high end of the HBA is also affected by RFI due to a few strong and broadband digital broadcast transmitters. Image gently provided by André Offringa.

technique for such a final processing step consists of detecting the RFI in time, frequency and antenna space, and ignoring the contaminated data in further data processing. This step, called *data flagging*, was till nowadays performed by the astronomer. Given the amount of data produced by recent telescopes (an 8-hours LOFAR observation can easily produce $\gtrsim 1$ TB of data) this approach cannot be used any more. Therefore, on new instruments the tendency is to implement automated RFI flagging pipelines directly in the observing pipeline (for the LOFAR case, see Offringa et al. 2010a, 2012).

### 3.3.2 Ionosphere

The ionosphere is a layer of the atmosphere which starts at $\sim 100$ km above the Earth surface and terminates at $\sim 1000$ km (see Fig. 3.9). This layer of the atmosphere is highly ionised ($n_e = 10^4 - 10^6$ electrons cm$^{-3}$) and the ionization is due to the interaction between solar radiation and cosmic rays with the Earth's atmosphere. Clearly, the elevation of the Sun and the Sun activity influence the intensity of the solar radiation which in turn affect the concentrations of free electrons in the ionosphere. Therefore, the properties of the ionosphere show daily, seasonal and decadal variations. Furthermore, they are also dependent on the geographic latitude and on

(a) Time-frequency plot before flagging

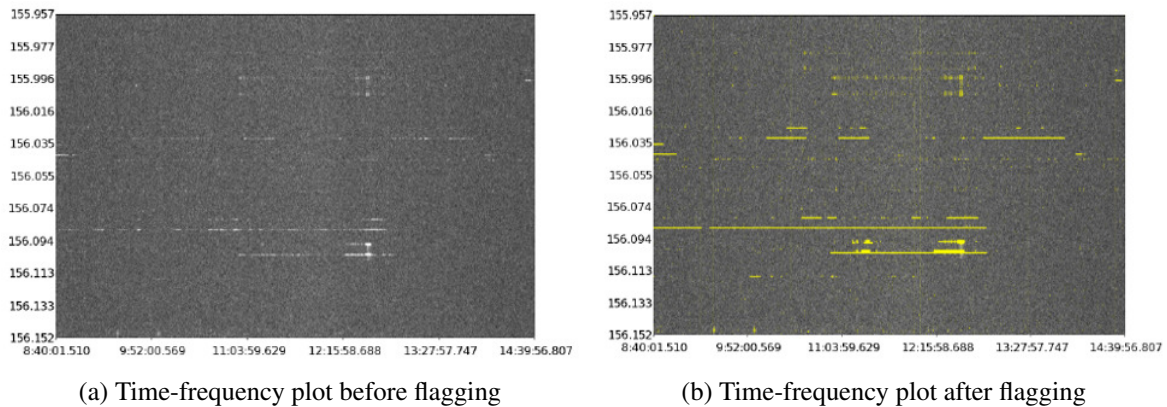(b) Time-frequency plot after flagging

Figure 3.8: Flagging results on a sub-band around 156 MHz for a 1.5 km baseline of a 6 hour LOFAR observation, from Offringa et al. (2010b). Horizontal axis is time and vertical axis is frequency. In the right image yellow pixels are flagged.

the geomagnetic field strength[6].

In the ionosphere the propagation of radio waves is modified by the presence of free electrons. In fact, when a radio wave reaches the ionosphere, the electric field in the wave forces the electrons to oscillate at the same frequency as the radio wave. Some of the radio-frequency energy is then given up to this resonant oscillation. The oscillating electrons will then either be lost to recombination or will re-radiate the original wave energy. At frequencies below $\simeq 300$ MHz, the ionosphere affects radio waves via (i) refraction, (ii) absorption, (iii) Faraday rotation and (iv) total reflection (for a detailed explanation see Intema et al. 2009 and Sec. 13 of Thompson et al. 2001).

The refractive index for an incident wave of frequency $\nu$ on a plasma is

$$ n \simeq \sqrt{1 - \frac{4\pi e^2 n_e}{m_e \nu^2}} = \sqrt{1 - \left(\frac{\nu_p}{\nu}\right)^2} \tag{3.29} $$

where $e$ is the electron charge, $m_e$ is the electron mass, $n_e$ is the free electron density and $\nu_p$ is called the *plasma frequency* and in the ionosphere is about $1 - 10$ MHz for typical electron densities of $10^4 - 10^6$ electrons cm$^{-3}$. When $\nu < \nu_p$, the refractive index becomes imaginary and there is total reflection and it is impossible for a telescope to observe. It is interesting to note that $n \propto \nu^{-1}$, therefore the ionospheric effect is more and more important at lower frequencies. Furthermore, the refractive index is function of the electron density $n_e$ which in turn is not uniform across the wide field of view of LOFAR. To summarise, the effect of refraction is the introduction of time (i.e. phase) delays (due to the refractive index being $\neq 1$) that are direction dependant.

---

[6]And up-to-date status of the ionosphere total electron content (TEC) obtained by mapping GPS observables collected from ground stations is available on http://iono.jpl.nasa.gov/latest_rti_global.html.
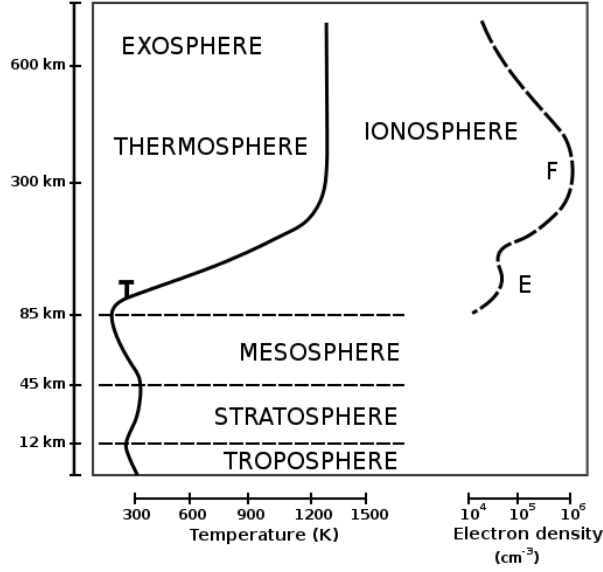
Figure 3.9: Relationship of the atmosphere and ionosphere. Solid line is the temperature [K] while dashed line is the electron density [cm$^{-3}$]

Ionospheric absorption instead is a relatively small amplitude effect (e.g. 0.1 dB at 100 MHz and $ZA = 60°$, Thompson et al. 2001, Sec. 13), and is mostly absorbed in the telescope overall gain calibration. Differential absorption are also present and they are a non-trivial DDE, but it is a smaller effect.

Faraday rotation is due to the interaction between light and a magnetic field in a medium and causes a rotation of polarization plane which is proportional to the component of the magnetic field in the direction of propagation. Quantitatively, the angle variation is

$$\Delta\Phi = 2.6 \times 10^{-17} \nu^{-2} \int_{\text{LoS}} n_e \, B_\parallel \, \mathrm{d}l = \text{RM} \, \nu^{-2} \text{ [rad]}, \tag{3.30}$$

where $\nu$ [Hz] is the frequency, $n_e$ [cm$^{-3}$] is the electron density, $B_\parallel$ [$\mu$G] is the magnetic field along the line of sight and d$l$ [m] is the path length along the line of sight (LoS). RM is called the *rotation measure* and provides information on the medium crossed by the radiation during its journey from the source to the telescope. In the RIME formalisms (in a linear-coordinate polarization basis) the Faraday rotation is a rotation matrix of the form

$$\boldsymbol{F} = \text{Rot}\,\beta = \begin{pmatrix} \cos\beta & -\sin\beta \\ \sin\beta & \cos\beta \end{pmatrix}, \quad \beta \propto \nu^{-2} \int_{\text{LoS}} n_e \, B_\parallel \, dl, \tag{3.31}$$

while in a circular basis is a diagonal matrix which encode a simple phase delay. Therefore, the Faraday effect causes left and right circularly polarized waves to propagate at slightly different speeds. In an instrument like LOFAR which has linear polarization receivers this effect moves

some flux of the diagonal terms in Eq. 3.8 to the off-diagonal terms. This is the reason why, when long baselines are used, and thus the crossed ionosphere is particularly different for two antennas, it is common practice to convert the data from linear to circular polarisation, where this effect is a simple delay that can be compensated with a standard calibration.

Finally, ionospheric scintillation is another effect that can alter the propagation of a radio signal. They are the consequence of small-scale variations in the ionospheric electron density $n_e$, and generate diffraction and scattering in the propagating rays. Ionospheric scintillations are characterized by random temporal fluctuations both in amplitude and in phase of a radio signal and can happen both during day or night-time.

### The Lonsdale scenarios

In Lonsdale (2004) three ionospheric calibration scenarios have been identified. The scenarios compare the array aperture (the length of the largest baseline) and the FoV with the ionosphere isoplanatic patch size, i.e. the scale at which the ionosphere can be considered constant. Lonsdale (2004) work has been revisited and adapted for LOFAR by Wijnholds et al. (2010).

**Scenario 1** (Fig. 3.10a) in this scenario the baselines lengths are short and the FoV of each station is small compared to the size of the isoplanatic patches. In this situation all the receivers and all the lines of sight within the FOV experience the same propagation conditions. We do not have direction dependant effects and the term[7] $E$ in Eq. 3.21 is a scalar. Since the FoV is small standard calibration can be applied using single strong point sources to solve for the $G$ terms.

**Scenario 2** (Fig. 3.10b) in this scenario the array is large but the FoV is still small. Lines of sight from different elements towards the region of interest are subject to different propagation conditions but within the FoV of a single element all lines-of-sight are experiencing the same conditions. The propagation effects can therefore be merged with the unknown receiver gains of each element, this means that $E$ does not depend on $(l, m)$ and can be taken out of the integral in Eq. 3.21 and merged with $G$. The calibration procedure is then the same of the previous scenario. This scenario is valid for most of the interferometers built in the 70s and 80s, such as the WSRT and the VLA, and for VLBI.

**Scenario 3** (Fig. 3.10c) here the elements have a large FOV, but the array is small. Therefore, all lines of sight go through the same propagation path, but there could be differences in propagation conditions towards distinct sources within the FoV. The ionosphere thus

---

[7]I use here the $E$ term as a general DDE effect, while usually the "E" letter is connected to the beam effect. The Jones matrix associated to the ionosphere is commonly called with a T.

(a) Scenario 1

(b) Scenario 2

(c) Scenario 3
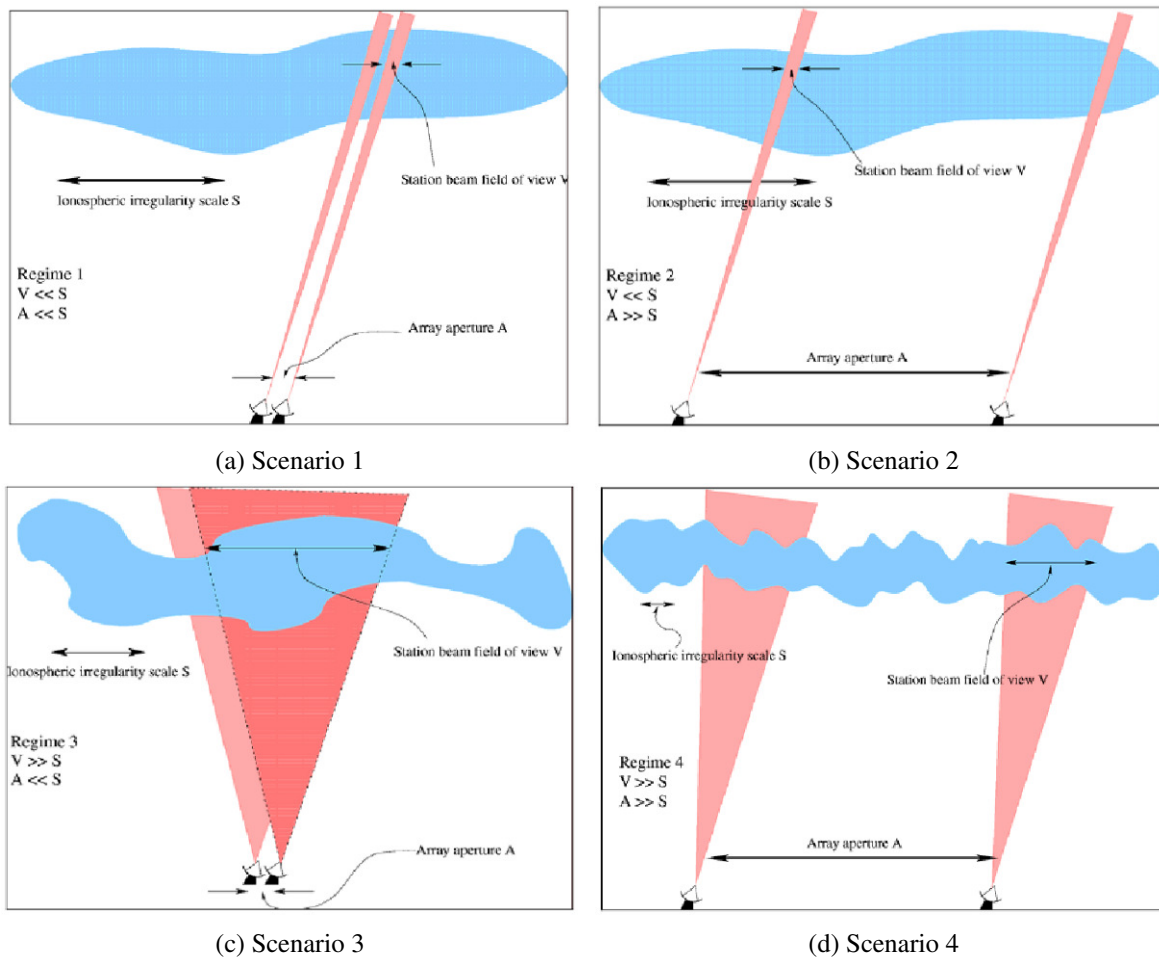
(d) Scenario 4

Figure 3.10: The four Lonsdale scenarios. Where A is the interferometer maximum baseline, V is the the beam size and S is the typical size of an ionospheric irregularity.

create a refractively distorted but coherent image, since the direction dependent effect is the same for all elements. This means that in Eq. 3.21, $E$ term depends on $(l, m)$ but not on $(p, q)$ and it is a scalar again.

**Scenario 4** (Fig. 3.10d) the elements have a large FoV and the array has at least some long baselines. This is the LOFAR situation and a clear example of direction dependent effect. This scenario implies that distinct complex gain corrections may be required for each source and each receiving element. The techniques to deal with this situation are outlined in Sec. 3.3.4.

### 3.3.3 Beam

LOFAR station beams are the source of many challenges. Firstly they are slightly different from station to station, this is due to unavoidable differences in the dipoles positions, and this effect can be particularly relevant when some of the antennae fall out (something quite common with so many dipoles). Moreover, in tracking a position in the sky, the station beams will change with time since no dish is compensating. So the beam is expected to be highly variable in time as well as in frequency. Furthermore, the station beams will have high side-lobes[8], therefore strong sources entering through them may make a large contribution to the signal. This requires that LOFAR calibration be an all-sky calibration and some techniques to deal with this aspect are explained in Sec. 3.4. Finally, the antennae are fixed to the ground and the X and Y voltage beams differ one another, so, depending on its position, a source could be seen stronger in a polarisation than in the other, consequently an intrinsic instrumental polarization is expected. Other important effects connected to the beam are the leakage that is due to cross-talk between the two polarisation channels or a miss-alignment of the receivers and further instrumental polarisation due to the beam patterns of two antennas being not equal.

A standard assumption in radio calibration is that the interferometer observes some true sky $B(l, m)$, attenuated by a power beam $|E(l, m)|^2$ (the Fourier transform of the effective aperture $A$ squared), that is equal for all antennas. If a beam model is available, the final images can be multiplied by $|E(l, m)|^{-2}$ to correct the flux scale and thus the beam effect. For what explained above, this is definitely not the case for LOFAR where each antenna has a (direction-, time- and frequency-dependant) specific beam. Furthermore, all the described beam effects, that are usually treated separately, are blend in the LOFAR case. The main reason being that LOFAR dipoles are fixed on the ground, therefore $E(l, m)$ towards any specific sky direction exhibits complex time-dependent behaviour in all four matrix elements which are consequences of a mix of the aforementioned effects.

### 3.3.4 Solving DDEs

In this section I will draw some possible solutions for DDEs like those caused by the ionosphere and the beam assuming that its effects (i.e., the relative Jones matrix) is known. In the case of the LOFAR beam we currently have models of both the high-band and low-band station beams. Much harder is instead to reconstruct the proper Jones matrix for the ionospheric effect. Van der Tol (2009) and Intema et al. (2009) have shown that the effect of the ionosphere at 74 MHz may be modelled by a 2-dimensional time dependent phase screen situated at a certain height above the interferometer. Once a solution is found, the best fit model gives the ionosphere

---

[8]*Side-lobes* are the lobes (local maxima) of the far field radiation pattern that are not the main lobe.

Jones matrix as a function of direction for all individual stations.

A possible solutions to DDEs is the use of facets that means to correct for DDE in multiple single directions assuming that the solutions are valid also for the surrounding areas (for a detailed description see Cornwell & Perley 1992). Formally, for a direction $l_0$, we can apply to the visibilities correction factors of $E_p^{-1}(l_0)\,G_p^{-1}$ and $(E_q^{-1}(l_0)\,G_q^{-1})^H$. The resulting visibilities will then be given by

$$\mathsf{V}_{pq}^{(0)} = \mathcal{F}(\tilde{E}_p \mathsf{B} \tilde{E}_q^H)\,, \tag{3.32}$$

where $\tilde{E}_p(l) = E_p(l)E_p^{-1}(l_0)$. Then, we use a standard imaging techniques (i.e. the inverse Fourier transform) to compute $\mathsf{B}^{(0)} = \mathcal{F}^{-1}\mathsf{V}^{(0)}$. Since $\tilde{E}_p \to 1$ with $l \to l_0$, the resulting image is equal to the "true" sky at $l_0$ ($\mathsf{B}^{(0)}(l_0) = \mathsf{B}(l_0)$) as long as we are close to $l_0$. If we then proceed correcting for many $l$ we can recover the full sky free from DDEs. Clearly this procedure is computationally expensive, and even if the Jones term $E_p^{-1}(l)$ was known in every direction its time variability could not be taken into account.

Another approach applicable once the DDE is known, is the so called A-projection (Bhatnagar et al. 2008), a generalisation of the W-projection correction (Cornwell 2008). Since the $E_p$ terms are multiplication in the *lm*-plane, they correspond to convolutions in its Fourier counterpart, the *uv*-plane. Therefore, DDEs convolve the "ideal" visibilities, with a different kernel per every antenna and time sample. This relation can be efficiently computed by the AW-algorithms both in the forward direction, during the degridding step (when predicting visibilities from an image), or in the reverse direction (when gridding visibilities for imaging). This method is used in the official LOFAR imager: AWimager (Tasse et al. in prep.).

If a known sky model is available, the most straightforward way of dealing with a known DDE is to subtract the model from the observed visibilities once transformed it in the visibility space (taking the DDE into account). Once imaged, these visibilities will still be subject to DDEs, however, if a significant portion of the flux is accounted for by the sky model, then the absolute level of DDE-related artefacts will be much lower. The sky model itself can be restored directly into the residual images with no error. This method is applied in sagecal (Kazemi et al. 2011).

Finally, a complex topic that I do not discuss in detail here, is how an unknown DDE can be removed (Smirnov 2011b). One of the possibility, initially proposed in Noordam (2004), is the *peeling* procedure. In this calibration algorithm data are calibrated in the direction of a source (typically the brightest) and this source is cleaned and subtracted, then the procedure is repeated for other sources. Anyway, every time a source is subtracted some errors due to the presence of other (uncalibrated) sources are frozen in the data. Kazemi et al. (2011) proposed instead a computationally cheaper method where they minimise a "distance" between the optimal solution (the true value of the unknowns) and the solution obtained by calibration.

In this way they can solve simultaneously in many directions.

## 3.4   LOFAR imaging pipeline

Most of LOFAR data processing is done by pipeline software. The back-end of LOFAR takes the data from the dipoles, forms the beams and correlates the output to ultimately generate images of the radio-sky. A detailed description of the whole process is illustrated in Noordam (2004) and Heald et al. (2010). The LOFAR survey team aims to develop a pipeline for deep extragalactic surveys, reaching the limit of $\sim$ 6 $\mu$Jy at 150 MHz with angular resolution of a 5″. Here I will describe its components.

After correlation, data are recorded on storage nodes in the current LOFAR offline processing cluster. The first data processing step is to flag radio-frequency interference (RFI) and optionally compress the data in time and frequency. Automated flagging is required for the LOFAR data volume, which is performed by the AOFlagger (Offringa et al. 2010a, 2012). This software estimates the astronomical signal by carrying out a surface fit in the time-frequency plane and flags outliers using combinatorial thresholding and morphological detection. Compression and further flagging is performed by the New Default Pre-Processing Pipeline, or NDPPP.

In cases where the contributions of other bright sources in the sky are not negligible, a subtraction of these sources directly from the visibilities is required. The technique we used is called *demixing* and it is described in van der Tol et al. (2007). This approach is computationally cheap and shows remarkably good results in some circumstances, where the source to *demix* and subtract is not too close to the main target, but fails in more complex scenarios, for instance where a strong source is a few degrees away from a weak target.

During LOFAR commissioning, we conducted some tests to establish empirically the minimum distance required for the *demixing* to work. After applying this procedure to some sources extracted from the 3C catalogue at different distances from strong A-team sources (typically Cygnus A, Cassiopeia A or Virgo A), we found that at 58 MHz the *demixing* does not work for 3C sources $\lesssim 23°$ away from an A-team source. This critical distance scales with frequency. For instance at 120 MHz (HBA), it is 15°.

The calibration step is performed with the BlackBoard Selfcal (BBS) software, developed explicitly for LOFAR. This calibration package is based on the Hamaker-Bregman-Sault Measurement Equation (Hamaker et al. 1996; Smirnov 2011a, and Sec. 3.1.1). BBS is thus able to handle complicated calibration tasks like simultaneous multi-directions calibration, full polarization calibration as well as correcting for the position dependence of the element beam and synthesized beam. BBS can also simultaneously solve a large portion of the bandwidth taking

into account frequency-dependant effects like the ionosphere phase-dependence ($\propto \nu^{-1}$) and the stations clocks errors ($\propto \nu$).

The imaging step is now routinely performed using the AWimager software (Tasse et al. in prep.). The AWimager is specially adapted to image wide fields of view and data produced by non-coplanar arrays. In this cases the $w$ term in the exponential of the measured visibilities (Eq. 3.21) is not negligible and must be taken into account. Furthermore, AWimager corrects for direction dependent effects (LOFAR beam and, in the future, ionosphere) varying in time and frequency using the A-projection algorithm (Bhatnagar et al. 2008). The software in practice must know the beam shape (reconstructing it using using data recorded at observing time and models) and the ionospheric phase/amplitude screen  (that is harder to obtain, see Van der Tol 2009; Intema et al. 2009) as a function of time and position. During the cleaning procedure AWimager is able to correctly subtract the cleaned flux from the visibilities by applying the proper phase/amplitude corrections. These corrections are derived by deconvolving the aforementioned phase/amplitude screen during the degridding step (when predicting visibilities from an image) and the gridding step (when creating an image from visibilities).

In the next sections I will describe some example of the commissioning activity in which I were directly involved:

### Gain solutions transfer

One of the new and most important LOFAR capabilities is the contemporary observation in multiple directions with different beams. Reducing its bandwidth, LOFAR can synthesize up to 240 beams. Many tests have been conduced in this direction, one of the most relevant being the first LOFAR survey: the Multifrequency Snapshot Sky Survey (MSSS). For this survey the observing strategy was to have 1 beam on a calibrator and 3 beams on 3 target fields at the same time and observing the same frequency coverage. The gain solutions obtained by observing the calibrator field were then extracted and transferred to the target fields, so no time-interpolation was needed. This is the cleanest solution possible, but it has some drawbacks: (i) the same amount of bandwidth used to observe the target must be used to observe also the calibrator, (ii) any phase error introduced by ionospheric effect cannot be corrected (because the ionosphere is different in the calibrator and target fields), (iii) when the gain solution are calculated using the calibrator data, the beam effect (that is also different for the calibrator and the target field) must be evaluated and subtracted, to be then re-computed in the target direction and re-added to the gain solutions.

Problem (ii) can be solved once a reliable beam model is provided, problem (iii) instead can only be solved with some self-calibration procedure. The first issue instead, can be mitigated
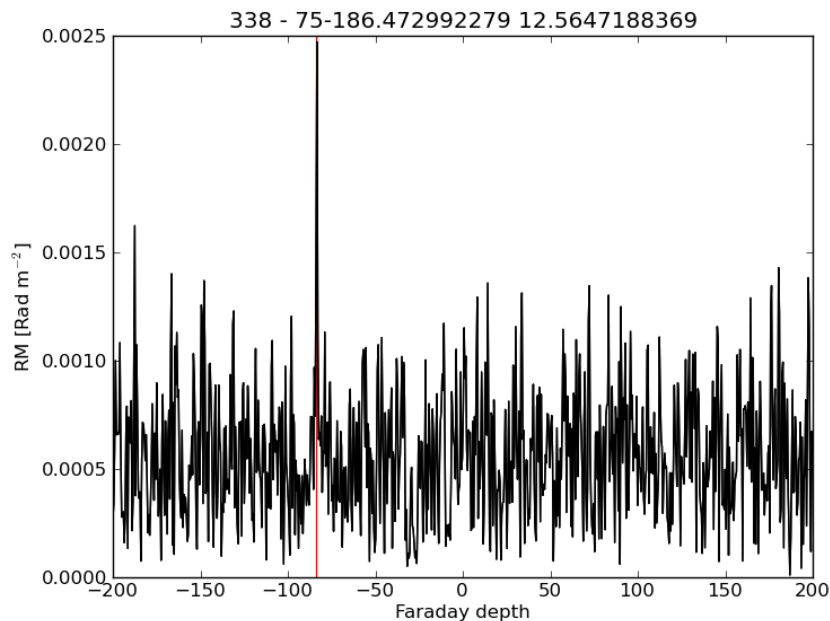
Figure 3.11: An example of a detection (red line) in the source extractor. In this case the detection is at a Faraday depth of −80.

by observing the calibrator with a limited amount of band[9], carefully chosen in order to sample the (wider) band of the target beam. Consequently, some kind of interpolation to fill the missing calibrator band must be done. I wrote a versatile python code to transfer gain solutions from the calibrator field to the target field allowing a reduced band on the calibrator. The software use either a linear interpolation or a *nearest* algorithm to extend the solutions to the frequencies (or times) not directly observed by the calibrator's beam.

Test on real data using this algorithm provided encouraging results. Although subsequent phase self-calibration is always needed to correct for ionospheric disturbances, this is currently the only way to obtain a fully reliable absolute flux calibration in fields were no other absolute flux calibrators are already present.

Some tests on the more classical solutions transfer in time (instead that in frequency) were also attempted. Unfortunately, at these low-frequencies the solutions vary so rapidly that we were not able to obtain a good starting model for a subsequent self-calibration, and this strategy was put aside.

---

[9]For example, 1/4 of the total bandwidth, leaving for the target field the other 3/4.

**RM source extractor**

Faraday rotation in the interstellar/intergalactic medium is imposed on light over the course of its propagation from its origin to the Earth. The effect is caused by the presence free electrons and a magnetic field oriented in the direction of the light propagation and can be characterized as a difference in the refractive index seen by the two circularly polarized propagation modes. This is quantitatively described by Eq. 3.30.

One of the most innovative techniques in radio-astronomy is the Rotation Measurement (RM) synthesis (Brentjens & de Bruyn 2005). The RM synthesis technique was originally conceived for analysing data along a single line of sight. However, many polarized sources are resolved, and it is now common to perform it for every spatial pixel in full Stokes Q and U data cubes. The output of such an operation is referred to as an "RM cube", with $\Phi$ (as defined in Eq. 3.30) as the third axis. Analysing these data cubes by eye can be tedious and inaccurate. Therefore, I developed a python code for RM source extraction which explore the RM cube looking for peaks, statistically evaluating their reliability and generate maps and spectra of detections. An example of a detection is shown in Fig. 3.11.

<div align="right">

# 4

</div>

---

<div align="right">

# Virgo A

</div>

---

---

## 4.1  Introduction

As discussed in Sec. 1.4, accreting supermassive black holes in active galactic nuclei (AGN) can release enormous amounts of energy into their surroundings, which may profoundly influence the black hole's hosting environment up to the cluster scale. The way energy is transported to large distances, its amount and the typical time-scales of these processes are still not clear. New-generation radio-telescopes such as the Low-Frequency Array (LOFAR) allow us to study these mechanisms with unprecedented quality and resolution in a hitherto neglected wavelength range. One of the best studied examples of black hole – host galaxy feedback in action is the AGN in the nearby giant elliptical galaxy M87 (NGC 4486), in the core of the Virgo cluster.

A particularly large amount of study, including hundreds of published papers, has been devoted to M87. This galaxy owes its popularity to several reasons, among others: it is one of the nearest[1] radio galaxies, it is at the centre of the nearest rich cluster of galaxies (the Virgo cluster), it is the fourth brightest radio source in the northern sky, and it hosts in its nucleus one of the most massive active black holes discovered so far ($M_{BH} \simeq 6.4 \pm 0.5 \times 10^9\ M_\odot$, Gebhardt & Thomas 2009).

The interaction between the AGN of M87 with its host galaxy and the intra-cluster medium (ICM) has been the subject of a large fraction of the aforementioned studies. The emission generated directly and indirectly by the AGN has been widely observed at radio (Bolton et al.

---

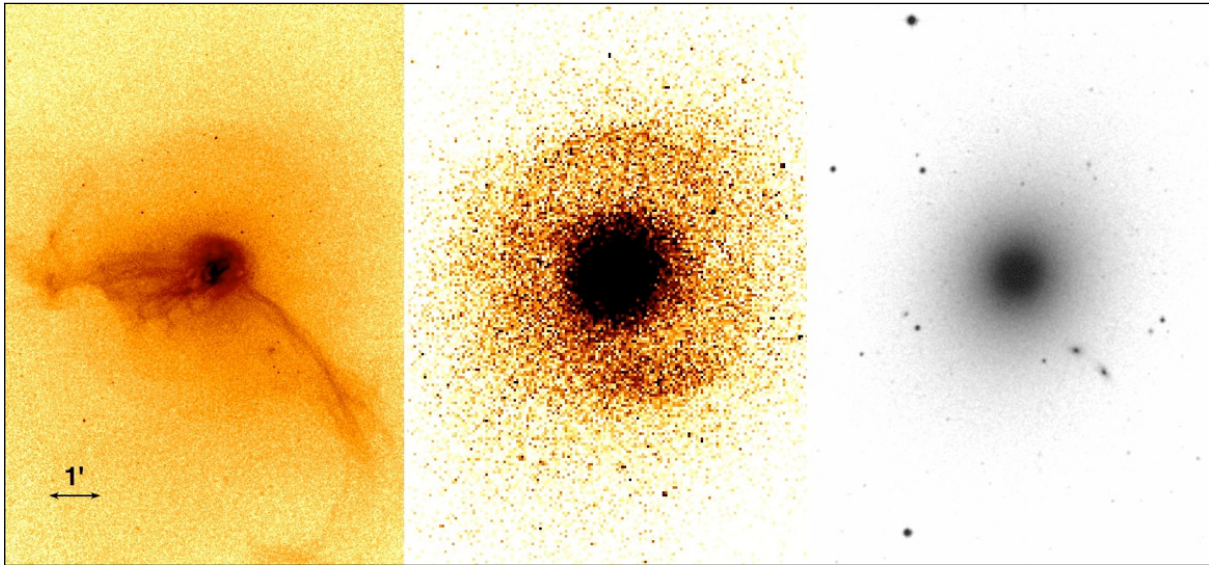[1]M87 is at a distance of ~ 17 Mpc, where 1″ corresponds to ~ 85 pc.

Figure 4.1: M87 at observed at different frequencies. The Images are matched to scale. *Left*: soft X-ray, which shows filaments and bubbles borders. *Centre*: hard X-ray, this is a pressure map and shows spherical shocks. *Right*: optical image of the stellar component. Image from Forman et al. (2007).

1949; Mills 1952; Baade & Minkowski 1954; Owen et al. 2000), infrared (Shi et al. 2007), optical (Biretta et al. 1999) and X-ray (Fabricant et al. 1980; Feigelson et al. 1987; Bohringer & Nulsen 1995; Young et al. 2002; Forman et al. 2007; Million et al. 2010) wavelengths. Theoretical and numerical models to interpret these observations have also been developed by e.g. Churazov & Kaiser (2001) and Brüggen & Kaiser (2002).

The radio source associated with this galaxy is named Virgo A (3C 274). Its inner region ($1.3' \times 0.5'$) contains a collimated relativistic jet, which points towards the north-west and is embedded in a halo with a diameter up to $15'$ ($\sim 80$ kpc). The extended radio emission, discovered by Mills (1952) and Baade & Minkowski (1954), is responsible for much of the radio flux, especially at the lower frequencies. Due to the high surface brightness of the compact central region and the relatively faint surface brightness of the extended emission, high dynamic-range imaging of Virgo A has always been a big challenge. In the past years Owen et al. (2000) presented a high-resolution ($7''$), high-dynamic range map of the halo of M87 observed at 327 MHz with the Very Large Array (VLA). At higher frequencies Rottmann et al. (1996) mapped the extended Virgo halo at 10.55 GHz with the single-dish Effelsberg radio telescope at $69''$ resolution. At lower frequency (74 MHz) a $20''$ resolution map of Virgo A was made by Kassim et al. (1993). This work will extend the high resolution imaging into the previously almost unexplored very low frequency range of $15 - 162$ MHz and present some of the highest-dynamic-range images ever made at these frequencies of extended source structures.

M87 lies at the centre of the Virgo cluster X-ray luminous atmosphere, first detected with the Einstein Observatory by Fabricant et al. (1980). An asymmetry in the X-ray emission, in the form of two spectacular outflow-like structures extending from the nucleus towards the east and south-west, was discovered by Feigelson et al. (1987), who also found a correlation between X-ray and radio emitting features (see Fig. 4.2). One of the first explanations for such a correlation was that the relativistic electrons that produce the synchrotron radio emission were also responsible for the inverse Compton scattering of cosmic microwave background (CMB) photons, thus producing X-ray radiation (Feigelson et al. 1987). However, Bohringer & Nulsen (1995) showed with a ROSAT PSPC observation, that the excess emission had a thermal spectrum and it is colder than the ambient gas which is at a temperature of $\gtrsim 2$ keV. This feature was explained by Churazov & Kaiser (2001) as buoyant bubbles of cosmic rays, injected into the inner halo (or "cocoon") by the relativistic jet, which subsequently rise through the cooling gas at about half the sound speed. During their rise they uplift gas at the temperature of $\sim 1$ keV from the central regions. Sub-arcsecond *Chandra* X-ray images (Million et al. 2010) confirmed this picture and provided an unprecedented view of the physical and chemical properties of the ICM. In Fig. 4.1 I show the soft and hard X-ray emission, where filaments, shocks and cavities are visible.

Although Virgo A is a unique object because of its properties, close proximity and sheer quantity of available data, it remains a fundamental example to study the more general behaviour of AGNs located at the centre of galaxy clusters. Knowledge of its energetics and of the interaction between its jets and the ICM, may help solve open problems such as the suppression of the cooling flows (for a review see Peterson & Fabian 2006) and the AGN duty cycle. This, in turn, will provide important clues on the physical nature of AGN feedback in massive galaxies and on its relevance to a cosmological framework (Croton et al. 2006; Fabian 2012). Furthermore, it has been claimed that jet sources like Virgo A and its southern sibling Centaurus A are potential candidate sources for the production of ultra-high energy cosmic rays (UHECR, Abraham et al. 2007).

In this work, together with my collaborators, I extend the study of Virgo A to long, so far unobserved, wavelengths. We also retrieved available observations of Virgo A at 1.4 and 1.6 GHz (VLA, from the data archive), at 325 MHz (VLA, provided by Frazer Owen) and at 10.55 GHz (Effelsberg radio telescope, provided by Helge Rottmann). This enabled us to assess the source energetics, the halo age and the main mechanisms which contributed to its spectral evolution. The chapter is organized as follows: in the next section we outline the LOFAR features and characteristics. In Sect. 4.2 we present new LOFAR observations of Virgo A and we describe the data reduction technique. In Sects. 4.3 and 4.4 we respectively present the outcome of these observations and perform a spectral analysis of them, discussing the physical interpretation of our results. In the last two Sects. (4.5 and 4.6), we discuss the results and
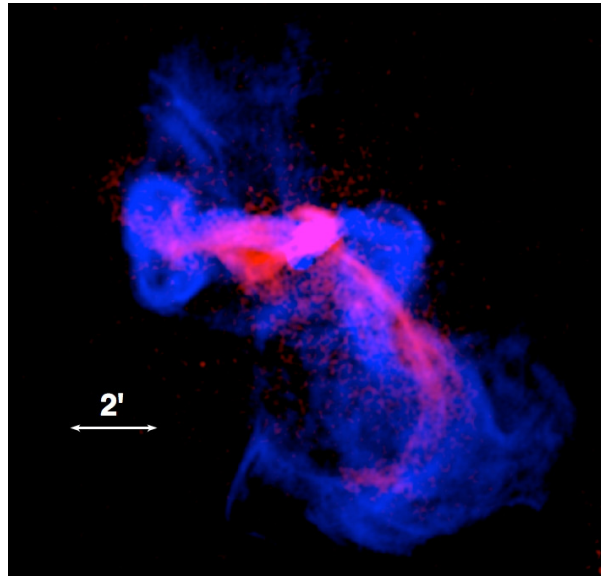
Figure 4.2: The relation between X-ray (magenta) and radio (blue) emission in M87. Image courtesy of William Forman.

Table 4.1: Details of the observations

| Obs. ID | Antenna type | Frequency range [MHz] | Date | Obs. length [h] | Samp. time [s] | FWHM[1] [deg] | Maximum resolution [arcsec$^2$] | Number of stations |
|---|---|---|---|---|---|---|---|---|
| L24923 | HBA-DUAL[3] | $115 - 162$ | 2/3-4-2011 | 8 | 1 | $\sim 5$ | $19 \times 14$ | 45 (7)$^2$ |
| L25455 | LBA-INNER | $30 - 77$ | 14/15-4-2011 | 8 | 2 | $\sim 10$ | $37 \times 30$ | 24 (7)$^2$ |
| L29694 | LBA-OUTER | $15 - 30$ | 16-7-2011 | 8 | 2 | $\sim 10$ | $85 \times 44$ | 25 (8)$^2$ |

[1] FWHM of the primary beam when points at the zenit, its shape changes during the observation time and is not circular. [2] in brackets the number of remote stations. [3]"DUAL" means that the two sub-stations of the core stations are treated separately (see text for details). This is why the number of stations in the HBA observation is higher with respect to the LBA observations.

outline our conclusions.

## 4.2   The observations

In this chapter I present a set of three observations performed during the LOFAR commissioning phase. The phase centre was set on the core of Virgo A (RA: 12:30:49.420 – DEC: +12:23:28.0 – J2000) and the observational details are listed in Table 4.1. Each observation was 8 hours in duration and all four polarization products (XX, YY, XY, and YX) were stored. Each observation had its frequency coverage divided into sub-bands (SB) of 0.1953 MHz of
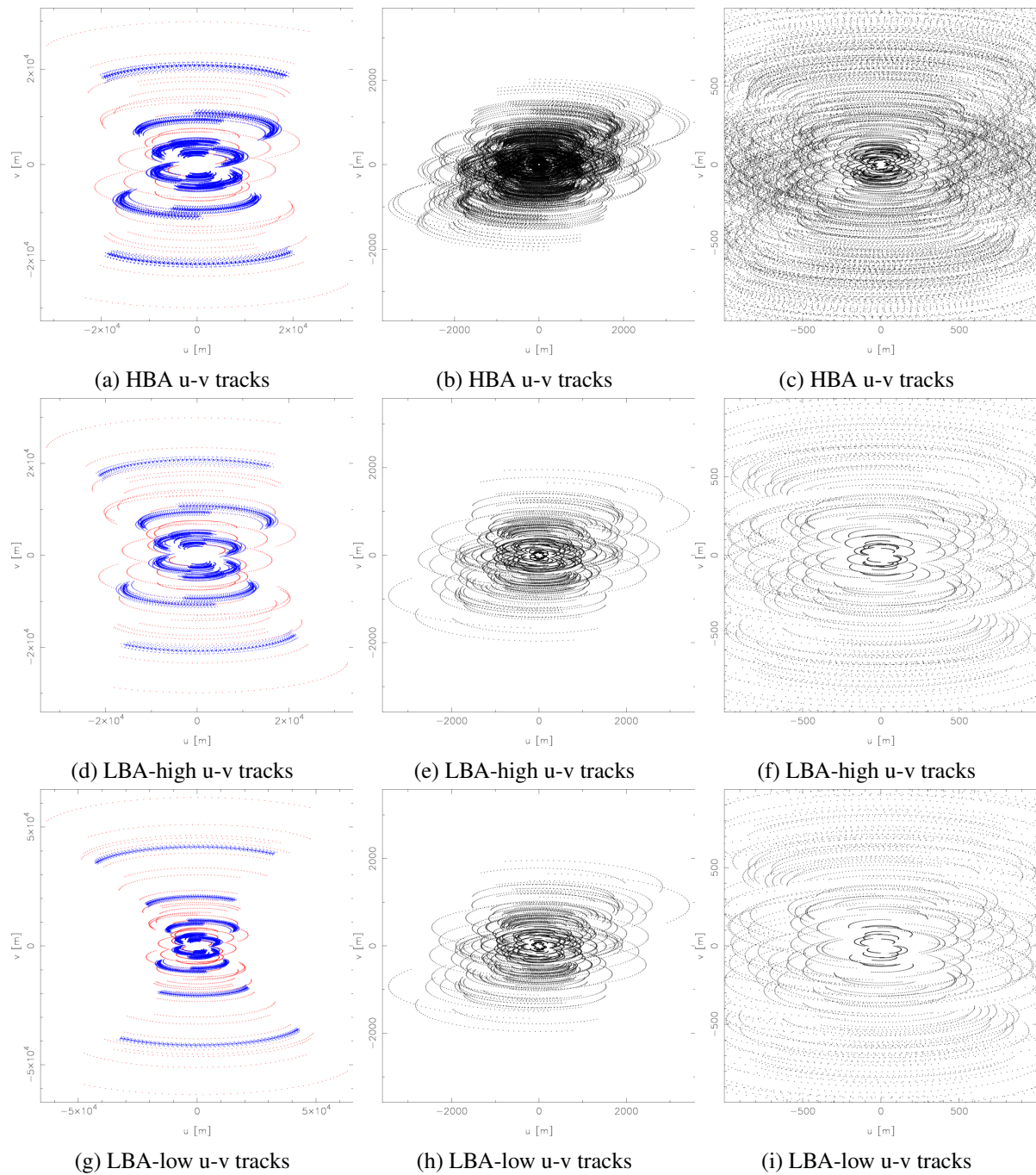
Figure 4.3: *uv*-coverage for the three observations of Virgo A: the first row is the HBA observation, the second row the LBA-high observation and the third row the LBA-low observation. In the first column are plotted only tracks involving remote stations (blue: core-remote baselines – red: remote-remote baselines). In the second column only tracks of core-core baselines are plotted. The last column is a zoom-in on the centre of the *uv*-plane.
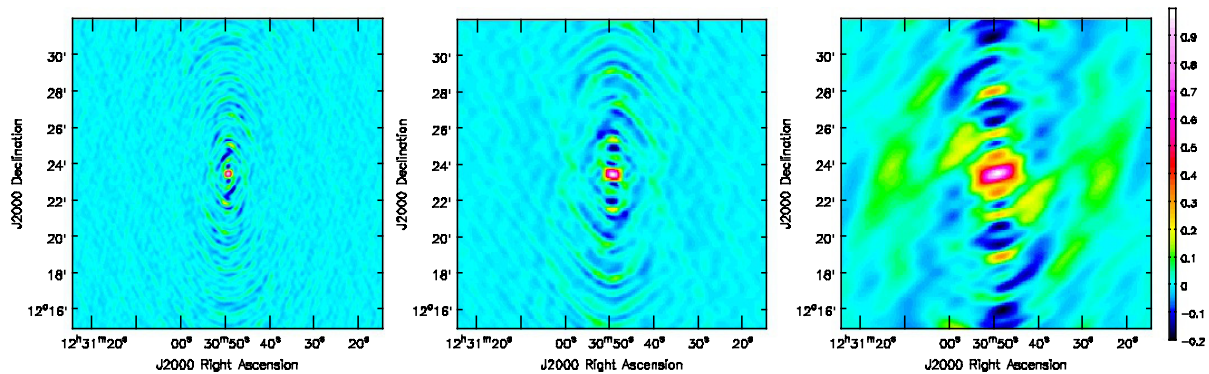
Figure 4.4: *Left*: dirty beam used in the deconvolution step for the HBA observation (at a frequency of ~ 140 MHz). *Centre:* dirty beam used in the deconvolution step for the LBA-high observation (at a frequency of ~ 54 MHz). *Right*: dirty beam used in the deconvolution step for the LBA-low observation (at a frequency of ~ 22 MHz).

bandwidth and each SB was divided into 64 channels of $\simeq$ 3 kHz of bandwidth. The following observations were performed:

**HBA** (115 − 162 **MHz**): we observed the target with the HBA on the 2nd and 3rd of April, 2011. The visibility sampling time was 2 s. Two stations (CS021HBA0 and CS021HBA1) were flagged by the correlator and their data were not used. All 244 SBs were correctly processed and stored by the correlator.

**LBA-high** (30 − 77 **MHz**): a second observation was performed with the LBA system on 14th and 15th of April, 2011, using a 30 MHz high-pass filter. The visibility sampling time was 1 s. The LBA-INNER configuration was used. At the end of the data reduction procedure 36 SBs out of 244 (15%, 7.2 MHz of bandwidth) were not usable due to computing-cluster or correlator failure.

**LBA-low** (15 − 30 **MHz**): a third observation was performed with the LBA system on 16th of July, 2011, using a 10 MHz high-pass filter. The visibility sampling time was 1 s. Three SBs out of 77 (4%) were corrupted during the data processing. We did a visual inspection of the 74 residual SBs and only 41 (55%, 8.2 MHz of bandwidth) contained usable data, the others were unusable due to high RFI levels. One antenna (CS302) was flagged at correlation time. An LBA-OUTER configuration was used to keep the FoV comparable to that of the LBA-high observation.

International stations were not used in these observations, therefore the longest baseline available was about 80 km (for the observation at 15 − 30 MHz) and 40 km (for the others), while
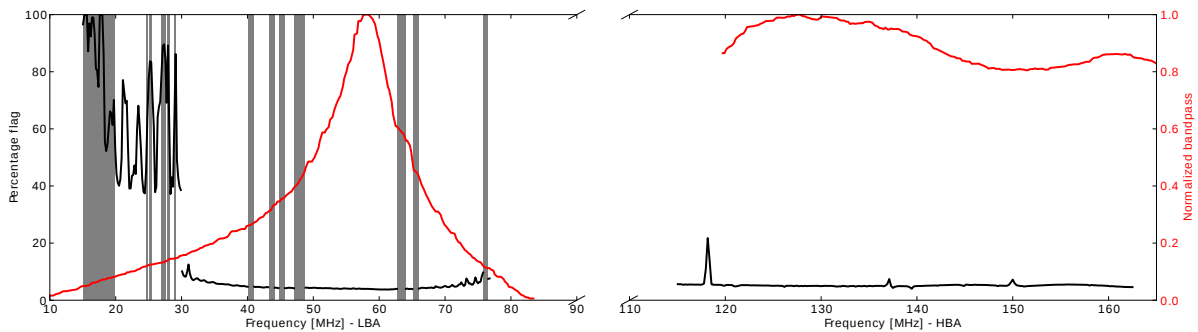
Figure 4.5: Black line: percentage of flagged data. In the frequency range $15 - 30$ MHz, the last 37% of the observation was manually flagged. Red line: normalized bandpass (for HBA it is only available for a slightly shifted frequency range). The SBs removed because of corrupted data or a computer failure are coloured in grey. Completely flagged stations are not taken into account to compute the percentage of flagged data.

the shortest was $\simeq 90$ m. A plot of the full *uv*-coverage is shown in Fig. 4.3, while the dirty beams used for deconvolution are shown in Fig. 4.4.

### 4.2.1 Data reduction

Although some steps were common, the data reduction procedure followed different schemes for the three observations. A preliminary common step is the use of the automated AOFlagger on the full resolution (in time and frequency) datasets. With a further visual inspection of the data, we did not recognise any visible RFI effects left in the raw data. After this step the procedures were different for each dataset, and therefore we explain them in detail:

**HBA (**$115 - 162$ **MHz):** first all baselines related to the two substations within the same station were flagged ($\sim 1$% of data), this was necessary due to a possible cross-talk effect that was found in the intra-station baselines. Then, we applied the *demixing* procedure to the dataset, subtracting in this way the two strongest sources in the sky, Cassiopeia A ($\sim 107°$ from Virgo A) and Cygnus A ($\sim 98$ deg from Virgo A). This procedure was necessary only in the second half of the observation, where the two aforementioned sources were above the horizon. After that we compressed the dataset to one channel (excluding the first and last two channels) per SB and 20 s of sampling time. This reduced the data volume to the level of $\sim 400$ MB per SB, where a cycle of self-calibration lasts $\sim 1$ h. The model for the self-calibration was extracted from VLA data at 325 MHz (Owen et al. 2000), which had a resolution high enough for our case ($\sim 7''$). For each SB we rescaled the total flux of the model according to the source global spectral index value (see Sect. 4.2.2). Several cycles of self-calibration (phase and amplitude) performed with BBS and using the imaging algorithm in CASA, were necessary to converge to the final

image. The imaging step at these frequencies was performed using a standard CLEAN for the bright central region, followed by the use of a multi-scale cleaning.

**LBA-high** ($30 - 77$ **MHz**): after *demixing*, that was performed as described for the HBA dataset, the data were averaged to one channel (excluding the first and last two channels) per SB and to 10 s of sampling time. The model for self-calibration was extracted from a VLA observation at 74 MHz (Kassim et al. 1993) with the total flux rescaled to the appropriate frequency (see Sect. 4.2.2). We did several cycles of self-calibration (phase and amplitude) with BBS and using the imaging algorithm in CASA. The central region of Virgo A was CLEANed using standard pixel-by-pixel cleaning while for the extended emission we used a multi-scale approach.

**LBA-low** ($15 - 30$ **MHz**): the attempt to use the *demixing* procedure failed since the data taken in the last 3 hours of observation were severely affected by ionospheric disturbances. Since this was the part of the observation also corrupted by Cassiopeia A and Cygnus A signals, we decided not to use it and simply average the rest of data to 5 s and one channel (excluding the first and last two channels) before the calibration procedure. Finally, several cycles of self-calibration (phase and amplitude), using BBS for the calibration and CASA for the imaging, were performed. The model for self-calibration was again extracted from a VLA observation at 74 MHz with the total flux rescaled to the appropriate frequency (see Sect. 4.2.2). The imaging step was done in the same way as for the LBA-high dataset. At the end of the calibration procedure, a visual inspection of the images revealed that for 33 SBs (out of 74) we were unable to correctly calibrate the data due to the RFI level. The majority of these SBs are indeed concentrated in the frequency range $15 - 20$ MHz and where the RFI presence was critically high. We did not use those SBs for the following analyses.

In Fig. 4.5 we plot the amount of flagged data for each SB, together with the shape of the bandpass functions. The amounts of flagged data reflect only partially the amount of RFI. Firstly because the RFI flagging is performed at full time-frequency resolution and during the subsequent data averaging flags are ignored if at least one datum is valid in the averaged block. Therefore, it was not possible to track those flags due to RFI which are narrow-frequency or shorter than the average time. Secondly because new flags are applied to remove outliers produced in the calibration phase. In the high frequency regime, the percentage of unusable data is more or less constant, at $\sim 5\%$, apart from a small increment at 118 MHz. Almost all of these are due to the manual-flagging of the first two hours of data from RS208 and RS307 and the last two hours from RS208. At lower frequencies the RFI is stronger and the peaks in Fig. 4.5 are related to it. Below 30 MHz all SBs had a flagged data percentage above 37%

because, as explained, we removed the last 3 h of observation. In the LBA-high frequency range (30 − 77 MHz) the amount of flagged data is rising towards the band edges, where it also presents some systematic oscillations. These behaviours are due to the lower sensitivity of the instrument at these frequencies, which produces some outliers during the calibration procedure and principally during the *demixing* process. These outliers are due to a poor signal to noise in the calibration step and were flagged by an automated procedure through NDPPP after every selfcal cycle. This increases the amount of flagged data, but these flags are not RFI-related. The oscillating pattern is introduced by flagging outliers after the *demixing* procedure, which may suggest that the *demixing* is less effective at those frequencies where the strong (*demixed*) sources are in particular configurations with respect to the beam side-lobe pattern.

### 4.2.2   Absolute flux density

The flux density of Virgo A integrated over all the extended emission was rescaled to its expected value to compensate for the absence of an absolute flux calibrator, while the relative fluxes of different components in the radio morphology is correctly recovered by self-calibration. To do that, we collected the total flux measurements available in the literature in the frequency range from 10 to 1400 MHz (Braude et al. 1969; Bridle & Purton 1968; Roger et al. 1969; Viner & Erickson 1975; Kellermann et al. 1969; Wright & Otrupcek 1990). Each data-point was corrected to match the Roger et al. (1973) (RBC) flux scale with correction factors from Laing & Peacock (1980) and Scaife & Heald (2012). A model of the form

$$\log S = \log(A_0) + A_1 \log\left(\frac{\nu}{150 \text{ MHz}}\right) + A_2 \log^2\left(\frac{\nu}{150 \text{ MHz}}\right) + ... \tag{4.1}$$

where $\nu$ is the observing frequency and $S$ the observed flux, was used to fit this data set (see Fig. 4.6).

The model was applied in linear frequency space, i.e.

$$S\,[\text{Jy}] = A_0 \sum_{i=1}^{N} 10^{A_i \log^i [\nu/150 \text{ MHz}]} , \tag{4.2}$$

in order to retain Gaussian noise characteristics. Parameters were fitted using a Maximum Likelihood (ML) approach through a Markov Chain Monte Carlo implementation (Scaife & Heald 2012).

This process used a simulated annealing method to calculate the Bayesian evidence Z, implemented through the METRO algorithm (Hobson & Baldwin 2004) for models with different polynomial orders N. Average Z values were calculated from multiple runs, in each case using a $\pm 3\sigma$ prior volume centred on the ML parameter values, with $\sigma$ determined for each parameter directly from the posterior distribution. Results of the fits are listed in Table 4.2.
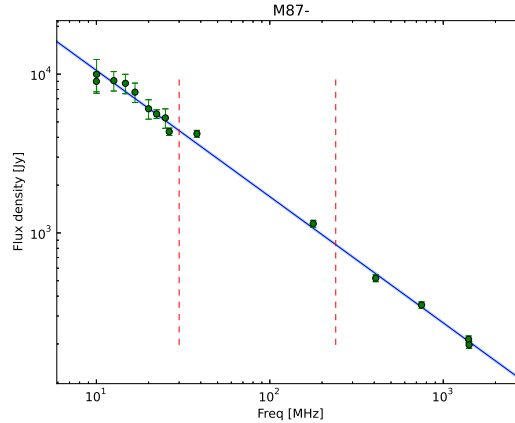
Figure 4.6: Integrated flux of Virgo A at different frequencies obtained from archival data. The line is a linear fit (slope: −0.79) obtained as described in the text. The two vertical dashed lines indicate the boundaries of the LOFAR observing band.

Table 4.2: Polynomial fit parameters for the integrated flux spectrum of Virgo A (see Fig. 4.6)

| Order | $A_0$ | $A_1$ | $A_2$ | $A_3$ | $A_4$ | $\chi^2_{\rm red}$ | ln Z |
|-------|-------|-------|-------|-------|-------|--------|------|
| 1° | 1228 ± 17 | −0.789 ± 0.008 | – | – | – | 1.28 | −131.75 ± 0.06 |
| 2° | 1234 ± 26 | −0.788 ± 0.009 | −0.004 ± 0.014 | – | – | 1.35 | −133.06 ± 0.15 |
| 3° | 1235 ± 26 | −0.816 ± 0.025 | −0.007 ± 0.015 | 0.037 ± 0.031 | – | 1.37 | −134.44 ± 0.18 |
| 4° | 1236 ± 33 | −0.815 ± 0.024 | −0.008 ± 0.054 | 0.035 ± 0.029 | −0.000 ± 0.047 | 1.47 | −136.62 ± 0.42 |

We tested polynomial fits up to the fourth order and found that a first order polynomial function ($A_0 = 1226 \pm 17$ and $A_1 = -0.79 \pm 0.008$) is the best-fit model (as already pointed out by a number of authors, e.g. Roger et al. 1973). We derived the expected total flux of Virgo A at the frequency of each observed LOFAR SB and rescaled the model used for that SB to match it at the beginning of each cycle of self-calibration.

The primary beam attenuation at the edge of Virgo A is < 3% for HBA images and < 1% for LBA images. We did not take this effect into account and included the systematic error in the error budget.

The map at 325 MHz was also rescaled to match the RBC flux scale, but at higher frequencies our first order polynomial model is probably no longer valid. However, at frequencies $\gtrsim$ 300 MHz, the RBC scale is in agreement with the KPW scale (Kellermann et al. 1969), for which we have conversion factors from the Baars scale (Baars et al. 1977, Table 7). Therefore, we used those factors to rescale the maps at 1.4, 1.6, and 10.55 GHz from the Baars scale to the RBC scale.
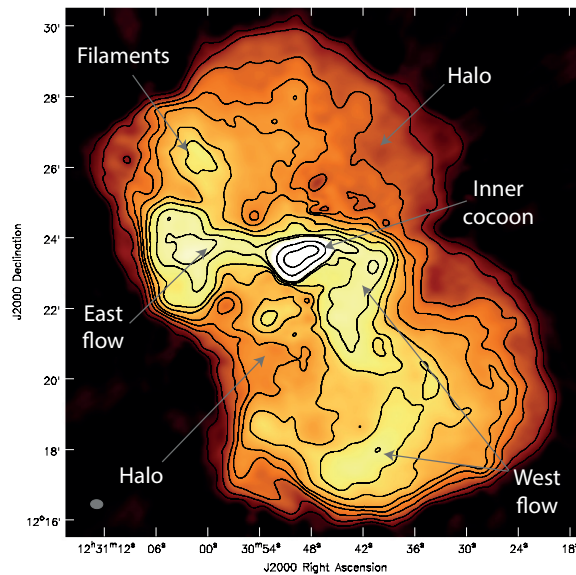
Figure 4.7: Same as Fig. 4.8 with most prominent features described in the text labelled. Contour lines are at $(1, 2.5, 5, 7.5, 10, 15, 20, 25, 30, 35, 45, 250, 1000) \times 3\sigma$.

## 4.3 Virgo A images

In Fig. 4.8 we show the image of Virgo A as seen with the LOFAR-HBA at an average frequency of 140 MHz. This image is an average over the entire 48 MHz of bandwidth and the imaging step has been performed with CASA using the multi-scale deconvolution algorithm with a Briggs weighting (robust = −0.5). In Fig. 4.11 we show four images of Virgo A obtained with the LOFAR-LBA. Each image is realised with CASA using a multi-scale multi-frequency deconvolution algorithm (Cornwell 2008; Rau & Cornwell 2011) on a subset of 60 SBs (12 MHz of bandwidth) with uniform weighting. Finally in Fig. 4.10 we present a very low frequency (25 MHz) image of Virgo A. This image was obtained in CASA using a multi-scale multi-frequency deconvolution algorithm with uniform weighting on all usable SBs of the LBA-low dataset ($20 - 30$ MHz). The rms error in the images is set by deconvolution errors which limit our dynamic range to $\sim 5000$ (for the HBA map). Our ability to recover flux not in the model was confirmed by the detection of several sources which were not included in it. We recovered $> 50$ sources in LBA wide-field and $> 300$ sources in the HBA wide-field (de Gasperin et al. in prep.). The morphological structure of Virgo A instead appear similar from 20 MHz up to the GHz regime, a part from those differences caused by spatial changes in the spectral index.

Virgo A has a $\sim 5$ kpc-wide inner cocoon, where a one-sided jet is visible. The jet, detected also in the optical and X-ray bands, points towards the north-west. The counter-jet, although not visible due to the effect of relativistic de-boosting, is probably responsible for the emission
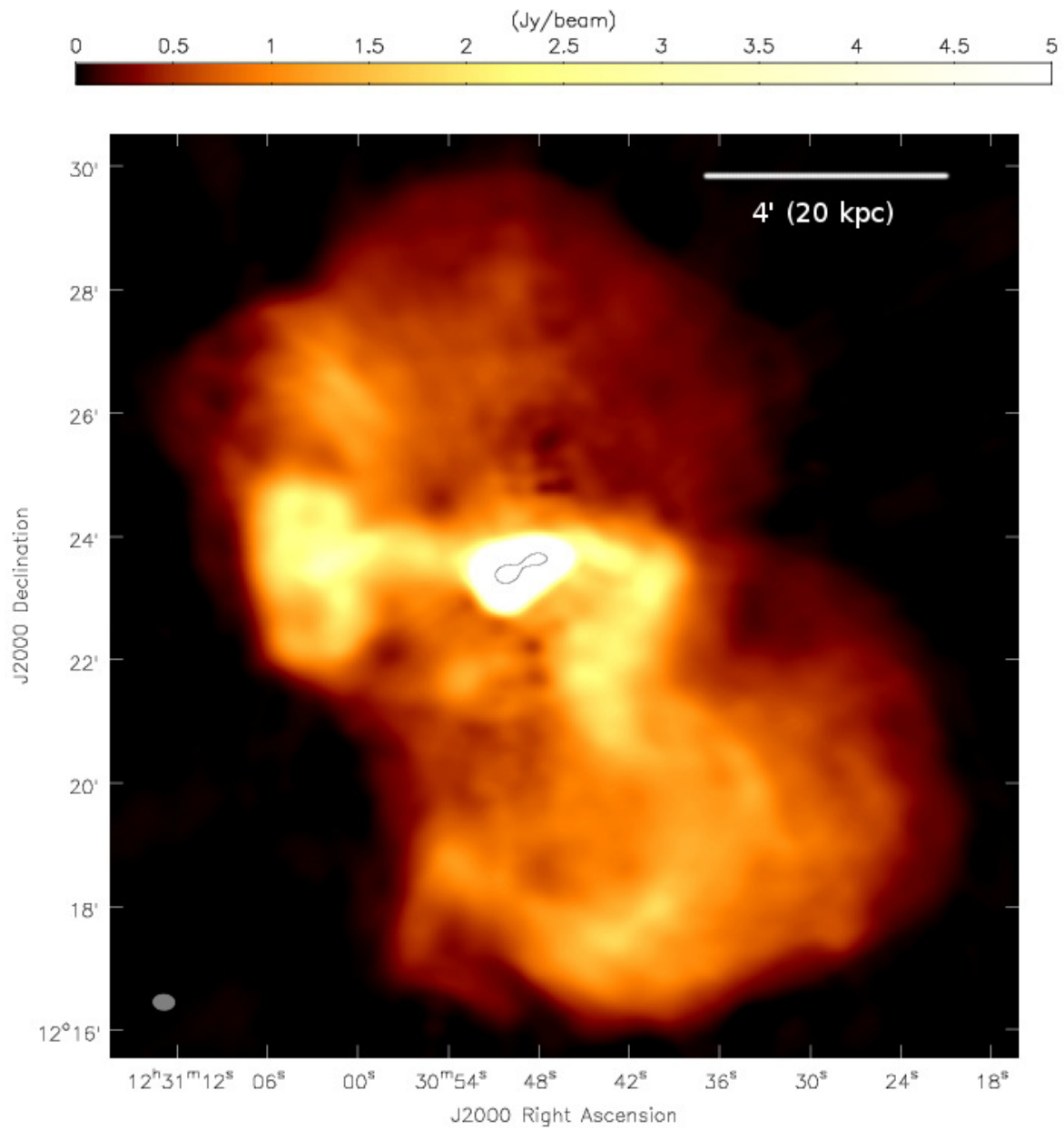
Figure 4.8: LOFAR-HBA image of Virgo A at 140 MHz. The rms noise level is $\sigma = 20$ mJy beam$^{-1}$, the flux peak is 101 Jy beam$^{-1}$ and the beam size is $21'' \times 15''$ (ellipse in the bottom-left corner). The contour line at 80 Jy beam$^{-1}$ emphasizes the direction of the core jets. Some deconvolution errors are visible as small holes slightly above and below the bright core.
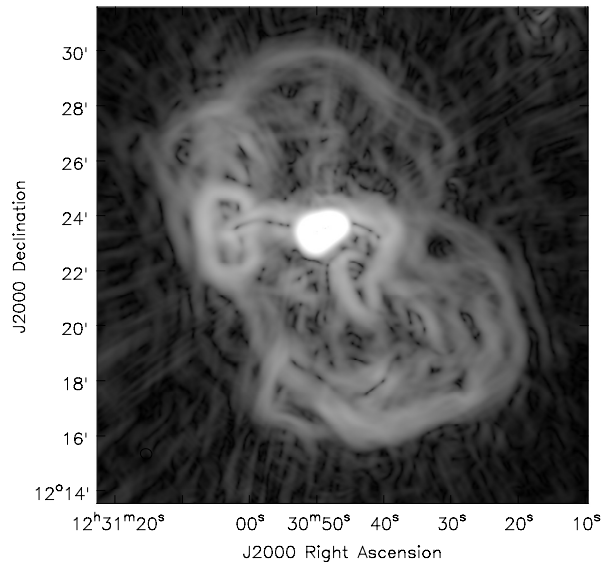
Figure 4.9: The same image shown in Fig. 4.8 Sobel filtered to enhance the edges of the structures.

in the east part of the inner region. In this case, the contour outline in Fig. 4.8 shows the orientation of the jet/counter-jet pair. The inner region is surrounded by two much fainter, much larger "bubbles" ($\sim$ 40 kpc wide, see Fig. 4.7) that are overlapping in the central region because of projection effects. The inner and the outer haloes are connected by two large "flows" (see Fig. 4.7). The first is oriented almost exactly east-west and the second slightly to the north of west, aligned with one of the inner jets. The eastward-flow proceeds straight, forming a well-defined cylinder, and ends in a pair of bright lobes, whose edges are brighter than their central part. The westward-flow, on the other hand, quickly changes its direction projected into the sky plane and twists as soon as it leaves the inner region. The flow then proceeds towards the south and is composed of a number of thinner structures that, following Owen et al. (2000), we call "filaments". Both flows originate in the inner region and reach the border of the outer haloes. Once the halo edge is reached both flows disperse, although only the west-flow seems to fill the entire halo with its plasma-filaments. In Fig. 4.9 the Sobel-filtered image of Virgo A help to disentangle the described features. The presence of these flows which connect the inner halo to the outer edges indicate that the diffuse emission is not a simple relic of a previous outburst, but fresh energetic particles still flow from the central cocoon. Plasma ages derived from spectral fits along the flows, confirm this picture (see Sect. 4.4.2).

The 140 MHz image shown in Fig. 4.8, although less resolved than the 7″ resolution 325 MHz image presented in Owen et al. (2000), confirms some characteristics of this source. First, the outer halo has a sharp edge and all the radio-emitting plasma seems to be confined within its boundaries. Second, although less visible than in the 325 MHz image, part of these
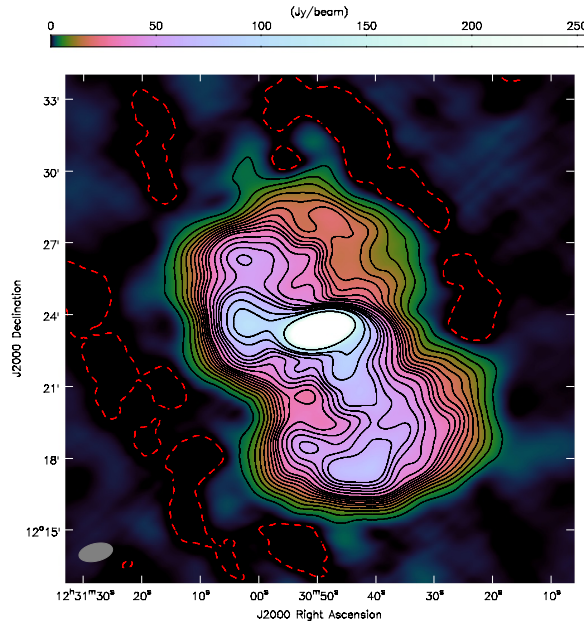
Figure 4.10: Image of Virgo A at 25 MHz. The map noise level is $\sigma = 0.6$ Jy beam$^{-1}$ and the beam size is $85'' \times 44''$ (grey ellipse in the bottom-left corner). Positive contour levels are represented by black lines at (1, 2, 3, 4, 5, 6, 8, 10, 12, 14, 16, 18, 20, 25, 30, 25, 40, 45, 50, 75, 100) $\times 5\sigma$. Negative contour levels at $-1\sigma$ are represented by a red dashed line.

edges are limb brightened, reinforcing the previous statement.

Interestingly, we can confirm that this picture is valid down to 25 MHz (see Fig. 4.11 and 4.10). If relic emission of past AGN activities extending beyond the sharp edges had been present, it would have been detectable thanks to its steep spectra. However, even at 25 MHz all visible emission is confined within the same boundaries that we see at higher frequencies. This fact also supports the picture that all of the emitting plasma is well confined by the strong pressure of the ICM, as we will discuss in more detail in Sec. 4.4.2.

## 4.4   Spectral analysis of the extended halo

### 4.4.1   Spectral index map

The low-frequency spectral index map shown in Fig. 4.12 was obtained by extracting a pixel-by-pixel linear regression using three images: one extracted from the LOFAR-HBA (115 − 162 MHz), one extracted from the LBA (45 − 77 MHz) observations and a third one from the VLA at 325 MHz. We excluded the very low frequency part ($\leqslant$ 45 MHz) of the LBA observations to retain an angular resolution of 50''. We produced an image from each SB and we convolved them to a resolution of 50''. Then, we averaged all LBA and HBA images separately,

(a) 36 MHz - RMS: 0.2 Jy/beam - beam: $73'' \times 58''$

(b) 48 MHz - RMS: 0.09 Jy/beam - beam: $55'' \times 43''$

(c) 59 MHz - RMS: 0.07 Jy/beam - beam: $45'' \times 36''$

(d) 71 MHz - RMS: 0.05 Jy/beam - beam: $37'' \times 30''$
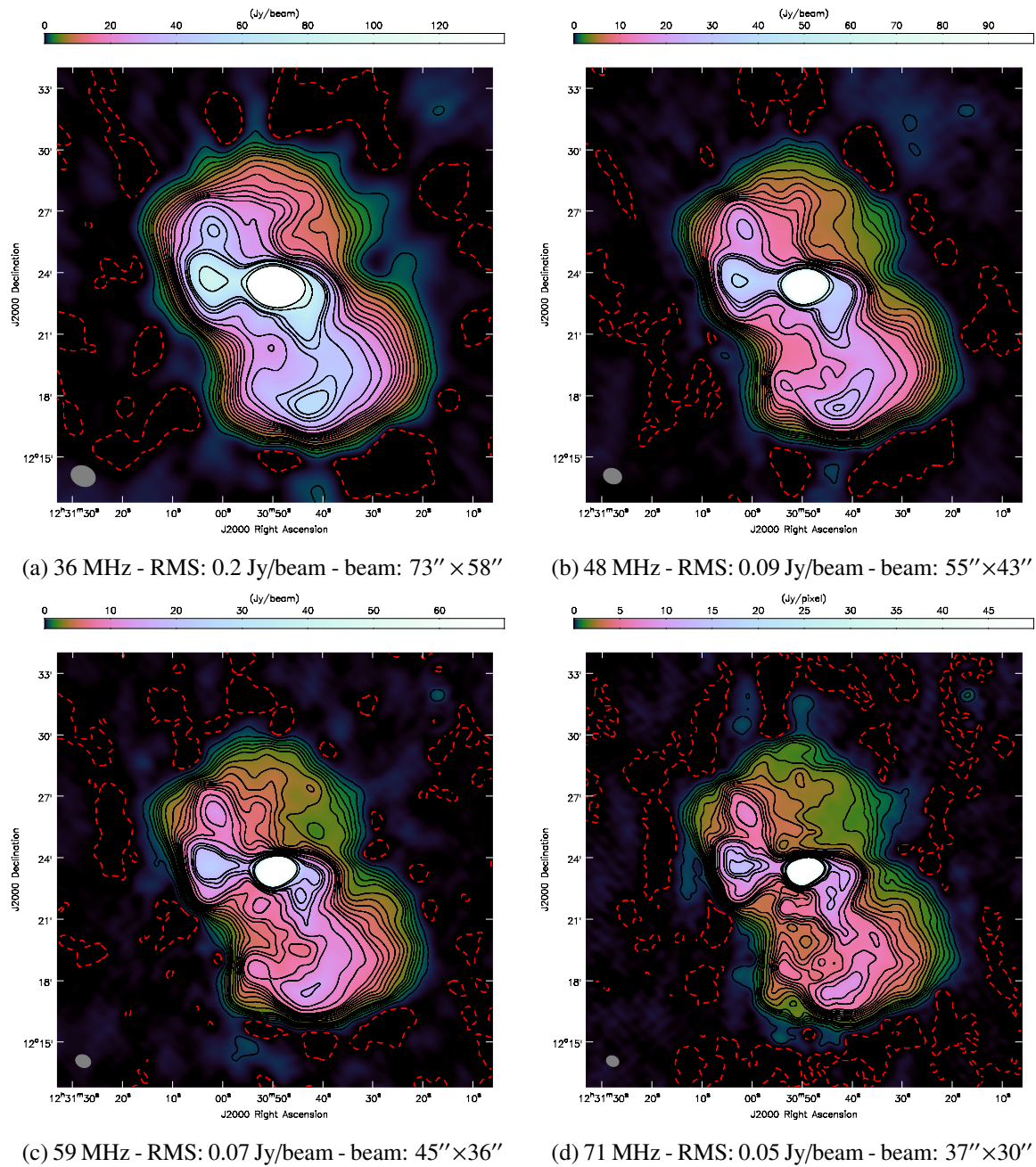
Figure 4.11: LOFAR-LBA images of Virgo A at frequencies ranging from 36 to 71 MHz. Each image is a result of a multi-scale multi-frequency cleaning on a subset of 60 SBs. The beam shape is visible in the bottom-left corner of each image. Positive contour levels are represented by black lines at (1, 2, 3, 4, 5, 6, 8, 10, 12, 14, 16, 18, 20, 25, 30, 25, 40, 45, 50, 75, 100) $\times 5\sigma$. Negative contour levels at $-1\sigma$ are represented by a red dashed line.

Figure 4.12: *Left figure*: Low-frequency spectral index map obtained from LOFAR-LBA $(45 - 71 \text{ MHz only})$ and LOFAR-HBA $(115 - 162 \text{ MHz})$ observations, together with VLA map at 325 MHz. All maps were convolved to a resolution of 50″ (see circle in the lower left corner) and a pixel-by-pixel linear regression was extracted. Pixels where the error were above $3\sigma$ are blanked. Contour lines are from the 325 MHz map. *Right figure*: spectral index $1\sigma$ error map.

obtaining one image in the HBA frequency range and one image in the LBA frequency range.

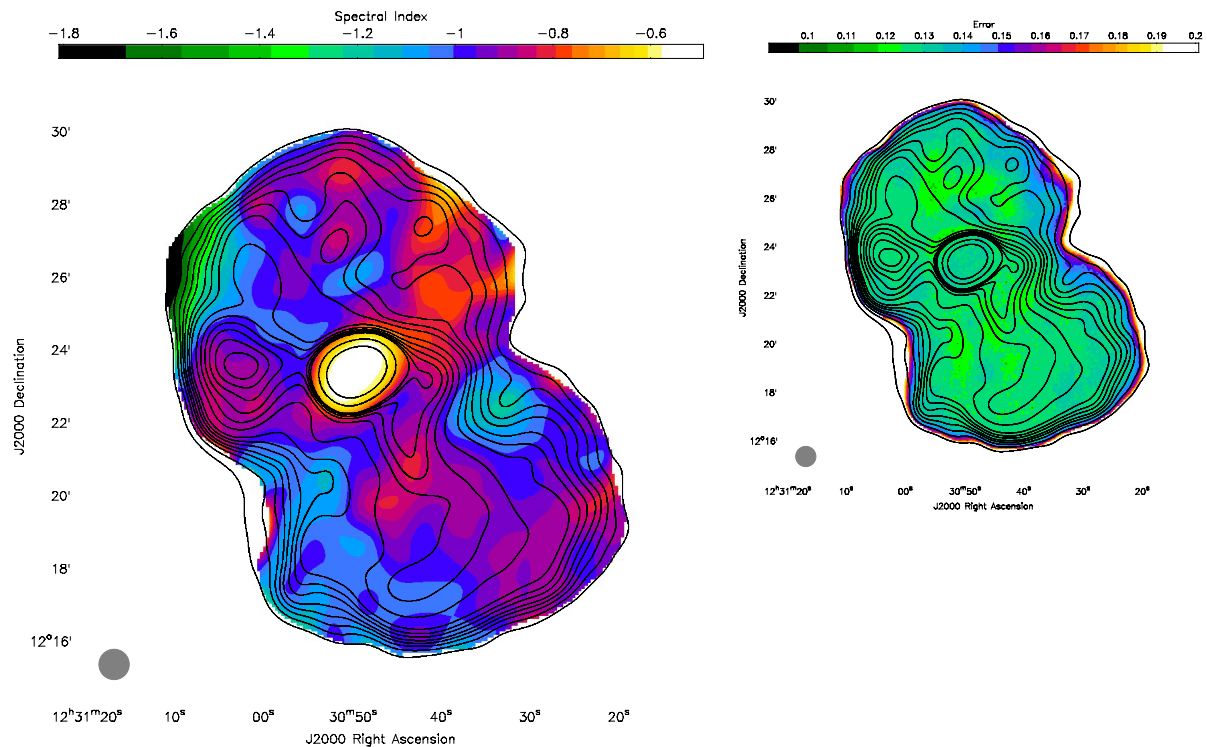The central cocoon of the source has a spectral index[2] ranging from $\sim -0.55$ to $\sim -0.6$, consistent with what has been observed by other authors at higher frequencies up to the optical band (Biretta et al. 1991). The spectrum is a straight power-law down to 30 MHz (see Fig. 4.13). No evidence of a turnover due to self-absorption is visible down to these frequencies. From the total integrated spectrum shown in Fig. 4.6 a possible sign of a turnover in the source integrated flux is visible at frequencies $\lesssim 20 \text{ MHz}$, so outside our frequency coverage. Features north and south of the bright core are likely affected by deconvolution errors and should not be trusted as real.

In the southern lobe the spectral index flattens by $10 - 20\%$ where the bright flow twists and bends with respect to the surrounding areas. The northern halo is related to the counter-jet, and therefore farther away from the observer. The spectral index in the east "ear" is comparable to

---

[2]In this and next chapter the spectral index $\alpha$ is defined as: $F_\nu \propto \nu^\alpha$

what is observed in the southern lobe in the radio-brightest zones. The two prominent filaments above the "ear" on the other hand, do not present any peculiar spectral index structure, although this is probably related to the low resolution of our spectral index map. The faint extension towards the north-west is the steepest part of the halo, reaching in our map a spectral index of $-1.8$. Interestingly this feature is co-located with what Forman et al. (2007) identify as an external cavity in the X-ray halo. The rest of the northern lobe has the lowest signal to noise ratio of the map, therefore it could be affected by spurious features.

Differences between north and south lobes were also found by Rottmann et al. (1996) at 10 GHz. They observed a higher degree of polarization in the southern lobe (due to the Laing-Garrington effect, Laing 1988; Garrington et al. 1988) and a total flux from the southern lobe that is 20% higher than from the northern one.

In general, there is no noteworthy relation between the spectral index and surface brightness maps, although a steepening of the spectral index is present (at the north-east and south-east edges of the map), where a reduction in the flow-related activity is present and a flattening is visible in some of the flow-active locations (the "ear" and the initial part of the west jet). Although in the lowest signal-to-noise zone of the map, we report a flattening of the spectrum by $\sim 20\%$ compared to the rest of the halo in the north-west part of it. This feature seems not to be related with any structure in the brightness maps.

### 4.4.2 Spectral index fits

We will now make a detailed analysis of the source radio spectrum, in specific regions of interest. For this analysis we decided to retain all of the frequencies down to 30 MHz, which limits our angular resolution to $75''$. The LOFAR maps have been averaged in blocks of 10 (bandwidth of 2 MHz), resulting in 24 maps in the LBA and HBA frequency range each. We also used three archival VLA maps at 325, 1400 and 1600 MHz and a single-dish Effelsberg map at 10.55 GHz (Rottmann et al. 1996). All of these maps were convolved to a resolution of $75''$ and spectral index fits were performed using *Synage++* (Murgia 2001). At low-frequencies ($< 325$ MHz) the spectra are almost straight and their slopes are the same reported in Fig. 4.12, although in the following analysis the resolution is lower compared to that used for the figure. To assess the reliability of a spectral index study with images produced by different interferometers, the same model of Virgo A was simulated in the used LOFAR and VLA configurations and frequencies. We imaged those data using the same weighting scheme (uniform), cell-size and iterations and convolved the CLEANed maps at the same resolution to compare the outcomes of the different datasets. Virgo A is never resolved out, but the different *uv*-coverages and, to a lesser extent, the missing short baselines at higher frequencies, create artifacts. Although the ratio between maps produced with different instruments shows errors up to 10% in

a single pixel in the zones where the signal-to-noise ratio is low, we note that such errors are not in the form of an overall bias but of patches of higher/lower flux (the average error of the pixel fluxes across the whole source is +0.3%). However, in our analysis we have always used the flux integrated over a certain solid angle, therefore we extracted the error for all the zones described in Sect. 4.4.2, finding in every case an integrated flux discrepancy below 1%.

In the following analysis of the spectral data, we tested three different models:

**The JP model (Jaffe & Perola 1973):** models spectral ageing as due to synchrotron and inverse Compton losses, with the pitch angles of the synchrotron emitting electrons continuously isotropized on a time-scale shorter than the radiative time-scale.

**The KP model (Kardashev 1962; Pacholczyk 1970):** as in the JP model, but now the pitch angle of the electrons remains in its initial orientation with respect to the magnetic field.

**The CI model (Pacholczyk 1970):** in the "continuous injection" model, an uninterrupted supply of fresh particles is injected by the central source. These particles age following the JP model. This model is applicable only if the injected particles cannot escape from the selected region. Therefore, we used it only on the integrated flux from the whole halo.

Compared to the KP model, the JP model is more realistic from a physical point of view, as an anisotropic pitch angle distribution will become more isotropic due to scattering, magnetic field lines wandering in a turbulent medium, and changes in the magnetic field strength between different regions (e.g., Carilli et al. 1991). Furthermore, since inverse Compton losses due to scattering by CMB photons can isotropise the electron population, a true KP model can be visible only for strong magnetic fields ($\gtrsim 30$ μG, Slee et al. 2001), where inverse Compton losses are negligible. In all of these models the injected particles are assumed to have a power-law energy spectrum $N(\gamma) \propto \gamma^{\delta_{\text{inj}}}$ (where $\gamma$ is the particles' Lorentz factor), which results in a power-law radiation spectrum with spectral index $\alpha_{\text{inj}} = \left(\delta_{\text{inj}} + 1\right)/2$. Finally, the magnetic field strength is assumed constant for the entire radiating period.

Since the most energetic particles radiate their energy more efficiently, they are the first to be depleted. Therefore, the source radio spectrum evolves and displays a break to a steeper slope at a break frequency $\nu_{\text{b}}$, which relates to the time elapsed from the injection and to the magnetic field as $\nu_{\text{b}} \propto B^{-3}t^{-2}$ (Jaffe & Perola 1973). Major differences between the models are visible at frequencies higher than $\nu_{\text{b}}$, while at lower frequencies all models are expected to have a spectral index equal to $\alpha_{\text{inj}}$. There are three free parameters in these models: the first is the spectral slope $\alpha_{\text{inj}}$ of the synchrotron emission generated by an injected electron population, the second is the break frequency $\nu_{\text{b}}$ and the third is the overall normalization.

A modification to the CI model that was also tested is the CIOFF model (Komissarov & Gubanov 1994), which allows the source to switch off after a certain time, encoded in an extra
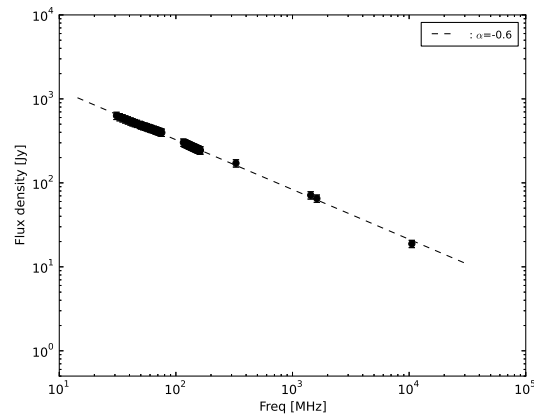
Figure 4.13: Fit to the integrated flux spectrum of the central region. The dashed line is a linear fit with a slope of $\alpha = -0.6 \pm 0.02$.

free parameter $\eta_{\mathrm{off}} = t_{\mathrm{relic}}/t_{\mathrm{source}}$, where $t_{\mathrm{source}}$ is the time since the beginning of the outburst and $t_{\mathrm{relic}}$ is the time since the source switched off. In this case the spectrum would show a first break frequency that depends on $t_{\mathrm{source}}$, which separates two power-laws like in the standard CI model, and an exponential cut-off at higher frequencies which depends on $t_{\mathrm{relic}}$.

**Central cocoon and macro-regions**

First, a spectral fit was made to the central region (Fig. 4.13) defined by C in Fig.4.16. As the data appear to be described by a straight line down to 30 MHz, we fitted a simple power-law, obtaining a slope of $\alpha = -0.6 \pm 0.02$. In this and in the subsequent fits, the errors on the integrated fluxes are computed from the RMS on the individual maps (multiplied by the square root of the number of beams covering the area) plus a 10% error due to systematics[3] combined in quadrature.

---

[3]The systematic errors considered are: a 1% error due to the different *uv*-coverages (Sec. 4.4.2), 3% due to the uncorrected beam shape (Sec. 4.2.2), and 4% for the uncertainty in the absolute flux rescaling (Sec. 4.2.2). A conservative total systematic errors budget of 10% has been adopted. However, this value overestimates the real error in the brightest parts of the source, therefore providing particularly low $\chi^2_{\mathrm{red}}$ values.
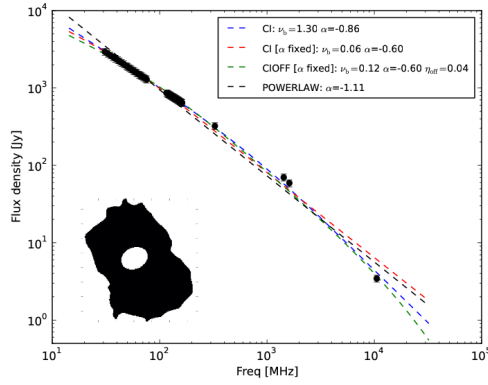
(a) Halo (without central cocoon)
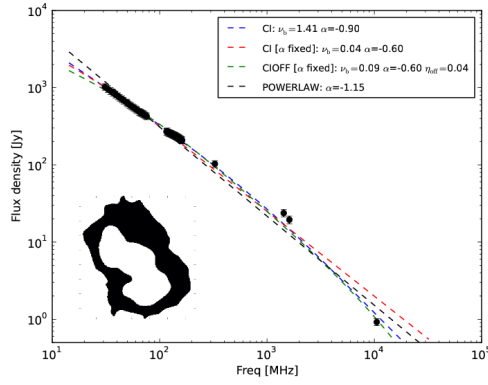


(b) Halo (without central cocoon and flows)
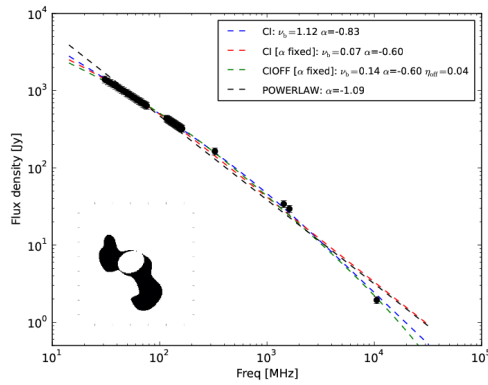


(c) Flows (without central cocoon)

Figure 4.14: Spectral fits of the three macro-regions identified in Sect. 4.4.2. In each panel the mask used to select the region is shown in the bottom-left corner. A simple power-law fit (black line) is shown together with two fits of the CI and CIOFF models. Red line: fit obtained fixing $\alpha_{inj}$ to $-0.6$. Blue line: with $\alpha_{inj}$ allowed to vary. A CI model with $\alpha_{inj} = -0.6$ is in general not able to fit the data. Finally, green lines show the fit of a CIOFF model with $\alpha_{inj}$ fixed to $-0.6$. $\nu_b$ is in GHz.

Table 4.3: Global spectral fits

| Region | — CI Model — | | | CI Model ($\alpha_{\text{inj}} = -0.6$) | | CIOFF Model ($\alpha_{\text{inj}} = -0.6$) | | | — Power-law — | |
|---|---|---|---|---|---|---|---|---|---|---|
| | $\chi^2_{\text{red}}$ | $\nu_{\text{b}}$ [GHz] | $-\alpha_{\text{inj}}$ | $\chi^2_{\text{red}}$ | $\nu_{\text{b}}$ [GHz] | $\chi^2_{\text{red}}$ | $\nu_{\text{b}}$ [GHz] | $\eta_{\text{off}}$ | $\chi^2_{\text{red}}$ | $-\alpha_{\text{inj}}$ |
| Central cocoon | – | – | – | – | – | – | – | – | 0.060 | $0.60^{+0.02}_{-0.02}$ |
| Halo (no core) | 0.198 | $1.3^{+0.3}_{-0.7}$ | $0.86^{+0.02}_{-0.06}$ | 1.471 | $0.06^{+0.01}_{-0.01}$ | 0.282 | $0.12^{+0.03}_{-0.04}$ | $0.04^{+0.01}_{-0.01}$ | 1.997 | $1.11^{+0.02}_{-0.02}$ |
| Halo (no flows) | 0.371 | $1.4^{+0.3}_{-0.8}$ | $0.90^{+0.03}_{-0.06}$ | 2.607 | $0.04^{+0.01}_{-0.01}$ | 0.439 | $0.09^{+0.02}_{-0.03}$ | $0.04^{+0.01}_{-0.01}$ | 2.156 | $1.15^{+0.01}_{-0.02}$ |
| Flows (no core) | 0.121 | $1.1^{+0.2}_{-0.7}$ | $0.83^{+0.02}_{-0.07}$ | 0.970 | $0.07^{+0.02}_{-0.01}$ | 0.182 | $0.14^{+0.03}_{-0.04}$ | $0.04^{+0.01}_{-0.02}$ | 1.905 | $1.09^{+0.02}_{-0.02}$ |

Then, we defined three macro-regions to obtain the average spectra of the halo and the flows.

- The first region (Fig. 4.14a) was obtained by cutting the 36 MHz map at the $5\sigma$ level and removing the central cocoon. We chose this frequency to maximise the flux from the halo (which is higher at lower frequencies).

- The second region (Fig. 4.14b) was obtained by removing from the previous map all the area with a surface brightness above 30 Jy/beam, i.e. the parts of the halo dominated by the flows.

- The final region (Fig. 4.14c) was obtained by retaining only the flows-dominated part of the halo (surface brightness > 40 Jy/beam), and removing the central region.

A spectral fit using the CI and the CIOFF models has been performed on each of these zones and the results are shown in Fig. 4.14 and in Table 4.3. Firstly, we performed a standard linear regression, from which it can be seen that the spectra are curved at high frequencies and, to a lesser extent, also at low frequencies. Then, we fitted the data using the CI model and fixing $\alpha_{inj} = -0.6$, equal to the core spectral index. In this case the model is not able to reproduce the data (see Fig. 4.14).

We decided then to relax some constraints and we repeated the fit using a CI model with all three parameters ($\nu_b$, $\alpha_{inj}$ and the normalization) free to vary. In this case we found a $\nu_b$ between 1.1 and 1.4 GHz and an $\alpha_{inj}$ between $-0.83$ and $-0.9$. This result suggests that the extended halo is quite young: $\lesssim 50$ Myr, assuming an average magnetic field strength of 10 μG (see Sect. 4.4.3) and using equation 4.3. We also observe a steepening of $\alpha_{inj}$ moving from the central region ($\alpha_{inj} = -0.6^{+0.02}_{-0.02}$), to the flows ($\alpha_{inj} = -0.83^{+0.02}_{-0.07}$) and the halo ($\alpha_{inj} = -0.90^{+0.03}_{-0.06}$), while taking the errors into account only a marginal steepening is detected moving from the flows to the halo. Although the core and the flows are surrounded by the halo, the projection effects should not alter these results, in fact the halo is on average $\simeq 20$ times and $\simeq 4$ times fainter in flux density than the core and the flow regions respectively. In Fig. 4.15 we plot the ratio between the power-law fit to the central cocoon data and the CI-model fit to the flow zones, and the ratio between the latter and the CI-model fit to the halo without flows. If the emission in these zones were related to the same outburst of relativistic particles, simple synchrotron ageing would have left the low-frequency part of the spectrum untouched at $\alpha = -0.6$, producing a constant ratio until the break frequency. Therefore, some other mechanism must have steepened the spectra at the lowest frequencies.

We list here some possible explanations.

(1) Adiabatic expansion of the relativistic plasma will shift the spectra towards lower frequencies and lower intensities, therefore can also affect the low frequency end of the spectrum.
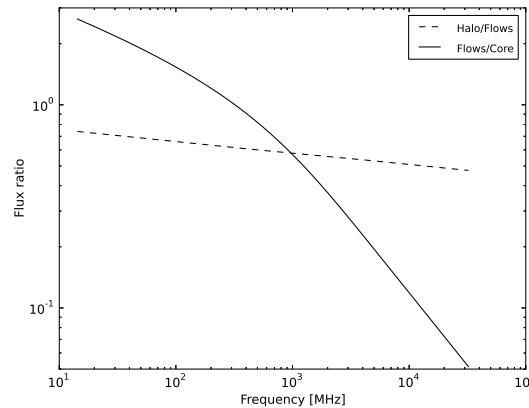
Figure 4.15: The solid line shows the ratio between the power-law fit to the cocoon zone (Fig. 4.13) and the CI-model fit to the flow zones (Fig. 4.14c). The dashed line shows the ratio between the CI-model fits to the flow zones (Fig. 4.14c) and to the halo (Fig. 4.14b). Simple synchrotron ageing would have left untouched the low-frequency part of the spectrum, producing in this plot a horizontal line until the point where the break frequency occurs. We notice instead a steepening in the spectrum, going from the central region to the flows and, to a lesser extent, from the flows to the halo.

A model was developed by Kardashev (1962) and revisited by Murgia et al. (2002). They propose a continuous injection of particles which subsequently expand adiabatically (CIE model). Such a model produces a low-frequency slope of the spectrum that is dominated by the plasmas at different ages after adiabatic expansion which results in a steepening of the spectra compatible with that seen in the lobes of Virgo A. A similar model was developed in Blundell et al. (1999) for double radio sources. The authors proposed that adiabatic expansion of plasma may happen as soon as the plasma leak out from the hot-spot regions. Particles leaving the hot-spots have spent different amounts of time in these regions with high magnetic fields, experiencing different ageing. Consequently, the final particle spectral distribution will be again a sum of spectra with many break frequencies and adiabatically expanded. This idea was claimed by Blundell & Rawlings (2000) to explain the "injection index discrepancy" discussed in Carilli et al. (1991). In this last paper, the authors observe that the low frequency spectral index measured in the lobe of Cygnus A should reflect either the low-frequency spectral index of the hot-spot ($\alpha = -0.5$, marginal adiabatic losses) or the high-frequency spectral index of the hot-spot ($\alpha = -1$, strong adiabatic losses). They observe instead a low-frequency spectral index of $-0.7$. These numbers are not particularly different from what we observe in Virgo A. Although these sources are remarkably different, the underlying physical effect which dominates at the low-frequency end of the spectrum might be similar.

(2) During their lifetime, relativistic electrons crossed a wide range of magnetic field strengths. As a result, their final spectrum is the sum of many spectra with many different break

frequencies. Particles that have spent much of their life within strong magnetic fields will have a very low break frequency, which can modify the low frequency slope of the radio spectrum.

(3) A third scenario is that the radio spectrum is intrinsically curved even in the core (Blundell & Rawlings 2000). In the source core the magnetic field strength is few mG while it is $\simeq 10\ \mu G$ in the halo (see Sect. 4.4.3), implying that the radio emission from the core is powered by electrons with energy $\sim 20$ times smaller than those emitting in the lobes, according to $\gamma \propto (\nu/B)^{1/2}$, $\gamma$ being the typical Lorentz factor of electrons emitting at the frequency $\nu$ in a magnetic field of strength $B$. Thus it is possible that the low-frequency synchrotron spectrum of the extended halo reflects a curvature of the spectrum of the emitting particles in the core at higher energies; this is expected in the context of particle acceleration models (Amato & Arons 2006). Fig. 4.13 does not provide compelling evidence in favour of this scenario, as the spectrum does not appear to steepen significantly at higher frequencies, yet future observations with higher resolution will test this possibility.

(4) Another scenario is that we are observing the relic emission of a source that had been active for an extended period and recently stopped injecting plasma in the halo. In this case the flatter spectral index ($\alpha_{inj} \simeq -0.6$) tail of the spectrum lies at lower frequencies, where we cannot detect it, and the $\alpha_{inj} \simeq -0.85$ slope is the steepened part of the spectrum. Following a simple CI prescription, we should expect the high-frequency part to have a slope of $-1.1$. However, to fit the data, a simple CI model is not enough and an exponential cut-off must occur at a frequency of $\sim 5$ GHz, implying a recent switching off of the fresh particles flow. This model (CIOFF) retains an initial injection index of $\alpha_{inj} = -0.6$, but fits the data much better than the standard CI-model with the same initial slope (see Fig. 4.14 and Table 4.3). In the CIOFF case the halo is older ($t_{halo} \simeq 150$ Myr, assuming an average magnetic field of $10\ \mu G$ and using equation 4.3) than in the CI scenario and the source must have switched off only a few Myr ago. This "switching off" should be interpreted as the most recent detaching of a bubble from the source central region, while in the central cocoon a new bubble is forming. In this case, the steeper low-frequency slope is the consequence of the integration over a wide area of the source, which again implies the addition of many spectra with different break frequencies as a consequence of ages differences.

**Zone by zone spectral analysis**

To check the validity of these hypotheses through an in-depth spectral analysis, we selected ten relevant zones (defined in Fig. 4.16) considered to be representative of the different parts of the source: central cocoon, flows/filaments (zones W1, W2, W3 and W4 for the west flow; zones E1 and E2 for the east flow), and halo (zones H1, H2 and H3). We deliberately avoided those zones where the signal to noise ratio is low and data could be dominated by calibration
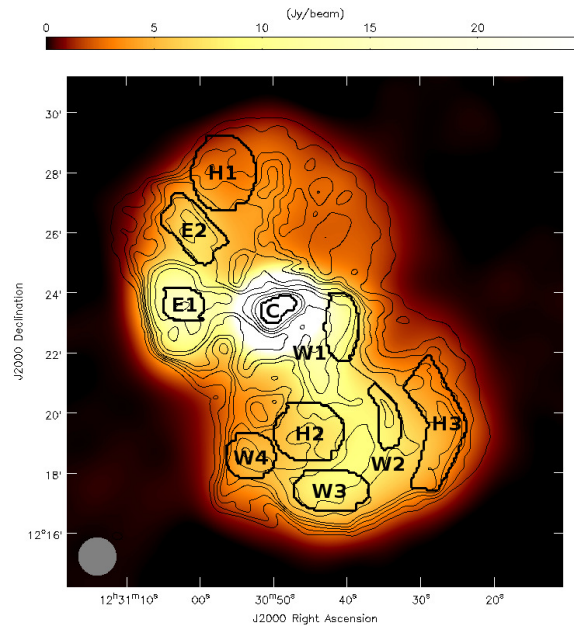
Figure 4.16: Image of Virgo A at 31 MHz convolved to a resolution of 75″. The ten different zones we analysed have been outlined in the map.

or deconvolution errors. For each zone we extracted the averaged flux at each frequency and performed a spectral analysis (see results in Table 4.4). Since our data are well approximated by a straight line in the LOFAR bands, with the curvature determined only by the three higher frequency values, both JP and KP models are able to fit the data comparably well (see Fig. 4.17) when leaving free to vary all the parameters. To reduce the degrees of freedom, we fit the data by fixing $\alpha_{inj} = -0.6$ and $\alpha_{inj} = -0.85$ (see Fig. 4.18).

A fixed $\alpha_{inj} = -0.6$ fails to fit our data, and when all of the parameters are left free to vary, we find $\nu_b \gtrsim 5$ GHz. These results are in contradiction with the CIOFF scenario (model 4 in Sect. 4.4.2), where we would have expected a wide range of $\nu_b$ and $\alpha_{inj} = -0.6$. On the other hand, we can fit both these and the global spectra if we assume an $\alpha_{inj} \simeq -0.85$. This steeper slope can be due to the intrinsically different and rather steep injection spectrum of a previous outburst. However, in that case, the presence of uninterrupted flows from the cocoon to the outer halo would be harder to explain.

Alternatively, we argue that a global steepening of the spectrum may occur at a very early stage, when the bubble detaches from the central cocoon. This can be related to an adiabatic expansion of the bubble, which happens as soon as it leaves the high-pressure central region (Churazov & Kaiser 2001; Carilli et al. 1991). In this case, a mix of plasmas at different ages would quickly expand and the high frequency parts of their spectra, which is indeed curved and steeper than −0.6 (Cotton et al. 2009), would be shifted towards lower frequencies. The sum of

Table 4.4: Spectral fits to representative regions

| Region | | JP Model $\chi^2_{\rm red}$ | $\nu_{\rm b}$ [GHz] | $-\alpha_{\rm inj}$ | KP Model $\chi^2_{\rm red}$ | $\nu_{\rm b}$ [GHz] | $-\alpha_{\rm inj}$ | Power-law $\chi^2_{\rm red}$ | $-\alpha_{\rm inj}$ |
|---|---|---|---|---|---|---|---|---|---|
| West Flow | W1 | 0.090 | $15.6^{+0.7}_{-4.3}$ | $0.83^{+0.02}_{-0.04}$ | 0.083 | $8.3^{+0.3}_{-2.6}$ | $0.83^{+0.02}_{-0.04}$ | 1.551 | $1.04^{+0.02}_{-0.02}$ |
| | W2 | 0.028 | $9.1^{+1.2}_{-1.9}$ | $0.82^{+0.02}_{-0.04}$ | 0.029 | $4.5^{+0.8}_{-1.2}$ | $0.81^{+0.02}_{-0.05}$ | 3.030 | $1.13^{+0.02}_{-0.02}$ |
| | W3 | 0.060 | $9.8^{+1.2}_{-2.1}$ | $0.88^{+0.01}_{-0.04}$ | 0.047 | $4.8^{+0.5}_{-1.3}$ | $0.87^{+0.02}_{-0.05}$ | 3.120 | $1.19^{+0.01}_{-0.02}$ |
| | W4 | 0.034 | $8.1^{+1.3}_{-1.8}$ | $0.90^{+0.02}_{-0.05}$ | 0.033 | $3.8^{+1.1}_{-1.2}$ | $0.89^{+0.03}_{-0.05}$ | 3.259 | $1.23^{+0.01}_{-0.02}$ |
| East Flow | E1 | 0.022 | $7.6^{+0.2}_{-1.3}$ | $0.83^{+0.02}_{-0.04}$ | 0.010 | $3.4^{+0.2}_{-0.9}$ | $0.81^{+0.02}_{-0.05}$ | 4.370 | $1.19^{+0.01}_{-0.01}$ |
| | E2 | 0.034 | $9.6^{+0.4}_{-2.1}$ | $0.91^{+0.03}_{-0.05}$ | 0.042 | $4.9^{+0.9}_{-1.3}$ | $0.90^{+0.01}_{-0.05}$ | 2.943 | $1.23^{+0.02}_{-0.02}$ |
| Halo | H1 | 0.056 | $8.3^{+1.2}_{-1.7}$ | $0.82^{+0.04}_{-0.05}$ | 0.068 | $4.1^{+0.2}_{-1.2}$ | $0.82^{+0.02}_{-0.05}$ | 3.088 | $1.15^{+0.01}_{-0.02}$ |
| | H2 | 0.034 | $11.4^{+0.7}_{-2.6}$ | $0.82^{+0.01}_{-0.04}$ | 0.035 | $6.0^{+0.4}_{-1.7}$ | $0.82^{+0.03}_{-0.05}$ | 2.229 | $1.09^{+0.01}_{-0.02}$ |
| | H3 | 0.045 | $9.2^{+0.9}_{-1.9}$ | $0.83^{+0.01}_{-0.04}$ | 0.044 | $4.6^{+0.2}_{-1.3}$ | $0.82^{+0.02}_{-0.05}$ | 2.997 | $1.14^{+0.02}_{-0.02}$ |

The assumed 10% error in the flux densities overestimates the real random normally distributed error providing artificially low $\chi^2_{\rm red}$ values.

these spectra produces a resulting spectrum that has a low-frequency end steeper than the initial ones (Murgia et al. 2002). Furthermore, an abrupt lowering in the spectra normalization is also expected, this can account for the strong brightness contrast between the cocoon and the halo. After that no further strong expansions occurred, otherwise a gradient in the surface brightness across the halo would be visible.

Regardless of the mechanism responsible for the observed steepening, in what follows we assume $\alpha_{\rm inj} = -0.85$ at the point where the plasma bubbles leave the cocoon. This provides a $t_{\rm halo} \simeq 40$ Myr (from equation 4.3, based on the break frequency in the CI model fit to the entire halo and assuming an average magnetic field strength of 10 μG).

### 4.4.3  Magnetic fields and synchrotron ageing

Equipartition magnetic field strengths were computed in the same regions shown in Fig. 4.16. We made the standard assumption that each zone of the radio source contains relativistic particles and uniformly distributed magnetic fields under energy equipartition conditions (e.g. Miley 1980). The radio luminosities for the computation were extracted from the lowest frequency map (31 MHz). To perform this analysis we made the following assumptions:

- The particle energy $U$ is equally divided between electrons and protons, setting $U_{\rm pr}/U_{\rm el} \equiv k = 1$. However, in Table 4.5 we also list the results for the assumption of $k = 0$, where all of the particle energy is in the relativistic electrons (and positrons), in line with the idea that the jets could be mainly composed of these constituents (Reynolds et al. 1996). We show also the results for the assumption of $k = 10$, as un upper limit from what predicted

(a) Zone W1  (b) Zone W2  (c) Zone W3

(d) Zone W4  (e) Zone E1  (f) Zone E2
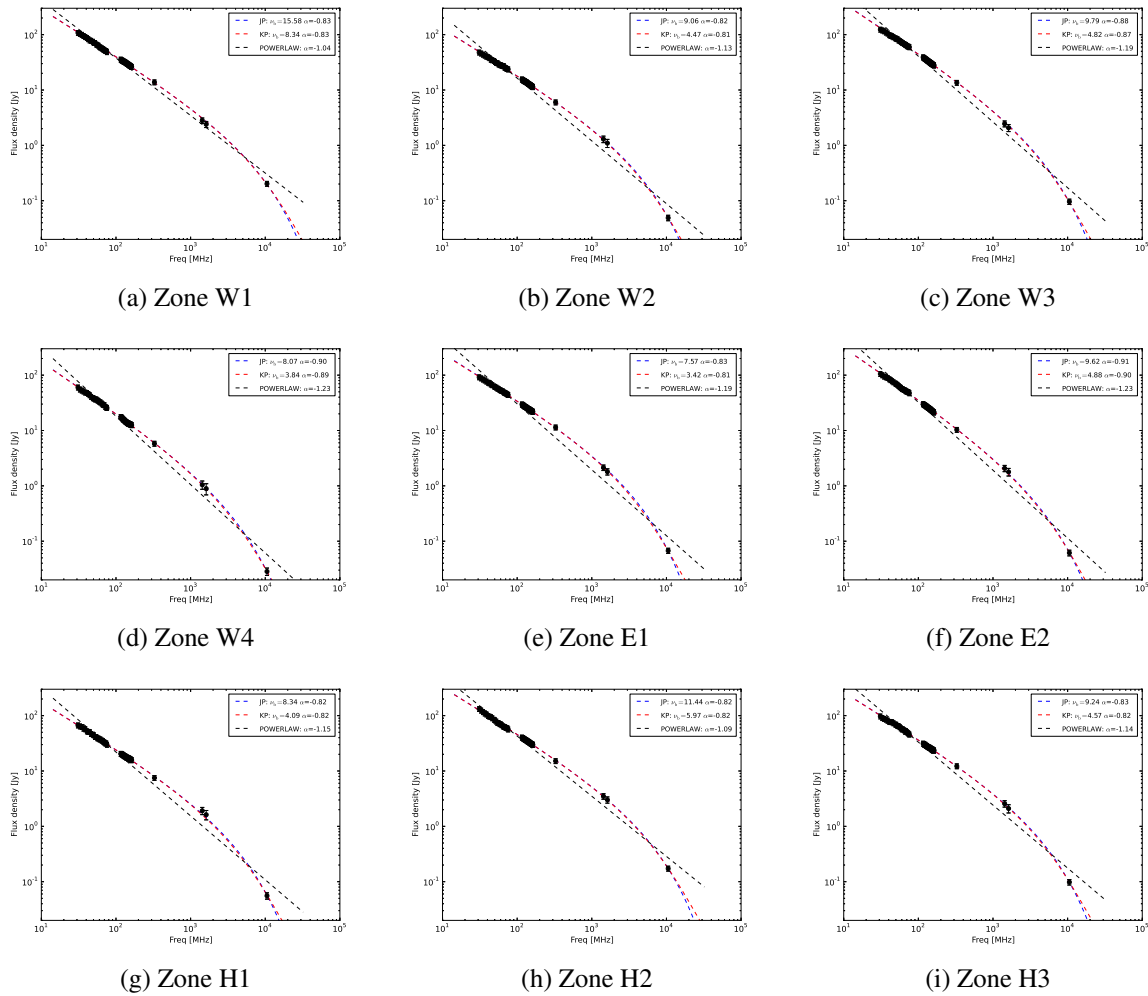
(g) Zone H1  (h) Zone H2  (i) Zone H3

Figure 4.17: Fit of the JP (blue), KP (red) models to the zones related to the halo. The zones are defined in Fig. 4.16. The black line is a simple linear regression fit to emphasize the curvature in the spectrum. $\nu_b$ is in GHz.

(a) Zone W1 (fixed $\alpha_{inj}$)

(b) Zone W2 (fixed $\alpha_{inj}$)

(c) Zone W3 (fixed $\alpha_{inj}$)

(d) Zone W4 (fixed $\alpha_{inj}$)

(e) Zone E1 (fixed $\alpha_{inj}$)

(f) Zone E2 (fixed $\alpha_{inj}$)

(g) Zone H1 (fixed $\alpha_{inj}$)

(h) Zone H2 (fixed $\alpha_{inj}$)

(i) Zone H3 (fixed $\alpha_{inj}$)

Figure 4.18: Fit of the JP (dotted cyan and magenta lines) and KP (dashed blue and red lines) models for the zones related to the halo. The zones are defined in Fig. 4.16. The slope of the injected electron population was fixed to $\alpha_{inj} = -0.6$ (cyan and blue lines) or $\alpha_{inj} = -0.85$ (magenta and red lines). The black line is a simple linear regression fit to emphasize the curvature in the spectrum. $\nu_b$ is in GHz.

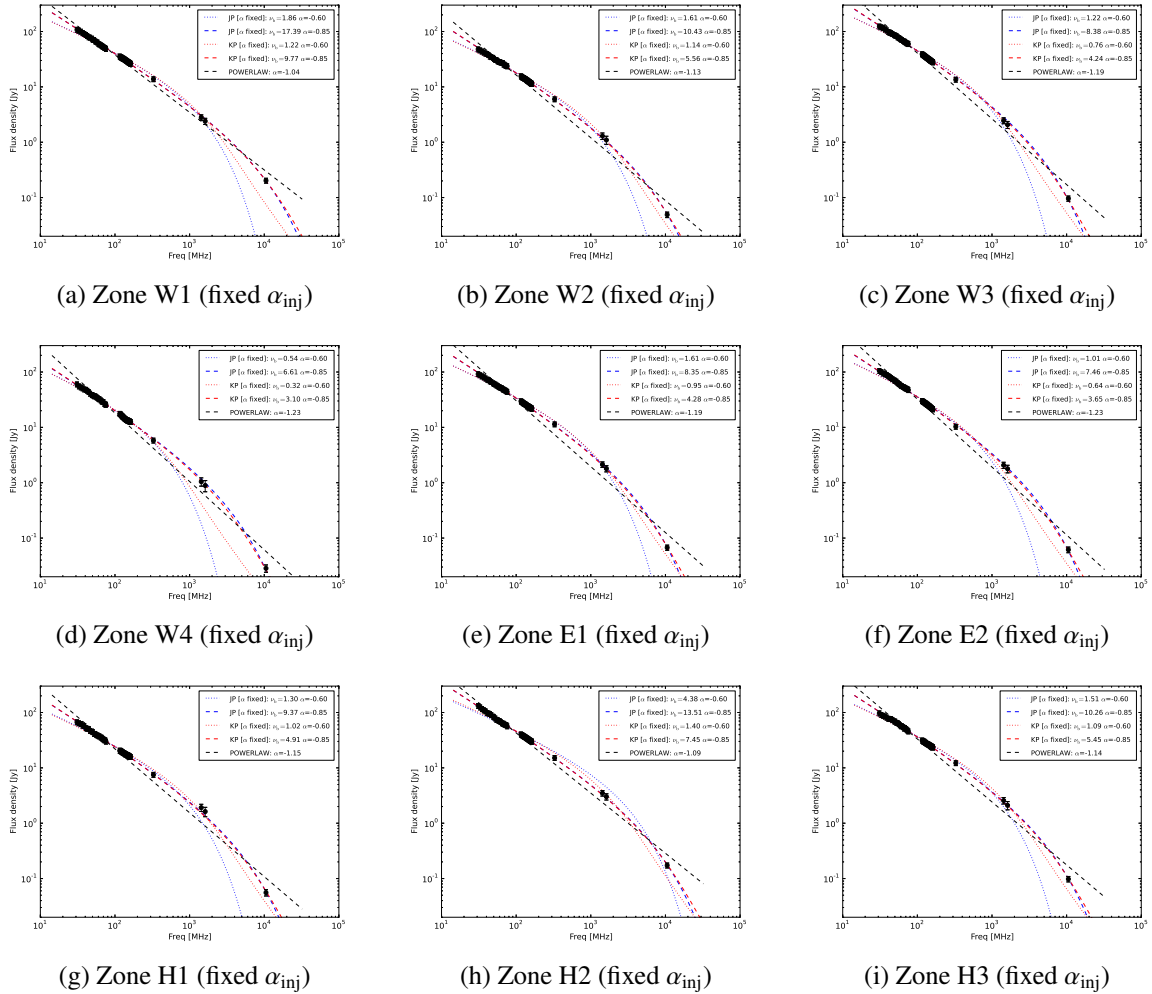by electromagnetic acceleration models involving protons and electrons.

- The equipartition magnetic field is usually computed assuming that the relativistic particle energies are confined between a minimum $\epsilon_{\min}$ and a maximum $\epsilon_{\max}$ value, corresponding to an observable frequency range, typically assumed to be 10 MHz – 100 GHz (Pacholczyk 1970). However, a fixed frequency range corresponds to an energy range that depends on the magnetic field, which varies in different parts of the source. Therefore, we decided to put limits directly on the electron population energies (Brunetti et al. 1997; Beck & Krause 2005). This approach, compared to the standard one, provides slightly higher $B$ values (see Appendix A, Brunetti et al. 1997). Reynolds et al. (1996) and Dunn et al. (2006) put constraints on the maximum value of $\gamma_{\min}$ noting that the synchrotron self-Compton flux density generated in the source core, which depends on $\gamma_{\min}$, cannot exceed the observed X-ray flux density. They obtained $1 \lesssim \gamma_{\min} \lesssim 100$ for an electron-positron jet and $50 \lesssim \gamma_{\min} \lesssim 100$ for an electron-proton jet. Falcke & Biermann (1995) also argue for radio loud AGN a $\gamma_{\min} \simeq 100$. We repeated our analysis for two values of $\gamma_{\min}$: 10 (with $k = 0$) and 100 (with $k = 1$ and with $k = 10$), corresponding to $\epsilon_{\min}$ of 5 and 50 MeV respectively. Above $\gamma_{\min} \simeq 1000$ we would expect a turnover in the low frequency part of our spectra that we do not detect. The $\epsilon_{\max}$ value does not affect the results, and we used an arbitrarily high value of 5 GeV ($\gamma_{\max} \simeq 10000$).

- For each zone we assumed a cylindrical configuration and we repeated the computation for two depth $D = 20$ kpc and $D = 40$ kpc. In the rest of the chapter the flows zones are assumed to have a depth of 20 kpc and the halo zones are assumed to have a depth of 40 kpc. The depth of the core is assumed to be 5 kpc.

- The low frequency spectrum slopes have been assumed to be equal to $-0.85$, as observed.

The equipartition magnetic fields, the minimum pressures and the corresponding synchrotron ageing times are listed in Table 4.5. In the first part, we list the equipartition analysis results assuming that all of the energy resides in the electrons and positrons only ($k = 0$) and that $\gamma_{\min} = 10$. In the middle and third parts of the table, we assume a $\gamma_{\min}$ values of 100 and we relax the electrons to protons energy ratio to $k = 1$ and $k = 10$ respectively. In the rest of the paper we will refer to the values in the second part ($k = 1$ and $\gamma_{\min} = 100$) only, while we notice that the other two combinations of parameters provide ages so small that the plasma bubbles should move at a velocity higher than the sound speed ($\simeq 900$ km s$^{-1}$ in the outskirts).

The source age is obtained by (see e.g. Murgia et al. 2011):

$$t_{\mathrm{s}} = 1590 \frac{B^{0.5}}{\left(B^2 + B_{\mathrm{IC}}^2\right)\left[(1 + z)\,\nu_{\mathrm{b}}\right]^{0.5}}, \tag{4.3}$$

where the synchrotron age $t_s$ is in Myr, the magnetic field strength in $\mu$G and the break frequency $\nu_b$ in GHz, while $B_{IC} = 3.25(1 + z)^2$ $\mu$G is the inverse Compton equivalent magnetic field strength with energy density equal to that of the CMB (Slee et al. 2001). The break frequencies were obtained from the fit of the JP model (see Table 4.4). We assumed a constant and uniform magnetic field strength and neglected any influence on the spectra from e.g. expansion or local re-energization of electrons.

Table 4.5: Equipartition analysis

| Reg. | D [kpc] | $\gamma_{min} = 10,\ k = 0$ | | | $\gamma_{min} = 100,\ k = 1$ | | | $\gamma_{min} = 100,\ k = 10$ | | | $p_{th}$ $\left[10^{-12}\frac{dyn}{cm^2}\right]$ |
|---|---|---|---|---|---|---|---|---|---|---|---|
| | | $B_{eq}$ [μG] | $p_{min}$ $\left[10^{-12}\frac{dyn}{cm^2}\right]$ | t [Myr] | $B_{eq}$ [μG] | $p_{min}$ $\left[10^{-12}\frac{dyn}{cm^2}\right]$ | t [Myr] | $B_{eq}$ [μG] | $p_{min}$ $\left[10^{-12}\frac{dyn}{cm^2}\right]$ | t [Myr] | |
| C | 5 | 55.1 | 83.9 | – | 36.0 | 35.7 | – | 56.0 | 86.5 | – | 640 |
| W1 | 20 | 21.9 | 13.2 | $3.9^{+0.7}_{-0.1}$ | 14.3 | 5.6 | $7.1^{+1.3}_{-0.2}$ | 22.2 | 13.6 | $3.8^{+0.7}_{-0.1}$ | 104 |
| W1 | 40 | 18.3 | 9.2 | $5.0^{+0.9}_{-0.1}$ | 11.9 | 3.9 | $9.1^{+1.6}_{-0.2}$ | 18.6 | 9.5 | $4.9^{+0.9}_{-0.1}$ | ” |
| W2 | 20 | 20.0 | 11.0 | $5.8^{+0.7}_{-0.4}$ | 13.0 | 4.7 | $10.6^{+1.3}_{-0.7}$ | 20.3 | 11.4 | $5.6^{+0.7}_{-0.4}$ | 53 |
| W2 | 40 | 16.7 | 7.7 | $7.5^{+0.9}_{-0.5}$ | 10.9 | 3.3 | $13.5^{+1.7}_{-0.9}$ | 17.0 | 7.9 | $7.3^{+0.9}_{-0.5}$ | ” |
| W3 | 20 | 20.9 | 12.1 | $5.2^{+0.7}_{-0.3}$ | 13.7 | 5.2 | $9.5^{+1.2}_{-0.5}$ | 21.3 | 12.5 | $5.1^{+0.6}_{-0.3}$ | 49 |
| W3 | 40 | 17.5 | 8.4 | $6.7^{+0.8}_{-0.4}$ | 11.4 | 3.6 | $12.2^{+1.5}_{-0.7}$ | 17.8 | 8.7 | $6.6^{+0.8}_{-0.4}$ | ” |
| W4 | 20 | 19.0 | 10.0 | $6.6^{+0.9}_{-0.5}$ | 12.4 | 4.2 | $12.0^{+1.6}_{-0.8}$ | 19.3 | 10.3 | $6.4^{+0.9}_{-0.4}$ | 58 |
| W4 | 40 | 15.9 | 7.0 | $8.5^{+1.1}_{-0.6}$ | 10.4 | 3.0 | $15.3^{+2.1}_{-1.1}$ | 16.1 | 7.2 | $8.3^{+1.1}_{-0.6}$ | ” |
| E1 | 20 | 23.9 | 15.7 | $4.9^{+0.5}_{-0.1}$ | 15.6 | 6.7 | $9.0^{+0.9}_{-0.1}$ | 24.2 | 16.2 | $4.8^{+0.5}_{-0.1}$ | 81 |
| E1 | 40 | 19.9 | 11.0 | $6.3^{+0.6}_{-0.1}$ | 13.0 | 4.7 | $11.6^{+1.2}_{-0.2}$ | 20.2 | 11.3 | $6.2^{+0.6}_{-0.1}$ | ” |
| E2 | 20 | 20.2 | 11.2 | $5.5^{+0.7}_{-0.1}$ | 13.2 | 4.8 | $10.1^{+1.3}_{-0.2}$ | 20.5 | 11.6 | $5.4^{+0.7}_{-0.1}$ | 68 |
| E2 | 40 | 16.9 | 7.8 | $7.1^{+0.9}_{-0.1}$ | 11.0 | 3.3 | $12.9^{+1.6}_{-0.2}$ | 17.1 | 8.1 | $7.0^{+0.9}_{-0.1}$ | ” |
| H1 | 20 | 16.0 | 7.1 | $8.2^{+1.0}_{-0.5}$ | 10.5 | 3.0 | $14.8^{+1.8}_{-1.0}$ | 16.3 | 7.3 | $8.1^{+1.0}_{-0.5}$ | 59 |
| H1 | 40 | 13.4 | 5.0 | $10.6^{+1.3}_{-0.7}$ | 8.7 | 2.1 | $18.7^{+2.3}_{-1.2}$ | 13.6 | 5.1 | $10.4^{+1.3}_{-0.7}$ | ” |
| H2 | 20 | 20.0 | 11.1 | $5.1^{+0.7}_{-0.2}$ | 13.1 | 4.7 | $9.4^{+1.3}_{-0.3}$ | 20.3 | 11.4 | $5.0^{+0.7}_{-0.2}$ | 65 |
| H2 | 40 | 16.7 | 7.7 | $6.6^{+0.9}_{-0.2}$ | 10.9 | 3.3 | $12.0^{+1.6}_{-0.4}$ | 17.0 | 8.0 | $6.5^{+0.9}_{-0.2}$ | ” |
| H3 | 20 | 17.0 | 7.9 | $7.2^{+0.9}_{-0.3}$ | 11.1 | 3.4 | $13.1^{+1.6}_{-0.6}$ | 17.2 | 8.2 | $7.1^{+0.9}_{-0.3}$ | 46 |
| H3 | 40 | 14.2 | 5.5 | $9.3^{+1.2}_{-0.4}$ | 9.2 | 2.4 | $16.6^{+2.1}_{-0.7}$ | 14.4 | 5.7 | $9.1^{+1.1}_{-0.4}$ | ” |

D is the depth of the region assuming a cylindrical configuration. $B_{eq}$ and $p_{min}$ are the magnetic field and the pressure from the equipartition analysis. t is the estimated zone age. Errors on t are derived from errors on $\nu_b$ in Table 4.4.
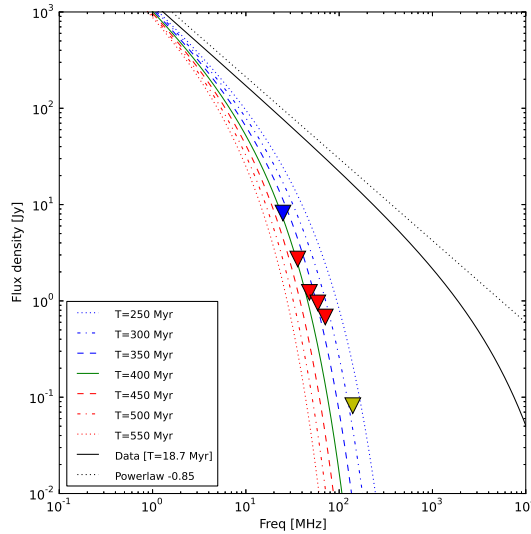
Figure 4.19: To estimate our capability to detect ancient outbursts we determined the maximum age of an emission we would be able to detect given the sensitivity of our maps. We took the zone H1 (Fig. 4.16) as representative for an old and inactive zone in the halo. Using its $\nu_b$ = 8.3 GHz and its estimated age of 18.7 Myr we let its spectrum evolve. In this figure we show the fit to the observed data as a black line. Coloured lines show the evolution of the expected spectral shape as time passes by (from top to bottom, after 250, 300, 350, 400, 450, 500 and 550 Myr, respectively, after the electron injection). Triangles indicates the $3\sigma$ detection limit for our maps. Blue is for the LBA-low map (Fig. 4.10), red for the four LBA-high maps (Fig. 4.11), while yellow for the HBA map (Fig. 4.8).

The equipartition analysis provides us with reasonable values for the lifetimes of the bubbles. For example, following the various zones sampled in the west flow (W1, W2, W3, and W4), a bubble escapes from the source cocoon after $\simeq$ 7 Myr (Churazov & Kaiser 2001, estimated $\sim$ 10 Myr with simulations) and reaches the outer edge of the lobe after $\simeq 12 - 15$ Myr (zone W4). This confirms the picture of a flow continuously replenished with fresh particles. In the east flow the centre of the lobe (zone E2) is reached after $10 - 13$ Myr. This lifetime is about a fourth of what is derived by dynamical models. A difference between these age estimations and the global halo age ($\simeq$ 40 Myr) is expected, as the latter takes into account many regions which have a lower break frequency than those in the flow zones.

In Fig. 4.19 we plot the theoretical temporal evolution of the radio spectrum in the halo zone H1 using the standard JP model. We simulated how the spectrum of a zone with these characteristics can evolve and how old it must be in order to go undetected in our maps. We find that in this illustrative example we would be able to detect emission as old as $\sim$ 400 Myr. This number is rather optimistic and it would decrease if adiabatic expansion had played an important role or if we had overestimated the current age of the zone. Finally, given the confinement

of the source discussed in Sect. 4.2.2, it is possible that particles from older AGN events were mixed with those from recent events. This can also play a role in steepening the low-frequency end of the lobes' spectrum. Such a scenario was observed in simulation by Morsony et al. (2010), where the authors simulated AGN driven jets in a dynamic, cosmologically evolved galaxy cluster. They found that largest scale reached by AGN jets is only proportional to the AGN power ($R \propto P_j^{1/3}$) and does not depend on the activity time. In this case the estimated halo age should be interpreted as a lower limit.

## 4.5   Discussion

Radio morphological evidence (Sect. 4.3) and spectral analysis (Sect. 4.4), show that the Virgo A halo is an active and living part of the source and not a relic of past activities (as already pointed out by Owen et al. 2000). Its radio emission is confined inside sharp boundaries.

The low-frequency spectral index map is fairly uniform, apart from a flattening in the central cocoon and in the northern lobe, and a steepening in the regions where the flow activity is fading. Thanks to the LOFAR data, together with high frequency observations up to 10 GHz, we were able to extract wide-band radio spectra of the source halo to an unprecedented detail. A continuous injection model applied to the whole halo shows cut-off frequencies at $\sim 1.3$ GHz, which provides an estimation of the halo age of $\simeq 40$ Myr.

We performed a detailed spectral analysis of nine different zones in the halo. Leaving all the parameters free to vary, we obtain a good fit only assuming $\alpha_{\text{inj}} \simeq -0.85$ (see Fig. 4.17). In order to reduce the number of free parameters we tried to set the slope of the energy distribution of the injected electron population to $\delta_{\text{inj}} = -2.2$ ($\alpha_{\text{inj}} = -0.6$), as we observe in the source central region, and which is also in perfect agreement with the broad-band spectrum of the jet of M87 (Perlman & Wilson 2005). However, in this case the JP and KP models fail to reproduce the observed spectra, while fixing $\alpha_{\text{inj}} \simeq -0.85$ produces reasonable results with both models (see Fig. 4.18). Observationally, this reflects the presence of a steep low-frequency end in the spectra of all regions in the halo, even those just outside the central cocoon. We speculate that this steep spectrum is the consequence of the strong adiabatic expansion of a mix of plasmas at different ages that takes place as soon as the plasma bubbles leave the dense central area, shifting their already steepened high-frequency part of their spectrum down to the MHz region. Once we assume $\alpha_{\text{inj}} \simeq -0.85$, we are indeed able to follow the ageing of the plasma bubbles along their path. For example, in the west flow we observe a shift of the break frequency (15 GHz $\rightarrow$ 9 GHz $\rightarrow$ 8 GHz), which reflects an ageing of the electrons (7 Myr $\rightarrow$ 10 Myr $\rightarrow$ 12 Myr), as we move farther from the source centre along the flow. It is worth noting that between region W2 and W3 the results with error-bars are consistent with

no-ageing, we can speculate that those two regions are, in projection, at the a similar distance from W1 but on different fronts of the flow, which is then creating a mushroom-like structure close to the edge of the halo (as in the east flow) instead of flowing along it. This picture can also explain the spectral index map in the southern lobe, where the flatter values, which seem to be connected with the active flow and initially follow it, end directly at the edge of the lobe that is where the flow should separate and create the top of the mushroom-shaped lobe. This picture is very much in line with the source three dimensional reconstruction proposed in Churazov & Kaiser (2001).

The minimum-pressure analysis in nine different zones in the source provides equipartition magnetic field values and relative pressures. These values are compatible with those found by Owen et al. (2000), although some of the initial assumptions were different: a different low-energy cut-off, different spectral slope and a different model for the synchrotron emissivity. Nevertheless, the net balance of these modifications reduces only slightly the values of the magnetic field strength we estimated for the Virgo A halo. It is worth pointing out that all the obtained $B_{eq}$ values are a few times above 3.25 μG, below which the Inverse Compton scattering of CMB photons is the dominant effect compared to synchrotron losses.

We compared our minimum pressure values with those derived from XMM observations (Matsushita et al. 2002), listed in the last column of Table 4.5. The thermal gas pressure is always more than an order of magnitude higher than the minimum pressure obtained from equipartition analysis. This could imply that the regions where plasma electrons and magnetic fields are co-located are much smaller than the assumed zone volumes (a "filling factor" < 1), or that much of the energy is contained in the thermal gas, or that the source is not at the equipartition. Yet another possibility is that much of the energy is stored in the relativistic protons (see e.g. Dunn & Fabian 2004; Bîrzan & McNamara 2008). In this case, to keep the equipartition principle valid, we would have to assume a $k \gtrsim 1000$, although this would generate much higher magnetic field strengths and therefore unrealistic short plasma ages. It is well known that inside the inner cocoon radio jets create cavities in the thermal gas, whereas on the larger halo scales there is evidence for the uplift of cold thermal gas (see e.g. Forman et al. 2007; Million et al. 2010) along the radio-flows. This has been explained by Churazov & Kaiser (2001) as gas uplifted by buoyant bubbles from the cold cluster core. In such a scenario the amount of pressure provided by thermal gas cannot be neglected and accounts for a not-negligible fraction of the total pressure. Furthermore, using X-ray and optical data, Churazov et al. (2008) also found that the combined contribution of cosmic rays, magnetic fields and micro-turbulence to the total pressure in the core of M87 is ~ 10% of the gas thermal pressure. This is in line with our findings.

### 4.5.1 Plasma age and dynamical time

Hydro-dynamic simulations of buoyant bubbles suggest that the halo outskirts can be reached in $42 - 67$ Myr (Churazov & Kaiser 2001, the proper number depending on the orientation and assumed distance). These estimations are a factor of $\sim 4$ greater than what was found in our synchrotron spectral analysis. Gull (1973) first noticed that the lifetime of synchrotron-emitting particles is short compared with dynamical time-scales. Some reasons that can explain this discrepancy are presented in Churazov & Kaiser (2001), Blundell & Rawlings (2000), and Owen et al. (2000): (i) the bubbles may be filled with a mix of weak and strong magnetic fields, the relativistic electrons may survive for a long time in the weak magnetic fields and then radiate most of their energies as soon as they diffuse in the strong magnetic field regions. This picture would also account for the filamentary structure visible in the radio images. (ii) In situ acceleration of particles may play an important role (Parma et al. 1999; Prieto et al. 2002). In both these cases the age of the radiating particles can hardly be determined by radio observations. (iii) New plasma can also flow along pre-existing channels and replenish aged plasma.

Finally, the buoyant rise time may not necessarily be the correct time, the radio plasma that forms bubbles comes from a jet which likely leaves it with a momentum. Brüggen & Kaiser (2002) simulated this situation in an environment compatible with that of Virgo and found in this case that the plasma can reach the distance of 20 kpc in $\simeq 15$ Myr, which is very much similar to what we measure.

### 4.5.2 Energetics

In Owen et al. (2000) the authors derived an estimate of the halo age using energetic conservation arguments, following Eilek & Shore (1989), from

$$\frac{\mathrm{d}U_{\mathrm{int}}}{\mathrm{d}t} = P_j - p\frac{\mathrm{d}V}{\mathrm{d}t} - L_{\mathrm{rad}}. \tag{4.4}$$

where $p$ the pressure of the halo plasma, $V$ the volume, $U_{\mathrm{int}}$ the internal energy, $P_j$ the jet power and $L_{\mathrm{rad}}$ is the radiative losses from the halo, which is small compared to $P_j$ and can be neglected. We can solve the equation assuming that the halo is spherically symmetric with a radius $R$ and that it expands due to its own internal energy up to $R = 35$ kpc. We also assumed that $P_j$ is time-independent. If the expansion is slow, the pressure of the bubble can be approximated with the pressure of the surrounding medium, which we obtained from XMM temperature and density profiles (Matsushita et al. 2002). For a non-relativistic plasma (most of the bubble content is thermal, with $\Gamma = 5/3$), we obtain a halo age of $\sim 250 P_{j44}^{-1}$ Myr, where $P_j = P_{j44} 10^{44}$ erg s$^{-1}$. For a bubble dominated by relativistic particles and magnetic

fields ($\Gamma = 4/3$), we obtain $\sim 400 P_{j44}^{-1}$ Myr. It is important to notice that a shorter burst of energetic particles would require a much higher $P_j$ (although for a shorter duration) than a long continuous injection of particles. In this simple model, our measurements of the halo age based on equipartition ($t \simeq 40$ Myr), provide an estimate of the jet power of $P_j \simeq 6 \times 10^{44}$ erg s$^{-1}$ for $\Gamma = 5/3$ and of $P_j \simeq 10 \times 10^{44}$ erg s$^{-1}$ for $\Gamma = 4/3$. This result is consistent with the conclusions of Owen et al. (2000) where the jet power $P_j$ is estimated to be $\sim$ few $\times 10^{44}$ erg s$^{-1}$ and with Di Matteo et al. (2003) which predict a $P_j \simeq 5 \times 10^{44}$ erg s$^{-1}$ for accretion at the Bondi rate. The result is instead above what has been found by other authors, e.g. Reynolds et al. (1996) find $P_j \simeq 10^{43}$ erg s$^{-1}$. This energy supply is $\sim 100$ times higher than the X-ray luminosity of the cooling flow region around M87, that is $\sim 3 \times 10^{43}$ erg s$^{-1}$ (Mushotzky & Smith 1980). Therefore, even a modest efficiency of energy dissipation into heat, is able to exceed the radiative cooling of the gas. Finally, we notice that a proton-rich plasma ($k \simeq 1000$) would lower by a factor of $\sim 10$ the age of the halo, boosting the necessary jet power up by the same amount which would drive the source at quasar luminosity (Falcke & Biermann 1995), which is not observed.

### 4.5.3   Ultra high energy cosmic rays

A debated argument is the possibility for a radio galaxy like M87 to accelerate ultra high energy cosmic rays (UHECR) of $\sim 10^{20}$ eV directly in the radio lobes. The Abraham et al. (2007) found a correlation between the arrival directions of cosmic rays with energy above $6 \times 10^{19}$ eV and the positions of AGN within $\sim 75$ Mpc, with a small excess of detections in the direction of Centaurus A, but no event detected in the direction of Virgo A. Ghisellini et al. (2008) correlated the position of UHECR events with the directions of HI-selected galaxies, and proposed that the UHECR coming from the direction of Centaurus A instead originate from the more distant Centaurus cluster, whose galaxies are in fact richer in HI than the galaxies of the Virgo cluster, explaining why there is no UHECR event from the Virgo direction. This opens the possibility that UHECR are produced by gamma ray bursts or newly born magnetars, but does not rule out an AGN origin.

In Centaurus A, the lobe radius ($\sim 100$ kpc wide) and estimated magnetic field strength ($B \simeq 1$ μG, Hardcastle et al. 2009) satisfy the Hillas argument (Hillas 1984), which requires that the Larmor radius $r_L$ of the accelerated particles fits within the source. The maximum particle energy $E_p = E_{20} \, 10^{20}$ eV that can be accelerated inside the Virgo A lobes is

$$E_{20} = Z \, e \, r_L \, B \simeq Z \, r_{100} \, B_{-6} \text{ eV}, \tag{4.5}$$

where $r_{100} = r_L \, 100$ kpc and $B_{-6} = B \, 10^{-6}$ G. Using an average magnetic field of 10 μG and a lobe radius of 20 kpc, we estimate the maximum particle energies to be $E_p \simeq Z \, 2 \times 10^{20}$ eV,

where $Z$ is the atomic number. However, efficient stochastic acceleration processes due to resonant interaction between particles and magnetic field turbulent perturbations require lobe contents to be predominantly relativistic plasma, and this is probably not the case for Virgo A.

## 4.6  Conclusions

In this chapter I presented the first LOFAR observation of Virgo A in the $15 - 162$ MHz frequency range and an analysis of its radio spectra. The major results are:

- Virgo A halo is an active and living part of the source and not a relic of past activities (as already pointed out by Owen et al. 2000).

- Going down to 25 MHz no previously unseen steep-spectrum features were detected. The source appears instead to be well confined within boundaries that are identical at all frequencies.

- A low-frequency spectral index map of Virgo A shows no obvious relation between spectral index and brightness. Generally, a steepening of the spectral index is present where the morphological evidences of flow activities are reduced in the southern lobe and at the position of the north-east X-ray cavity. A flattening of the spectral index, instead, is visible at the northern lobe towards west and in the position of enhanced radio flux density.

- A spectral analysis of the extended halo was performed. With the assumption of $\alpha_{\mathrm{inj}} = -0.6$ as in the core region, characterized by the flatter spectral slope, none of models tested is able to fit the data. Instead, $\alpha_{\mathrm{inj}} = -0.85$ is required, outside the central cocoon, to explain the spectra. This steepening in the low-frequency end of the spectra can be connected to a strong adiabatic expansion of the plasma bubbles that happens as soon as they leave the dense central region.

- An equipartition analysis was conducted and an average magnetic field strength of $\simeq$ 13 $\mu$G was found in the flow regions, while a magnetic field of $\simeq$ 10 $\mu$G is present in the halo regions. In the inner cocoon the average magnetic field reaches $\simeq$ 30 $\mu$G.

- A synchrotron ageing analysis provided a global halo age of $\simeq$ 40 Myr. The particle age tends to increase with distance from the centre in the flow regions and reaches a maximum of $\simeq$ 15 Myr where the flows end. This age is about a factor of $\sim$ 4 less than the dynamic time of a buoyantly raising bubble.

- Minimum pressure analysis reveals that, given our assumptions, the pressure generated by the plasma and the magnetic fields is much less than what is required to sustain the halo against external pressure. Probably, thermal gas is also playing a role in sustaining the halo. On the other hand, some of the parameters we assumed, or the equipartition hypothesis itself, may not be correct.

- We estimate the jet power $P_j$ to be $6 - 10 \times 10^{44}$ erg s$^{-1}$. This energy supply is 10 to 100 times higher than the X-ray luminosity of the cooling flow region around M87 ($\sim 3 \times 10^{43}$ erg s$^{-1}$) and is therefore able to exceed the radiative cooling of the gas.

To summarise, the extended radio-halo of Virgo A is a composite of many plasma bubbles of different ages. They are inflated in the central cocoon, where clear cavities in the thermal gas are visible, by the source's powerful jets. As soon as they leave the dense central area, a strong adiabatic expansion shifts their radio emission towards lower frequencies and lower fluxes. Then they buoyantly rise towards the halo outskirts where they disperse. During their motion, the travelling bubbles lift up cold X-ray emitting gas from the centre of the cluster.

As a final consistency check we can now estimate the accretion rate of M87. Using Eq. 1.10, we find

$$L_{\text{edd}} = 1.5 \times 10^{38} \frac{M}{M_\odot} \simeq 10^{48} \text{ erg s}^{-1} \, , \tag{4.6}$$

where we used $M_{\text{BH}} = 6.4 \times 10^9 \, M_\odot$ (Gebhardt & Thomas 2009). Which provides an Eddington accretion rate of

$$\dot{M}_{\text{Edd}} = \frac{L_{\text{edd}}}{\eta c^2} \simeq 166 \, M_\odot \, \text{yr}^{-1} \, , \tag{4.7}$$

assuming a typical radiative efficiency $\eta = 0.1$. From the estimated jet power $P_j \simeq 5 \times 10^{44}$ erg s$^{-1}$, we can obtain the accretion rate of the black hole with

$$\dot{M} = \frac{P_j}{\eta_{\text{jet}} c^2} \sim 0.2 \, M_\odot \, \text{yr}^{-1} \, , \tag{4.8}$$

assuming a $\eta_{\text{jet}} \sim 0.04$, as obtained in Sec. 1.4.1. However, it must be emphasized that this value for $\eta_{\text{jet}}$ is an averaged value on the whole population of AGNs at all redshifts. Therefore, it can be nothing more than an order of magnitude estimation, but it will allow us to obtain a reasonable accretion rate of $\dot{M} \simeq 10^{-4} \dot{M}_{\text{Edd}}$ and a reasonable radiative efficiency of

$$\eta = \frac{L_{\text{bol}}}{\dot{M} c^2} = 3 \times 10^{-4} \, , \tag{4.9}$$

with $L_{\text{bol}} = 4 \times 10^{42}$ erg s$^{-1}$ (Owen et al. 2000) and $\dot{M}$ as estimated in Eq. 4.8. Therefore, as stated in Chap. 1, M87 has a very low accretion rate and is radiatively inefficient.

# The Virgo field

de Gasperin et al. in prep.

## 5.1 Introduction

In this chapter I will exploit the wide field of view of LOFAR to investigate the properties of the other sources present in the field. Among the $> 300$ sources detected in the $5 \times 5$ degrees around M87, I will focus on the galaxies belonging to the Virgo cluster.

The Virgo Cluster center is $16.5 \pm 0.1$ Mpc away (Tonry et al. 2001) from the Galaxy, in the constellation Virgo. It comprises approximately 1 300 galaxies and subtends a maximum arc of approximately $8°$. The cluster is an aggregate of at least three separate sub-clumps centred on the galaxies M87, M86, and M49. In the LOFAR observation only galaxies belonging to the first two sub-clumps are visible.

Recent works have revealed a high fraction of (low-level) AGN activity in Virgo galaxies: 77/213 among late type, based on optical spectroscopy (Decarli et al. 2007) and 29/100 among early types, based on both X-ray and high frequency radio observations (Gallo et al. 2008; Nagar et al. 2005). The bright radio sources M84 and M89, for which clear sings of jet-ambient interaction have already been found, are the two clearest examples present in the observed field.

A very famous relation that I will also be able to test with LOFAR data is the radio-FIR (far-infrared) correlation in normal (non active) galaxies. At high frequencies ($> 5$ GHz) this relation has a slope consistent with unity, while at lower frequencies the slope increases and the relation is non-linear (Price & Duric 1992). This behaviour is directly linked to the presence of two components which contribute to the radio emission: (i) a synchrotron component (at lower frequencies) and (ii) a thermal *bremsstrahlung* component (at higher frequencies). The

explanation of the relationship is that both the FIR and radio emission are caused by high-mass stars. These stars (i) heat the dust with their UV emission, which then re-emits FIR radiation, (ii) ionize the surrounding medium which emits thermal *bremsstrahlung*, and (iii) produce the relativistic electrons responsible for synchrotron radiation when they explode as supernovae (see e.g. Condon 1992, and references therein).

Another aspect I can investigate with LOFAR is the interaction between cluster galaxies and their environment. It is quite an established fact that spiral galaxies in clusters have less atomic gas than spirals in an isolated environment, i.e. they are HI deficient (see e.g. Giovanelli & Haynes 1985; Gavazzi 1989). Two kinds of mechanisms are responsible for the removal of the atomic gas: (i) tidal interactions and (ii) the interaction of the interstellar medium (ISM) with the hot intra-cluster medium (ICM).

Cayatte et al. (1990, 1994) mapped the gas content of spiral galaxies in the Virgo cluster and showed that the HI disc sizes of cluster spirals are considerably reduced. Moreover, they noticed that in the cluster central region many galaxies with a symmetric optical disc have an asymmetric HI gas distribution. These observational results indicate that the gas removal due to the rapid motion of the galaxy within the ICM (ram pressure stripping, Gunn & Gott 1972) is responsible for the HI deficiency and the distorted gas discs of the cluster spirals.

During the phase of active ram pressure stripping the ISM located in the outer disc is pushed to smaller radii where it is compressed (Vollmer et al. 2001). The magnetic field $B$ is frozen into the ISM, therefore it becomes compressed too and its strength is enhanced. The radio continuum emission due to relativistic particles moving in the magnetic fields is proportional to $B^{2-4}$, depending on the equipartition assumption. One might thus expect an enhancement of the radio continuum emission of spiral galaxies that undergo active ram pressure stripping and consequently a shift from the aforementioned radio-FIR relation. At lower frequency we expect to detect more ancient particles than at higher frequencies, therefore tail of cosmic rays stripped from the galaxy could also be more easily detectable.

This chapter is organised as follows, in Sec. 5.2 I will describe more in detail the data reduction procedure applied to the LOFAR-HBA data used also in the previous chapter. In Sec. 5.3 I will list the galaxies which have a positive detection and describe their emission. In Sec. 5.4 I will derive the FIR-radio correlation using LOFAR data. Finally, in the last section, I will draw some conclusions.

## 5.2 Data Reduction

To study the Virgo wide field I used one of the dataset described in Sec. 4.2, namely the HBA observation. Although LBA dataset would have provided a much wider field of view at an even

lower frequency, I decided to focus on the HBA dataset for two reasons: the higher resolution I can obtain and the less issues caused by ionospheric disturbances which make wide-field imaging at the LBA frequencies very challenging.

## 5.2.1 Model

As an initial model I used the image from Owen et al. (2000)[1]. The first steps were extract the clean components from it and generate a model. I used the DECONVOLVE task in CASA in multi-scale mode, with scales from zero (a single pixel) up to the size of the source. The procedure is rather slow and many cycles ($\gtrsim$ 1000) are necessary. Even if the starting image is particularly accurate, like in this case, this procedure has been only able to produce a very crude model. However, since the Owen et al. (2000) image is at 325 MHz and our observations are at much lower frequencies ($\sim$ 140 MHz), we cannot expect this model to be anything more than a polite first guess.

## 5.2.2 Self-calibration

Using the model extracted as explained in the previous section, I started an automatic self-calibration on a single SB at $\sim$ 143 MHz that is at one half of the bandwidth. This procedure is made by many cycles ($\sim$ 250 in this case) where the output of one cycle is used as the model for the next one. The procedure converges, although very slowly, to the real emission morphology and to the correct flux ratios between the different source zones. The slow convergence is particularly evident in the remote stations, this is due to the fact that only few of these stations provide all the long baselines, thus the sampling of high spatial resolution structures. While core stations converges to stable solutions after a few iterations for remote stations I needed more than a hundred cycles.

These are the steps performed during each self-calibration cycle:

- The MODEL_DATA column of the measurement set is filled with the visibilities extracted from the model image. For the first cycle I used the model obtained in Sec. 5.2.1. A direct Fourier transform is used so no w-projection terms are adopted. The flux of the model is rescaled to the source expected total flux (as described in Sec. 4.2.2). The rescaling must be performed every cycle, since the cleaning bias is particularly strong in our configuration where we ignore all the fluxes from other sources in the field but Virgo A and we have to deal with the LOFAR very wide field of view. The total flux from the other detected sources in the field is $\sim$ 100 Jy, that is a not negligible fraction of the flux of Virgo A ($\sim$ 1200 Jy, at HBA frequencies).

---

[1]Image gently provided by Frazer Owen.

- A standard calibration is performed with BBS, adopting its beam prediction capability. This last solution is not really necessary, since I solve only in the direction of the phase centre. Removing the beam prediction all the beam effects would have been absorbed inside the gain/phase solutions. What is instead important is to solve for all the four polarisation products (XX, YY, XY and YX) at once. This procedure allows BBS to correct for possible instrumental polarisation due to the beam patterns of any two antennas being not equal.

- After every run of BBS a run of NDPPP (with the MADFLAGGER algorithm) has been performed to remove possible outliers.

- Images were obtained using the CASA task CLEAN. Firstly, a standard cleaning with an high cycle-factor value of 10 and 300 iterations was done on the bright core. This is necessary due to the difficulties of the multi-scale algorithm in obtaining high dynamic range images when a strong compact source is co-located with an extended structure. Then, 15 000 iterations of multi-scale cleaning has been done with spatial scales equal to 1, 7, 14, 20, 40, 80, 150 and 300 pixels, where a pixel size was 3″. In this way the largest cleaned scale is comparable to the source extension.

- Finally, the model obtained by cleaning is used as a starting model in the first step, and the procedure iterated.

In Fig. 5.1 the improvements of the image quality with the self-calibration are shown. At the first step the difference in the the morphology and the flux ratio among the different source's zones are so strong between the model (extracted from a 327 MHz map) and the real data, that many artefacts and deconvolution errors are generated. The result improves as the self-calibration proceeds. After 100 cycles the image looks much better, with no evident artefacts apart from a few zones above and below the bright core. These residual artefacts are mostly due to the poor uv-coverage of this observation.

In Fig. 5.2 I plot these improvements in a more quantitative way. For each image produced during a cycle I extracted the fluxes of the core region and of the extended halo (excluding the core), together with the RMS extracted from the source-free space in the images. Since the core has a flatter spectral index compared to the extended halo (see Sec. 4.4) and the initial model was extracted from an image at higher frequency and rescaled to the expected flux, the initial flux in the central region was overestimated, while the extended halo, on the contrary, was underestimated. A proper self-calibration will compensate for this effect, transferring flux from the core to the halo, and this happens quite fast for the halo and slightly slower for the core, that is more compact and thus more affected by the remote stations data. Together with this, the RMS noise of the map decreases: another good sign.

(a) After 1 cycle

(b) After 5 cycles

(c) After 25 cycles
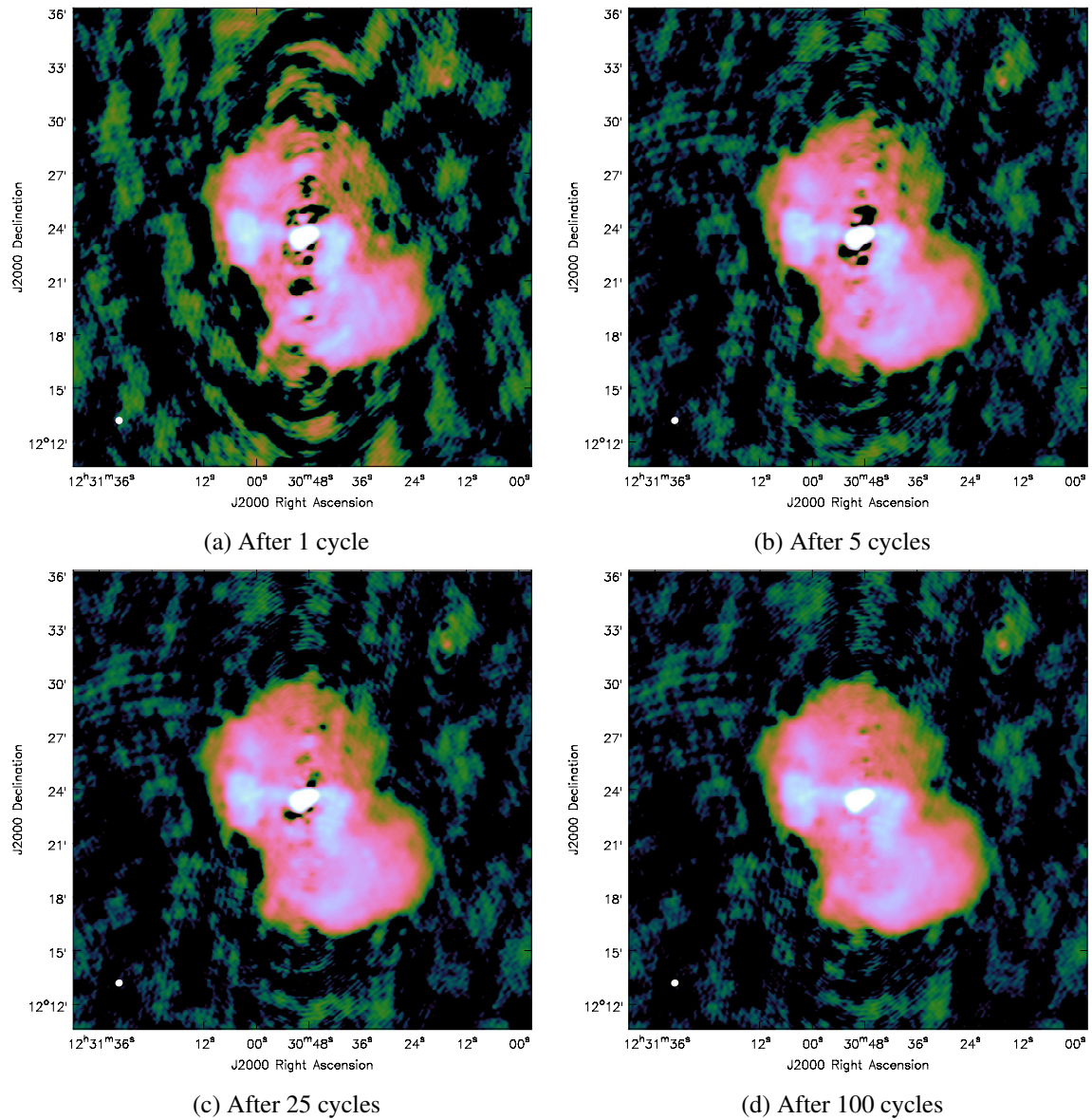
(d) After 100 cycles

Figure 5.1: Images of Virgo A during the self-calibration procedure after 1, 5, 25 and 100 cycles.
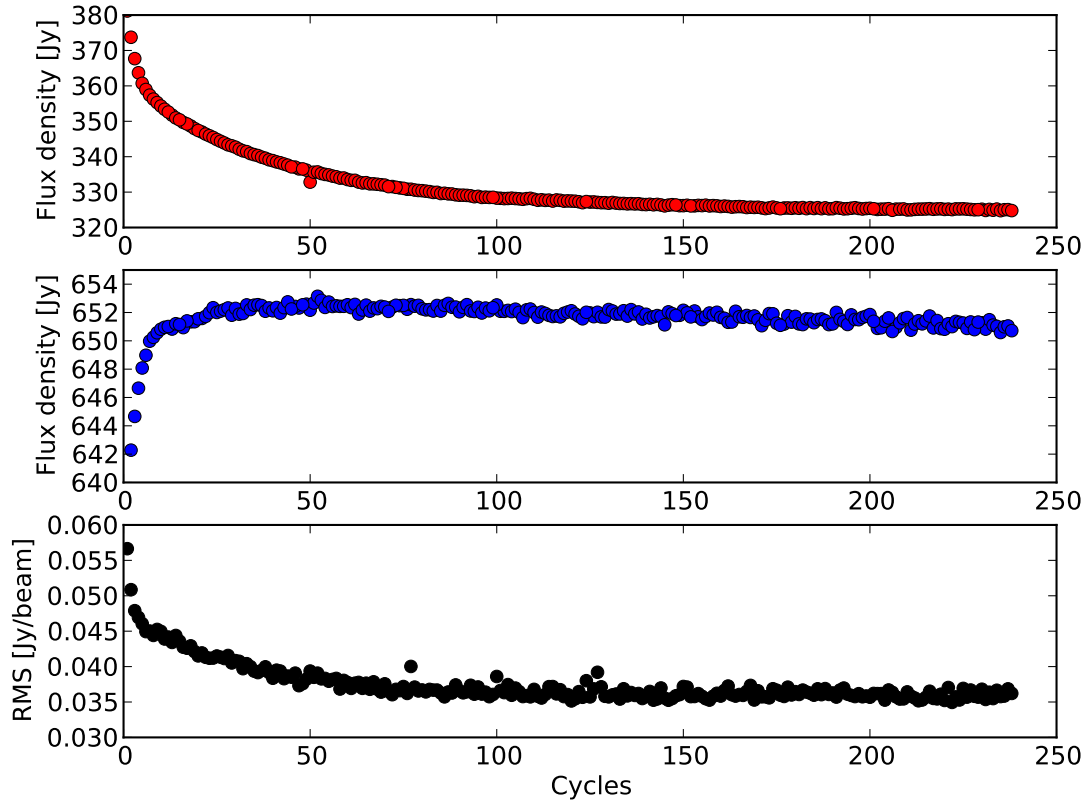
Figure 5.2: Evolution of the flux densities and the RMS noise of Virgo A HBA maps along the self-calibration procedure. In the first plot (red) the flux density of the core region is shown. In the second plot (blue) the flux density of the extended halo is show, while in the third plot (black) the evolution of the RMS is shown. Since the selfcal started from an image at different frequency (327 MHz) this plot shows how the procedure is capable to recover the correct flux-ratio between different zones of the source in the LOFAR-HBA map.

Once the whole initial self-calibration was concluded the 145 MHz model eventually obtained was used as an initial model for all the other SBs. In this case, given the smaller distance in frequency only 10 cycles of self-calibration were sufficient to stabilize the flux of the different regions.

## 5.2.3 Imaging

For each SB, I generated a image of Virgo A, the average of all these images was presented in Fig. 4.8. Virgo A was then subtracted from the data in the uv-space to improve the dynamic range of the wide-field image. Then, the Virgo A-subtracted data have been imaged using AWimager (described in Sec. 3.4) and an average of all these images is presented in Fig. 5.3.
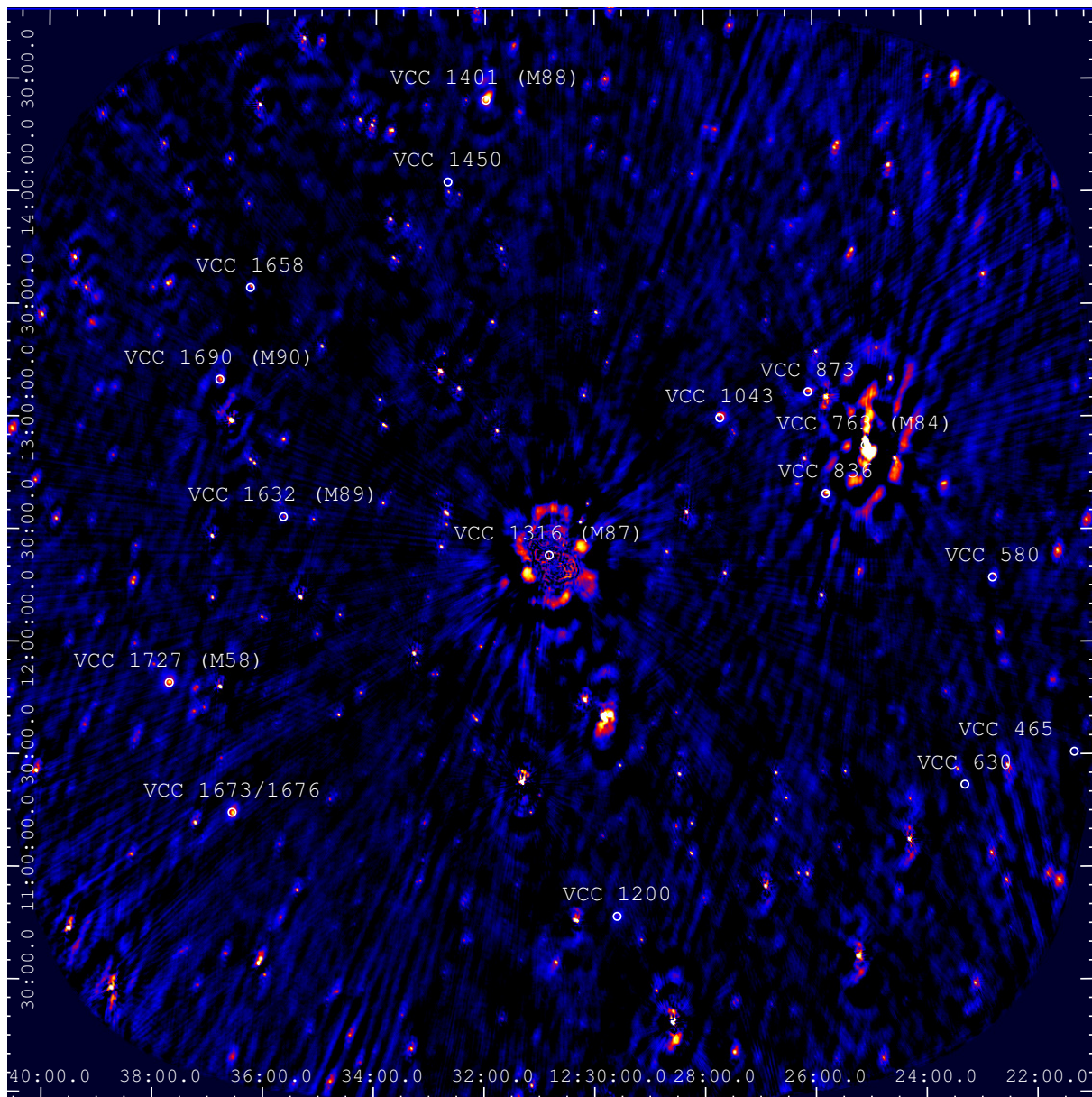
Figure 5.3: Wide-field map of the region around Virgo A (138.7 MHz, resolution: $23'' \times 29''$), Virgo A is subtracted and was in the centre of the field. Artefacts due to improper calibration or residual RFI are still visible in its former position. Artefacts around M84 are instead due to direction-dependant effects. Objects belonging to the Virgo cluster are marked with white circles.
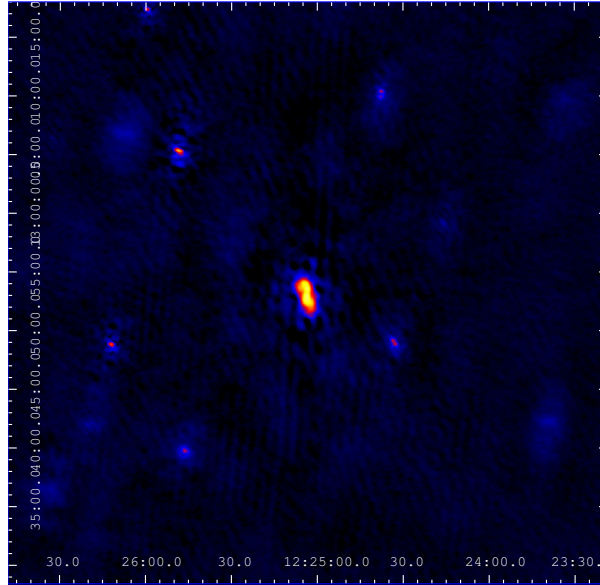
Figure 5.4: Image of M84 at 138.7 MHz after re-calibrating the data in its direction.

AWimager is capable of taking the beam variation effect into account, so any residual artefact or error present in this image should be mostly caused by ionospheric variations across the field of view.

Some artefacts due to an incomplete subtraction of Virgo A in the centre of the field are visible, together with even stronger artefacts coming from direction dependant errors from the second strongest source of the field: M84 (on the right side of the field). M84 is in fact ∼ 1°from the phase centre of the observation and ionospheric errors are a major source of problems in this scenarios. M84 itself shows artificial elongations towards the south and much attention should be paid in these circumstances to avoid false positive detections. A possible solution to obtain a good image of M84 and the surrounding zone is to calibrate again all the SBs in its direction, now that Virgo A is subtracted M84 is in fact the strongest source and we can self-calibrate on it. The result of this procedure is shown in Fig. 5.4. Now M84 is properly imaged and many of the direction dependant errors are absorbed in the calibration. This procedure is still experimental for LOFAR data and I could not relay on any flux measurement after its use. Therefore, the original map, although affected by substantial errors, has been used for source detection and flux measurements.

### 5.2.4   Source finder

In order to detect all the sources present in the field and make some quantitative assertions on the image, I used PyBDSM as a source extractor. More than 300 sources were detected with this procedure and a systematic shift of −2.9″ in RA and +6.6″ in DEC (compared with NVSS

Table 5.1: Sources detected in the Virgo cluster

| VCC | Other Names | RA | DEC | Type | Notes |
|---|---|---|---|---|---|
| 465 | NGC 4294 | 12h21m17.8s | +11d30m38s | Sc | PD[†]; Hɪɪ |
| 580 | – | 12h22m45.2s | +12d17m38s | BCD | Steep spectrum |
| 630 | NGC 4330 | 12h23m17.251s | +11d22m04.69s | Sd | PD[†]; Hɪɪ |
| 763 | NGC 4374 (M84) | 12h25m03.7433s | +12d53m13.139s | E | FR I |
| 836 | NGC 4388 | 12h25m46.7s | +12d39m44s | Sab | Seyfert |
| 873 | NGC 4402 | 12h26m07.6s | +13d06m48s | Sc | Hɪɪ |
| 1043 | NGC 4438 | 12h27m45.5938s | +13d00m31.775s | Sb | LINER |
| 1200 | – | 12h29m34.963s | +10d47m35.15s | Im | – |
| 1316 | NGC 4486 (M87) | 12h30m49.4233s | +12d23m28.043s | E (BCG) | Amorphous |
| 1401 | NGC 4501 (M88) | 12h31m59.161s | +14d25m13.39s | Sbc | Seyfert |
| 1450 | – | 12h32m41.9s | +14d03m02s | Sc | Hɪɪ |
| 1632 | NGC 4552 (M89) | 12h35m39.8073s | +12d33m22.829s | S0 | Seyfert/LINER |
| 1658 | – | 12h36m17.759s | +13d34m32.29s | dE | – |
| 1673/1676 | NGC 4567/NGC 4568 | 12h36m32.710s | +11d15m28.80s | Sc | Hɪɪ |
| 1690 | NGC 4569 (M90) | 12h36m49.793s | +13d09m46.58s | Sab | LINER |
| 1727 | NGC 4579 (M58) | 12h37m43.5220s | +11d49m05.498s | Sab | Seyfert |

[†] "PD" means a partial detection, probably because in the vicinity of some strong artefact in the image. No flux extraction was made in this cases.

data, Condon et al. 1998) has been discovered and corrected.

Cross-matching the detections with the Virgo cluster catalogue (VCC, Binggeli 1985) resulted in 15 objects, plus M87, which are known to be part of the Virgo cluster. These are listed in Table 5.1. For these objects I extracted the flux at 138.7 MHz although no direction dependent correction was applied to the map. Thanks to the beam-correction capability of AW-imager, all the beam-related errors and flux-deficit due to beam attenuation on the edges should have instead been removed. However, the software is still experimental and its reliability in complex fields like this has still to be assessed.

To extract the spectral energy distributions of the sources, I compared archival measurements of flux density at 10.55 GHz, 8.6 GHz, 4.85 GHz, 1.4 GHz and 0.6 GHz present in Vollmer et al. (2004), with those extracted from the LOFAR map (properly rescaled by a factor 0.84 to match the scale of Ott & Witzel 1994). The fluxes from LOFAR map were extracted following the $5\sigma$ contour, so not to include spurious artefacts but probably missing some of the faintest emission. In Table 5.1 the flux densities are listed, when the error was unknown I set it to 10%. From this comparison I extracted the spectra of a total of 13 objects in the frequency range $10.55 - 0.139$ GHz, reducing by a factor of 4 the previous minimum frequency available in the study of these objects.

Table 5.2: Flux densities of the detected galaxies

| Name | 139 MHz[1] | 600 MHz[2] | 1.4 GHz[2] | 4.85 GHz[1] | 8.6 GHz[3] | 10.55 GHz[3] | FIR[2] |
| | [mJy] | [mJy] | [mJy] | [mJy] | [mJy] | [mJy] | [Jy] |
|---|---|---|---|---|---|---|---|
| VCC 580* | 532 | – | 21 | 5 ± 1 | 4 ± 2 | – | – |
| VCC 763 (M84) | 17 976 | 10 802 | 6 067 | 2 270 ± 20 | 1 085 ± 20 | 864 ± 15 | 2.45 |
| VCC 836* | 1 036[†] | 383 | 119 | 84 ± 5 | 57 ± 3 | 36 ± 2 | 43.32 |
| VCC 873 | 713[†] | 149 | 60 | 21 ± 2 | 16 ± 2 | 12 ± 1 | 31.48 |
| VCC 1043* | 1 410 | 324 | 149 | 97 ± 9 | 49 ± 4 | 44 ± 4 | 20.97 |
| VCC 1200* | 294 | – | 13 | 9 ± 2 | 4 ± 2 | – | – |
| VCC 1401 (M88)* | 2 772 | 467 | 284 | 73 ± 17 | 52 ± 5 | 48 ± 4 | 106.37 |
| VCC 1450* | 42 | – | 10 | 10 ± 2 | – | 10 ± 2 | 7.87 |
| VCC 1632 (M89)* | 210 | 273 | 102 | 58 ± 2 | 47 ± 3 | 42 ± 6 | 0.98 |
| VCC 1658* | 324 | – | 11 | 3 ± 2 | – | – | – |
| VCC 1673/1676* | 1 780 | 222 | 124 | 65 ± 8 | – | 29 ± 3 | 109.33 |
| VCC 1690 (M90)* | 932 | 187 | 73 | 40 ± 6 | – | 30 ± 6 | 52.6 |
| VCC 1727 (M58)* | 2 024 | 282 | 97 | 99 ± 10 | 60 ± 7 | 82 ± 4 | 35.95 |

[1] from this work (scaled to Ott & Witzel 1994). [2] from the GOLDMine database (Gavazzi et al. 2003). [3] from Vollmer et al. (2004) and Niklas et al. (1995). [†] The vicinity with M84 and related spurious artefact on the map, could have severely modified the true flux density.

## 5.3   LOFAR sources in the Virgo field

Analysing the extended field I detected 15 resolved sources (excluding M87) that are related to galaxies which belong to the Virgo cluster. Only two of these are related to elliptical galaxies (M84 and M89), while all the others are spiral and irregular galaxies. Two objects (VCC 465 and VCC 630) had only a partial detection, I show them in Fig. 5.5. These are two spiral galaxies located ~ 2° away from the cluster centre, in a region unfortunately dominated by strong residual error deriving from the close presence of M84 and other strong sources not visible in the image. Given their low surface brightness, I was not able to reliably extract a flux value for these two objects and they are not considered in further analyses.

**VCC 580**   VCC 580 is a blue compact dwarf (BCD) galaxy, these objects are small galaxies which contain large clusters of young, hot, massive stars. VCC 580 has a unexpectedly steep spectral index of $-1.2 \pm 0.1$, which makes this object an ideal target for LOFAR. In our observation it presents an extended, strong radio emission not detected at higher frequencies. This emission might be related to its intense star-forming activity. In fact, BCDs are often characterised by high magnetic-field strengths, which might go up to 100 μG, comparable to starburst centres of galaxies. In addition, a very intense radiation field is present, dominated by FIR radiation, so inverse-Compton losses may not be neglected. In fact, they may be dominating.
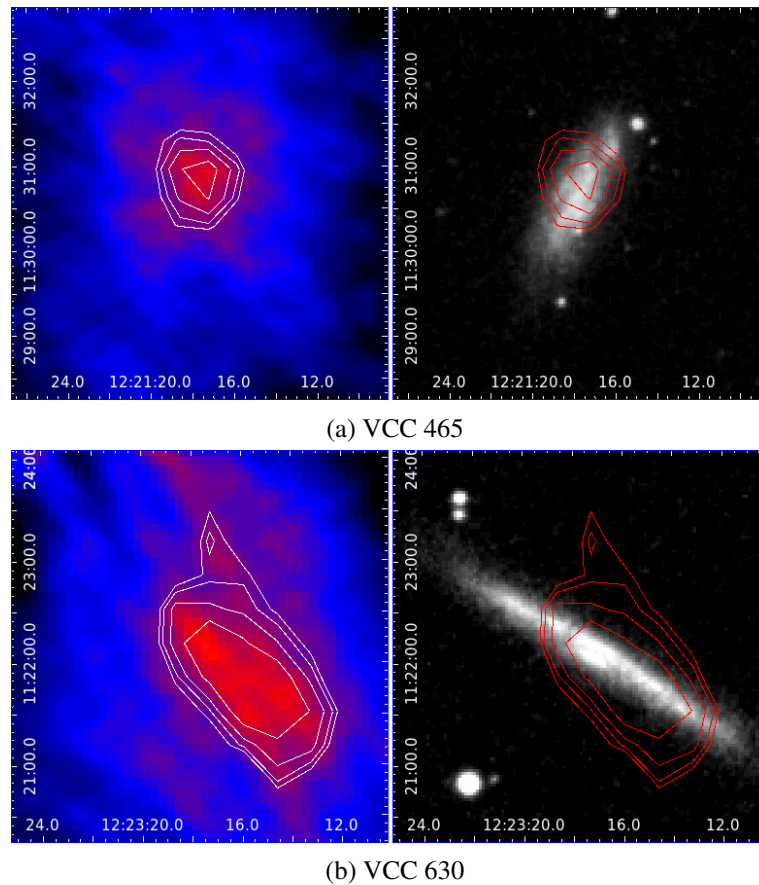
(a) VCC 465



(b) VCC 630

Figure 5.5: Images of VCC 465 and VCC 630. *Left*: LOFAR image at 138.7 MHz. *Right*: optical image from the SDSS with LOFAR contour superimposed.

Electrons would have very short lives of a few times $10^6$ yr, which implies very low break frequencies. Therefore, LOFAR might be measuring the spectrum of synchrotron radiation in the exponential decline before the break frequency.

**VCC 763 (M84)**    VCC 763 (M84) is one of the most famous radio source in the Virgo cluster and a prototype of FR I radio galaxy. In this galaxy, the spatial distribution of the soft X-ray emission is defined by the radio structure of the galaxy. In particular, low-density regions are present and are associated with the radio lobes and surrounded by higher density X-ray filaments (Fig. 5.8). VCC 763 is a very clear example of AGN-ICM interaction, with cavities in the X-ray emitting gas generated by the inflation of cosmic rays bubbles. Its radio spectrum is curved at lower frequency, probably because of self-absorption in the synchrotron emitting plasma but we cannot exclude that some of the flux was dispersed in the error generated around its position in the LOFAR map.

(a) LOFAR + Optical                                                                        (b) Spectrum
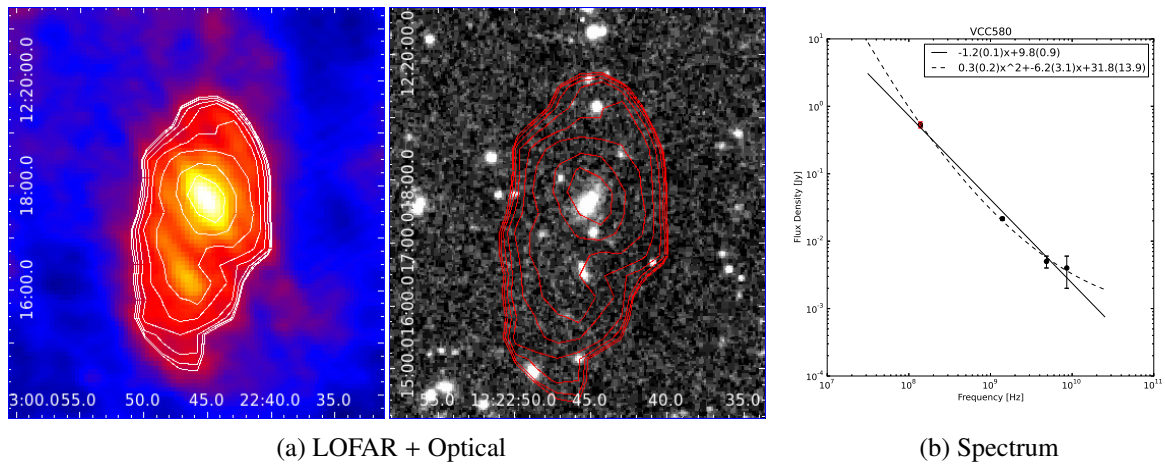
Figure 5.6: VCC 580, *Left*: LOFAR image at 138.7 MHz. *Centre*: optical image from the SDSS with LOFAR contour superimposed. *Right*: spectral energy distribution from 138.7 MHz (red point) up to the highest available frequency (data in Table 5.2). Solid line is a linear regression in the logarithmic space, while dashed line is a second order polynomial regression in the logarithmic space. The errors on the regressions parameters are in brackets. This object is a blue compact dwarf (BCD) galaxy with an unusually steep spectrum and an extended emission of unknown origin.



(a) LOFAR + Optical                                                                        (b) Spectrum
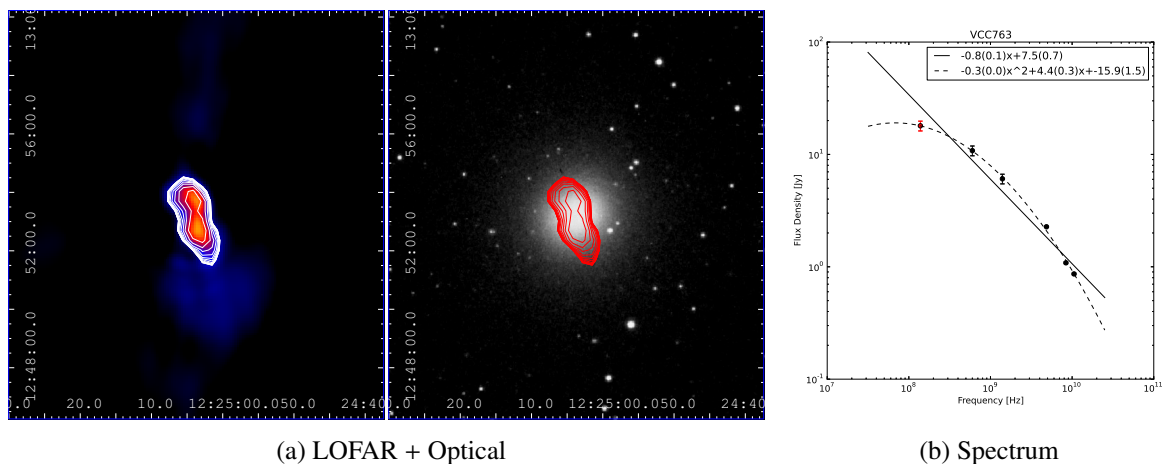
Figure 5.7: VCC 763 (M84), image as explained in Fig. 5.6. It is a typical FR I radio galaxy, with the two jets directed almost perfectly towards the north and the south, creating two more extended diffuse emissions which bend counter-clockwise.

**VCC 836**   VCC 836 is classified as a Seyfert galaxy where scattered light originating in a hidden broad-line region in the nucleus of this source is also detected (Shields & Filippenko 1996). Its spectrum is properly described by a power law with a typical spectral index of $\alpha = -0.8 \pm 01$ till the LOFAR frequencies.
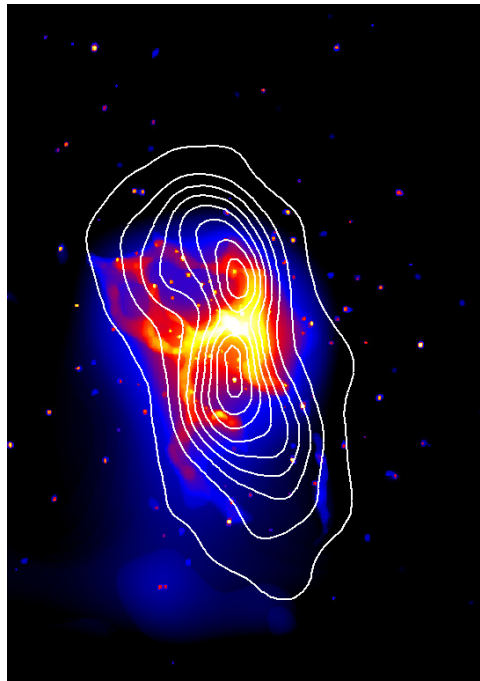
Figure 5.8: X-ray image of M84 made with the *Chandra* X-ray observatory (Finoguenov & Jones 2001) with LOFAR contour superimposed. Cavities excavated by the AGN jets are visible above and below the centre of the source.
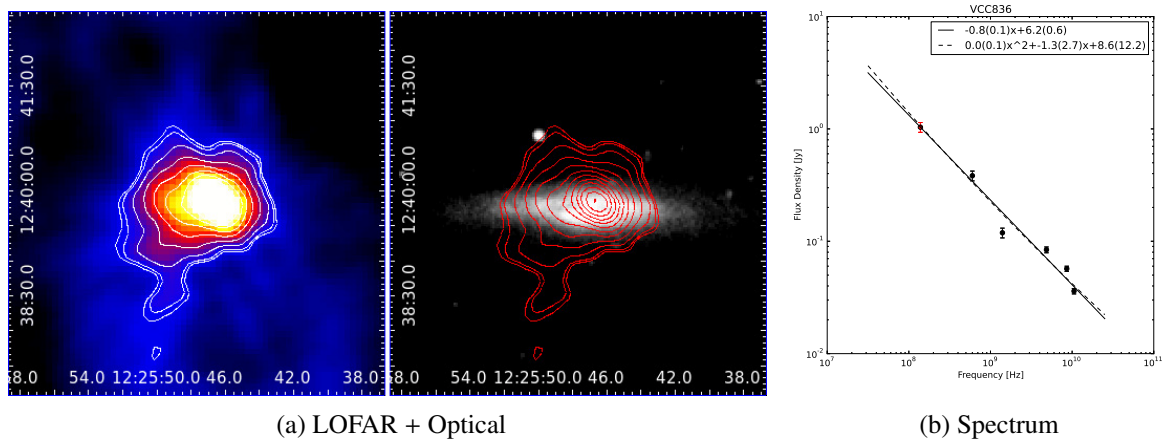


(a) LOFAR + Optical

(b) Spectrum

Figure 5.9: VCC 836, image as explained in Fig. 5.6. It is classified as a Seyfert galaxy.

**VCC 1043** This galaxy is classified as LINER (Ho et al. 1997). The peculiar structure of the galaxy is probably the consequence of a past interaction with its companion (NGC 4435). In Combes et al. (1988) the authors found CO emission located in the north-west direction of the galaxy (the same direction of the companion). They argue that molecular material is too dense to be easily swept by stripping from the hot ICM. Furthermore, the visible stellar tails can
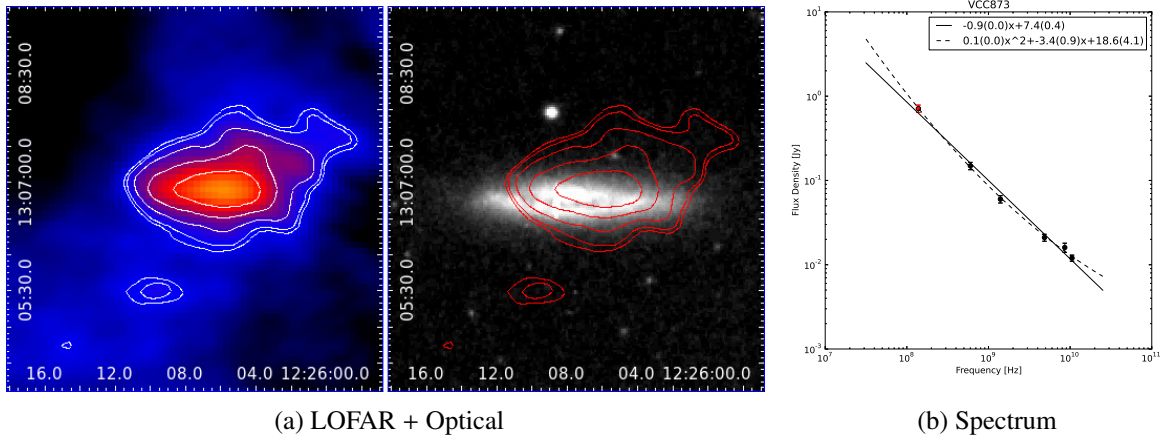
(a) LOFAR + Optical          (b) Spectrum

Figure 5.10: VCC 873, image as explained in Fig. 5.6.

only be of tidal origin. Therefore, they propose that a previous collision with its companion, caused the observed distortions in VCC 1043 and the radio and X-ray emission to the west of the galaxy. More recent X-ray and radio observations instead assign the radio emission to ram pressure stripping due to the interaction with the ICM. An extended X-ray halo has been in fact detected around this galaxy. The supersonic velocity of this galaxy, with respect to the ICM, causes bow shocks and consequently a Mach cone, shaped by the X-ray emitting gas, arises behind the galaxy (Marek Wezgowiecz priv. comm.).



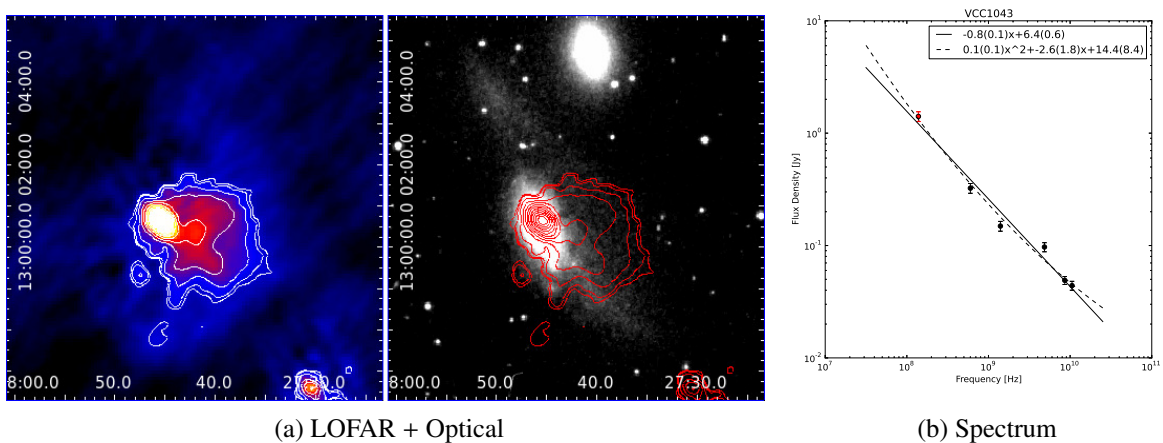(a) LOFAR + Optical          (b) Spectrum

Figure 5.11: VCC 1043, image as explained in Fig. 5.6. The unusual structure of the galaxy is probably due to a previous interaction with the companion (visible on the north-west). The radio emission could be either a consequence of this interaction (tidal stripping) or a consequence of the interaction with the ICM (RAM pressure stripping), which would be responsible also for the morphology of the X-ray halo present around this galaxy.
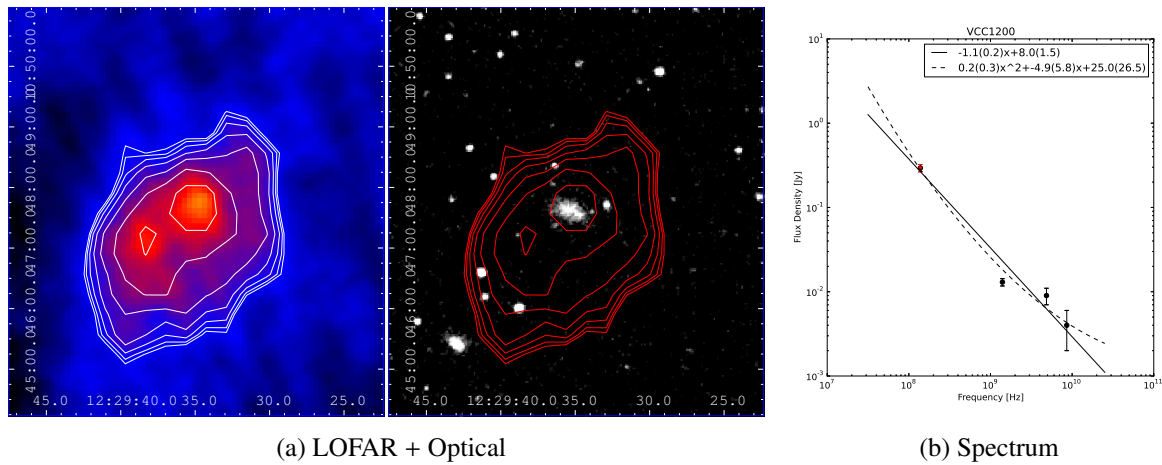
(a) LOFAR + Optical

(b) Spectrum

Figure 5.12: VCC 1200, image as explained in Fig. 5.6.

**VCC 1401 (M88)** VCC 1401 represents an especially clear example of early stage ram pressure stripping of a large cluster-spiral galaxy. It is in fact stripped nearly edge-on, while heading south-west, and it is $200 - 300$ Myr before the ram pressure peak, i.e. its closest approach to M87 (Vollmer et al. 2008). An extended X-ray emission beyond the H I disc is present and it might be due to stripped gas mixed with the ICM and/or a galactic wind due to star formation in the prominent north-western spiral arm (Wezgowiec et al. 2011). Its nucleus is active and classified as a Seyfert (Ho et al. 1997).
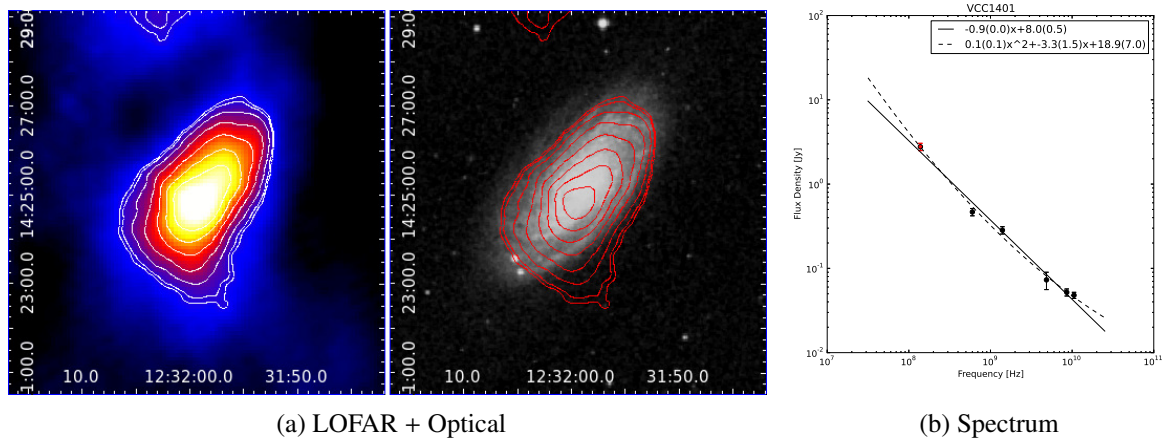


(a) LOFAR + Optical

(b) Spectrum

Figure 5.13: VCC 1401 (M88), image as explained in Fig. 5.6. Its nucleus is active and classified as a Seyfert.

**VCC 1450** The spectrum of VCC 1450 is rather flat (compatible with $\alpha = 0$) until 1.4 GHz but increases quite sharply at the lowest frequency. A mixing of optically thin synchrotron emission (typically $\alpha = -0.8$) with thermal emission (typically $\alpha = -0.1$) could be responsible

for its spectral shape. However, the extremely low surface brightness of this object could be the cause of relevant errors in the estimate of the LOFAR flux.



(a) LOFAR + Optical                                              (b) Spectrum
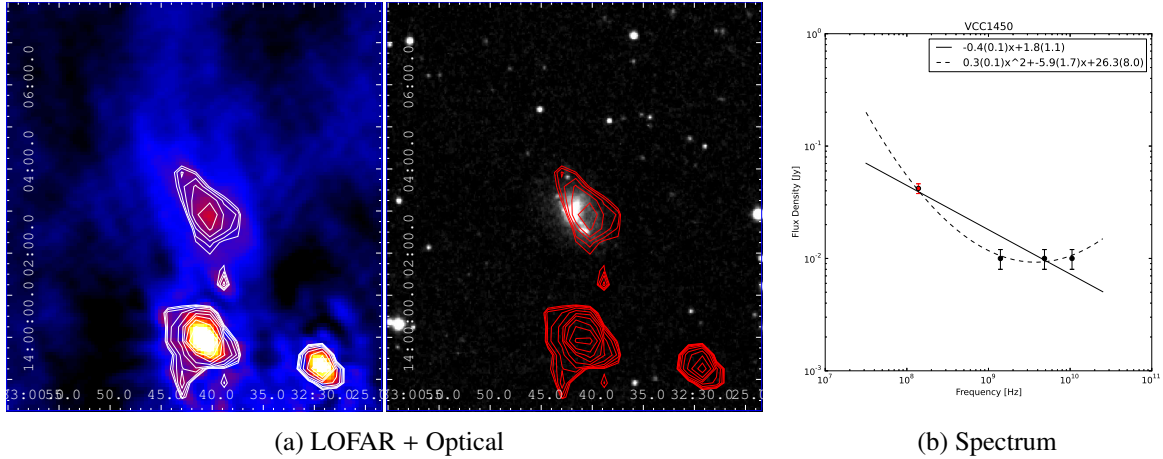
Figure 5.14: VCC 1450, image as explained in Fig. 5.6. The sharp steepening in the spectrum at low frequencies could be due to different emission mechanisms which become dominant at those frequencies. Most likely, at low-frequencies, synchrotron emission from supernovae remnants is the dominant effect.

**VCC 1632 (M89)**   VCC 1632 is classified as borderline between Seyfert galaxies and LINERs (Cappellari et al. 1999) and it is the only elliptical galaxy of the sample, beside the two radio galaxies M84 and M87. Its emission is rather compact (almost unresolved with LOFAR), and is likely entirely due to the AGN activity. From the spectrum I recovered a spectral index of $-0.5$, that is a common values for the radio emission in the core of active galaxies.

**VCC 1673/1676**   This pair of galaxies are in the early stage of the interaction. Their CO and HI gas distributions suggest VCC 1673/1676 are surely colliding (Kaneko et al. 2010). In the subsequent analyses we threat these galaxies as a single radio source, given the impossibility to disentangle their emissions.

**VCC 1690 (M90)**   VCC 1690 is one of the largest and most Hi deficient galaxies in the Virgo cluster. It has a giant hot gas diffuse (X-ray emitting) halo of $100 \times 100$ kpc (Wezgowiec et al. 2011) and large symmetric radio lobes which extend up to 24 kpc from the galactic disc. The lobes are not powered by an AGN, but probably by a nuclear starburst that occurred $\sim 30$ Myr ago (Chyzy et al. 2006). The LOFAR image shows small extensions in the direction of these lobes, the fact that LOFAR does not see a much extended emission shows that the lobes have a rather flat spectral index, that is typical of in-situ cosmic ray electron acceleration rather than an old AGN outburst.
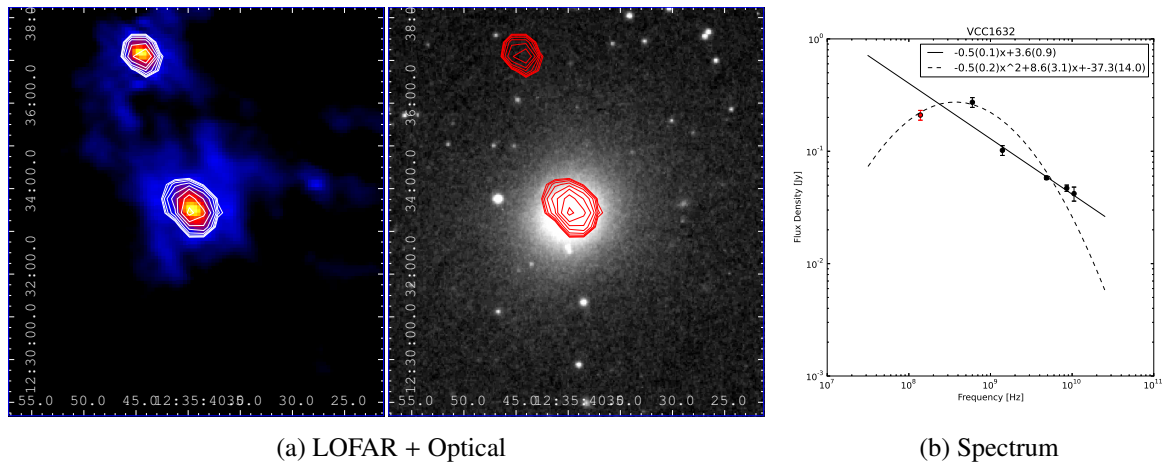
(a) LOFAR + Optical       (b) Spectrum

Figure 5.15: VCC 1632 (M89), image as explained in Fig. 5.6. This is the third elliptical galaxy of the sample with VCC 763 (M84) and VCC 4486 (M87). It shows an almost point-like radio emission with a rather flat spectrum, probably due to an AGN accreting in a radiative inefficient mode.
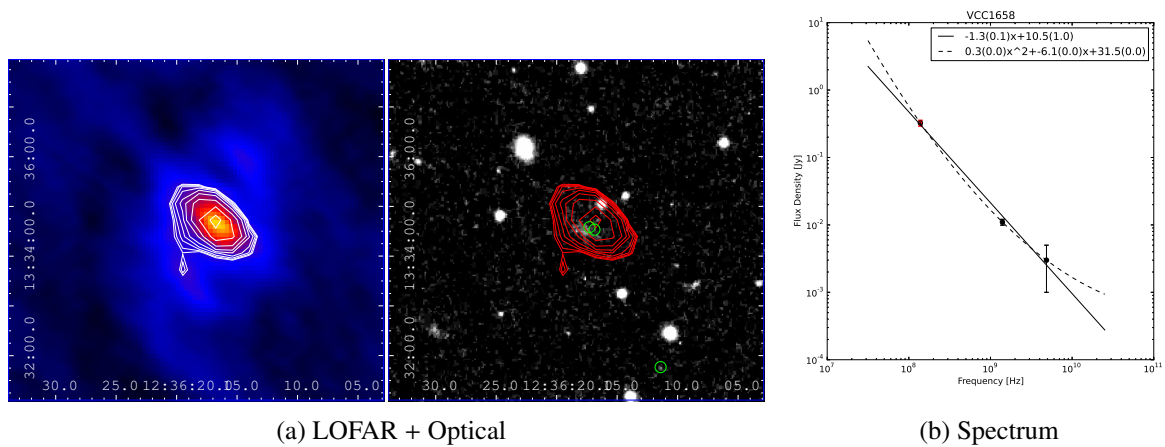


(a) LOFAR + Optical       (b) Spectrum

Figure 5.16: VCC 1658, image as explained in Fig. 5.6. The optical emission of the source is weak. To check the reliability of the matching, the FIRST survey (Becker et al. 1995) detections in the field (green circles) were superimposed in the optical image. Given FIRST high-resolution and good matching, I was confident that LOFAR radio emission is really related to VCC 1658.

**VCC 1727 (M58)** VCC 1727 is classified as a Seyfert galaxy with broad Balmer lines (Barth et al. 2001). The flattening of its spectrum at higher frequencies could be due to the thermal emission being dominant at those frequencies.
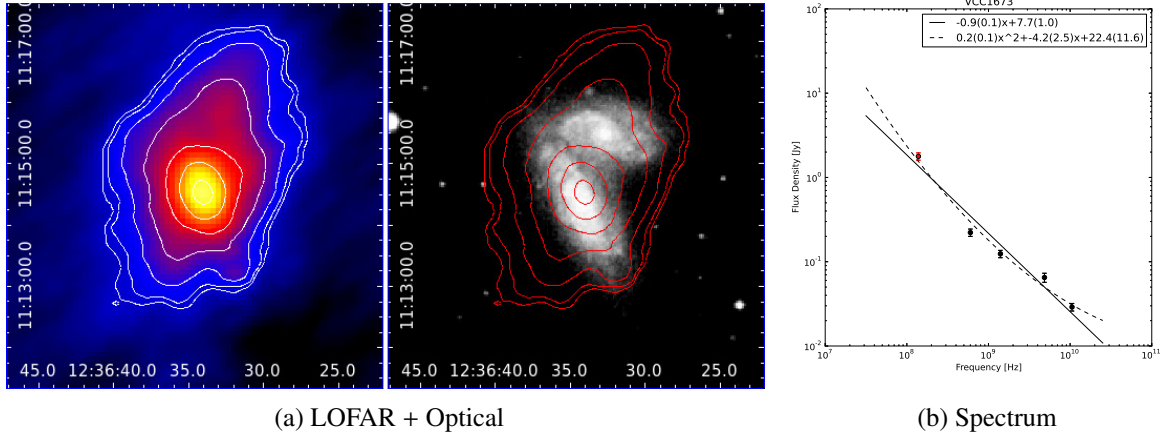
(a) LOFAR + Optical                              (b) Spectrum

Figure 5.17: VCC 1673/1676, image as explained in Fig. 5.6. The two galaxies are in an early stage of interaction that will conclude as a merger.



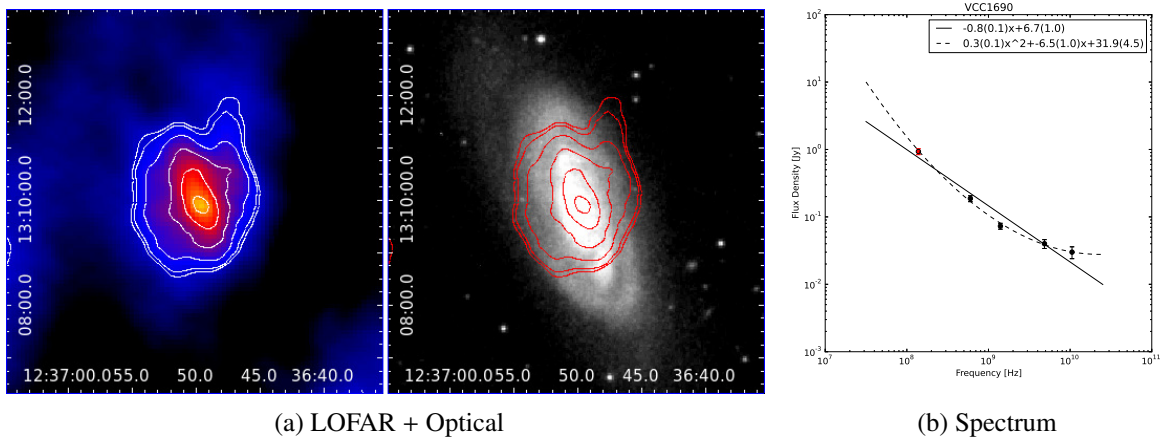(a) LOFAR + Optical                              (b) Spectrum

Figure 5.18: VCC 1690 (M90), image as explained in Fig. 5.6. One of the largest and most Hi deficient galaxies in the Virgo cluster, it has two prominent radio lobes, here not visible, in the direction of the small features in the radio contours on the north-west and south-east directions.

## 5.4   FIR-radio correlation

At these radio frequencies the emission from non-active galaxies is totally dominated by the non-thermal component and to confirm whether the radio-FIR correlation still holds, can give hints on its origin. Previous works also found that the correlation is present down to frequencies of 151 MHz (Cox et al. 1988).

The FIR flux is calculated according to Helou et al. (1988) in the following way

$$F_{\text{FIR}} = 2.58 F_{60\mu} + F_{100\mu} \,, \tag{5.1}$$

where $F_{60\mu}$ is the flux at 60 μm and $F_{100\mu}$ the flux at 100 μm as measured with IRAS and

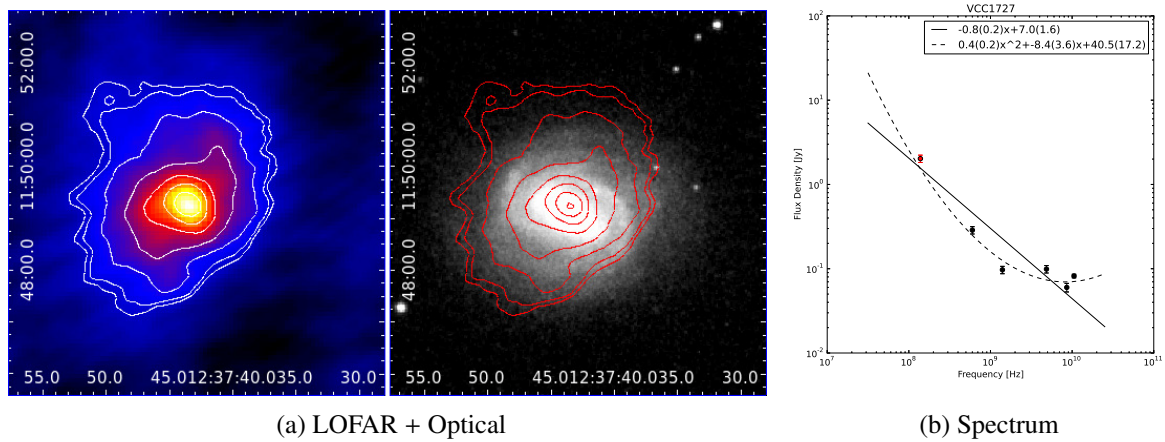(a) LOFAR + Optical                    (b) Spectrum

Figure 5.19: VCC 1727 (M58), image as explained in Fig. 5.6. It is classified as a Seyfert galaxy.
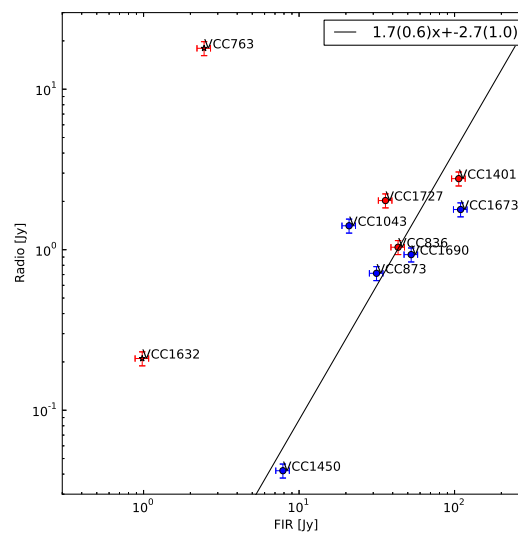


Figure 5.20: FIR-radio plane with the position of the 10 galaxies for which the FIR flux was available. Red points are for objects which have a known active nucleus, star-markers are for early-type galaxies and circles for late-type galaxies. The black line is a linear regression made using only galaxies without an active nucleus (blue points). Errors are set to 10% when unknown.

tabulated in the GOLDmine database[2].

   To study the FIR-radio correlation I used all the galaxies in the sample for which FIR data were available, but VCC 1316 (M87). Their position in the FIR-radio plane is show in Fig. 5.20, some of them present a clear radio excess, most likely due to their core activities. The two obvious outliers are VCC 1632 (M89) and VCC 763 (M84), which are the only elliptical

---

[2]http://goldmine.mib.infn.it – Gavazzi et al. (2003)

galaxies. The first has an AGN classified as Seyfert while the second is an FR I radio galaxy, consequently its strong radio emission is definitely due to AGN activity. I identified all the other galaxies with a know nuclear activity: VCC 836, VCC 1401 and VCC 1727 (M58) are classified as Seyfert galaxy. Removing those objects and the two elliptical galaxies, only five galaxies remain on the plane and they present to a much tighter (although statistically weak) relation with a slope of $1.7 \pm 0.6$. Since all these galaxies are at a similar distance, this relation cannot be driven by a Malmquist bias.

## 5.5   Conclusions

I analysed the radio properties of 15 galaxies of the Virgo cluster that were detected at 138.7 MHz by LOFAR-HBA. Two of these galaxies (VCC 465 and VCC 630) were too faint and close to stronger sources to allow a reliable measurement of the total flux density. The flux density of the remaining 13 galaxies was extracted and used together with data from the literature to generate wide band spectra.

Most of the spectra show an unexpected excess at low frequency where, according to the general idea of free-free absorption, a flattening was expected. In some cases this could be due to the presence of an AGN which enhances the low-frequency emission, increasing the non-thermal to thermal component ratio. The case of VCC 580 is instead particularly intriguing. This galaxy is a BCD and shows a very steep spectrum of $-1.2 \pm 0.1$ that is not related to the presence of any nuclear activity.

I investigated the FIR-radio correlation down to the frequency of 138.7 MHz and, once the active galaxies were removed, I found a good correlation, although my sample were restricted to only 5 objects. The standard interpretation is that the relativistic electrons responsible for the non-thermal radio emission are produced by supernova events. The slope of the correlations is of $1.7 \pm 0.6$, which is above but consistent with the value of $1.3 \pm 0.1$, found by Price & Duric (1992) considering only the synchrotron component of their radio spectra. An increasing of the steepening with wavelength is consistent with the idea that the lower the frequencies the more likely we sample the synchrotron component rather than the thermal component. The FIR and thermal-component are linearly related and related to the star forming rate (SFR) of the galaxy (Price & Duric 1992). The FIR and the synchrotron component instead are connected by a steeper relation, therefore this radio component is proportional to the $\text{SFR}^\gamma$ with ($\gamma > 1$).

When new data will become available, further, more complete studies will be performed. With new LOFAR data we will increase the sample size and the reliability of the measurements. With these and with the great amount of information presents in the archives, we will be able to explore the connection between the radio-FIR relation from low to high radio frequencies.

This relation could likely be more complex than its normal interpretation (Yun et al. 2001). Probably more correctly described as a plane in the $L_{\text{FIR}} - L_{\text{Radio}} - \nu_{\text{Radio}}$ 3-dimensional space, that thanks to the new radio-telescopes can now be sampled continuously.

This first experiment showed the possibility opened by an instruments as LOFAR in studying radio emission also from non-active galaxies. The limiting factor of the work explained in this chapter is definitely the current LOFAR wide-field imaging capabilities. Much better data are expected to come from new LOFAR observations and direction dependant corrections will play a fundamental role in improving their reliability.

<div style="text-align: right;">

# 6

</div>

# Conclusions and the future

In this Ph.D. thesis I have studied active galactic nuclei (AGN) in the low-accreting regime (sometimes called low-luminosity AGN or LLAGN) and their effects on the surrounding environment. This goal has been achieved by using well-known instruments as *Chandra* and the VLA, but also exploiting the capabilities of the next-generation radio-telescope LOFAR.

AGNs in radiative inefficient accreting mode could have a substantial impact on the intergalactic medium properties thanks to the strong kinetic feedback of their radio jets. Furthermore, although globally less luminous, they are by far the dominant AGN population in the local universe. M87, at the centre of the Virgo cluster is a prototype of this AGN family and, being at a distance of ~ 17 Mpc only, can be studied in great detail. M87 nuclear luminosity is many orders of magnitude smaller in comparison to its expected accretion rate (assuming a standard radiative efficiency of $\eta = 0.1$). Conversely, its jet power (estimated in this thesis) is consistent with the hypothesis that a big portion of the accretion energy goes into accelerating the jet and is available to power the feedback mechanisms.

Considering their total electromagnetic emission, LLAGNs are less powerful than bright quasars, therefore more elusive to detect and difficult to study. Nevertheless, in this Ph.D. thesis, I showed how with the observation of a well-selected sample of objects, together with archival data, it is possible to improve our knowledge about this population of AGNs. The main results on this topic is that in the radio–X-ray relation (and so in the fundamental plane of active black holes), LLAGNs have a smaller dispersion and a reduced X-ray production compared to other types of AGN (i.e. Seyfert galaxies and quasars). This can be explained associating X-ray and radio production to the same physical mechanism, i.e. synchrotron emission from the base of the jet. Therefore, LLAGNs lack (at least part of) the typical structures present in AGNs accreting in "quasars mode". The usual emission due to accreting material is not visible, so the accretion model must be different (probably an ADAF disc rather than a Shakura-Sunyaev

disc), while the jet base is visible and its emission is not absorbed by a dusty torus, which could be indeed completely missing in these population. Furthermore, radio steep spectrum LLAGNs have [OIII] emission lines about an order of magnitude more luminous than flat-spectrum sources with similar X-ray luminosity. I argue that the amount of interstellar medium available for interaction in the proximity of the AGN is responsible for this distinction in the radio spectrum and for the difference in the production of the [OIII] line.

In this Ph.D. thesis I have also presented some aspects of the great work carried out in these years on the commissioning of the new LOFAR radio-telescope. When this thesis started in 2009, the first LOFAR stations was just activated and from that moment a completely new approach to radio interferometry started being developed. Thanks to the work described here and similar other works pursued by other students and scientists, in three years we obtained astonishing results. One of these is presented in this Ph.D. thesis: the first LOFAR study of Virgo A in the 15–162 MHz frequency range.

Thanks to these observations we confirmed the view of Virgo A halo as an active and living part of the source and not a relic of past activities. In fact, going down to 25 MHz no previously unseen steep-spectrum features were detected. The source appears instead to be well confined within boundaries that are identical at all frequencies. The first low-frequency spectral index map of the whole Virgo A halo was presented and it shows a steepening of the spectral index where the morphological evidences of flow activities are reduced. The spectral analysis of the extended halo showed that with the assumption of $\alpha_{\rm inj} = -0.6$ as in the core region, none of the tested models is able to fit the data. Instead, $\alpha_{\rm inj} = -0.85$ is required, outside the central cocoon, to explain the spectra. This steepening in the low-frequency end of the spectra moving from the core to the halo can be connected to a strong adiabatic expansion of the plasma bubbles that happens as soon as they leave the dense central region. An equipartition analysis was conducted and an average magnetic field strength of $\simeq 13\ \mu{\rm G}$ was found in the flow regions, while a magnetic field strength of $\simeq 10\ \mu{\rm G}$ is present in the halo regions. A synchrotron ageing analysis provided a global halo age of $\simeq 40$ Myr. The particle age tends to increase with distance from the centre in the flow regions and reaches a maximum of $\simeq 15$ Myr where the flows end, which is about a factor of $\sim 4$ less than the dynamic time of a buoyantly raising bubble. Minimum pressure analysis reveals that the pressure generated by the plasma and the magnetic fields is much less than what is required to sustain the halo against external pressure. Probably, thermal gas is also playing a role in sustaining the halo. Finally, I estimated the jet power to be $6 - 10 \times 10^{44}$ erg s$^{-1}$. This energy supply is 10 to 100 times higher than the X-ray luminosity of the cooling flow region around M87 ($\sim 3 \times 10^{43}$ erg s$^{-1}$) and is therefore able to exceed the radiative cooling of the gas.

To summarize, the extended radio-halo of Virgo A is a composite of many plasma bubbles of different ages. They are inflated in the central cocoon, where clear cavities in the thermal

gas are visible, by the source's powerful jets. As soon as they leave the dense central area, a strong adiabatic expansion shifts their radio emission towards lower frequencies and lower fluxes. Then they buoyantly rise towards the halo outskirts where they disperse. During their motion, the travelling bubbles lift up cold X-ray emitting gas from the centre of the cluster.

I have also explored the radio properties of the detected members of the Virgo cluster, finding that the radio-FIR correlation of star-forming galaxies holds down to the LOFAR frequencies although it is steeper than at the GHz regimes. The reason is probably that low-frequencies radio emission is generated by different mechanisms (synchrotron emission from cosmic rays accelerated by supernovae) than at high-frequencies (thermal *bremsstrahlung* emission).

Future studies on LLAGN will have to consider a multi-wavelength approach, and radio observations (with LOFAR and the expanded VLA) will definitely open the way. With its impressive survey capability and its very low observing frequency, LOFAR should in fact uncover the vast, and mostly unknown, population of LLAGN. But the important information will arrive combining optical data (SDSS) and X-ray surveys (eRosita). My future plans involve indeed merging data from these three complementary surveys and pursue the study of LLAGN physics.

Virgo A is such an extraordinary and complex object that requires a complete independent campaign. To better constrain different synchrotron models and ultimately draw conclusions about the underlying physical mechanisms ruling the interaction between the AGN and the surrounding medium, further analyses have been planned. New LOFAR, GBT and VLA observations have indeed been requested. They will provide the higher angular resolution ($< 5''$, a factor of 2 better than the best map available) maps of the Virgo A halo ever obtained and a continuum coverage from 30 MHz up to 8 GHz. With this information we will be able to further study the many interesting phenomena that make M87 such an impressive object.

# Bibliography

Abazajian, K. N., Adelman-McCarthy, J. K., Agüeros, M. A., & Allam, S. S. 2009, The Astrophysical Journal Supplement Series, 182, 543

Abraham, J., Abreu, P., Aglietta, M., et al. 2007, Science, 318, 938

Akritas, M. G. & Siebert, J. 1996, Monthly Notices of the Royal Astronomical Society, 278, 919

Amato, E. & Arons, J. 2006, The Astrophysical Journal, 653, 325

Avni, Y. 1976, The Astrophysical Journal, 210, 642

Baade, W. & Minkowski, R. 1954, The Astrophysical Journal, 119, 215

Baan, W. A., Fridman, P. A., & Millenaar, R. P. 2004, The Astronomical Journal, 128, 933

Baars, J. W. M., Genzel, R., Pauliny-Toth, I. I. K., & Witzel, A. 1977, Astronomy and Astrophysics, 61, 99

Baldwin, J. A., Phillips, M. M., & Terlevich, R. 1981, Publications of the Astronomical Society of the Pacific, 93, 5

Balmaverde, B., Capetti, A., & Grandi, P. 2006, Astronomy and Astrophysics, 451, 35

Barnbaum, C. & Bradley, R. F. 1998, The Astronomical Journal, 116, 2598

Barth, A. J., Ho, L. C., Filippenko, A. V., Rix, H., & Sargent, W. L. W. 2001, The Astrophysical Journal, 546, 205

Barthel, P. D. 1989, The Astrophysical Journal, 336, 606

Batcheldor, D., Robinson, A., Axon, D. J., Perlman, E. S., & Merritt, D. 2010, The Astrophysical Journal, 717, L6

Beck, R. & Krause, M. 2005, Astronomische Nachrichten, 326, 414

Becker, R. H., White, R. L., & Helfand, D. J. 1995, The Astrophysical Journal, 450, 559

Berti, E. & Volonteri, M. 2008, The Astrophysical Journal, 684, 822

Best, P. N., Kaiser, C. R., Heckman, T. M., & Kauffmann, G. 2006, Monthly Notices of the Royal Astronomical Society, 368, L67

Best, P. N., Kauffmann, G., Heckman, T. M., & Ivezić, v. 2005, Monthly Notices of the Royal Astronomical Society, 362, 9

Bhatnagar, S., Cornwell, T. J., Golap, K., & Uson, J. M. 2008, Astronomy and Astrophysics, 487, 419

Binggeli, B. 1985, The Astronomical Journal, 90, 1681

Biretta, J. A., Sparks, W. B., & Macchetto, F. 1999, The Astrophysical Journal, 520, 621

Biretta, J. A., Stern, C. P., & Harris, D. E. 1991, The Astronomical Journal, 101, 1632

Bîrzan, L. & McNamara, B. 2008, The Astrophysical Journal, 686, 859

Blandford, R. D. & Konigl, A. 1979, The Astrophysical Journal, 232, 34

Blanton, E. L., Randall, S. W., Clarke, T. E., et al. 2011, The Astrophysical Journal, 737, 99

Blundell, K. M. & Rawlings, S. 2000, The Astronomical Journal, 119, 1111

Blundell, K. M., Rawlings, S., & Willott, C. J. 1999, The Astronomical Journal, 117, 677

Bohringer, H. & Nulsen, P. 1995, Monthly Notices of the Royal Astronomical Society, 274, L67

Bolton, J. G., Stanley, G. J., & Slee, O. B. O. 1949, Nature, 164, 101

Bondi, H. 1952, Monthly Notices of the Royal Astronomical Society, 112

Braude, S. Y., Lebedeva, O. M., Megn, A. V., Ryabov, B. P., & Zhouck, I. N. 1969, Monthly Notices of the Royal Astronomical Society, 143, 289

Brentjens, M. A. & de Bruyn, A. G. 2005, Astronomy and Astrophysics, 441, 1217

Bridle, A. H. & Purton, C. R. 1968, The Astronomical Journal, 73, 717

Broos, P. S., Townsley, L. K., Feigelson, E. D., et al. 2010, The Astrophysical Journal, 714, 1582

Brüggen, M. & Kaiser, C. R. 2002, Nature, 418, 301

Brunetti, G., Setti, G., & Comastri, A. 1997, Astronomy and Astrophysics, 325, 898

Buckley, J. & James, I. 1979, Biometrika, 66, 429

Burlon, D., Ajello, M., Greiner, J., et al. 2011, The Astrophysical Journal, 728, 58

Buttiglione, S., Celotti, A., Capetti, A., et al. 2009, Astronomische Nachrichten, 330, 237

Cappellari, M., Renzini, A., Greggio, L., et al. 1999, The Astrophysical Journal, 519, 117

Carilli, C. L., Perley, R. A., Dreher, J. W., & Leahy, J. P. 1991, The Astrophysical Journal, 383, 554

Cash, W. 1979, The Astrophysical Journal, 228, 939

Cavagnolo, K. W., McNamara, B. R., Wise, M. W., et al. 2011, The Astrophysical Journal, 732, 71

Cayatte, V., Balkowski, C., van Gorkom, J. H., & Kotanyi, C. 1990, The Astronomical Journal, 100, 604

Cayatte, V., Kotanyl, C., Balkowski, C., & van Gorkom, J. H. 1994, The Astronomical Journal, 107, 1003

Charlot, S. & Fall, S. M. 2000, The Astrophysical Journal, 539, 718

Chiaberge, M., Capetti, A., & Celotti, A. 2002, Astronomy and Astrophysics, 394, 791

Churazov, E., Forman, W., & Jones, C. 2000, Astronomy and Astrophysics, 794, 788

Churazov, E., Forman, W., Vikhlinin, A., et al. 2008, Monthly Notices of the Royal Astronomical Society, 388, 1062

Churazov, E. & Kaiser, C. 2001, The Astrophysical Journal, 10, 261

Chyzy, K. T., Soida, M., Bomans, D. J., et al. 2006, Astronomy and Astrophysics, 447, 465

Ciardi, B. & Ferrara, A. 2005, Space Science Reviews, 116, 625

Clark, B. G. 1980, Astronomy and Astrophysics, 89, 377, 378

Combes, F., Dupraz, C., Casoli, F., & Pagani, L. 1988, Astronomy and Astrophysics, 203, L9

Condon, J. J. 1992, Annual Review of Astronomy and Astrophysics, 30, 575

Condon, J. J., Cotton, W. D., Greisen, E. W., et al. 1998, The Astronomical Journal, 115, 1693

Cornwell, T. J. 2008, IEEE Journal of Selected Topics in Signal Processing, 2, 793

Cornwell, T. J. & Perley, R. A. 1992, Astronomy and Astrophysics, 261, 353

Cotton, W. D., Mason, B. S., Dicker, S. R., et al. 2009, The Astrophysical Journal, 701, 1872

Cox, M. J., Eales, S. A. E., Alexander, P., & Fitt, A. J. 1988, Monthly Notices of the Royal Astronomical Society, 235, 1227

Croton, D. J., Springel, V., White, S. D. M., et al. 2006, Monthly Notices of the Royal Astronomical Society, 365, 11

David, L. P., O'Sullivan, E., Jones, C., et al. 2011, The Astrophysical Journal, 728, 162

De Zotti, G., Ricci, R., Mesa, D., et al. 2005, Astronomy and Astrophysics, 431, 893

Decarli, R., Gavazzi, G., Arosio, I., et al. 2007, Monthly Notices of the Royal Astronomical Society, 381, 136

Deshpande, A. A. & Radhakrishnan, V. 1994, Journal of Astrophysics and Astronomy, 15, 329

Di Matteo, T., Allen, S. W., Fabian, A. C., Wilson, A. S., & Young, A. J. 2003, The Astrophysical Journal, 582, 133

Dickey, J. M. & Lockman, F. J. 1990, Annual Review of Astronomy and Astrophysics, 28, 215

Done, C. 2010, eprint arXiv:1008.2287

Dunelop, J. S. & Peacock, J. A. 1990, Monthly Notices of the Royal Astronomical Society, 247, 19

Dunn, R. J. H., Allen, S. W., Taylor, G. B., et al. 2010, Monthly Notices of the Royal Astronomical Society, 404, 180

Dunn, R. J. H. & Fabian, A. C. 2004, Monthly Notices of the Royal Astronomical Society, 355, 862

Dunn, R. J. H., Fabian, A. C., & Celotti, A. 2006, Monthly Notices of the Royal Astronomical Society, 372, 1741

Eilek, J. A. & Shore, S. N. 1989, The Astrophysical Journal, 342, 187

Elitzur, M. 2008, New Astronomy Reviews, 52, 274

Elitzur, M. & Ho, L. C. 2009, The Astrophysical Journal, 701, L91

Elvis, M., Wilkes, B. J., McDowell, J. C., et al. 1994, The Astrophysical Journal Supplement Series, 95, 1

Fabian, A. C. 1994, Annual Review of Astronomy and Astrophysics, 32, 277

Fabian, A. C. 1999, Monthly Notices of the Royal Astronomical Society, 308, L39

Fabian, A. C. 2012, eprint arXiv:1204.4114

Fabian, a. C., Sanders, J. S., Taylor, G. B., et al. 2006, Monthly Notices of the Royal Astronomical Society, 366, 417

Fabian, A. C., Vasudevan, R. V., & Gandhi, P. 2008, Monthly Notices of the Royal Astronomical Society, 385, L43

Fabricant, D., Lecar, M., & Gorenstein, P. 1980, The Astrophysical Journal, 241, 552

Falcke, H. & Biermann, P. L. 1995, Astronomy and Astrophysics, 293, 665

Falcke, H., Koerding, E., & Markoff, S. 2004, Astronomy and Astrophysics, 414, 895

Falcke, H. D., van Haarlem, M. P., de Bruyn, A. G., et al. 2007, Proceedings of the International Astronomical Union, 2, 386

Fallows, R. A., Asgekar, A., Bisi, M. M., Breen, A. R., & Ter-Veen, S. 2012, Solar Physics, 90

Feigelson, E. D., Wood, P. A. D., Schreier, E. J., Harris, D. E., & Reid, M. J. 1987, The Astrophysical Journal, 312, 101

Ferrarese, L. & Merritt, D. 2000, The Astrophysical Journal, 539, L9

Ferrari, C., Govoni, F., Schindler, S., Bykov, A. M., & Rephaeli, Y. 2008, Space Science Reviews, 134, 93

Finoguenov, A. & Jones, C. 2001, The Astrophysical Journal, 547, L107

Forman, W., Jones, C., Churazov, E., et al. 2007, The Astrophysical Journal, 665, 1057

Forman, W., Nulsen, P., Heinz, S., et al. 2005, The Astrophysical Journal, 635, 894

Frank, J., King, A., & Raine, D. 2002, Accretion power in astrophysics, Vol. 21

Freeman, P. 2001, Sherpa: a mission-independent data analysis application, Vol. 4477 (SPIE), 76–87

Gallo, E., Treu, T., Jacob, J., et al. 2008, The Astrophysical Journal, 680, 154

Garmire, G. P. 2003, Advanced CCD imaging spectrometer (ACIS) instrument on the Chandra X-ray Observatory, Vol. 4851 (SPIE), 28–44

Garrington, S. T., Leahy, J. P., Conway, R. G., & Laingt, R. A. 1988, Nature, 331, 147

Gavazzi, G. 1989, The Astrophysical Journal, 346, 59

Gavazzi, G., Boselli, A., & Donati, A. 2003, Astronomy and Astrophysics, 400, 451

Gebhardt, K., Bender, R., Bower, G., et al. 2000, The Astrophysical Journal, 539, L13

Gebhardt, K. & Thomas, J. 2009, The Astrophysical Journal, 700, 1690

Ghez, A. M., Salim, S., Weinberg, N. N., et al. 2008, The Astrophysical Journal, 689, 1044

Ghisellini, G., Ghirlanda, G., Tavecchio, F., Fraternali, F., & Pareschi, G. 2008, Monthly Notices of the Royal Astronomical Society, 390, L88

Giovanelli, R. & Haynes, M. P. 1985, The Astrophysical Journal, 292, 404

Goulding, A. D., Alexander, D. M., Mullaney, J. R., et al. 2011, Monthly Notices of the Royal Astronomical Society, 411, 1231

Gull, S. 1973, Nature, 244, 80

Gültekin, K., Richstone, D. O., Gebhardt, K., et al. 2009, The Astrophysical Journal, 698, 198

Gunn, J. E. & Gott, J. R. 1972, The Astrophysical Journal, 176, 1

Hamaker, J. P., Bregman, J. D., & Sault, R. J. 1996, Astronomy and Astrophysics Supplement, 117, 137

Hardcastle, M. J., Cheung, C. C., Feain, I. J., & Stawarz, L. 2009, Monthly Notices of the Royal Astronomical Society, 393, 1041

Hardcastle, M. J., Evans, D. A., & Croston, J. H. 2006, Monthly Notices of the Royal Astronomical Society, 370, 1893

Harris, D. E., Cheung, C. C., Stawarz, L., Biretta, J. A., & Perlman, E. S. 2009, The Astrophysical Journal, 699, 305

Hassall, T. E., Stappers, B. W., Hessels, J. W. T., et al. 2012, Astronomy and Astrophysics, 543, A66

Heald, G., McKean, J., Pizzo, R., et al. 2010, eprint arXiv:1008.4693

Heckman, T. M. 1980, Astronomy and Astrophysics, 87, 152

Heckman, T. M., Kauffmann, G., Brinchmann, J., et al. 2004, The Astrophysical Journal, 613, 109

Heckman, T. M., Ptak, A., Hornschemeier, A., & Kauffmann, G. 2005, The Astrophysical Journal, 634, 161

Heinz, S. & Sunyaev, R. A. R. 2003, Monthly Notices of the Royal Astronomical Society, 343, L59

Helou, G., Khan, I. R., Malek, L., & Boehmer, L. 1988, The Astrophysical Journal Supplement Series, 68, 151

Hillas, A. M. 1984, Annual Review of Astronomy and Astrophysics, 22, 425

Hine, R. G. & Longair, M. S. 1979, Monthly Notices of the Royal Astronomical Society, 188, 111

Ho, L. C. 2008, Annual Review of Astronomy and Astrophysics, 46, 475

Ho, L. C., Filippenko, A. V., Sargent, W. L. W., & Peng, C. Y. 1997, The Astrophysical Journal Supplement Series, 112, 391

Ho, L. C. L. 2002, The Astrophysical Journal, 564, 120

Hobson, M. P. & Baldwin, J. E. 2004, Applied Optics, 43, 2651

Högbom, J. A. 1974, Astronomy and Astrophysics Supplement, 15, 417

Hopkins, P. F., Hernquist, L., Cox, T. J., et al. 2006, The Astrophysical Journal Supplement Series, 163, 1

Intema, H. T., van der Tol, S., Cotton, W. D., et al. 2009, Astronomy and Astrophysics, 501, 1185

Isobe, T., Feigelson, E., & Nelson, P. 1986, The Astrophysical Journal, 306, 490

Jaffe, W. J. & Perola, G. C. 1973, Astronomy and Astrophysics, 26, 423

Jaroszynski, M., Abramowicz, M. A., & Paczynski, B. 1980, Acta Astronomica, 30, 1

Kaneko, H., Kuno, N., Iono, D., et al. 2010, Galaxy Wars: Stellar Populations and Star Formation in Interacting Galaxies ASP Conference Series, 423, 26

Kaplan, E. & Meier, P. 1958, Journal of the American statistical association, 53, 457

Kardashev, N. S. 1962, Soviet Astronomy, 6, 317

Kassim, N. E. N., Perley, R. A., Erickson, W. C. W., & Dwarakanath, K. S. K. 1993, The Astronomical Journal, 106, 2218

Kazemi, S., Yatawatta, S., Zaroubi, S., et al. 2011, Monthly Notices of the Royal Astronomical Society, 414, 1656

Kellermann, K. I., Pauliny-Toth, I. I. K., & Williams, P. J. S. 1969, The Astrophysical Journal, 157, 1

Kewley, L. J., Dopita, M. A., Sutherland, R. S., Heisler, C. A., & Trevena, J. 2001, The Astrophysical Journal, 556, 121

Kewley, L. J., Groves, B., Kauffmann, G., & Heckman, T. 2006, Monthly Notices of the Royal Astronomical Society, 372, 961

King, A. 2005, The Astrophysical Journal, 635, L121

Komatsu, E., Smith, K. M., Dunkley, J., et al. 2011, The Astrophysical Journal Supplement Series, 192, 18

Komissarov, S. S. & Gubanov, A. G. 1994, Astronomy and Astrophysics, 285, 27

Körding, E. G., Jester, S., & Fender, R. 2006, Monthly Notices of the Royal Astronomical Society, 372, 1366

Kraft, R. P., Burrows, D. N., & Nousek, J. A. 1991, The Astrophysical Journal, 374, 344

Krolik, J. H. & Di Matteo, T. 1999, American Journal of Physics, 68, 489

Laing, R. A. 1988, Nature, 331, 149

Laing, R. A., Jenkins, C. R., Wall, J. V., & Unger, S. W. 1994, The First Stromlo Symposium: The Physics of Active Galaxies. ASP Conference Series, 54, 201

Laing, R. A. & Peacock, J. A. 1980, Monthly Notices of the Royal Astronomical Society, 190, 903

Leshem, A., van der Veen, A., & Boonstra, A. 2000, The Astrophysical Journal Supplement Series, 131, 355

Lightman, A. P. & Eardley, D. M. 1974, The Astrophysical Journal, 187, L1

Longair, M. S. 1994, High energy astrophysics. Vol.2: Stars, the galaxy and the interstellar medium

Lonsdale, C. 2004, Calibration approaches, Tech. rep., MIT Haystack

Lynden-Bell, D. 1969, Nature, 223, 690

Mann, G., Vocks, C., & Breitling, F. 2012, in EGU General Assembly, 1305

Marconi, A. & Hunt, L. K. 2003, The Astrophysical Journal, 589, L21

Massardi, M., Bonaldi, A., Negrello, M., et al. 2010, Monthly Notices of the Royal Astronomical Society, 404, 532

Matsushita, K., Belsole, E., Finoguenov, A., & Boehringer, H. 2002, Astronomy and Astrophysics, 386, 77

McNamara, B., Wise, M., & Nulsen, P. 2000, The Astrophysical Journal, 534, L135

Merloni, A. & Heinz, S. 2008, Monthly Notices of the Royal Astronomical Society, 388, 1011

Merloni, A., Heinz, S., Matteo, T. D., & Matteo, D. 2003, Monthly Notices of the Royal Astronomical Society, 345, 1057

Miley, G. 1980, Annual Review of Astronomy and Astrophysics, 18, 165

Miley, G. & Breuck, C. 2008, The Astronomy and Astrophysics Review, 15, 67

Million, E. T., Werner, N., Simionescu, a., et al. 2010, Monthly Notices of the Royal Astronomical Society, 407, 2046

Mills, B. 1952, Nature, 170, 1063

Misner, C. W., Thorne, K. S., & Wheeler, J. A. 1973, Gravitation

Morsony, B. J., Heinz, S., Brüggen, M., & Ruszkowski, M. 2010, Monthly Notices of the Royal Astronomical Society, 407, 1277

Murgia, M. 2001, PhD thesis, Univ. Bologna

Murgia, M., Fanti, C., Fanti, R., et al. 2002, Astronomy and Astrophysics, 46, 307

Murgia, M., Parma, P., Mack, K.-H., et al. 2011, Astronomy and Astrophysics, 526, A148

Mushotzky, R. F. & Smith, B. W. 1980, Highlights of astronomy - International Astronomical Union, 5, 735

Nagar, N. M., Falcke, H., & Wilson, A. S. 2005, Astronomy and Astrophysics, 435, 521

Narayan, R. & Yi, I. 1994, The Astrophysical Journal, 428, L13

Netzer, H. 2008, New Astronomy Reviews, 52, 257

Niklas, S., Klein, U., & Wielebinski, R. 1995, Astronomy and Astrophysics, 293, 56

Noordam, J. E. 2004, in Proceedings of SPIE, Vol. 5489 (SPIE), 817–825

Nousek, J. A. & Shue, D. R. 1989, The Astrophysical Journal, 342, 1207

Offringa, A. R., de Bruyn, A. G., Biehl, M., et al. 2010a, Monthly Notices of the Royal Astronomical Society, 405, 155

Offringa, A. R., de Bruyn, A. G., Zaroubi, S., & Biehl, M. 2010b, eprint arXiv:1007.2089

Offringa, A. R., van de Gronde, J. J., & Roerdink, J. B. T. M. 2012, Astronomy and Astrophysics, 539, A95

Ogle, P., Whysong, D., & Antonucci, R. 2006, The Astrophysical Journal, 647, 161

Osterbrock, D. E. 1989, Astrophysics of gaseous nebulae and active galactic nuclei

Ott, M. & Witzel, A. 1994, Astronomy and Astrophysics, 284, 331

Owen, F., Eilek, J., & Kassim, N. 2000, The Astrophysical Journal, 543, 611

O'Neill, S. M., Tregillis, I. L., Jones, T. W., & Ryu, D. 2005, The Astrophysical Journal, 633, 717

Pacholczyk, A. G. 1970, Radio astrophysics. Nonthermal processes in galactic and extragalactic sources

Panessa, F., Barcons, X., Bassani, L., et al. 2007, Astronomy and Astrophysics, 467, 519

Parma, P., Murgia, M., Morganti, R., et al. 1999, Astronomy and Astrophysics, 16, 7

Perlman, E. S. & Wilson, A. S. 2005, The Astrophysical Journal, 627, 140

Peterson, J. & Fabian, A. 2006, Physics reports, 427, 1

Piran, T. 1978, The Astrophysical Journal, 221, 652

Plotkin, R. M., Anderson, S. F., Hall, P. B., et al. 2008, The Astronomical Journal, 135, 2453

Price, R. & Duric, N. 1992, The Astrophysical Journal, 401, 81

Prieto, L., Garcia, R., Diaz, J., Hernandez, E., & del Teso, T. 2002, Annales Geophysicae, 20, 2077

Randall, S. W., Forman, W. R., Giacintucci, S., et al. 2011, The Astrophysical Journal, 726, 86

Rau, U. & Cornwell, T. J. 2011, Astronomy and Astrophysics, 532, A71

Reber, G. 1940, The Astrophysical Journal, 91, 621

Rees, M. J. 1984, Annual Review of Astronomy and Astrophysics, 22, 471

Reynolds, C. 2003, Physics Reports, 377, 389

Reynolds, C. S., Di Matteo, T., Fabian, A. C., Hwang, U., & Canizares, C. R. 1996, Monthly Notices of the Royal Astronomical Society, 283, L111

Roger, R. S., Costain, C. H., & Bridle, A. H. 1973, The Astronomical Journal, 78, 1030

Roger, R. S., Costain, C. H., & Lacey, J. D. 1969, The Astronomical Journal, 74, 366

Romein, J. W., Broekema, P. C., Mol, J. D., & van Nieuwpoort, R. V. 2010, ACM SIGPLAN Notices, 45, 169

Röttgering, H., de Bruyn, A. G., Fender, R. P., et al. 2003, in Proceedings of the XXI Symposium on Relativistic Astrophysics (Singapore: World Scientific Publishing Co. Pte. Ltd.), 69–76

Rottmann, H., Mack, K.-H., Klein, U., & Wielebinski, R. 1996, Astronomy and Astrophysics, 309, L19

Ryle, M. & Hewish, A. 1960, Monthly Notices of the Royal Astronomical Society, 120, 220

Ryle, M. & Smith, F. G. 1948, Nature, 162, 462

Sanders, D. B., Soifer, B. T., Elias, J. H., et al. 1988, The Astrophysical Journal, 325, 74

Sanders, J. S., Fabian, A. C., Allen, S. W., et al. 2008, Monthly Notices of the Royal Astronomical Society, 385, 1186

Scaife, A. M. M. & Heald, G. H. 2012, Monthly Notices of the Royal Astronomical Society, 423, L30

Schwab, F. R. 1984, The Astronomical Journal, 89, 1076

Shakura, N. I. & Sunyaev, R. A. 1973, Astronomy and Astrophysics, 24, 337

Shang, Z., Brotherton, M. S., Green, R. F., et al. 2005, The Astrophysical Journal, 619, 41

Shi, Y., Rieke, G. H., Hines, D. C., Gordon, K. D., & Egami, E. 2007, The Astrophysical Journal, 655, 781

Shields, J. C. & Filippenko, A. V. 1996, Astronomy and Astrophysics, 311, 393

Sikora, M., Stawarz, L., & Lasota, J. 2007, The Astrophysical Journal, 658, 815

Slee, O. B., Roy, A. L., Murgia, M., Andernach, H., & Ehle, M. 2001, The Astronomical Journal, 122, 1172

Smirnov, O. M. 2011a, Astronomy and Astrophysics, 527, A106

Smirnov, O. M. 2011b, Astronomy and Astrophysics, 527, A107

Smolčić, V., Zamorani, G., Schinnerer, E., et al. 2009, The Astrophysical Journal, 696, 24

Soltan, A. 1982, Monthly Notices of the Royal Astronomical Society, 200, 115

Stappers, B. W., Hessels, J. W. T., Alexov, A., et al. 2011, Astronomy and Astrophysics, 530, A80

Taylor, G. B., Carilli, C. L., & Perley, R. A. 1999, Synthesis Imaging in Radio Astronomy II, Vol. 180

Thompson, A. R., Moran, J. M., & Swenson, George W., J. 2001, Interferometry and Synthesis in Radio Astronomy, 2nd Edition

Tonry, J. L., Dressler, A., Blakeslee, J. P., et al. 2001, The Astrophysical Journal, 546, 681

Tran, H. D., Lyke, J. E., & Mader, J. A. 2011, The Astrophysical Journal, 726, L21

Tremaine, S., Gebhardt, K., Bender, R., et al. 2002, The Astrophysical Journal, 574, 740

Urry, C. M. & Padovani, P. 1995, Publications of the Astronomical Society of the Pacific, 107, 803

Van der Tol, S. 2009, PhD thesis, Delft University of Technology

van der Tol, S., Jeffs, B., & van der Veen, A.-J. 2007, IEEE Transactions on Signal Processing, 55, 4497

van Weeren, R. J., Röttgering, H. J. A., Rafferty, D. A., et al. 2012, Astronomy and Astrophysics, 543, A43

Vanden Berk, D. E., Richards, G. T., Bauer, A., et al. 2001, The Astronomical Journal, 122, 549

Veilleux, S. & Osterbrock, D. E. 1987, The Astrophysical Journal Supplement Series, 63, 295

Vermeulen, R. C., Ogle, P. M., Tran, H. D., et al. 1995, The Astrophysical Journal, 452, L5

Viner, M. R. & Erickson, W. C. 1975, The Astronomical Journal, 80, 931

Vollmer, B., Cayatte, V., Balkowski, C., & Duschl, W. J. 2001, The Astrophysical Journal, 561, 708

Vollmer, B., Soida, M., Chung, A., et al. 2008, Astronomy and Astrophysics, 483, 89

Vollmer, B., Thierbach, M., & Wielebinski, R. 2004, Astronomy and Astrophysics, 418, 1

Walker, R. C., Ly, C., Junor, W., & Hardee, P. 2009, Approaching Micro-Arcsecond Resolution with VSOP-2: Astrophysics and Technologies ASP Conference Series, 402

Wezgowiec, M., Vollmer, B., Ehle, M., et al. 2011, Astronomy and Astrophysics, 531, A44

Whysong, D. & Antonucci, R. 2004, The Astrophysical Journal, 602, 116

Wijnholds, S., van der Tol, S., Nijboer, R., & van der Veen, A.-J. 2010, IEEE Signal Processing Magazine, 27, 30

Willott, C. J., Rawlings, S., Blundell, K. M., Lacy, M., & Eales, S. A. 2001, Monthly Notices of the Royal Astronomical Society, 322, 536

Wilson, A. S. & Colbert, E. J. M. 1995, The Astrophysical Journal, 438, 62

Wright, A. & Otrupcek, R. 1990, PKS Catalog

Young, A. J., Wilson, A. S., & Mundell, C. G. 2002, The Astrophysical Journal, 579, 560

Yuan, F. & Cui, W. 2005, The Astrophysical Journal, 629, 408

Yuan, F., Yu, Z., & Ho, L. C. 2009, The Astrophysical Journal, 703, 1034

Yun, M. S., Reddy, N. A., & Condon, J. J. 2001, The Astrophysical Journal, 554, 803

Zaroubi, S., de Bruyn, A. G., Harker, G., et al. 2012, eprint arXiv:1205.3449

# Acknowledgements

I am grateful to Dr. Andrea Merloni for the time he dedicated to me. I could have not found a better supervisor, not simply a teacher, but also a colleague and a friend. Beside the fundamental flow of knowledge, with him I learned *how* to do science: the relationship with colleagues, the importance of collaborations, the skills in outreaching my research and the curiosity about every sub-branch of the vast field of astronomy. I am grateful to Dr. Guinevere Kauffmann for being a guide. Not many Ph.D. students have the luck to find someone always ready to support him in the challenging word of science. I would like to thank her for the scientific advices and the great freedom given me in travelling and collaborating with people all around the world. This work would have been unfeasible otherwise. I must express my thanks to her and to my official supervisor Prof. Simon White, for providing me the possibility to work in this great environment that is the Max Planck Institute for Astrophysics: the most intellectually interesting, challenging and stimulating place I have ever had the luck to work in.

I am grateful to all the colleagues of the LOFAR collaboration, which taught me the black magic of radio-astronomy and with whom I spent many unforgettable days and nights of hard work. I would also like to thank also all the people which shared these three years of life with me in the beautiful city of Munich. And finally, I would like to thank Stefania, for many many things and principally for her love.

# Publications

**First author papers:**

- de Gasperin, F., A. Merloni, P. Sell, P. Best, S. Heinz, and G. Kauffmann "Testing black hole jet scaling relations in low-luminosity active galactic nuclei." Monthly Notices of the Royal Astronomical Society, 415, 2910-2919 (2011)
- de Gasperin, F. et al. "M87 at metre wavelengths: the LOFAR picture", accepted in Astronomy & Astrophysics (2012)
- de Gasperin, F. et al. "The Virgo field with LOFAR", in prep.

**Co-author papers:**

- Tasse, C. et al. "LOFAR calibration and wide-field imaging" Comptes Rendus Physique 13, 28-32 (2012)
- van Weeren, R. J. et al. "LOFAR Abell 2256 observations at low frequencies" Astronomy & Astrophysics, 543, A43 (2012)
- van Haarlem, M. at al. "LOFAR : The Low Frequency Array", submitted to Astronomy & Astrophysics (2012)

# Francesco de Gasperin

WORK    Max Planck Institut für Astrophysik
Karl Schwarzschild Straße 1
D-85748 Garching, Germany

HOME    Hortensien Straße 2
D-80939 München, Germany

T   +49 176 7014 7173 – mobile
T   +49 89 30000 2196 – work
F   +49 89 30000 2235
✉   fdg@mpa-garching.mpg.de
W   http://voo.it

Born: July 23, 1983 — Varese, Italy
Nationality: Italian

### CURRENT POSITION

*Research associate*, University of Hamburg

### AREAS OF SPECIALIZATION & INTEREST

**Astrophysics:** active galactic nuclei, clusters, galaxy evolution, cosmology
**Computing:** object oriented programming, data analysis
**Radio astronomy:** low frequency, surveys, calibration and imaging techniques, novel technologies

## Research & Education

9/2012
↓
PRES.

**Research associate**

Hamburger Sternwarte
University of Hamburg, Hamburg, Germany

5/2009
↓
9/2012

**Ph.D. in Astrophysics**
*Research project:* "The impact of radio emitting supermassive black holes on their environment: the LOFAR view of the Virgo cluster"
*Supervisors:* Dr. Andrea Merloni & Dr. Guinevere Kauffmann
*Final grade:* 1 (magna cum laude)

Max Planck Institut für Astrophysik, Garching, Germany
Excellence Cluster Universe, Garching, Germany
International Max Planck Research School for Astrophysics (IMPRS)
at the Ludwig Maximilians Universität, Munich, Germany

10/2006
↓
4/2009

**MSc. in Physics, curriculum of Astrophysics**
*Research project:* "Simulations and removal strategies of thermal systematic effects in Planck-LFI"
*Supervisors:* Prof. Davide Maino & Dr. Aniello Mennella
*Final grade:* 110/110 cum laude

Universitá degli Studi di Milano, Milano, Italy

10/2003
↓
10/2006

**Bachelor in Physics**
*Research project:* "Vasculogenesis models by means of statistical mechanical methods"
*Supervisor:* Prof. Giovanni Naldi
*Final grade:* 110/110

Universitá degli Studi di Milano, Milano, Italy

## Grants & Scholarships

5/2009 → PRES.  Three-year Ph.D. scholarship
Max Planck Institut für Astrophysik, Garching, Germany

7/2009 → 9/2009  ASTRON summer school studentship
ASTRON, Dwingeloo, The Netherlands

## Publications & Talks

### JOURNAL ARTICLES

7/2012  DE GASPERIN F. et al. "M87 at metre wavelengths: the LOFAR picture", submitted to A&A

7/2012  VAN WEEREN F. et al. "First LOFAR observations at very low frequencies of cluster-scale non-thermal emission: the case of Abell 2256" A& A, 543, id.A43

1/2012  TASSE C. et al. "LOFAR calibration and wide-field imaging", Comptes Rendus Physique, 13, 28-32

8/2011  DE GASPERIN F. et al. "Testing black hole jet scaling relations in low-luminosity active galactic nuclei", MNRAS, 415, 2910-2919

5/2011  DE GASPERIN F. et al. "Effect of Fourier filters in removing periodic systematic effects from CMB data", A&A, 529, id.A141

### PROCEEDINGS

12/2011  MORGANTI, R. et al. "LOFAR: opening a new window on low frequency radio astronomy" proceedings of the 11th Asian-Pacific IAU Meeting

3/2011  HEALD, G. et al. "LOFAR: Recent imaging results and future prospects" proceedings of the "Diffuse Relativistic Plasmas" conference, Bangalore, IN

3/2011  RÖTTGERING, H. et al. "LOFAR and APERTIF surveys of the radio sky: probing shocks and magnetic fields in galaxy clusters" proceedings of the "Diffuse Relativistic Plasmas" conference, Bangalore, IN

9/2010  MCKEAN, J. et al. "LOFAR: Early imaging results from commissioning for Cygnus A" proceedings of the "10th European VLBI Network Symposium and EVN Users Meeting: VLBI and the new generation of radio arrays" conference, Manchester, UK

6/2010  HEALD G. et al. "Progress with the LOFAR Imaging Pipeline" proceedings of the "ISKAF2010 Science Meeting", Assen, NL

### OTHER WORKS

2/2011  DE GASPERIN F., INTEMA H. AND ORRÚ E. "Estimating GMRT Pointing Errors", technical report

### TALKS & PRESENTATIONS

26/09/2012  **Talk:** "M87 at metre wavelengths: the LOFAR picture", Deutsche Astronomische Gesellschaft meeting, Hamburg, DE

16/07/2012  **Talk:** "M87 at metre wavelengths: the LOFAR picture", Institute seminar, Garching, DE

12/07/2012  **Talk (invited):** "The LOFAR view of the Virgo cluster", DFG Res. Unit 1254 meeting, Mainz, DE

15/05/2012  **Talk (invited):** "M87 at metre wavelengths: the LOFAR picture", LOFAR Cluster meeting, Nice, FR

21/02/2012  **Talk:** "M87 at metre wavelengths: the LOFAR picture", Cosmology seminar, Garching, DE

23/01/2012  **Talk:** "M87 at metre wavelengths: the LOFAR picture", Nijmegen, NL

23/11/2011  **Talk:** "Radioastronomy with LOFAR", IMPRS seminar, Garching, DE

15/09/2011  **Talk (invited):** "The Virgo field with LOFAR", LOFAR first science, Dalfsen, NL

07/07/2011  **Talk:** "Black hole jet scaling relations in Low Luminosity AGN", JENAM, St. Petersburg, RU

07/12/2010  **Talk:** "Scaling relations in Low Luminosity AGN", Cosmology Seminar, MPA, Garching, DE

05/10/2010  **Talk (invited):** "The LOFAR imaging pipeline cookbook", DFG Res. Unit 1254 meeting, Irsee, DE

20/09/2010  **Poster:** "Testing the mode of Black Hole activity with present and future radio data", at the conference: "Evolution of galaxies, their central black holes and large-scale environment", Potsdam, DE

22/07/2010  **Poster:** "Testing the mode of Black Hole activity with present and future radio data", COSPAR, Bremen, DE

22/04/2010  **Talk:** "LOFAR: to see what no man has seen before", IMPRS seminar, Garching, DE

05/11/2009  **Talk:** "LOFAR: new generation radio telescope", Excellence Cluster Ph.D. meeting, Burghausen,

DE

14/10/2009 **Talk**: "LOFAR: the new generation low-frequency radio telescope and its application to the study of black holes", Universe Cluster Science Week, Garching, DE

17/08/2009 **Lecture**: "An introduction to the LOFAR imaging pipeline", given during the first imaging busy week, ASTRON, Dwingeloo, NL

28/09/2009 **Lecture**: "An introduction to the LOFAR imaging pipeline", given during the second imaging busy week, ASTRON, Dwingeloo, NL

25/08/2009 **Talk**: "LOFAR and the effect of the Ionosphere ", final presentation for ASTRON summer-school, ASTRON, Dwingeloo, NL

---
### Scientific activities
---

4/2006 → 10/2006 Computational biophysical models.

4/2008 → 4/2009 ESA satellite *Planck*:

- Characterization of *Planck* 30 GHz radiometers beam-shape.
- Simulation of possible systematic effects that could affect the *Low Frequency Instrument*.
- Developing of removal strategies for these effects (a set of Fourier filters coded in C++).
- Implementation of the developed code in the official *Planck* data reduction pipeline.

5/2009 → PRES. LOFAR as a part of the Survey Key Science Project (commissioner):

- Define a data reduction pipeline and automatising its procedures, interpreting instrumental and software problems.
- Virgo A: observation campaign with LOFAR.
- Virgo A: spectral studies.
- Virgo A field: study of $\sim 350$ sources extracted from LOFAR map and cross-correlation with other catalogues.
- Many commissioning observations and developing of various codes.

5/2009 → PRES. Other works:

- Virgo A: observation campaign with GMRT.
- Study of GMRT pointing error using a new and fast procedure.
- Developing of an algorithm to reconstruct the super massive black hole mass function at any redshift starting from known luminosity functions and from the mass function at redshift zero.
- Multi-wavelength study (emission line properties, radio luminosity, radio spectral slopes and X-ray luminosity) of a sample of low luminosity AGN.

CONFERENCES ORGANISATION

6/2012 LOC/SOC for the "14th LOFAR imaging busy week", Max Planck Institute for Astrophysics, Garching, DE

SCHOOLS & WORKSHOPS

6/2010 12th NRAO Synthesis Imaging Workshop, Socorro, US

6/2009 → 9/2009 ASTRON summer school, Dwingeloo, NL

7/2008 MPI (Message-Passing programming) 7-day course, Catania, IT

## Computer skills

Operating systems: GNU/Linux, Os X
Programming languages: Python, C++ (MPI), IDL, bash, PHP
Scientific packages: CASA, BBS, AIPS, Difmap, HEALPix, GNUPlot
Tools: SQL, LaTeX

## Language skills

**Italian**: native speaker
**English**: fluent (CEF level: Understanding C2, Speaking and Writing C1)
27/10/2008    *IELTS – overall grade: 7*
**German**: basic (CEF level: Understanding A2, Speaking and Writing A1)